Micro-/Nano-Scale Simulation of Multiphase Flow Behaviours for Enhanced Oil Recovery Applications

Jin Zhao

Submitted in accordance with the requirements for the degree of
Doctor of Philosophy

The University of Leeds
School of Chemical and Process Engineering

October 2018

The candidate confirms that the work submitted is her own, except where work which has formed part of jointly-authored publications has been included. The contribution of the candidate and the other authors to this work has been explicitly indicated below. The candidate confirms that appropriate credit has been given within the thesis where reference has been made to the work of others.

Parts of this thesis are based on work as follows which has been either published in academic journals or submitted in reviewing:

Zhao, J. and Wen, D. 2017. Pore-scale simulation of wettability and interfacial tension effects on flooding process for enhanced oil recovery. RSC Advances. 7(66), 41391-41398.

Zhao, J., Yao, G., Ramisetti, S.B., Hammond, R.B. and Wen, D. 2018. Molecular Dynamics Simulation of the Salinity Effect on the n-Decane/Water/Vapor Interfacial Equilibrium. Energy & Fuels. 32(11), 11080-11092.

Zhao, J., Yao, G., Ramisetti, S.B., Hammond, R.B. and Wen, D. 2019. Molecular dynamics investigation of substrate wettability alteration and oil transport in a calcite nanopore. Fuel. 239, 1149-1161.

Zhao, J., Yao, G. and Wen, D. 2019. Pore-scale simulation of water/oil displacement in a water-wet channel. Frontiers of Chemical Science and Engineering. Accepted.

As co-author, the candidate also provided modelling processing, data collection, result analysis and evaluation for the following papers:

Hu, Z., Zhao, J., Gao, H., Nourafkan, E. and Wen, D. 2017. Transport and deposition of carbon nanoparticles in saturated porous media. Energies. 10(8), 1151.

Yao, G., Zhao, J., Ramisetti, S.B. and Wen, D. 2018. Atomistic Molecular Dynamic Simulation of Dilute Poly (acrylic acid) Solution: Effects of Simulation Size Sensitivity and Ionic Strength. Industrial & Engineering Chemistry Research. 57(50), 17129-17141.

Hu, Z., Gao, H., Ramisetti, S.B., Zhao, J., Nourafkan, E., Glover, P. and Wen, D. 2019. Carbon Quantum Dots with Tracer-like Breakthrough Ability for Reservoir Characterisation. Science of the Total Environment. Accepted.

This copy has been supplied on the understanding that it is copyright material and that no quotation from the thesis may be published without proper acknowledgement.

The right of Jin Zhao to be identified as Author of this work has been asserted by her in accordance with the Copyright, Designs and Patents Act 1988.

© 2018 The University of Leeds and Jin Zhao

Acknowledgement

This work was carried out thanks to funding from the European Research Council, China Scholarship Council (CSC) and the University of Leeds.

First and foremost, I would particularly like to express my great thanks to my primary supervisor, Professor Dongsheng Wen, for allowing me to join his research group, for his support, kindness, encouragement and always devoting time in his very busy schedule. I cannot have finished this PhD research without his support. I would also like to extend my gratitude to my co-supervisor, Dr Robert Hammond, for his continual kind, generous support and comments through this doctorate. Both of my supervisors always provided me with guidance and assistance whenever I needed it. The support and mentoring I received from them both are something I will remember always.

Much appreciation to all my officemates and our research group members (past and present). It has been a pleasure to be a member of this research group, which has a collaborative and vibrant environment that has led to much friendship and enjoyment. I would specially like to acknowledge the help, comments and great friendship from Dr Srinivasa Ramisetti and Mr Guice Yao. Collaboration with them provided valuable insight into a wide range of techniques.

I would also like to specially thank my former MSc supervisors, Prof Shanbo Huang and Prof Liang Gong at China University of Petroleum (UPC) for their ongoing care, encouragement and great support. Prof Gong was the one at UPC who identified my potential and encouraged me to start this doctorate journey.

The last but not the least, my sincere thank goes to my beloved parents for their constant motivation and love. This work is for them.

Abstract

Despite the volatility in the energy market, various predications have shown that the demand for oil and gas will continue to rise in the next a few decades. Hence, significant attention has been paid to increase hydrocarbon production using novel methods of enhanced oil recovery (EOR). Although numerous research work reported in the literature on the fundamental mechanisms of EOR, our understanding of multiphase flow behaviors is still very limited at the pore scale, especially for micro/nano EOR related processes.

Firstly, the effects of capillary number, *Ca*, wettability, viscosity and interfacial tension (IFT) on the oil/water flow characteristics in a capillary during the flooding process were numerically investigated using the computational fluid dynamics (CFD) method **at the pore scale**. Volume of fluid (VOF) model was used to capture the interface between oil and water in a pore-throat connecting structure. The results showed that during a water displacement process, an initial continuous oil phase could be snapped off in the water-wet pore due to the capillary effect. By altering the viscosity of the displacing fluid and the IFT between the wetting and non-wetting phases, the snapped-off phenomenon could be eliminated or reduced during the displacement. A flow chart was further developed relating the oil recovery factor with various flow states.

With a focus on the wettability, the second phase of this work looks **at the atomistic scale** using classical molecular dynamics (MD) simulation method to investigate the low salinity effect, which includes i) water salinity effect on the nano-scale water/oil interfacial equilibrium, ii) surface charge and water salinity effects on the wettability variation of a mineral surface, and iii) the wettability effect on oil displacement in a nano-pore via non-equilibrium molecular dynamics (NEMD) simulation. Increasing water salinity showed little effect on the wettability modification of a nano-pore comprised of neutral calcite surfaces, however it affected dipole-ion interactions significantly for charged surfaces, resulting in a more hydrophilic effect due to increased hydration effect of ions at higher salt concentrations. While a partially oil-wet neutral nonpolar calcite surface inhibited the movement of an oil droplet in the pore, greater oil mobility was achieved for dipolar nano-pores, especially at elevated salt concentrations.

Finally, to achieve both simulation efficiency and accuracy, a multi-scale hybrid CFD-MD coupling scheme for EOR applications was developed to resolve **multi-scale features** of multiphase fluid flow dynamics. An open source code, OpenFOAM, was employed for the continuum part of the simulation, and LAMMPS was adopted for the MD simulations. The coupling schemes and data

interfaces were implemented through developing C++ codes based on the OpenFOAM interface. The accuracy of this multi-scale hybrid CFD-MD coupling model was firstly demonstrated through the simulation of Couette flow with LJ argon liquid. An example study was then conducted to probe the effect of water salinity on the multi-scale single phase and multiphase flow dynamics in a calcite nano-pore. The hybrid model showed its good capability to achieve both continuum and atomistic scale phenomenon with great speedup performance as compared to a fully-atomistic simulation.

Consequently, with the identification of the governing parameters and their effects, this work advances our understanding of EOR related multiphase flow processes at both microscale and nanoscale, applicable to both conventional (i.e. sandstone, carbonates) and non-conventional reservoirs (i.e., shale gas, shale oil). The established hybrid scheme allows the simulation extending to a large domain, achieving both atomistic insight and good computational efficiency for multiscale multiphase flow processes.

Keywords: Multiphase flow, computational fluid dynamics, molecular simulation, multiscale coupling, enhanced oil recovery.

Table of Contents

List of Tables

List of Figures

Nomenclature

A	m^2	cross-sectional area
Ca	-	Capillary number, Ca = $u_m \cdot \mu / \sigma$
d	m	capillary diameter
F	$kg \cdot m/s^2$	body force
g	m/s^2	gravitational acceleration
k^*	m^2	permeability
L	m	length
p	Pa	static pressure
q		stress tensor
Q_D	m^3/s	volumetric flow rate of dispersed phase
R	m	capillary radius
S	-	source term
u_m	m/s	mixture velocity

Greek

α	-	volume fraction
μ	kg/m·s	dynamic viscosity
σ	N/m	interfacial tension
ρ	kg/m^3	fluid density
φ	-	porosity

Subscripts

D	dispersed phase
i	fluid phase i
j	fluid phase j
m	two-phase mixture
o	oil

p	phase
vol	volume
w	water

Abbreviations

A to C – Atomistic to Contunuum

C to A – Continuum to Atomistic

CFD – Computational Fluid Dynamics

CSF - Continuum surface force

EMD – Equilibrium Molecular Dynamics

EOR – Enhanced Oil Recovery

G - Gauche

IFT – Interfacial Tension

LJ – Lennard Jones

MC - Monte Carlo

MD – Molecular Dynamics

NEMD – Non-Equilibrium Molecular Dynamics

OOIP - Original Oil in place

PISO - Pressure-Implicit with Splitting of Operators

PRESTO - Pressure-Staggered Option

RDF – Radial Distribution Fuction

RF – Recovery Factor

T - Trans

VOF – Volume of Fluid

Chapter 1
Introduction

This chapter discusses the background, motivation and outline for the research described in this thesis. Section 1.1 gives a brief industrial background of enhanced oil recovery (EOR) and its multi-scale problem nature. The main motivation of the research is described in Section 1.2, highlighting the necessity of a multi-scale model to provide new insights into water/oil flow dynamics for EOR applications. A full structure outline of this thesis is provided in Section 1.3.

1.1 Research Background: Enhanced Oil Recovery

Techniques for EOR have been devoted to overcoming the limitations and problems of current situations. Water flooding is traditionally the preferred recovery technique for most reservoirs, because it is easy and economic (Morrow and Buckley, 2011). The 30-year history of this technology indicates that it is possible to recover an additional 7%-15% after water flooding. It has been concluded from water flooding that four efficiency factors affect the recovery factor RF with the following approximate relationship (Muggeridge et al., 2014; Smalley et al., 2009)

$$RF = E_{PS} \times E_S \times E_D \times E_C \tag{1-1}$$

where *RF* is defined as the volume of oil recovered over the volume of original oil in place (OOIP); E_{PS} is the microscopic displacement efficiency describing the fractions of oil displaced from the pores by injected water; E_S is the macroscopic sweep efficiency, equalling the proportion of the connected reservoir volume swept by injected water, which is principally related to the rock permeability and fluid gravitational segregation; E_D is the connected volume factor representing the proportion of the total reservoir volume connected to wells; E_C is the economic efficiency factor. It can be seen that if each of the efficiency factors is a very respectable 80%, then the overall *RF* is only 40.96%. Increasing overall *RF*, therefore, requires each factor to be increased close to 100%. The target with EOR methods in this project is focused on increasing the microscopic displacement efficiency E_{PS}.

Humans are accustomed to viewing the world at a particular time and length scale (Sayegh et al., 2004), however the physics that underpins flow in porous media ranges across orders of magnitude in terms of length and time scales. The theoretical treatments of flow in porous media for enhanced oil recovery are, typically, associated with four different length scales: field scale, core scale, pore

scale, and molecular/atomistic scale, corresponding with the so-called macroscale, mesoscale, microscale, and nanoscale, as shown in Figure 1.1.

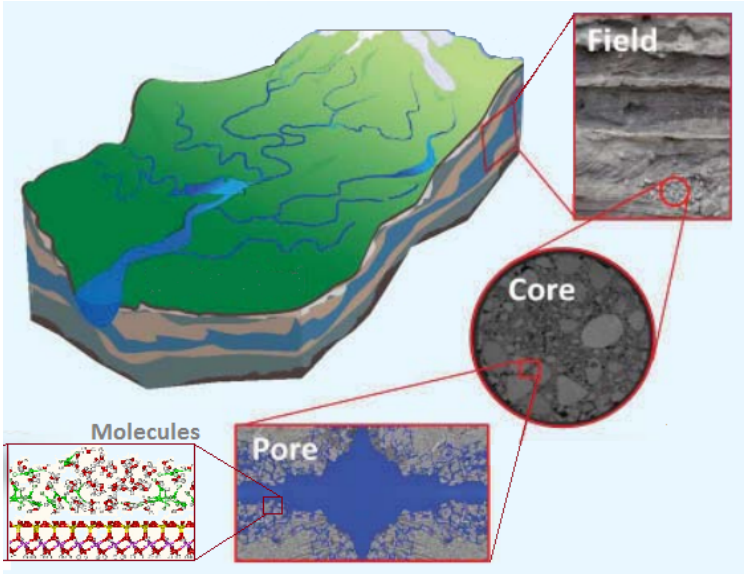

Figure 1.1 Schematic diagrams showing different scales for observations, experiments, and modelling, based on the figure of (Sayegh et al., 2004)

In petroleum engineering applications, (1) field scale is also called reservoir scale, ranging from meters to hundred meters. Oil displacement is dominated by gravity, viscous and capillary forces (Denney, 2009; Zerpa et al., 2005). To improve the sweep efficiency in field scale, it is essential to examine more details in core scale for enhanced oil recovery. (2) Core scale, which is also known as laboratory scale, ranges from centimetres to meters. In this scale, oil displacement is dominated by viscous and capillary forces. (3) Pore scale is defined as scales from micrometres to millimetres with capillary forces dominating the oil displacement (Andrew et al., 2014; Pak et al., 2013; Setiawan et al., 2014). Pore scale modelling is now established as a theoretical compliment to core analysis. It is being used in the oil and gas industry to adjust multiphase flow properties in column/core reservoir models and to predict how these properties vary with rock core type and wettability. (4) Molecular/atomistic scale describes materials from the molecular level. Molecular modelling techniques, such as Molecular Dynamics (MD) or Monte Carlo (MC) methods (Frenkel and Smit, 2001), require a specified force field which defines how molecules are represented and specifies the interactions between them.

1.2 Motivation

Despite the volatility in the energy market at the moment, various predictions have shown that the demand for oil and gas will continue to rise in the next few

decades. However, the understanding of multiphase flow is still limited; especially for micro/nano EOR related processes.

Research reported in the literature has been focused on sandstone reservoirs with pore sizes in the micrometre range, where the Navier-Stokes equation, Fick's law and the Young-Laplace equation are used to describe the multiphase flow dynamics characteristics. However, for many of the unconventional hydrocarbons, such as shale gas and shale oil, the pore space may well be below a few hundred nanometres, which is comparable to the mean free path of the molecules. The validity of these established fundamental equations becomes questionable. There are few experimental probes that can measure the interfacial structure with the accuracy and precision that can be achieved for bulk structures, e.g., using X-ray crystallography. Classical molecular dynamics simulations based on interatomic potentials (also referred to as force fields) are attractive as a means to assess deeper understanding of such interfaces, because of their ability to simulate systems having a large number of atoms over long simulation periods, with statistically significant results that can be compared directly to experimental observations and continuum fluid dynamics simulation.

This project aims to conduct a fundamental study to explore micro/nano-scale multiphase flow phenomenon, with a focus on the fluid-wall interactions and the effect of wettability, to underpin future EOR applications. Both pore-scale and atomistic scale simulation are conducted to investigate the multiphase transport phenomenon at both microscale and nanoscale, with a particular focus on the influence of wettability on multiphase flow (i.e. oil/gas, oil/water, and oil/solid).

1.3 Outline of this Thesis

This thesis is divided into seven chapters, an introduction chapter (Chapter 1), a literature review chapter (Chapter 2), a methodology chapter (Chapter 3), a conclusion chapter (Chapter 7) and three result chapters (Chapters 4-6) for multiscale EOR applications using three numerical simulation methods, as shown in Figure 1.2. Chapter 4 is based on the continuity approach to simulate the oil/water/solid interactions in a microscale pore via the computational fluid dynamics (CFD) methods. This Chapter reveals different influences of various parameters such as the capillary number, wettability, viscosity and interfacial tension (IFT) on EOR during a water flooding process. With a focus on the effect of wettability, Chapter 5 adopts molecular dynamics (MD) simulations to investigate multiphase flow interaction behaviours at the nanoscale. The effect of different water salinities, substrate surface charge and oil displacement in a nano-pore are revealed. To bride the studies between the microscale and the

nanoscale, Chapter 6 develops a multi-scale hybrid CFD-MD coupling scheme to resolve multi-scale features to achieve both simulation efficiency and accuracy. The coupling schemes and data interfaces are implemented through developing C++ codes based on the OpenFOAM interface, and an example study of the effect of salt on the water/oil flow is demonstrated. Conclusion and recommendations are summarized in Chapter 7.

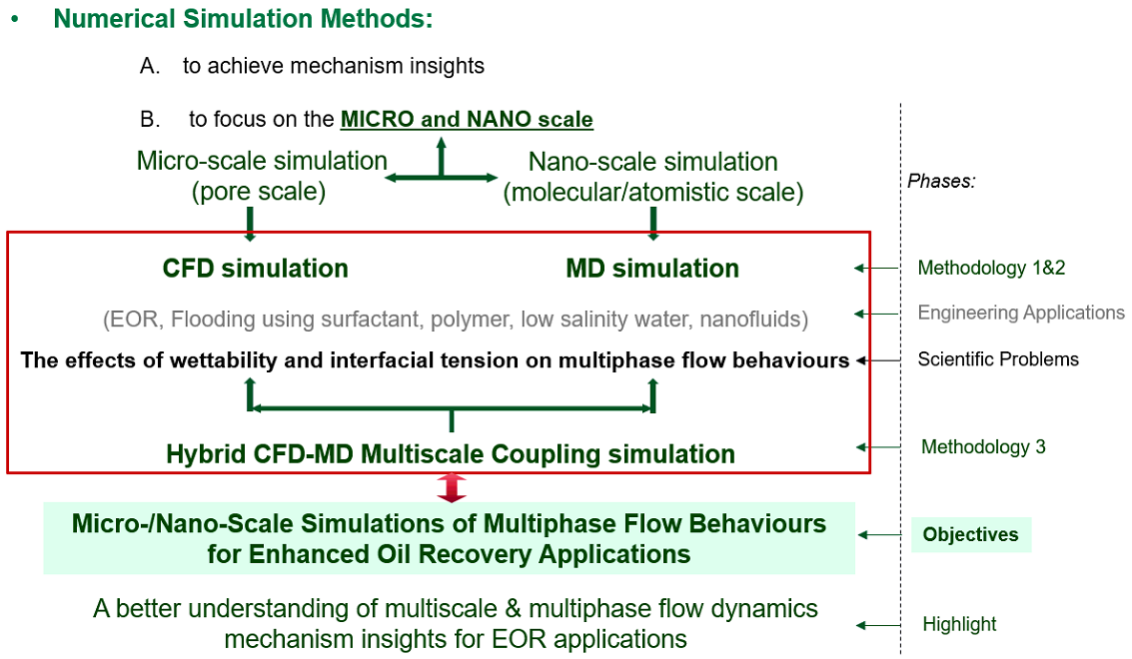

Figure 1.2 Thesis conceptual framework

Chapter 2
Micro/nano-scale modelling for EOR applications: Background and Development

2.1 Introduction

This chapter provides detailed literature review on the micro/nano-scale modelling for EOR applications from three different approaches. Firstly, the development and limitation of the continuity-based pore-scale EOR modelling investigations are discussed in Section 2.2., including multiple pore-scale simulation methodologies. Secondly, to address the microscopic understanding of the governing parameters, state-of-the-art EOR investigations using molecular dynamics simulation methods are presented and discussed in Section 2.3. Section 2.4 reviews the development of multi-scale CFD-MD coupling schemes that could potentially achieve both molecular-scale insight and computational efficiency, and the chapter summary is presented in Section 2.5.

2.2 Pore-scale modelling for EOR applications

2.2.1 Pore-scale EOR background and experimental observations

Although many giant oil reservoirs around the world have already implemented EOR processes, the main challenges, such as low sweep efficiency, costly techniques, possible formation damages, transportation of huge amounts of EOR agents to the fields, especially for offshore cases, and the lack of analysing tools in traditional experimental works and advanced simulation research, hinder the proposed EOR process (Ayatollahi and Zerafat, 2012).

Pore-scale capillary effects on displacements can be quantified by the capillary number:

$$Ca = u\frac{\mu}{\gamma} \tag{2-1}$$

where u is the fluid velocity, μ is the fluid viscosity and γ is the interfacial tension (IFT) between the displaced and displacing fluid (Arriola et al., 1983; Tiab and Donaldson, 2015). Using core-flooding experiments, the effect of capillary number on capillary trapping has been studied, as well as using micro-models and X-ray micro-tomography (CT) imaging techniques. Micro-tomography technology has the capability to image the location of residual oil inside the rock core and measure the contact angle at reservoir conditions, which provides the main input parameters for pore-scale numerical modelling and analysis.

X-ray computed micro-tomography (μ-CT) is an excellent non-destructive technique for capturing 3D digital images of the internal structure of objects. Previous pore-scale EOR experiments have been mainly performed on a mineral core plug for two-phase fluid displacement. This is because, recent advances in X-ray computed micro-tomography techniques now enable us to visualize and monitor these processes in 3D during in-situ core flooding experiments at pore-scale resolution. This provides new information on the spatial and temporal evolution of oil and water phase clusters and films.

In the context of petroleum geoscience, early μ-CT studies (Arns et al., 2002; Dunsmuir et al., 1991; Hunt et al., 1988) focused on characterising the pore structure of reservoir rocks including pore-size, pore shape, orientation, tortuosity and connectivity. With advances in μ-CT instrumentation and increases in computational power, detailed information extracted from μ-CT images of the pore structure of rocks started to be used in pore-scale modelling as a basis for numerical fluid flow simulations.

Subsequent attempts to image fluid saturated core plugs at micro-meter resolution have provided insights into fluid-fluid and fluid-rock interactions as well as the structure of residual oil saturation inside pores and throats of rocks. The first μ-CT images of a two-phase saturated sandstone core plug were obtained at $30\ \mu m$ resolution by Coles et al. (Coles et al., 1998) using a synchrotron light source at Brookhaven National Laboratories.

More recently, a number of researchers (Andrew et al., 2014; Berg et al., 2013; Kumar et al., 2010; Madonna et al., 2013; Pak et al., 2013; Raeini et al., 2015; Ranut et al., 2014; Setiawan et al., 2014) have monitored fluid saturation distributions in porous media using high resolution synchrotron imaging facilities as well as industrial micro-tomography instruments. Although previous experiments claimed that they conducted pore-scale multiphase flooding research with micro-tomography imaging techniques, the general scale of their work was in fact at the laboratory/core scale, instead of the strict definition of “pore scale”. The real effects of wettability, interfacial tension or other key factors on the flooding process would be confused by the interaction among different effective pore-channels in rocks. However, less single pore-scale channel experiments have been performed. Currently, only very limited single pore-scale channel simulation work has been conducted (Lv and Wang, 2015; Otomo et al., 2015).

2.2.2 Chemical EOR technology and its challenge

As a new and advanced technology, chemical EOR has the potential to introduce revolutionary changes in several areas of the oil and gas industry. However, the mechanism describing chemical-EOR method by chemical flooding is still uncertain. Understanding the wettability and interfacial tension effects on the water/oil phase flow interaction in microscopic reservoir pores for EOR purposes can bring significant benefits: improved understanding of the theoretical background and better utilisation of emerging technology.

Using nanotechnology for oil exploration and production is a recent development, where nanoscience and engineering come across. It has developed largely over the past decade and revealed its potential applications in oil and gas industries. Previous observation from lab-scale experiments and molecular scale simulation reported that nanoparticles may alter the reservoir fluid composition and rock-fluid properties to assist in mobilizing trapped oil, which suggests a new mechanism and a new prospective application of nanoparticles for enhanced oil recovery. Wasan and Nikolove (Wasan and Nikolov, 2003) have investigated experimentally the wetting behaviour of nanofluids and proved that the wetting behaviour changes if the liquid contains nanoparticles. This investigation has been further extended by Kondiparty (Kondiparty et al., 2011) that the disjoining pressure gradient drives further spreading of the nanoparticles and it can be large enough to separate an oil droplet from the solid surface. Because the spreading of liquids on solid substrates is of interest in many practical applications and industrial processes, the dynamic motion of three-phase triple lines for nanoparticles was studied both in experimental investigations and theoretical work (Vafaei and Wen, 2010). Actually, the dynamics of contact lines is decided by the driving force due to the out of balance surface tension force, the adhesion force between solid and liquid phase and the resistance force due to viscosity (Sefiane et al., 2008). Recently, Wang et al. (Wang, F. and Wu, H., 2013) found that the local volume concentration plays a significant role on the shape of the nanofluids/oil interface. Large nanoparticle concentration may enhance the effect of the disjoining pressure on the spreading of the nanofluid film. Wang et al. (Wang, F.-C. and Wu, H.-A., 2013; Wang, F.-C. and Zhao, 2013) further observed a significant enhancement in the oil removal efficiency using nanofluids with nanoparticles. Moreover, when the surface charge on each particle exceeds a threshold value, the oil droplet could detach from the solid surface spontaneously and completely. However, the above mechanism has been challenged by some researchers, because they claimed that their experimental results show that nanofluids have little effect on enhanced oil recovery. Contradictory results have

been reported regarding the effect of nanoparticles on EOR, for instance, Hendraningrat et al. (Hendraningrat et al., 2013) showed that the maximum oil recovery was increased by 14.29% of OOIP by using nanofluid; Hu et al. (Hu et al., 2017) reported that the best total cumulative recovery occurred with a total oil recovery of 41.8% of OOIP (original oil in place); whereas Bayat et al. (Esfandyari Bayat et al., 2014) observed only a 2% increase over OOIP for tertiary oil recovery using the same nanofluid.

Three approaches have been used previously for studying the chemical flooding process for EOR: (i) experimental, (ii) molecular dynamics simulation and (iii) numerical computational fluid dynamics simulation. With the experimental approaches, previous experiments mainly focus on the core-scale (or lab-scale) flooding process. Different nanoparticles and surfactant materials have been used as the displacing fluid to investigate their transport breakthrough curve, pressure drop and oil recovery percentages (Gou et al., 2015; Hu et al., 2017; Peng et al., 2017; Yan et al., 2015). The disadvantage of core-scale experiments lies in the limitation of observation resolution during the capture. Nano-scale multiphase modelling has also been conducted by molecular dynamic methods (Kunieda et al., 2012), which can provide more atomistic insights into the mechanism of multiphase interactions. However, the high cost of molecular dynamics simulation method leads to the difficulty of simulating the multiphase flow characteristic due to both the length scale and time scale limitation. For the numerical simulation method, previous computational fluid dynamics simulations mostly focus on study of multiphase flow in the connecting micro-channels of core plugs or microfluidic systems (Afsharpoor et al., 2012; Clemens et al., 2013; Lv and Wang, 2015). The interaction of fluid flows from the crossing channel systems brings huge obstacles to focus on the insight description of the immiscible multiphase flow interaction mechanism.

2.2.3 Numerical investigations of the capillary effect and snap-off phenomenon at the pore scale

At the pore scale, capillary forces play an important role and can prevent a non-wetting phase from flowing. A dominant mechanism for residual trapped oil in porous media is ‘snap-off’. When a non-wetting fluid displaces a wetting fluid in porous media, the non-wetting fluid could break up into separate ganglia due to surface tension, and vice versa. This phenomenon is usually called ‘snap-off’ (Roof, 1970). Capillary force by a snap-off mechanism makes the oil phase unconnected and difficult to mobilize. It is believed trapped oil is restricted from being drawn out of the tight pores because the pressure force across the oil droplet in water or nanofluid flooding is not high enough to overcome the capillary

pressure forces. If the pressure gradient is sufficiently high, the oil droplet is stretch out toward the adjacent pore, squeeze through the constriction, and then flow to the next pore.

The typical microscopic displacement efficiency from a water flood is 70% or less (Doscher and Wise, 1976). This is mainly because of the capillary effects and relative wettability conditions, trapping the oil in the pore space (Buckley and Leverett, 1942; Muskat, 1953). Increasing microscopic displacement efficiency depends on finding ways to reduce capillary effects and modify the rock wettability to the optimum state. When $Ca < 10^{-5}$, flow is dominated by capillary effects and capillary trapping is likely to occur. Capillary effects are also influenced by the wettability of rocks in oil reservoirs. A relative, higher residual oil saturation could be found if the rock is water wet. This is caused by the growth in the water film on the rock surface during water injection, which ultimately leads to the so called 'snap-off', trapping oil droplets within the pores (Roof, 1970).

For single pore-scale simulation of a snap-off process, Roof (Roof, 1970) first presented his criterion based on theoretical and experimental methods, which has since been regarded as the classic criterion for snap-off. The main idea of Roof's theoretical model for circular pores was that when the capillary pressure at the oil front was less than the local capillary pressure at the throat of the pore, the wetting fluid would flow back into the pore throat leading to snap-off. Roof's results have been also subsequently verified by other researchers. Kiss et al. (Kiss et al., 1982) investigated the dynamic oil/water displacement in pores by means of experiments using microphotography. The results showed that both the extent of hydrodynamic trapped oil and the way it occurred depended on the local geometry. Li et al. (Yu and Wardlaw, 1986) studied the conditions for snap-off in a single pore-throat pair with experiments under quasi-static conditions. The work provided the basis for computer modelling of two-phase fluid displacement processes in porous media of specified geometry and topology. Based on Roof's snap-off mechanisms for circular pores, Ransohoff et al. (Ransohoff et al., 1987; Ransohoff and Radke, 1988) presented his quasi-static criterion for non-circular pores by citing a dimensionless interfacial curvature, which varied for capillaries with different cross-sectional shapes. The snap-off mechanism of the non-wetting fluid in Ransohoff's numerical research was also due to the imbalance between the capillary pressure across the meniscus in the pore body, and the local capillary pressure at the pore throat and was considered as Roof snap-off regardless of the wettability and the flow situation.

Later, Mohammed (Al-Gharbi, M.S. and Blunt, 2003; Al-Gharbi, M.S.H., 2004) presented a dynamic pore-scale network model for modelling drainage and

imbibition processes to predict efficiently the meniscus oscillations and snap-off, which were observed in micromodel experiments. The results showed that with a viscosity ratio greater than one (oil more viscous than water) and high flow rates, a large number of oil ganglia were formed by snap-off. For a viscosity ratio less than one, the oil fingered through the water and there was less snap-off.

Beresnev and Deng (Beresnev and Deng, 2010) proposed a nonlinear dimensionless equation as a purely geometric criterion to describe the dynamics of snap-off and calculated the snap-off time, which was verified by the results of CFD simulations (Deng, 2010). The comparison between the theoretical and numerical results showed that if the geometric criterion were satisfied, it could be expected to be sufficient to complete snap-off. Deng et al. (Deng et al., 2014) further extended the Roof and Ransohoff criteria by considering the force imbalance between the pore body and the pore throat when a wetting film exists between the non-wetting fluid and wall. The primary difference in snap-off for the mechanisms between drainage and imbibition conditions was its impact on residual trapping. Recently, Deng (Deng et al., 2015) analysed the dynamics of the wetting/non-wetting interface instability in sinusoidal constricted capillary tubes by using a theoretical model to couple the wetting film thickness to the local capillary number at the pore throat. The analysis showed that snap-off could be inhibited by a sufficiently large local capillary number even in cases where the static snap-off criterion had been met. In previous research, the wetting/non-wetting fluids were mainly super-critical carbon dioxide and water. The application of EOR system for snap-off process simulation is still limited.

2.2.4 Methodologies of pore-scale numerical modelling for EOR applications

Numerical simulations of pore-scale processes not only can improve our understanding of flooding oil processes, but also help to design effective recovery schemes. Several approaches exist to model multiphase flow at pore scale. These approaches can be categorized into two groups: (1) direct simulations, in which the flow equations are directly solved on a discretized pore space extracted from images of rock samples or from analogical samples; (2) network modelling, which is a technique to approximate a porous medium as an interconnected network of pores and pore throats; here simplified flow equations are solved in an idealized pore-network derived from the real geometry (Blunt et al., 2013).

Since Fatt et al. (Fatt, 1956) first presented network models in 1956, pore-network modelling has been largely used to investigate pore-scale processes. The comparison between quasi-static pore-network models and experiments showed that they could predict multiphase flow characteristics (Blunt et al., 2002; Joekar

Niasar et al., 2009; Lerdahl et al., 2000). In pore-network modelling methods, pore invasion is controlled by a certain number of filling rules that often rely on quasi-static considerations. This method has advantages of computational efficiency and allowing consideration of relatively large numbers of pores. However, the continuous increase in computational facilities over the sixty years has made it possible to use several alternative methods that explicitly describe the pore geometry and interface between fluids. In the meantime, although some current pore-network models are able to account for dynamic effects and reproduce some new features of the displacement structures (e.g., fractal dimensions, distributions of the sizes of trapped clusters) for large capillary numbers (Aker et al., 2000a; Aker et al., 2000b), their validity is still always limited due to a number of simplifying assumptions introduced in this network modelling method (Ferrari and Lunati, 2013; Meakin and Tartakovsky, 2009).

Direct models include Lagrangian particle-based (mesh-free) methods, such as smoothed particle hydrodynamics (SPH), and mesh-based methods, such as lattice-Boltzmann method (LBM), finite element method (FEM).

One of the most commonly used of these alternative approaches is the lattice-Boltzmann method (LBM), in which particles move and collide on a discrete lattice, the average motion of a large number of particles is solved from application of the Navier-Stokes equations (He and Luo, 1997; Shan and Chen, 1993). Viscosity, surface tension and contact angle are modelled by means of special forces between the lattice nodes. Porter et al. (Porter et al., 2009) found that there was good agreement between interfacial areas calculated in column scale experiments and LBM simulations during drainage, but there were more discrepancies during imbibition; Vogel et al. (Vogel et al., 2005) simulated pressure-saturation curves using a full morphology model, pore-network model and LBM model, respectively, and found good correspondence between all three approaches; Schaap et al. (Schaap et al., 2007) applied a multiphase LBM model to simulate the flow through a geometry obtained from micro-tomographic data, and found encouraging agreement between observed and simulated water-air pressure-saturation characteristics, but less satisfactory results for a water-Sotrol system. Otomo et al. (Otomo et al., 2015) simulated the oil slug displacement in a sinusoidal channel with an effective LBM multi-component model. The main drawback was the ambiguity of the relationships between internode forces and physical parameters. Moreover, numerical instability issues arose gradually in case of multiphase flow simulations.

The smoothed particle hydrodynamic method (SPH) is a fully Lagrangian particle method, which has many advantages for modelling multiphase flow in porous

media (Bandara, U. et al., 2013; Monaghan, 1994). In particular, SPH does not require complex interface tracking schemes and it is free of numerical dispersion. Similar to LBM, fluid-fluid and fluid-solid interactions are accounted for by adding special forces between different particles. SPH has a wide range of applications in simulating droplet flow characteristic (Tartakovsky and Meakin, 2005) and the capillary trapping mechanism (Bandara, U. et al., 2013; Bandara, U.C. et al., 2011). However, the result comparison between SPH simulation and experiments is still limited due to the much smaller domain considered in simulations compared with experiments.

To model flow through porous media, computational fluid dynamics (CFD) can be used to solve first-principles equations (e.g. Momentum equations and Continuity equation) and can give accurate results. Traditional CFD methods perform direct numerical simulations based on a straightforward discretization of Navier-Stokes equations on a Eulerian mesh. It not only develops highly refined numerical methods, but also allows dealing with large density and viscosity ratios (Meakin and Tartakovsky, 2009). This method couples an efficient Navier-Stokes solver with a tracking method or a capturing method to describe the configuration of interfaces. Despite its superior numerical efficiency and the conceptually straightforward extension of CFD to pore-scale modelling, the implementation for multiphase flow is much more complex than previous approaches. A Navier-Stokes solver has to be coupled with an interface-capturing or interface-tracking method, which is used to describe the configuration of flow interfaces.

An interface tracking method (Fukai et al., 1995; Tryggvason et al., 2001) based on Lagrangian algorithms is normally not well suited to describe flows with interfaces undergoing complex deformations (such as coalescence or break up); in contrast, interface capturing methods based on Eulerian algorithms are more appropriate for complex interface motion. Interface capturing methods, such as Volume of Fluid (VOF) or Level-Set method (LSM), are normally preferred to interface tracking algorithms because they employ static meshes and are more appropriate to model complex interface deformations (Ferrari and Lunati, 2013).

The VOF method was first introduced by Hirt and Nichols (Hirt and Nichols, 1981), and treats the immiscible phases as a single fluid with variable properties. The distribution of the phase is described by a fluid function that carries information about the phase present, and the interface is identified as the region in which the gradient of the fluid function is nonzero. In the presence of solid obstacles, the VOF method can naturally account for the contact angle by imposing appropriate boundary conditions to the direction of the fluid-function gradient at the solid wall and capture all relevant mechanisms, which include hysteresis of the contact

angle and film flow (Afkhami et al., 2009; Brackbill et al., 1992; Tomin and Lunati, 2013).

Recently, a VOF method has been used to model experiments of single and two-phase flow in porous media: Yang et al. (Yang et al., 2013) compared steady state single-phase pore velocity in bead pack with magnetic resonance observations and found very similar spatial patterns; Horgue et al. (Horgue et al., 2013) studied the spreading of a liquid jet in a small array of cylinders and the VOF simulation results showed good agreement with experiments; Ferrari and Lunati (Ferrari and Lunati, 2013) demonstrated that the VOF method could correctly model the transition process during stable displacement and viscous fingering under drainage. Lv et al. (Lv and Wang, 2015) investigated the hot water displacement process inside a two-dimensional pore-throat structure using a VOF method.

Overall, the VOF method is able to model multiphase flow through porous media with sub-pore resolution and naturally describes flow interface phenomena, such as viscous deformation of the meniscus, snap-off and coalescence, jumps and abrupt reconfiguration of the interface. Although it is more expensive than traditional pore-network models, the VOF method only relies on conservation principles, classic surface-tension model and contact-angle model. The fact that no additional modelling assumption is required, is an obvious advantage when numerical pore-scale simulations are used to investigate the relationship between pore-scale and Darcy-scale variables and to test macroscopic models. Compared to other methods providing pore-scale resolution (e.g., SPH or LBM techniques), VOF method could also model the physical properties of the fluids (typically viscosity, density, and wettability), which guarantees a faithful description of the flow characteristic.

2.2.5 Objectives of present work with pore-scale simulations

Having reviewed the potential modelling approaches, the VOF method was to model the physical properties and transport of the multi-phase fluid flows in the present work, in order to guarantee a reliable description of the flow dynamic characteristic at pore scale. Previous CFD simulations have mostly focused on modelling multiphase flow in the connecting micro-channels of core plugs or microfluidic systems. The interaction of fluid flows in the crossing channel systems has brought huge obstacles to focus on the insight description of the immiscible multiphase flow interaction mechanism. The effects of wettability, interfacial tension or other key factors on the flooding process have hence been blurred by the interaction among different effective pore-channels in rocks. However, less single pore-scale channel simulation work has been performed.

The complex flow dynamics simulation for the application of chemical EOR technology is still limited. Therefore, a single pore-throat connecting channel is established under water-wet condition in this work; and a parametric study of the effect of viscosity and IFT at the same capillary number on oil displacement is investigated, the aim is to the establishment of a flow map and the identification of the different roles of viscosity and IFT. Moreover, the pore-scale flooding process for both oil-saturated and oil-unsaturated pores is selected for investigation with volume of fluid method for enhanced oil recovery. A single pore body/throat connecting channel is also established to investigate the wettability and interfacial tension effects on the water/oil flow interaction in pore scale. The results shall provide some insights into the basic understanding of the nanoparticles, surfactant, and nanoparticles-surfactant hybrid flooding process for improving oil recovery rate.

2.3 Molecular/Atomistic-scale simulation for low-salinity EOR applications

The mechanisms of wettability modification, especially in the presence of different salts, and the low salinity water flooding technique, are reviewed in this section.

2.3.1 The application of Molecular dynamics simulation on the Low-salinity (LS) EOR technology

Low salinity flooding, i.e. injecting lower-salinity water (usually specified as having a 1:1 electrolyte concentration of less than about 5,000 ppm) into formation water, has been of interest as an EOR technique (Morrow and Buckley, 2011) since the publication of the first experimental evidence by Jadhunandan and Morrow (Jadhunandan, 1990). It was soon found that an enhancement is not observed consistently but is dependent on a number of factors, including connate water saturation, the salinity of connate water, injection water salinity, and wettability (Austad et al., 2011). No less than seventeen recovery mechanisms behind the low-salinity EOR process have been proposed in the literature, but many of them are related to one another (Sheng, 2014). Due to the complexities of oil components and reservoir rock formations, the recovery mechanisms underpinning the low-salinity EOR process are still unclear. Two physical properties which, when manipulated, are influential on low-salinity EOR phenomena are substrate wettability and the interfacial tension (IFT) between the oil and brine when reduced (Nasralla and Nasr-El-Din, 2014). The interfaces between immiscible liquids are therefore fundamental in understanding EOR mechanisms. Interfaces are, by definition, discontinuities in nature but it must also be recognised that there is a fundamental difference between a single interface

considered in isolation, e.g. between two immiscible liquid components in the bulk, and two or more interfaces in very close proximity for example having two solid-surfaces separated by a thin liquid-layer comprised of two immiscible liquid-components such as aqueous electrolyte and a hydrocarbon.

The interfacial tension (IFT) between oil and water is one of the key properties determining the mobility of trapped oil in reservoir rocks (Nicolini et al., 2017; Olajire, 2014; Underwood, T. et al., 2015; Zhang, Haiyan et al., 2010). Experimentally the effect of salts on IFT and consequently on oil recovery efficiency has been investigated for several decades, but with contradictory results. For instance, Aveyard et al. (Aveyard and Saleem, 1976) first reported that the IFT increased linearly for the dodecane-water system as the molality of electrolyte of different kinds is increased except in the case of potassium iodide, which showed a decreasing trend. Later, Ikeda et al. (Ikeda et al., 1992) measured the IFT of water/hexane as a function of sodium chloride concentration using the pendant drop method and showed an increase of IFT when increasing the salt concentration from 0 to 1 molar, which is consistent with results from Badakshan et al. (Badakshan and Bakes, 1990) and Cai et al. (Cai et al., 1996). In contrast, Serrano et al. (Serrano-Saldaña et al., 2004) observed fluctuations in IFT values for oil/brine at different salt concentrations, and Alotaibi et al. (Alotaibi and Nasr-El-Din, 2009) indicated that low salinity did not always reduce the IFT of water/n-dodecane. After reaching equilibrium at five minutes of elapsed time, the IFT of the 5 wt% NaCl solution decreased in contrast with two other concentrations 2 and 10 wt% respectively. The exact causes of such contradictory observations regarding the effect of salts on IFT remain unclear and require fundamental insights at the molecular level. To this end, a few experimental studies at the molecular scale have been carried out at liquid/solid interfaces, e.g., by X-ray crystallography, to understand the properties of water molecules located next to hydrophobic surfaces, including the orientation of water molecules and their hydrogen bonding interactions (Fenter, Paul et al., 2013; Khusainova et al., 2015). However, experimental measurements for liquid-liquid interfaces at nanoscale are still very difficult to achieve because such interfaces are diffuse in comparison with solid/liquid interfaces. Consequently, experimental measurements at liquid/liquid interfaces are often associated with large uncertainties, and the detection of the influence of structural properties of oil at the interface is challenging.

When the scale is too small to conduct precise experiments with the requirement of high-quality equipment, numerical simulation becomes a more straightforward way. Continuity assumption breaks down as the spatial scale of flows approaches

close to the molecular mean free path. In most cases, the breakdown of the continuum assumption is confined to limited domains, such as fluid/fluid and fluid/solid interfaces. Atomistic descriptions, e.g. MD simulations, are capable of modelling the nano-scale phenomenon. Molecular dynamics simulation is a powerful tool to analyse molecular-scale characteristics of heat and fluid flow, especially determined by dynamics of molecular motion. A number of studies using MD simulation method are performed for the application of heat transfer and fluid flow for enhanced oil recovery, which include thermo-physical properties (such as viscosity and thermal conductivity), interfacial phenomena (such as absorption and condensation), surface tension, and thermal energy and momentum transfer through the interfaces. Generally, molecular-scale analysis of thermal and fluid phenomena is becoming important in the vast movement of science and engineering towards micro/nano scale nowadays. In this background, people are now interested in the fundamental mechanism of thermal and fluid phenomena such as energy and momentum transfer and interfacial phenomena in nano scale. Due to the constraints in conducting accurate experiments in nano scale, the optimization of micro scale flow and heat transfer could profit from the systematic use of molecular-scale modelling tools in nano scale for enhanced oil recovery. Indeed, in combination with recently developed intermolecular potentials, molecular modelling tools can provide precise information about microscopic phenomena and lead to accurate estimation for EOR application.

2.3.2 Liquid-liquid interface investigations for LS-EOR applications by MD method

Some experimental work has been carried out to understand the properties of water next to a hydrophobic surface, including the orientation of water and its hydrogen bonding (Du et al., 1994; Scatena et al., 2001). The interfaces between immiscible liquids are ubiquitous and play an important role in many natural and technological processes. In the past, much experimental work has been carried out to understand the properties of water next to hydrophobic surface, including the orientation of water and its hydrogen bonding. However, there has been little exploration of the structural properties of oil next to the interface, and experimental measurements for liquid-liquid interfaces are still challenging because of the nature of the interface (De Serio et al., 2006).

A few MD studies have been conducted for EOR applications (Turgman-Cohen et al., 2013; Zhang, Hua et al., 2014), including the prediction of thermo-physical properties such as viscosity and thermal conductivity (Bankura et al., 2013; Berendsen et al., 1987; Jorgensen and Tirado-Rives, 1988). On the interfacial

properties, Jungwirth et al. (Jungwirth and Tobias, 2006) investigated the effect of inorganic ions on the air/water interface by MD simulation and found that the simulation results were consistent with experimental evidence. Bresme et al (Bresme et al., 2008) investigated the water-oil interface using molecular dynamics simulations of realistic models of alkanes and water with the intrinsic sampling method. The results showed that the intrinsic structure of water next to the oil phase was remarkably similar to the bare water-vapour interface. D'Auria et al. (Brown et al., 2008; D'Auria and Tobias, 2009) carried out both dissipative particle dynamics (DPD) and classical MD simulations of aqueous solutions of sodium chloride at two different concentrations using polarizable and standard additive force fields, showing that the presence of chloride ions at the air-solution interface is reconcilable with the classical thermodynamics results of Gibbs absorption theory. Sun et al. (Sun, L. et al., 2012) investigated surface tension and structure of salt solutions and clusters and showed that the van der Waals interactions had a large impact on the distribution of the halide anions and that conventional force field parameters needed to be optimized to increase the accuracy of IFT prediction. Buuren et al. (Van Buuren et al., 1993) performed MD simulations on the sensitivity of surface properties to the van der Waals parameters for the decane/ water interface, followed by Zeppieri, Jang, and Mitrinovic et al. (Jang et al., 2004; Mitrinović et al., 2000; Zeppieri et al., 2001). Kunieda et al. (Kunieda, 2012; Kunieda et al., 2012) investigated the spreading of multi-component oils on water with MD simulations, and predicted the IFTs between water and oil-mixture components including decane, toluene and heptane. Zhang et al. (Zhang, C. and Carloni, 2012) investigated the structural and dynamical properties of the NaCl solution/n-decane interface, and found that NaCl salts did cause an increase in the surface tension but did not affect the molecular orientation significantly.

These studies showed that properly used, MD could provide fundamental information, inaccessible via experimental measurements, into the structure properties of interfacial systems. The current MD studies, however, have been exclusively focused on two-phase equilibrium between water and a single oil component, the presence of salts and the vapour phase, which could have a significant influence on the interfacial properties, has not been considered explicitly.

2.3.3 Substrate wettability investigations for LS-EOR applications with MD simulation approach

Since low-salinity water flooding has been of interest as a promising method for EOR, a number of laboratory and field studies have shown that use of low-salinity

water injection could modify the substrate wettability and increase oil recovery rate in sandstone reservoirs (Pereira et al., 2014). Understanding the wettability of mineral surfaces is crucial not only for EOR from conventional and non-conventional oil fields, but also for the geological sealing of oil and gas by cap rocks (Ershadi et al., 2015; Morrow and Buckley, 2011). Though there is general agreement that the EOR effect by low-salinity water flooding is related to modification of substrate wettability creating more hydrophilic surfaces, the underpinning mechanism leading to wettability change is still a matter of debate (Al Shalabi et al., 2014; Myint and Firoozabadi, 2015; Puntervold et al., 2015; Tian and Wang, 2018).

It has been noted that the observed low-salinity EOR effects have been mainly for sandstone reservoirs containing clay minerals, where organic materials initially adsorbed on the clay may be desorbed due to an increase in pH caused by the desorption of active ions in the presence of low salinity (Barnaji et al., 2016; Hilner et al., 2015; McMillan et al., 2016). In addition, a number of mechanisms such as sweep-efficiency improvement, interfacial tension (IFT) reduction, multi-component ionic exchange, and electrical double layer (EDL) expansion (Lashkarbolooki et al., 2016; Nasralla and Nasr-El-Din, 2014) have been proposed to explain the wettability alteration. However, the low-salinity effect in carbonate rocks, the largest share in reservoirs, has been less explored and the results are very contradictory (Ghanbari and Dehghanpour, 2015; Nasralla et al., 2013). It has been shown experimentally that the effects of salinity on carbonates are quite different to those on sandstone cores (Al-Anssari et al., 2016; Sheng, 2014; Yousef et al., 2011). The rock minerology, especially the presence of anhydrite in carbonate rocks, could affect the low salinity effect significantly (Austad et al., 2011; Jackson, M.D. et al., 2016; RezaeiDoust et al., 2011; Shariatpanahi, S. et al., 2016; Shariatpanahi, S.F. et al., 2010). The effect of multiple-component ionic exchange between adsorbed oil components, cations in the salt water and mineral surfaces has been proposed (Zhang et al., 2007), and the effect of IFT reduction was found to be too small to explain the experimental results (Chen et al., 2018; Mahani et al., 2015; Sakthivel et al., 2017).

It is believed that controversies relating to experimental observations of the low-salinity effect are caused, mainly, by the complexities of oil components, the water environment and the minerology of reservoir rocks. From the perspective of design of experiments, many of the key process parameters are closely interrelated making it very challenging to change one while keeping others unchanged, which in turn makes identification of the mechanism difficult. With

rapid advances in high-performance computers and continuous development of force field potentials in the last few decades, molecular dynamics (MD) simulation has been widely used to investigate the complicated interactions between minerals, water, and organic materials at the atomic level. For instance, Wang et al. (Wang, F.-C. and Wu, H.-A., 2013; Wang, F.-C. and Zhao, 2013) investigated oil droplet detachment from virtual solid surfaces and demonstrated wettability alteration by charged hydrophobic nanoparticles, leading to highly efficient removal of oil droplets from solid surfaces. Underwood et al. (Underwood, T. et al., 2015; Underwood, T.R. and Greenwell, 2018) carried out MD simulations of oil detachment from clay surfaces and discussed three mechanisms related to low-salinity flooding, namely EDL expansion, multi-component ionic exchange and pH effects. Zhang et al. (Zhang, L. et al., 2016) simulated the interactions between clay minerals and confined pore fluids and showed that the salt ions adsorption onto clay surfaces could promote surface hydrophilicity. These studies have advanced our understanding of the low salinity effect from an atomistic perspective for clay sandstones, whereas an understanding for carbonate rocks remains very limited.

2.3.4 MD force field development for carbonate rocks

The material type of minerals used in this project is calcite, which has been widely studied due to its relative abundance and significance in terms of occurrence and usage. Calcium carbonate commonly occurs as three distinct anhydrous minerals, namely calcite, aragonite, and vaterite, as well as further polymorphs at high pressure. Calcite and aragonite have well-characterized structures, with the former transforming to the latter at moderate pressure. Vaterite is metastable with respect to calcite and aragonite and readily transforms in contact with solution in many environments. However, it can be important during nucleation and growth as an intermediate phase between amorphous calcium carbonate and the formation of the other two more common polymorphs.

Many research group have helped develop our understanding of calcite surface behaviour using a variety of experimental and theoretical techniques (Fenter, P et al., 2000; Geissbühler et al., 2004; Kerisit et al., 2005; Kerisit et al., 2003; Rohl et al., 2003; Wright et al., 2001). Considerable information concerning the structure of the carbonate-water interface and growth mechanisms has been obtained by experiments. In particular, the advent of atomic force microscopy has allowed dynamical investigations of in situ growth to be performed under a variety of conditions. While such studies can provide a wealth of valuable details, there are limits to the resolution achievable and the certainty of the interpretation, and

therefore computer simulations of the aqueous-mineral interface offer the potential to be a useful, complementary technique to achieve further insights.

Fortunately, recent advances in computing and processor speeds have allowed molecular simulation to become a powerful tool for predictive modelling of interactions in these complex systems. However, the validity of the simulation is rooted in developing the appropriate parameters to accurately describe a given system, especially for a system too large to be accurately described by state-of-art electronic structure methods. Additional complicated are heterogeneous systems, especially those involving interfaces, where molecular dynamics simulations require the transfer of energy and momentum across an interface. For example, cleavage of a calcite crystal leads to a carbonate surface that atomically rearranges in response to water exposure that, in turn, forms hydration layers in response to the structure of the substrate and associated electrostatic potential.

The initial MD research related to calcite focused on developing a force field for $CaCO_3$ both in anhydrous and aqueous conditions (Yuen et al., 1978). The year 1992 saw considerable activity within this area, with three separate force fields being published: Dove et al. (Dove, M. et al., 1992; Dove, M.T. et al., 1992), Pavese et al. (Pavese et al., 1996; Pavese et al., 1992) and Jackson and Price (Jackson, R. and Price, 1992). All three studies took similar approaches, in that the carbonate group was treated as a molecular entity with harmonic angle-bending and improper torsions to supplement the ionic model.

Subsequent to this period, there have been several other attempts to refine the potential model. Fisler et al. (Fisler et al., 2000) retained the shell model approach of Pavese et al (Pavese et al., 1996), but changed the description of the carbonate group to be in the spirit of molecular mechanics (i.e., distinct interatomic potentials for intra- versus intermolecular interactions with cut-offs determined by bonding connectivity). Further refinements were later made to this model by Rohl et al. (Rohl et al., 2003) to yield one of the most refined force-fields for structural and vibrational properties. This model was able to verify the reconstruction of the (1 0 4) surface of calcite under dry conditions. A more sophisticated approach was taken by Thackeray and Siders (Thackeray and Siders, 1998), who used a four-state valence bond approach to capture the distortions and polarizability of the carbonate anion. However, this has also limited its wider use.

Recently, attention has shifted from deriving improved models for calcium carbonate alone to creating force-fields that are capable of describing the interface of this material with water, and even organics, with a view to addressing bio-mineralization. de Leeuw et al. (de Leeuw, NoraáH and Parker, 1997; De

Leeuw, NH and Parker, 2000; De Leeuw, NH et al., 1999; De Leeuw, NH et al., 1998; de Leeuw, N.H. and Parker, 1998) developed a shell model description of water and combined this with the shell model of Pavese et al. (Pavese et al., 1996) to consider the hydrated surfaces of calcite, aragonite and vaterite. Kerisit and Parker (Kerisit et al., 2005; Kerisit and Parker, 2004; Kerisit et al., 2003; Spagnoli et al., 2006a; Spagnoli et al., 2006b) later introduced a revised water model in an attempt to overcome the tendency of the water to freeze at room temperature. Arguably, the best force-field to date for the simulation of calcium carbonate in water is that of Bruneval et al. (Bruneval et al., 2007). Here they blended parameters from both of the models of Rohl et al. and Archer et al. (Rohl et al., 2003), both of which were from the revision of the Fisler et al. (Fisler et al., 2000) model, while adjusting a few further quantities and combining it with a well-tested description of water in the form of the polarizable SWM4- NDP force-field. For the calcium and carbonate to water interactions they maintained the parameters of de Leeuw and Parker. One further force-field is worthy of note, which is that of Freeman et al. (Freeman et al., 2009; Freeman et al., 2007), where parameters were developed with the specific aim of being able to study bio-mineralization. Again, several existing models were combined, with TIP3P being employed for water and de Leeuw and Parker for the cross-species interactions. For calcium carbonate itself, the revised model of Pavese et al. from 1996 was chosen, though for reasons of efficiency the shells were omitted. Furthermore, the oxygen-oxygen interaction was modified by removing the dispersive attraction and adjusting the repulsive parameters to compensate. Julian et al. (Raiteri et al., 2010) stressed the importance of thermodynamics and designed a force field model to specifically model the crystallization and growth of calcite, in contrast to previous studies.

The focus of the majority of these previous studies has been to obtain an accurate description of the solid-state properties of this substance, with particular emphasis on the structure, mechanical hardness and phonon spectra. Recently, with co-workers, some of the present authors have developed a simple, yet accurate, methodology for describing the interface between inorganic minerals and an organic phase: Simulating organic-bio-mineral interfaces has long provided challenges for simulations based on potential parameters. Any successful model must simulate the mineral, the organic molecules, the solvent (usually water), and the interactions among these three groups (cross-term potentials). Cooke et al. (Cooke et al., 2010) reported on its use to study the interface between the (1 0 4) surface of calcite and pure ethanol and validated results by comparing them with atomic force microscopy images of calcite surfaces cleaved in ethanol and in the open lab.

Overall, for nano-EOR in petroleum engineering, the recovery factor does not only relate to the interfacial behaviour between oil and water, but also relate to the wettability between minerals and oil-water system. However, most of previous research focused on the minerals and pure-water interaction behaviours. The investigations for the systems including minerals, organics, water and the salt components for low-salinity EOR applications are still very limited.

2.3.5 Objectives of present work with atomistic-scale simulations

The microscipic mechanisms of wettablity modification, especially in the presence of different salts, are investigated to advance our understanding on low-salinity EOR technology at the molecular/atomistic scale. The salinity effect on the interface between water and oil is investigated in this work using the MD simulation method. Furthermore, the water salinity effects on the wettability alteration of nano-slit pores are studied with EMD simulations. Finally, non-equilibrium MD simulations (NEMD) are conducted to reveal the influence of wettability on the oil transport properties in a nanopore under different salt concentrations of sodium chloride. The HPC platforms, ARC2 and ARC3, in University of Leeds are used to simulate the EOR system to achieve both larger length scale and longer time scale.

2.4 Multiscale coupling simulation techniques

2.4.1 Motivation

Conflicting views on matter as either continuous or discrete date back at least to early Greek philosophy: Aristotle has been taken to represent the continuous point of view and Democritus the discrete, atomistic standpoint. Modern physics has reconciled the conflicting views by considering continuum description as local averages of the underlying, fundamentally discrete, atoms.

Molecular Dynamics (MD) provides a valuable tool for modelling systems at the nanoscale. However, the atomistic modelling of macroscopic problems is still beyond the reach of current MD simulations due to their prohibitive computational requirements. Recently, there has been an increasing interest in simulating dynamical phenomena of multiscale systems. The development of hybrid techniques that combine continuum and atomistic descriptions can alleviate limitations of length and time scales. This can be accomplished by limiting the use of MD to regions where the atomistic scales need to be resolved, while using a continuum-based solver for the remainder of the domain. The computational savings of such a formulation strongly depend on the relative size of the MD

region to that of the continuum, and the extent of the overlap where information is exchanged between the two subdomains.

Such methods are crucial for the proficient advancement and better understanding of micro/nano-scale effects on macro-scale phenomenon with multiple engineering applications, for instance, EOR. Taking low-salinity EOR technology as an example, on the one hand, CFD simulation with continuum assumptions loses some critical details when calculating at the atomistic-scale ions dissolved into low-saline water flooding process; On the other hand, though MD simulation could capture atomistic-scale interaction behaviours, it is limited due to the high computational cost. The optimal option is to apply a hybrid CFD-MD coupling simulation technique to achieve both computational efficiency and accuracy for EOR engineering applications.

2.4.2 The development of hybrid continuum-atomistic model and key challenges

The first hybrid atomistic continuum (HAC) model was proposed by O'Connell and Thompson (O'connell and Thompson, 1995) through combining MD with a continuum approach for fluid dynamics simulation of one dimensional Couette flow. The atomistic region was calculated by MD simulation method and further coupled to a continuum-scale Navier-Stokes based model by an overlap region to ensure the consistency of the flow dynamic variables. Since the initial HAC model proposed by O'Connell and Thompson, it has been further developed from different perspectives of the coupling strategy and the imposition of the boundary conditions, evolving to two and three dimensional flows; Later, the heat transfer was also considered as part of the coupling strategies of the HAC models: Hadjiconstantinou et al. (Hadjiconstantinou and Patera, 1997) developed a method for simulating incompressible flow. A steady channel flow with an obstacle (Hadjiconstantinou and Patera, 1997) and the moving contact-line problem (Hadjiconstantinou, 1999) were simulated and the results were fairly consistent with full continuum or full MD simulations. Later, Flekkoy et al. (Flekkøy et al., 2000) presented a new hybrid method for isothermal, compressible flow based on continuity of mass and momentum fluxes across the MD–continuum interface. Steady Couette flow and steady Poiseuille flow were simulated to demonstrate the method. Nie et al. (Nie et al., 2004) introduced a robust hybrid method, where the continuum solution was obtained by numerically integrating the Navier–Stokes equations with boundary conditions that include information from the MD solution, and the MD equations are integrated with a much smaller time step with boundary conditions obtained using 'constrained dynamics'. The MD equations in the interface region were modified to constrain the mean local

particle velocity to equal the instantaneous continuum velocity, rather than relaxing it over some time scale (O'connell and Thompson, 1995).

Resently, Smith et al. (Smith, E., 2014) proposed the mathematical framework, which allowed a discrete molecular system to be expressed in terms of the control volume (CV) formulation from continuum fluid dynamics. A discrete form of Reynolds' transport theorem was thus obtained allowing both molecular and continuum systems to be expressed in a consistent manner. To link the CFD and MD solvers in a rigorous and physically consistent manner, the CV framework was combined with the variation principles of classical mechanics. In order to provide an efficient and easy-to-use software framework for field users, Ren et al. (Ren et al., 2017) proposed a hybrid atomistic–continuum parallel coupling framework, named HACPar, based on open-source software platforms. The software architecture of the hybrid atomistic–continuum coupling framework was based on geometric decomposition. In depth research was presented on the coupling-oriented parallel issues which may improve the flexibility and efficiency of other multiscale parallel applications. Wang et al. (Wang, Q. et al., 2016) proposed the coupling procedures of the hybrid atomistic-continuum (HAC) method based on geometric coupling under the conventional parallel decomposition. The results of the benchmark case showed the decomposition style under the guiding rules instruction performed better than the default decomposition method. Cosden et al. (Cosden and Lukes, 2013) developed a fully parallelized hybrid atomistic–continuum model to resolve nanoscale features associated with a liquid-vapor phase change. The domain was decomposed into an atomistic domain, where individual atomic interactions are computed, and a continuum domain, where the Navier–Stokes equations are solved. The two domains are coupled through an overlap region in which the solutions in both domains are consistent. The accuracy of this HAC model was demonstrated through the simulation of sudden start Couette flow. Fattah-Hesary et al. (Fattah Hesary, 2017) further developed a coupled CFD-MD scheme for simulating multi-scale (micro- and nano-) fluidic systems. The coupling process involved three domains i.e. CFD, MD and an overlap hybrid region. A commercial continuum code, ANSYS/FLUENT was employed for the continuum part of the simulation, and LAMMPS was adopted for the MD part. Coupling schemes and data interfaces were implemented in ANSYS/FLUENT using its User Defined Function (UDF) capability. In the overlap region a file-based information exchange method was applied between atomistic and continuum fluidic information to define boundary conditions for the continuum region and the appropriate constraint for the atomistic one. The coupling was applied to Couette flow where the fluid-solid interface was modelled at molecular level and, by choosing suitable fluid-solid

interaction parameters, the results were validated by comparing with analytical solutions.

Only simple examples of fluid dynamic cases were used to verify the reliability of all previously proposed CFD-MD coupling process, like steady or unsteady state Couette shear flow, Poiseuille flow, and channel flow passing a rough wall. However, there are few investigations to apply this hybrid CFD-MD coupling approach for EOR applications to address the phenomenon from both continuum and atomistic perspectives.

Four key challenges and the corresponding solutions which must be addressed by any coupling schemes are highlighted and concluded from previous research (Smith, E., 2014):

(1) Determine the spatial relationship between the two regions: The molecular system can be embedded in the continuous system or overlapping part and exist in a separate region. Embedding uses the molecular simulation as a local refinement of the continuum system while using two separate systems, each covers a distinct special region and an overlap between the two regions, allowing a gradual relaxation and agreement between the two different descriptions.

(2) Termination of the MD domain: A restraint mechanism is required at the boundary of the molecular region to prevent the molecules from escaping. This termination could be a generic force (Nie et al., 2004; O'connell and Thompson, 1995), or based on a previous simulation or calculated from the radial distribution function (Werder et al., 2005), or a buffer zone of molecules (Hadjiconstantinou, 1999).

(3) Procedure for averaging the MD region to obtain the continuum boundary conditions: In practise, average values in the discrete region are obtained by summing over time and space to establish them (Allen and Tildesley, 1987) or using the least squares method to fit instantaneous data (Li et al., 1998). The removal of statistical noise is a key issue, as is the choice of which properties are transferred (density and velocity, or stress and fluxes), as well as the averaging methods.

(4) Constraints applied to the molecular region to match properties to the continuum phase: This can be performed by an applied force derived as a constraint using a variational-principle formulation of mechanics (Goldstein, 2011), a numerical favourable control style algorithm (Borg et al., 2010), a selective permeable membrane (Li et al., 1998), or Maxwell's demon type approach (Hadjiconstantinou, 1999). A method of inserting and removing molecules is also required to match the mass flux from the continuum phase.

2.4.3 State variable coupling techniques of multiscale hybrid atomistic-continuum models

There are two main coupling techniques of multiscale hybrid atomistic-continuum models, explicit and implicit coupling, which are introduced in this section: Explicit coupling means that equations in both continuum and molecular domains are solved locally and directly with an exchange between them to evolve the coupled system. For implicit coupling, the entire system is evolved globally solving the equations in both domains together, by iteration and matrix inversion. Various principle algorithms subject to constraints are key to derive physically meaningful coupling schemes.

2.4.3.1 Explicit Coupling

The first attempt at coupling the two descriptions of dense fluids was by O'Connell and Thompson (O'connell and Thompson, 1995). The nanochannel domain was decomposed to describe the proposed hybrid atomistic continuum (HAC) coupling model. Emphasis was placed on ensuring the continuity of thermodynamic and transport properties across the interface between atomistic and continuum descriptions, which was termed as hybrid solution interface (HSI). The mass continuity was attained by using the averaged particle velocities at HSI as the boundary condition of the continuum description. The difficulty arose when trying to link the continuum stress field to an atomistic description to guarantee the momentum continuity. To overcome this difficulty, the average momentum of the overlap particles was relaxed to that of the corresponding continuum fluid element through the application of constraint dynamics. The Couette shear flow case was used to demonstrate the validity of this hybrid scheme using an overlap region mediating between a particle ensemble and a continuum described by the incompressible Navier-Stokes equation. With a full MD computation as a reference, results from this HAC model for velocity and stress field were in close agreement.

One limitation of this HAC model by O'Connell and Thompson is that there was no mass and energy exchange between the discrete and the continuous phases. Moreover, the same timescale in this algorithm was shared by the continuum and discrete equations. Aiming to remove these disadvantages, O'Connell and Thompson's approach was further developed in the paper by Nie et al. (Nie et al., 2004). In O'Connell and Thompson's theory, the constraint was consistent with the continuum boundary condition and was of the form of minimise the difference in momentum between the two regions. Nie et al. (Nie et al., 2004) also introduced mass transfer using a mass flux scheme across the interface with the particle number. The Nie et al. model has been applied to a large coupled simulation by

Yen et al. (Yen et al., 2007). The model of Nie et al has been further extended to include heat transfer by Liu et al. (Liu et al., 2007) in the same group. A further extension of the average force model was deployed by Sun et al (Sun, J. et al., 2010) who applied the same force on all molecules which varied linearly across the overlap region to provide the required velocity profile. Similarly, the temperature was controlled using a series of Langevin thermostats with set points based on the QUICK (Quadratic Upstream Interpolation for Convective Kinematics) scheme.

Except for the different consideration about the constraint force $\boldsymbol{F}^C$, Werder et al. (Werder et al., 2005) suggested that the boundary force $\boldsymbol{F}^B$ can be infinitely large and proposed a modified form which is defined to be zero outside a certain range. Werder et al. (Werder et al., 2005) also proposed an improved form of the molecule trapping force which approximated the structure of the missing fluid base on a pre-calculated Radial Distribution Function $g(r)$ for the system at equilibrium.

So far, the simultaneous evolution of both domains has been considered explicitly (both systems evolve together and exchange data at regular intervals). The boundary conditions at the interface between the domains are specified by the other domain. The major disadvantage of explicit coupling methods is that the time scales of the continuum phase and atomistic phase have to be comparable. Explicit coupling methods are not the only way to couple continuum approach with molecular dynamics. The next section describes at the implicit coupling, where the two systems evolve iteratively until the description at the boundaries agree.

2.4.3.2 Implicit Coupling

The previous methods couple the continuum and atomistic regions explicitly by applying the forces and boundary conditions to enforce agreement between the two regions, which evolve together in time. To overcome the disadvantage that the time scales of the continuum phase and atomistic phase have to be comparable, an alternative implicit coupling approach is proposed to repeatedly re-run multiple realisations of both regions until certain properties agree in the overlap region between the domains.

The mathematical technique for ensuring agreement at the interface between scales was formalised in the work of Hadjiconstantinous and Patera (Hadjiconstantinou, 1999). The assumption was that the coupled simulations were steady or could be modelled as a number of pseudo-steady states. The Schwarz alternating method was an iterative method used to split a domain into connected sub-domains and solve each separately. The solution of each sub-

domain provided the boundary condition for adjacent sub-domains. The iterative scheme ensured close agreement at the boundaries. Over a short run, the molecular simulation converged to a constant value and was used to represent a much longer time step of the continuum phase. This implicit coupling scheme has the advantage that it allows decoupling of time scales. However, they are limited due to the assumption of steady state cases or multiple pseudo-steady steps in an unsteady simulation. The coupling is implicit and iterative which means using the Schwarz decomposition to obtain the state properties of density and momentum which are then used as boundary conditions for the other domain.

2.4.4 Other Multiscale Strategies

It is notable that this work only focuses on the coupling of dense fluid mechanics using a continuum-based Navier-Stockes solver and molecular dynamics. There are also other considerable continuum-atomistic scale coupling approaches, which are outside the scope of the current work and are not reviewed in a detailed way in this work, e.g., pairing MD with Lattice Boltzman Method (LBM) (Neumann et al., 2016), MD with Dissipative Particle Dynamics (DPD) (Chang et al., 2016), and CFD with Discrete Element Method (Goniva et al., 2009).

2.4.5 Objectives of present work with hybrid continuum-atomistic scale simulations

There are three main objectives of hybrid continuum-atomistic scale simulations in this present work. Firstly, the hybrid CFD-MD coupling scheme is implemented based on the platforms of OpenFOAM and LAMMPS. Then, Couette flow in a nanochannel with LJ argon liquid is employed to verify this hybrid CFD-MD coupling simulation method against an analytic solution and the published study. Finally, this multiscale hybrid CFD-MD coupling scheme is employed for low-salinity EOR applications: a) Couette flow dynamics simulation with water liquid in a calcite channel is conducted, where the water salinity effects on multiscale shear flow dynamics are investigated to reveal the salt effect on the water wettability in a calcite slit pore; b) The shear flow dynamics investigation of oil phase with hybrid CFD-MD coupling simulation method is also presented to analyse the calcite surface wettability; c) The multiscale shear flow dynamics study is extended from single phase to multi phases. The water salinity effect on the multiphase flow shear dynamics is investigated.

2.5 Chapter summary

The research related to micro/nano-EOR systems employing CFD and MD simulation methods has been reviewed in this chapter, culminating with a review

of advanced CFD-MD coupling, simulation methods. It is clear from the review that the investigation of EOR related multiphase flow processes are very scattering. Both CFD and MD have been widely studied, with the focus of different domains and different phenomena. Multiscale coupling simulation is rarely applied in the background of EOR, no mentioning the effect of multiphase flow. Our understanding of the multiscale and multiphase interactions is far from satisfactory.

i) At the continuum scale, contradictory experimental results have been reported regarding to the capillary and wettability effects on EOR. By using CFD numerical simulation method, previous computational fluid dynamics simulations mostly focus on study of multiphase flow in the connecting micro-channels of core plugs or microfluidic systems. The interaction of fluid flows from the crossing channel systems brings huge obstacles to focus on the insight description of the immiscible multiphase flow interaction mechanism.

ii) The assumption of continuity breaks at the nanoscale. Molecular information on liquid-liquid interfaces and liquid-solid interfaces is required to underpin the flow mechanisms of shale-gas, shale oil, as well as the low-salinity effect at the nanoscale for both conventional and non-conventional oil fields, as well as the geological sealing of oil and gas by cap rocks. Though there is general agreement that the EOR effect by low-salinity water flooding is related to modification of substrate wettability, creating more hydrophilic surfaces, the underpinning mechanism leading to wettability change is still a matter of debate.

iii) CFD simulation methods, while capable of solving macro-scale problems efficiency, is incapable of resolving features and flow dynamics on the scale of nanometres due to the breakdown of the continuum assumption. MD simulation method is capable of fully resolving flow fields in such confined flows. Macroscopic problems, however, are still far beyond the reach of MD simulations due to the prohibitively large computational expense of modelling discrete particles. To meet the twin goals of both accuracy and efficiency, the multi-scale hybrid CFD-MD coupling simulation method offers a reasonable solution by limiting MD calculation to only a small region where atomistic-level resolution is necessary and using continuum methods away from this region. A hybrid CFD-MD coupling scheme for simulating multi-scale (micro- and nano-) fluidic systems is a promising method on the investigations for EOR applications.

Three levels of studies are performed in this work:

At the microscale, CFD approach is used to simulate the multiphase transport and water-oil displacement process based on the VOF model. The effects of

wettablity, viscosity and IFT are identified with a special focus on their relative contributions at the same capillary number and the development of a flow map. Moreover, the pore-scale flooding process for both oil-saturated and oil-unsaturated pores is studied to provide insights for some emerging EOR techniques based on nanoparticles, surfactant, and nanoparticles-surfactant hybrids. This shall advance our understanding of EOR related multiphase flow process at the pore scale.

With a focus on the wettablity, the second phase of this work looks **at the nanoscale** using classical molecular dynamics (MD) simulation method to investigate the low salinity effect. This phase includes three main parts aiming to identify i) effect of water salinity on the nano-scale water/oil interfacial equilibrium, ii) effect of surface charge and water salinity on the wettability variation of a mineral surface, and iii) the wettability effect on oil displacement in a nano-pore via non-equilibrium molecular dynamics (NEMD) simulation. This shall advance our understanding of the multiphase flow nature in nanoscale pores and reveal the fundamental roles of water salinity on the wettability change.

Finally, to achieve both molecular/atomistic insights and the computation efficiency, the advanced **multiscale hybrid CFD-MD coupling** techniques is implemented, including a continuum domain, an atomistic domain and an overlapping hybrid region. An example study is conducted to probe the effect of water salinity on the multi-scale single phase and multiphase flow dynamics in a calcite nanopore, with both improved atomistic insight and computational efficiency.

Chapter 3
Methodology

3.1 Introduction

In this chapter, the governing equations of continuum fluid dynamics (CFD) and molecular dynamics (MD) calculations are introduced. Based on the flow dynamics coupling strategy between the continuum scale and discrete atomistic scale, the mathematical link between these two scales are discussed in the purpose of matching reference frames, spatial and definition of equivalent densities, momenta and stresses between both systems. Section 3.2 introduces the continuum formulation, starting with the control volume form and discussing the approximations required to obtain the Navier-Stokes equation. Section 3.3 introduces the governing equations of molecular dynamics. In addition, a number of forms of variation principle are discussed in detail, which is essential to the coupling scheme. Four available packages are chosen to develop to meet the requirement of this project, which are reviewed in Section 3.4, and Section 3.5 focuses on the hybrid CFD-MD coupling scheme by using domain decomposition method.

3.2 Continuum Fluid Dynamics Mechanics

3.2.1 Basic assumptions

Four assumptions are made to simplify the proposed CFD calculations: i) both the water and oil phase are assumed to be immiscible, and there is no mass transfer through the water/oil interface; ii) both the water and oil liquid are assumed to be incompressible; iii) the gravity effect is neglected due to at the pore scale; iv) the wettability effect is considered with the representative of the static contact angle, where the dynamic wettability effect are not considered. Though the dynamic contact angle may affect the displacement process, this factor is neglected to simplify this full CFD calculation.

Moreover, the governing equations used in the CFD calculation based on the continuum assumption. The continuum assumption here states that the fluid flow being considered is continuous in both space and time. This continuum assumption is reasonable as long as the length scales of the problem are much larger than the mean free path of the individual molecules. This continuum assumption underpins the majority of engineering simulations at the macro scale.

3.2.2 Governing Equations

A continuous fluid consists of a single chemical component with mass density $\rho(\boldsymbol{r};t)$ and local velocity $\boldsymbol{u}(\boldsymbol{r};t)$ at the point $\boldsymbol{r}$ at the time t. The mass of the fluid within a fixed region ω is given by,

$$\int_{\omega} \rho(\boldsymbol{r};t)\, d\omega \tag{3-1}$$

The continuity equation could be expressed as,

$$\frac{\partial}{\partial t}\rho(\boldsymbol{r};t) = -\nabla_{\boldsymbol{r}}[\rho(\boldsymbol{r};t)\boldsymbol{u}(\boldsymbol{r};t)] \tag{3-2}$$

The hydrodynamic equation of motion could be derived by equating the rate of change of momentum within region ω plus the rate of flow of momentum out through the surface of ω,

$$\int_{S} \rho(\boldsymbol{r};t)\, \boldsymbol{u}(\boldsymbol{r};t)\boldsymbol{u}(\boldsymbol{r};t)d\boldsymbol{S} = \int_{\omega} \nabla_{\boldsymbol{r}}\, [\rho(\boldsymbol{r};t)\boldsymbol{u}(\boldsymbol{r};t)\boldsymbol{u}(\boldsymbol{r};t)]d\omega \tag{3-3}$$

The forces acting on the fluid within region ω could be described with the sum of external body force and the surface force,

$$\int_{\omega}\boldsymbol{X}\,(\boldsymbol{r};t)d\omega + \int_{S}\boldsymbol{\sigma}(\boldsymbol{r};t)\, d\boldsymbol{S} = \int_{\omega}\boldsymbol{X}\,(\boldsymbol{r};t)d\omega + \int_{\omega}\nabla_{\boldsymbol{r}}\boldsymbol{\sigma}(\boldsymbol{r};t)\, d\omega \tag{3-4}$$

where $\boldsymbol{X}$ is the force per unit volume due to external source, $\boldsymbol{\sigma}$ is the symmetric stress tensor. Since region ω is arbitrary, the resulting differential equation of motion (momentum transport equation) is,

$$\frac{\partial}{\partial t}\rho(\boldsymbol{r};t)\boldsymbol{u}(\boldsymbol{r};t) + \nabla_{\boldsymbol{r}}[\rho(\boldsymbol{r};t)\boldsymbol{u}(\boldsymbol{r};t)\boldsymbol{u}(\boldsymbol{r};t)] = \boldsymbol{X}(\boldsymbol{r};t) + \nabla_{\boldsymbol{r}}\boldsymbol{\sigma}(\boldsymbol{r};t) \tag{3-5}$$

3.2.3 Volume of Fluid (VOF) Method

In the CFD calculations, the FVM-based CFD package ANSYS FLUENT is applied to investigate the flow dynamics problems of water/oil two-phase immiscible flow. There are three modules available for the multiphase flow dynamics phenomenon, which are the volume-of-fluid (VOF) module, mixture module, and the Eulerian module, respectively. Among these three methods, the VOF module has been identified to have a good performance to track the position of an interface between two or more immiscible fluid. Therefore, the VOF method has been abundantly applied to investigate the steady and transient tracking of liquid-liquid or liquid-gas interface for multiple engineering applications, which thus select the VOF module to simulate the multiphase flow dynamics in the presented work.

The volume of fluid method, first introduced in 1976 by Noh and Woodward (Noh and Woodward, 1976), uses the colour function to model the displacement of a fluid surface. Assume a computational domain occupied by two different fluids. The volume conservation of one fluid can be expressed as,

$$\frac{\partial C}{\partial t} + V \cdot \nabla C = 0 \tag{3-6}$$

In this method, the computational domain is divided into a number of computational cells which can be referenced by the index pair (i, j) in two dimensions. The interface is represented by the value of the colour function C in each cell and denoted by $C_{i,j}$. $C_{i,j}$ taking the value of the volume fraction of one of the two immiscible fluids. There are two steps in the VOF methods: the reconstruction of the interface and the advection of the interface. Various techniques have been proposed for reconstructing and advecting a well-defined interface using $C_{i,j}$. These are based on either an algebraic or a geometric approach.

For Continuum Surface Force (CSF) Model,

$$F_{CSF} = \frac{2\rho}{\rho_w + \rho_o} \sigma_{wo} \kappa \nabla \alpha_w \tag{3-7}$$

where κ denotes the curvature of the oil-water interface, σ_{wo} is the water-oil surface tension, α_w is the water volume-fraction and ρ is the volume-averaged mixture density:

$$\rho = \alpha_w \rho_w + \alpha_o \rho_o \tag{3-8}$$

Wall adhesion is modelled by assuming a contact angle between the fluid-fluid interface and the solid wall.

3.3 Molecular Dynamics Mechanics

Molecular Simulation is a computational approach in materials science, physics and chemistry, and can be defined as a kind of particle simulation where the individual position of every atom in the system is explicitly accounted for. Once proper potential function and parameters for atoms composing molecules are given, it allows us to obtain thermodynamic properties of the system consisting of molecules at given pressure and temperature conditions. Macroscopic properties are always ensemble averages over a representative statistical ensemble of molecular systems. In this project, molecular dynamics (MD) simulation is employed to investigate the interfacial equilibrium of various materials at the atomistic scale, including oil, water, salts and minerals. Fundamental algorithm of MD methods and thermodynamic ensembles used in this project are described in this section.

3.3.1 Governing Equations

MD involves solving Newton's second law for each particle i of the N-atom system,

$$m_i \ddot{\boldsymbol{r}}_{\boldsymbol{i}} = \boldsymbol{F_i} \tag{3-9}$$

where m_i and $\ddot{r}_i$ is the mass and acceleration of atom i; F_i is the force exerted on the atom i, expressed as the gradient of the potential energy (force field).

$$\boldsymbol{F_i} = -\nabla_i E(\boldsymbol{r_i}) \tag{3-10}$$

where the potential E is a function of all the relative atom positions only.

Combining these two equations yields

$$-\frac{dE}{d\boldsymbol{r_i}} = m_i \frac{d^2 \boldsymbol{r_i}}{dt^2} \tag{3-11}$$

Newton's equation of motion can then relate to the derivative of the potential energy to the changes in position as a function of time. Solving these equations for a system of N atoms, means solving $3N$ coupled 2^{nd} order differential equations to yield the position vectors $\boldsymbol{r_i}$ as a function of time.

The total configuration field potential E of an N-atom system could be written as:

$$E(\boldsymbol{r_1}, \boldsymbol{r_2}, \cdots, \boldsymbol{r_N}) = E_{intramolecular} + E_{intermolecular} + E_{external} \tag{3-12}$$

$$E_{intramolecular} = \sum_{i_{bond}=1}^{N_{bond}} E_{bond} + \sum_{i_{angle}=1}^{N_{angle}} E_{angle} + \sum_{i_{dihedral}=1}^{N_{dihedral}} E_{dihedral} + \cdots \tag{3-13}$$

$$E_{intermolecular} = \sum_{i=1}^{N-1} \sum_{j>i}^{N} E_{2-body}^{(vdW, electrostatics)} + \sum_{i=1}^{N} \sum_{j\neq i}^{N} \sum_{k\neq j}^{N} E_{tersoff} + \sum_{i=1}^{N-2} \sum_{j>i}^{N-1} \sum_{k>j}^{N} E_{3-body} + \sum_{i=1}^{N-3} \sum_{j>i}^{N-2} \sum_{k>j}^{N-1} \sum_{l>k}^{N} E_{4-body} \cdots \tag{3-14}$$

This function computes the system potential energy as a sum of terms that describe intramolecular interactions, intermolecular interactions and external field potential. It is assumed that the two body terms (terms for non-bonded pairs of atoms) arise from van der Waals interactions (regarded as short-ranged) and electrostatic interactions (coulombic, also regarded as long-ranged).

Most of the time, the pair wise potential field is approximated using the Lennard-Jones (L-J) potential (Rahman, 1964), which is commonly used to monatomic liquid argon, but is actually a good representation of more complex fluids,

$$E(\boldsymbol{r_{ij}}) = 4\varepsilon \left[(\frac{\sigma}{\boldsymbol{r_{ij}}})^{12} - (\frac{\sigma}{\boldsymbol{r_{ij}}})^{6} \right] - 4\varepsilon \left[\left(\frac{\sigma}{\boldsymbol{r_c}}\right)^{12} - \left(\frac{\sigma}{\boldsymbol{r_c}}\right)^{6} \right], |\boldsymbol{r_{ij}}| \leq |\boldsymbol{r_c}|$$

$$E(\boldsymbol{r_{ij}}) = 0, |\boldsymbol{r_{ij}}| > |\boldsymbol{r_c}| \tag{3-15}$$

Although the L-J potential describes the interaction of pairs of molecules, it also shows very good agreement to experimental data for real systems which have two and greater body interactions (Tildesley and Allen, 1987). This is because $E(\boldsymbol{r_{ij}})$ here is now an effective pair potential whose parameters incorporate, in a mean field sense, the three body and higher order terms which are formally absent. It therefore represents a good balance between simulation efficiency and accuracy.

3.3.2 Potential Energy and Force Field Models

Differing from the quantum mechanics by considering the electrons for a certain system, the mechanics of the molecular dynamics simulation derive the system energy as a function of the sole nuclear position to carry out the calculation for a system with a large number of atoms. Therefore, the molecular simulation with MD method is based on the interaction calculations among the atoms within a certain system, e.g., the intramolecular interactions by considering the stretching of bonds, the rotation of bonds, and the opening and closing of angles, the torsions and dihedrals of molecules; the intermolecular interactions by considering both the short-range van der Waals interaction and long-range electrostatic interaction.

There are various force fields to capture both intra and intermolecular forces through using different forms for the various interactions within and between molecules. The functional form of a force field depends on the accuracy required for its purpose. The force fields have been developed by using high-level quantum calculations and/or by fitting to experimental data. The common force fields carried out in molecular dynamics simulations are, for instance, CHARMM, OPLS, TraPPE, CVFF and NERD, etc. Three different types of force fields are designed based on different assumptions and optimisations: all-atomistic force field (AA-FF, e.g. CHARMM22, CHARMM27, OPLS-AA…), united-atom force field (UA-FF, e.g. CHARMM19, OPLS-UA, TraPPE-UA) and coarse-grain force field (CG-FF, e.g. TraPPE-CG). The united-atom (UA) and coarse-grain (CG) force field can drive the calculations of MD simulations faster for a certain system by assuming the atom groups as a united site, which assumption may lead to under-/overestimation of the physical properties through previous investigations. Therefore, the all-atom (AA) force fields are chosen to simulation both the inorganic and organic species for liquid and solid phase in the presented MD simulations to ensure the calculation accuracy.

3.3.3 Statistical Mechanics

In molecular dynamics simulation, the connection between microscopic simulations and macroscopic properties is made via statistical mechanics, which provides mathematical expressions that relate macroscopic properties to the distribution and motion of the atoms and molecules of the N-body system. The thermodynamic state of a system is usually defined by a small set of parameters, e.g. the temperature T, the pressure p, and the number of particles N.

The mechanical or microscopic state of a system is defined by the atomic positions $\boldsymbol{r}(\boldsymbol{t})$ and momenta $\boldsymbol{p}(\boldsymbol{t})$ at a time t; this can also be considered as

coordinates in a multi-dimensional phase space. For a system of N particles, a convenient framework to consider this system is a $6N$ dimensional phase space, in which each combination of molecule position and velocity has a unique value.

Consider a probability function f which describes how likely a given point in phase space is to contain a molecule.

$$f = f(\boldsymbol{r_1}, \cdots, \boldsymbol{r_N}, \boldsymbol{p_1}, \cdots, \boldsymbol{p_N}, t) \tag{3-16}$$

This can be normalised to unity over the whole of phase space,

$$\int_{6N} \cdots \int f(\boldsymbol{r_1}, \cdots, \boldsymbol{r_N}, \boldsymbol{p_1}, \cdots, \boldsymbol{p_N}, t) d\boldsymbol{r_1} \cdots d\boldsymbol{r_N} d\boldsymbol{p_1} \cdots d\boldsymbol{p_N} = 1 \tag{3-17}$$

which, in this form, represents the canonical ensemble (NVT) formulation of statistical mechanics. It is based on the idea of an average over an arbitrary number of independent molecular systems (an ensemble). This average is used as a probability f of finding a molecule at a point in phase space. In other words, for a given r and p how likely it is to find a molecule with these properties in any of the ensemble of different system. This is called a mesoscopic system as it is not based on the macroscopic continuum hypothesis and does not follow individual microscopic discrete molecules. An ensemble is a collection of points in phase space satisfying the conditions of a particular thermodynamic state. A molecular dynamics simulation generates a sequence of points in phase space as a function of time; these points belong to the same ensemble, and they correspond to the different configurations of the system and their respective momenta. The requirement is that a statistically significant number of molecules exist across the arbitrary number of systems. The evolution in time of f is governed by the well-known Liouville equations of statistical mechanics.

$$\frac{\partial f}{\partial t} = \sum_{i=1}^{N} [\boldsymbol{F_i} \cdot \frac{\partial f}{\partial \boldsymbol{p_i}} - \frac{\boldsymbol{p_i}}{m_i} \cdot \frac{\partial f}{\partial \boldsymbol{r_i}}] \tag{3-18}$$

The Liouville equation contains all the complexity of the averaged MD system, including the internal structure. For a property α, the expectation value of α can be obtained by evaluating the inner product with the probability function,

$$\langle \alpha; f \rangle = \int \cdots \int \alpha(\boldsymbol{r_1}, \cdots, \boldsymbol{r_N}, \boldsymbol{p_1}, \cdots, \boldsymbol{p_N}) f(\boldsymbol{r_1}, \cdots, \boldsymbol{r_N}, \boldsymbol{p_1}, \cdots, \boldsymbol{p_N}, t) d\boldsymbol{r_1} \cdots d\boldsymbol{r_N} d\boldsymbol{p_1} \cdots d\boldsymbol{p_N} \tag{3-19}$$

where angled bracket notation $\langle \alpha; f \rangle$ is introduced to define the ensemble average. Here α is any dynamic variable expressed as a function of position and velocity. Assuming phase space is bounded, the evolution in time of the expected value of a property α is,

$$\frac{\partial}{\partial t} \langle \alpha; f \rangle = \sum_{i=1}^{N} \langle \boldsymbol{F_i} \cdot \frac{\partial \alpha}{\partial \boldsymbol{p_i}} + \frac{\boldsymbol{p_i}}{m_i} \cdot \frac{\partial \alpha}{\partial \boldsymbol{r_i}}; f \rangle \tag{3-20}$$

which is obtained by Irving & Kirkwood (Irving and Kirkwood, 1950) from the Liouville equation.

There exist different ensembles with different characteristics, e.g. micro canonical ensemble (NVE), canonical ensemble (NVT), isobaric-isothermal ensemble (NPT), grand canonical ensemble (μVT), etc.

Molecular dynamics is most easily performed in the constant NVT ensemble. As temperature is directly related to the average kinetic energy of all the particles in the system,

$$E_k = \sum_{i=1}^{N} \frac{1}{2} m_i \boldsymbol{v_i}^2 \tag{3-21}$$

For a system of N particles in equilibrium, at absolute temperature T, it has an average total energy of $\frac{1}{2} N k_B T$, where k_B is the constant.

Considering these two equations,

$$E_k = \sum_{i=1}^{N} \frac{1}{2} m_i \boldsymbol{v_i}^2 = \frac{1}{2} N k_B T \tag{3-22}$$

and,

$$T = \sum_{i=1}^{N} \frac{m_i \boldsymbol{v_i}^2}{3N k_B} \tag{3-23}$$

Therefore, constant temperature simulations can be carried out by scaling the velocity of the particles. There are different types of thermostats for MD simulations, e.g. Anderson thermostat, Nóse-Hoover thermostat, Berendsen thermostat. Each on has advantages and disadvantages. All thermostats have a good temperature control, but they differ in how they drive the system to equilibrium. More details regarding to the thermostats are given in the next Section 3.3.4.

3.3.4 Integration algorithm

3.3.4.1 Leapfrog Verlet Algorithm

The potential energy is a function of the atomic positions $(3N)$ of all the atoms in the system. Due to the complicated nature of this function, there is no analytical solution to the equations of motion. Instead they must be solved numerically. Numerous numerical algorithms have been developed for integrating the equations mainly by using finite difference algorithms, e.g. leap-frog Verlet algorithm (LFV), velocity-Verlet algorithm (VV). Most integration algorithms assume the positions, velocities and accelerations can be approximated by a form of Taylor series expansion.

The work described in this study use the LFV scheme due to its simplicity and speed, which can be easily applied to complex molecular systems and combined with constraint algorithms. The LFV algorithm is derived from the atom position ***r***, force f at the time *t*, and velocity ***v*** at half a timestep behind (t – 1/2 Δt). The forces

of atoms in the system are firstly updated from time ($t - \Delta t$) to time t since the atom positions have change from the last step:

$$\boldsymbol{f}(t - \Delta t) \rightarrow \boldsymbol{f}(\mathrm{t}) \tag{3-23}$$

where Δt is the timestep. Then the velocity is advanced by a timestep to (t + 1/2 Δt) by integrating the new force:

$$\boldsymbol{v}(t - 1/2\,\Delta t) + \Delta t \cdot \boldsymbol{f}(\mathrm{t})/\mathrm{m} \rightarrow \boldsymbol{v}(t + 1/2\,\Delta t) \tag{3-24}$$

where m is the mass of an atom site, thus the positions are advanced to a full step ($t + \Delta t$) using the new half-step velocities:

$$\boldsymbol{r}(\mathrm{t}) + \Delta t \cdot \boldsymbol{v}(t + 1/2\,\Delta t) \rightarrow \boldsymbol{r}(t + \Delta t) \tag{3-25}$$

MD simulations normally require both position and velocity properties at the same time, e.g., the sum of potential and kinetic energy. The velocity at time t is obtained from the average of the velocity half a timestep of time t:

$$[\boldsymbol{v}(t - 1/2\,\Delta t) + \boldsymbol{v}(t + 1/2\,\Delta t)\,] \rightarrow \boldsymbol{v}(t) \tag{3-26}$$

The instantaneous kinetic energy, for instance, can then be obtained from the atomic velocities with the equation as follows:

$$E_{kin}(t) = \frac{1}{2}\sum_1^N m_i v_i^2(t) \tag{3-27}$$

3.3.4.2 Berendsen Thermostat

In the presented MD work, the Berendsen algorithm is applied to ensure that the average system temperature in maintained closed to the requested temperature T_{ext}. In the Berendsen algorithm, the instantaneous temperature is pushed towards the desired temperature T_{ext} by scaling the velocities at each step by,

$$\chi(t) = [1 + \frac{\Delta t}{\tau_T}(\frac{\sigma}{E_{kin}(t)} - 1)]^{1/2} \tag{3-28}$$

where the target thermostat energy is given as follows, depending on the external temperature, the system total degrees of freedom and a specified time constant for temperature fluctuations with 0.5 ps.

$$\sigma = \frac{f}{2} k_B T_{ext} \tag{3-29}$$

The LFV implementation of the Berendsen algorithm is iterative as an initial estimate of χ(t) at full step is calculated using an unconstrained estimate of the velocity at full step.

3.3.4.3 Berendsen Barostat

The thermostat is coupled with a Berendsen barostat during the presented MD simulations in order to obtain an average pressure and isotropic stress tensor.

With the Berendsen barostat algorithm, the system is made to obey the equation of motion at the beginning of each step,

$$\frac{dP(t)}{dt} = \frac{P_0 - P(t)}{\tau_P} \tag{3-30}$$

where P_0 is the target pressure and $P(t)$ is the instantaneous pressure, and τ_P is the barostat relaxation time constant. In the isothermal implementation, at each step the MD cell volume is scaled by a factor η, and the coordinates and cell vectors by $\eta^{1/3}$,

$$\eta(t) = 1 - \frac{\beta \Delta t}{\tau_P}[P_0 - P(t)] \tag{3-31}$$

where β is the isothermal compressibility of the system.

3.4 Modelling Packages Selection

Due to this project based on simulation methods, it is worth taking pages to review the code selection for the proposed EOR modelling project. The issues under considered to select proper codes for this project is presented as follows:

1. All-in-one or separate products? Taking CFD packages as an example, the advantage of an all-in-one offering is that, all the grid generator, fluid dynamics solver, and post-processor are integrated into a single CFD code. So, there is no need to worry about incompatibilities between the different components.

2. Will it model all the physics processes required? The physics processes of fluid dynamics allow for several key combinations of factors which can become important. No codes can solve all possible flow regimes accurately.

3. Are the underlying algorithms well-suited for the problems? Even of the codes have the capability to model the physics process of a particular problem; it should be considered whether or not the basic algorithms being used are good choices for the applications.

4. Who else uses the code? How healthy is the developer company? How often the newest update versions are released? It will be no good to spend a code package if the developer company goes out of business next month. It's worth taking time to make sure that the software provider is well managed and has a good customer base. It would be a good option to refer other users about using the code.

5. What support options are available? Is any local support available? There is nothing like having a local office where users can go to ask questions face to face and encourage the staff to go the extra mile.

6. Have any in-house experience-base with the code? No matter how friendly the user interface is, all codes have a learning curve. If already having experience with one package of another, it can greatly speed up the process of bringing the package into the current project use.

Following these above considerations, selected codes in this project are decided by planning and budgeting for the code package, analysing software requirements analysis, code vendor research and making final decisions.

3.4.1 CFD codes

3.4.1.1 Commercial CFD Packages: FLUENT

Even though there is an option of using non-commercial CFD codes, it has to be admitted that commercial packages are a good solution for many organizations. Using commercial CFD codes makes a lot of sense for many projects – most commercial CFD codes are user friendly and satisfy most of engineering needs.

With FLUENT and CFX solvers, ANSYS controls more than half of the commercial CFD market (Ansys, 2006; Fluent, 2009). Both of the solvers come as integrated packages with grid generation (e.g. ICEM) and post-processing utilities (e.g. CFD-Post). By reputation, CFX has traditionally been focused on turbomachinery applications, while FLUENT is seen as a more general code. FLUENT is an extremely versatile code that has probably been applied with success to more kinds of flow than any others. FLUENT's greatest advantage is that it provides reasonably powerful tools in a tightly integrated package. This allows engineers in a wide variety of industries to run a CFD analysis of the problems relevant to them.

Though there are a lot of advantages of ANSYS FLUENT package, due to limitations in the interpreter used to compile interpreted user defined function (UDF) source code in FLUENT, interpreted UDFs are limited in their use of the C programming language. In particular, some elements of C cannot be used in interpreted UDFs, for example, direct data structure references, declarations of local structures, arrays of functions, and multi-dimensional arrays, etc. These limitations will restrict the application of FLUENT package on multi-scale coupling application.

Another disadvantage of FLUENT package is due to its commercial product nature, which users do not know what's going on in the black box. The high cost of commercial code license is another issue required to be considered into the budget quote at the same time.

3.4.1.2 Non-Commercial CFD Packages: OpenFOAM

One size does not fit all, however, and sometimes it could be found that a different approach is required either for a single project, or for all of their CFD simulations. In this project, with the consideration of the hybrid CFD-MD coupling application, there are some high quality CFD solvers which are freely available from one source to another. One of popular packages is OpenFOAM (Jacobsen et al., 2012).

OpenFOAM, as a highly modular, parallelized, finite volume code, is a free and open source CFD software developed primarily by OpenCFD Ltd. since 2004. It has a large user base across most areas of engineering and science, from both commercial and academic organisations. OpenFOAM has an extensive range of features to solve issues from complex fluid flows involving chemical reactions, turbulence and heat transfer, to acoustics, solid mechanics and electromagnetics. This code is a real library of C++ routines which facilitate the numerical solution of partial differential equations. Using this library, many different solvers have been built to address many classes of problems in fluid dynamics and other fields as well. Applications range from laminar incompressible flow to fully turbulent reacting compressible flow options. OpenFOAM is freely available worldwide under the GNU Public License.

Though OpenFOAM doesn't have a high-performance user interface, as an open-source package, it can fill the vacancy of free transferring complicated data structure and multi-dimensional arrays. With full library of C++ routines, it provides the basic flexibility capabilities, which are necessary to realise the multi-scale coupling process.

3.4.1.3 CFD code selection overview and available modules

For CFD simulation packages used in this project, FLUENT and OpenFOAM are selected to compensate each other's limitations and satisfy the requirements of pore-scale simulation and multi-scale coupling process.

Two models are available in FLUENT for simulating where two or more fluid are present. The Volume of Fluid (VOF) model (Hirt and Nichols, 1981) is designed for two or more immiscible fluids where the position of the interface between the fluids is of interest. The Eulerian model is designed for two of more interpenetrating fluids. Whereas the Eulerian model makes use of multiple momentum equations to describe the individual fluids, the VOF model does not. In the VOF model, a single set of momentum equations is shared by the fluids, the volume fraction of each of the fluids is tracked throughout the domain. In this project, VOF with continuum surface force model (CSF) solver is used to capture

the interface between flooding fluids and oil phase. Wall adhesion option is selected to specify the contact angle among different phases. Correspondingly, a standard solver called ‘interFoam’ is distributed with OpenFOAM for two incompressible, immiscible fluid using the VOF phase-fraction based on interface capturing approach. In incompressibleTransportModels , the libraries of incompressible transports models are contained, e.g. interfaceProperties , twoPhaseProperties , etc.

Considering the risk of the tricky ‘user defined function’ (UDF) for real-time transferring complicated data arrays in and out of the commercial FLUENT package, OpenFOAM package is adopted when comes to the coupling process from CFD side.

3.4.2 MD codes

Comparing with different CFD codes, MD simulation packages are complicated to select by the fact that each program supports certain features that may not be available in another. Typically, time step integrators or temperature and pressure controllers are implemented with different algorithms or techniques. As most of current MD codes are open-source and license-free, the analysis of different MD codes in this section is carried out on aspects of code structure, performance comparison and user assessments, by focusing on three popular molecular dynamics (MD) packages, DL_POLY, LAMMPS and GROMACS in this section.

3.4.2.1 MD Code introduction

The most time-consuming part of an MD simulation algorithm is the computation of the non-bonded interactions and the electrostatic interactions. Most MD codes have similar features, but the real differences consist in their speed, parallel scalability and the class of the force fields.

DL_POLY (Smith, W. et al., 2002) is a general purpose classical molecular dynamics simulation software developed at Daresbury Laboratory by I.T. Todorov and W. Smith. It is a general purpose classical molecular dynamics simulation software providing scalable performance from a single processor workstation to a high-performance parallel compute. The friendly JAVA GUI and matched force field generation tools become an advantage of using DL_POLY package. As a UK local developed code, it is quite popular applied by UK researchers to conduct some fundamental investigation for molecular dynamics. DL_POLY users in UK could not only be provided good technique support, but also have led the trends of world-wide application already. This code supports very general potential functions and is therefore not optimised for biomolecular simulations. Therefore,

aiming to this project, it could provide efficient accuracy and performance for EOR application.

Another one of the most popular all-atom MD codes would be LAMMPS (Plimpton et al., 2007), which is a classical molecular dynamics code, and an acronym for 'Large-scale Atomic/Molecular Massively Parallel Simulator', developed by Sandia National Labs and Temple University. It could model an ensemble of particles in the liquid, solid, or gaseous state; and also, atomic, polymeric, biological, metallic, granular, and coarse-grained systems using a variety of force fields and boundary conditions. LAMMPS has been in development for many years by now but has gone through several changes in the programming language used from Fortran 77 (LAMMPS 99) to Fortran 90 (LAMMPS 2001) to currently C++ (after 2006). As switching the language essentially means rewriting the software, it is likely that further development has an impact on the performance. At the moment, the source code comes with a set of separate optimised routines for the computation of the long-range forces. It can be used as standalone code or as library; and can include several external modules. However, due to undergoing changes in the programming languages used, the code had less time to mature and there is still potential for optimisation as the separate long-range routines demonstrate. Besides, LAMMPS, researchers will also often consider DL-POLY, and GROMACS. All of them are very efficiently parallelepiped.

GROMACS (Hess et al., 2008) is a versatile package to perform molecular dynamics, i.e. simulate the Newtonian equations of motion for systems with hundreds to millions of particles. However, GROMACS is known to be primarily designed for biochemical molecules like proteins, lipids and nucleic acids that have a lot of complicated bonded interactions. Since GROMACS is extremely fast at calculating the non-bonded interactions (that usually dominate simulations), many groups are also using it for research on non-biological systems, e.g. polymers.

3.4.2.2 User assessment

Based on a general statistics conclusion from Google Scholar search, three typical MD codes mentioned above were analysed and compared from different standpoints, as shown in Figure 3.1, which are respectively LAMMPS, DL_POLY and GROMACS. Different key words of the search input were listed respectively of each column. The relative population of each code applied in specific fields were displayed intuitively here.

From the last column of the chart, it could be seen that GROMACS occupies relatively the larger market than other three codes among all the molecular dynamics research contributions and followed with LAMMPS. DL_POLY is relatively with the smallest user number, though it is known to be the most popular MD code among UK researchers for molecular dynamics simulation.

Due to the project requirement, the selected codes should have the reliable performance to successfully describe all the inorganic systems (e.g. solvent systems like water, mineral systems like calcite and quartz materials), organic systems (e.g. alkane molecules) and nanofluid systems. Therefore, five standard keywords plus “molecular dynamics” were looked at, “oil”, “alkane”, “calcite”, “quartz”, and “nanoparticles”. Though GROMACS processes more users in molecular dynamics research, compared with its total occupation population in MD market, its application rate in the focused area of this research project is not that optimistic due to its different application preference of biological fields. DL_POLY turns out to be the most proper package in this research interest field. Besides, due to the multi-scale requirements, LAMMPS also need to be considered. This is because its more world-wide application and current available socket existence for message passing interface (MPI) processing.

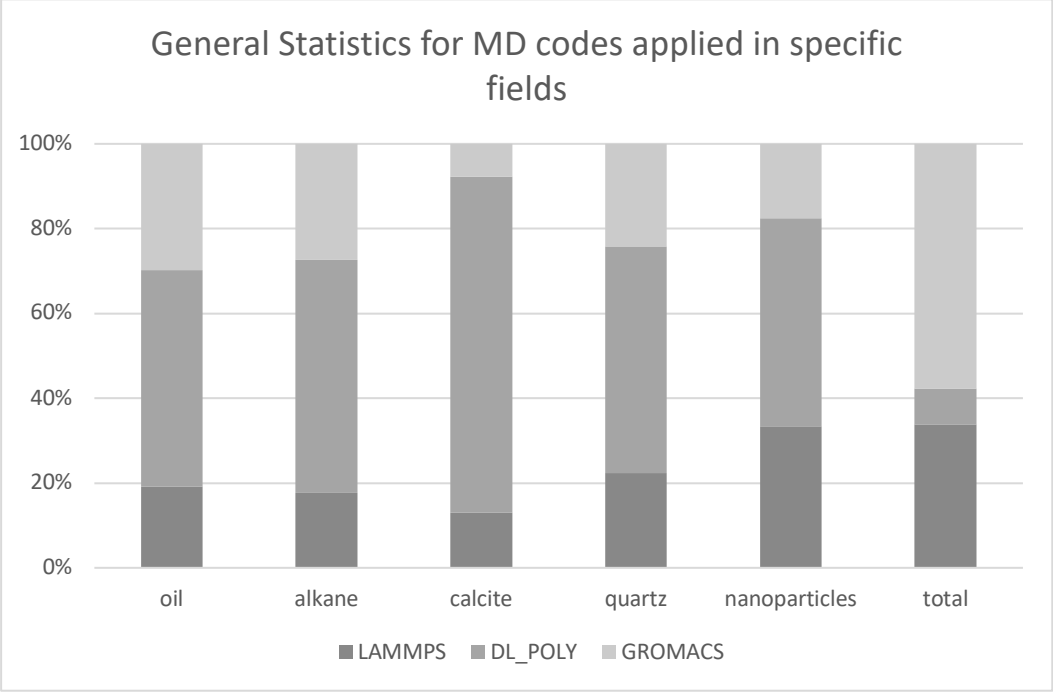

Figure 3.1 General Statistics for MD codes applied in specific fields

3.4.2.3 MD code selection overview

Considering the developer health, physics process requirements, user statistics and other factors, both DL_POLY and LAMMPS are selected to be used in this

project. They both are not only the two main-stream MD simulation packages, but also satisfy all the project requirements in the field of EOR application. Besides, as a UK local production of DL_POLY code, technical supports could be easily achieved by surrounded UK developers and researchers. At the same time, LAMMPS is preferred as well in this project, due to its common applications in advanced multiscale coupling techniques. Both of these two packages share the same theoretical methodology.

3.4.3 Modelling code selection conclusion

According to the above consideration, four codes in total are selected for the application of CFD and MD simulations, which are respectively ANSYS FLUENT, OpenFOAM, DL_POLY and LAMMPS: i) ANSYS FLUENT and DL_POLY are applied to the full CFD and full MD simulation, respectively. Both codes offered a number of advantages over the CFD code and in-house molecular dynamics code. ii) OpenFOAM and LAMMPS are chosen as the building blocks from which the hybrid continuum-atomistic model can be built. Each has been in development for over 15 years and as a result represents a much more mature collection of solvers and features than could be realistically created from scratch; Moreover, because they are both open source, free access to all levels of the source code was possible, a feature necessary when making any changes to software; In addition, both codes are written in a highly modular fashion using the programming language C++, which provided the ability to make substantial changes to certain aspects of the codes. More details about the application of OpenFOAM and LAMMPS on the implementation of the hybrid continuum-atomistic model can be found in next section (Section 3.5).

3.4.4 Prerequisite skills

The basic skills of using these software through graphic user interface (GUI) or command mode is necessary, as well as other corresponding pre/post-processor packages, for example, CFD grid-generation tools ICEM, post-processor CFD-Post, the MD system preparation and post-processing with the package Material Studio (Module, 2011), Packmol (Martínez et al., 2009), VMD (Humphrey et al., 1996), VESTA (Momma and Izumi, 2008), ATEN (Youngs, 2010), DL_FIELD (Yong, C., 2010), DL_ANALYSER (Yong, C.W. and Todorov, 2017), MD Analysis (Michaud-Agrawal et al., 2011), etc.

Several programming languages are also required. (1) From CFD simulation side, the code for user defined function in FLUENT is based on C programming; the base language of OpenFOAM is C++; (2) From MD side, a) both DL_POLY and LAMMPS use the mix programming language of C++ and FORTRAN; b)

considering the coupling project in the final goal of this research, the basic knowledge of MPI programming is also required besides of basic C/C++ and FORTRAN programming skills; c) to post-process the MD results, python programming is used with the application of MD Analysis (Michaud-Agrawal et al., 2011) package.

To proceed the numerical simulation more efficiently, High Performance Computing (HPC) platform in Leeds is applied in this project. Therefore, the skills regarding to the usage of Linux operating system and HPC scripts are required at the same time.

3.5 The hybrid continuum-atomistic (CFD-MD) Coupling

3.5.1 Introduction

Continuity assumption is one of the most fundamental assumptions in the macroscopic fluid mechanics which is governed by the Navier-Stokes equations. However, this assumption breaks down as the spatial scale of flows approaches close to the molecular mean free path. In most cases, the breakdown of the continuum assumption is confined to limited domains, such as fluid/fluid and fluid/solid interfaces. Atomistic descriptions, e.g. MD simulations, are capable to model the nano-scale phenomenon. However, it is unrealistic to apply full MD simulations to investigate the microscale flow dynamics so far due the memory and computation capability limitations. Hence, it is desirable to develop hybrid methods by combining continuum fluid dynamics CFD and molecular dynamics MD together, to take the most efficient description in each region. The adopted domain decomposition method associated with the implementation development is discussed in this chapter.

3.5.2 Domain Decomposition Method

The relaxation method proposed by O'Connell & Thompson (O'connell and Thompson, 1995) are applied to force the average MD velocity in a region to follow the continuum solution. The difficulty occurs when trying to link the continuum stress field to an atomistic description to guarantee the momentum continuity. To overcome this difficulty, the average momentum of the overlap particles is relaxed to that of the corresponding continuum fluid element through the application of constraint dynamics.

For the molecular to continuum exchange, the continuum boundary condition is determined from the average in a cell I. This can reduce all the N_I degrees of freedom of the cells' molecules to a single averaged value. For example, the momentum $M_I \boldsymbol{u}_I$ is obtained from the momentum density defined as followed,

$$M_I \boldsymbol{u}_I = \frac{1}{N_I}\sum_{n=1}^{N_I}\langle m_n \dot{\boldsymbol{r}}_{\boldsymbol{n}} ; f\rangle \cong \frac{1}{\Delta t_{CFD} N_I}\sum_{t=0}^{\Delta t_{CFD}}\sum_{n=1}^{N_I} m_n \dot{\boldsymbol{r}}_{\boldsymbol{n}} \tag{3-32}$$

where the statistical average notation was replaced by a time-averaged value. This average is typically taken on the cell below the overlap region, corresponding to the cell used to set the CFD boundary conditions.

For the continuum to molecular exchange, the momentum in the molecular region is adjusted to be the same with the continuum by applying a constraint force to the molecular equations of motion.

$$m_i \ddot{\boldsymbol{r}}_i = \sum_{j\neq i}^{N} \boldsymbol{f}_{ij} + \boldsymbol{F}^C \tag{3-33}$$

where $\boldsymbol{F}^C$ is a constraint force which adjusts the molecule's average velocity to correspond with the velocity field in the continuum at the same region of space.

In addition to the constrained dynamics force, a second force, termed as 'boundary force' $\boldsymbol{F}^B$, is applied to the molecules in the overlap region to prevent the molecules from leaving the molecular domain. The boundary force was chosen to maintain a prescribed density in the interface regions,

$$\boldsymbol{F}^B = -\alpha P_0 \rho^{-\frac{2}{3}} y_T \tag{3-34}$$

where P_0 denotes the pressure in the domain, ρ is the prescribed density in the interface region, α is a scaling constant and y_T specifies the distance from the top of the MD domains.

One limitation of this HAC model by O'Connell and Thompson is that there was no mass and energy exchange between the discrete and the continuous phases. Moreover, the same timescale in this algorithm was shared by the continuum and discrete equations.

Aiming to this disadvantages, O'Connell and Thompson was further developed in the paper by Nie et al. (Nie et al., 2004). In O'Connell and Thompson's theory, the constraint was consistent with the continuum boundary condition and was of the form of minimise the difference in momentum between the two regions.

$$g_\alpha(\dot{r_{\alpha n}}) = M_I u_{\alpha I} - \sum_{n=1}^{N_I} m_n \dot{r_{\alpha n}} \tag{3-35}$$

where the quantity of M_I was the mass of a fluid region I, containing N_I molecules and $u_{\alpha I}$ ($\alpha \in \{x, y, z\}$) was the component of velocity of the continuum element I. Instead, Nie et al. used a non-holonomic constrain of the form:

$$g_\alpha(\dot{r_{\alpha n}}) = u_{\alpha I}(t) - \frac{1}{N_I}\sum_{n=1}^{N_I} \dot{r_{\alpha n}} = 0 \tag{3-36}$$

where the α index represented one of the three Cartesian coordinates in which the constraint was applied.

Therefore, the different derivations are shown below, using the constraint Euler-Lagrangian equation for holonomic constraints (O'Connell and Thompson (O'connell and Thompson, 1995)) and the non-holonomic form of the constraint equation (Nie et al. (Nie et al., 2004)).

$$\frac{d}{dt}\frac{\partial \mathcal{L}}{\partial \dot{r}_i} - \frac{\partial \mathcal{L}}{\partial r_i} = \sum_{\alpha \in \{x,y,z\}} \lambda_\alpha \frac{\partial f_\alpha}{\partial r_{\alpha i}} \tag{3-37}$$

$$\frac{d}{dt}\frac{\partial \mathcal{L}}{\partial \dot{r}_i} - \frac{\partial \mathcal{L}}{\partial r_i} = \sum_{\alpha \in \{x,y,z\}} \lambda_\alpha \frac{\partial g_\alpha}{\partial \dot{r}_i} \tag{3-38}$$

Nie et al. model has been applied to large coupled simulations by previous coupling research and hence been also adopted in this present work.

3.5.3 Implementation Overview

To implement the hybrid CFD-MD coupling simulations, OpenFOAM is employed as the main code while LAMMPS is built as a library to be called from within it. The implementation of the hybrid CFD-MD coupling scheme is based on further developing the native OpenFOAM single-phase solver, which is named as icoFoam. icoFOAM is designed for the single-phase incompressible, isothermal fluid. To implement the hybrid coupling method, the icoFoam solver requires substantial modifications, especially regarding to the LAMMPS build-in process. The LAMMPS simulation can initialize through OpenFOAM input files. All communication between the two codes is handled through specific functions built into the LAMMPS library class. For instance, the overlap region is created through the function of LAMMPS, which requires inputs of the size and number of bins, etc. Within the namespace of LAMMPS, a new fix (An operation performed at regular intervals within LAMMPS is called a fix) is created to scale velocities to the velocity and temperature set points from the continuum solver. Hence, a new class is created to output data aiming to the new coupling functions. The bin averages of the entire domain for property values, i.e., velocity, density, etc., are taken and written to the output file by this new class. To avoid repetition, more details of the implementation on this multiscale hybrid CFD-MD coupling scheme can be found in Chapter 6.

3.6 Chapter summary

The VOF model is introduced in Section 3.2, which is employed to investigate the multiphase flow dynamics for the pore-scale full CFD simulations, implemented by ANSYS FLUENT software. DL_POLY package is adopted in this work for the full MD simulations, which details are presented in Section 3.3. To realise the multiscale hybrid CFD-MD coupling simulation scheme, OpenFOAM and LAMMPS packages are considered as the basis of the coupling code

developments. Domain decomposition method is used in this hybrid CFD-MD coupling simulation, with the non-holonomic form of the constraint equation proposed by Nie et al. (Nie et al., 2004), as shown in Section 3.4. Other required prerequisites and skills to fulfil this project are also discussed in this chapter.

Chapter 4
Pore-Scale Simulation of Multiphase Flow Interactions with Computational Fluid Dynamics Method

4.1 Introduction

4.1.1 The oil snap-off phenomenon in water-wet pore channels

Immiscible flow in porous media is fundamental to a range of applications such as underground pollutants transport, oil spillage and treatment, soil remediation and enhanced oil recovery (EOR), where pore scale understanding of the phase displacement is crucial. Pore scale ranges from a few micrometres to millimetres where the capillary force dominates the displacement process (Kallel et al., 2016; Schlüter et al., 2016; Setiawan et al., 2014).

Previous pore-scale study of multiphase flow has been focused on EOR, and the fluid displacement process is investigated experimentally by X-ray computed micro-tomography (CT) techniques for different core samples (Andrew et al., 2014; Arns et al., 2002; Raeini et al., 2015). Pore-scale modelling by computational fluid dynamics (CFD) method has recently been established as a complimentary to the costly core analysis method. It is being used in the petroleum and environment sectors to model multiphase flow in column/core samples and to predict the effects of various dependent factors such as rock type, interfacial tension (IFT) and wettability (Meakin and Tartakovsky, 2009).

There are generally two main methods to model the phase displacement. Interface tracking method based on Lagrangian algorithms is normally not well suited for flow with interfaces undergoing complex deformations (such as coalescence or break up). In contrast, interface capturing method based on Eulerian algorithms is more appropriate for complex interface motion (Fukai et al., 1995; Tryggvason et al., 2001). Volume of Fluid (VOF) method was first introduced by Hirt and Nichols (Hirt and Nichols, 1981), which treated the immiscible phase as a single fluid with variable properties. Many studies have shown that VOF method is able to model multiphase flow through porous media with sub-pore resolution and to capture detailed interfacial phenomena, such as viscous deformation of the meniscus, snap-off and coalescence, jumps and abrupt reconfiguration of the interface (Afkhami et al., 2009; Brackbill et al., 1992; Ferrari and Lunati, 2013; Horgue et al., 2013; Lv and Wang, 2015; Tomin and Lunati, 2013; Yang et al., 2013). At the pore scale, capillary force plays an important role in the fluid displacement. For example, in the EOR applications, a dominant mechanism for residual oil left in reservoirs is the “snap-off”

phenomenon, which has been extensively studied. Although the pore-scale snap-off process has been extensively investigated , there are still three main limitations: i) Most of previous research was based on core-scale study with a main focus on the flow displacement in a crossing pore network , and detailed study at a single pore scale is still insufficient; ii) Previous pore-scale studies are mainly focused on super-critical carbon dioxide as the non-wetting fluids, which cannot represent water/oil displacement suitable for EOR and oil remediation applications; and iii) Few study has been investigated on potential ways to suppress the snap-off process at the pore scale to decrease the amount of trapped oil.

On the other hand, to suppress the snap-off phenomenon at the pore scale, many chemicals have been used after the secondary water flooding process, which is termed as chemical EOR (Raffa et al., 2016). The main idea is to increase the value of the capillary number, $Ca = v \cdot \mu / \sigma$, (i.e., decreasing the interfacial tension by using surfactants, or increasing the invading fluid's viscosity by using polymers), and to decrease the snap-off probability, leading to a reduction of the residual oil saturation. Though many core flooding experiments have been performed (Hirasaki et al., 2011; Ko et al., 2014; Samanta et al., 2011; Yu et al., 2010), only very limited studies have been conducted at the pore scale, with inconsistent results reported (Abidin et al., 2012; Liu et al., 2007; Meybodi et al., 2011; Olajire, 2014; Raffa et al., 2015; Wever et al., 2011). Ultralow IFT injection has also been proposed recently as a promising EOR technology; however it is still debatable on the exact role that IFT plays in the process (Raffa et al., 2016). It has been accepted generally that a high capillary number can lead to a large oil recovery factor, regardless the modification of viscosity or IFT.

4.1.2 The capillary trapping of oil droplet during EOR processes

The significance of improving oil production efficiency by enhanced oil recovery techniques is highly acknowledged because in many of the world's reservoirs about two thirds of the oil in place cannot be recovered by conventional methods (Matteo et al., 2012). As a new and advanced technology, nanotechnology has the potential to introduce revolutionary changes in several areas of the oil and gas industry, especially enhanced oil recovery. However, the mechanism of nano-EOR method by chemical flooding is still ambiguous for enhanced oil recovery. Understanding the wettability and interfacial tension effects on the water/oil phase flow interaction in microscopic reservoir pores for EOR purposes can bring significant benefits to understand the theoretical background and utilize this emerging technology.

Nanofluid technology, as a part of nanotechnology, is a new interdisciplinary area of great importance where nanoscience, nanotechnology, and thermal engineering come across. It has developed largely over the past decade and revealed its potential applications in oil and gas industries. Previous observation from lab-scale experiments and molecular scale simulation reported that nanoparticles may alter the reservoir fluid composition and rock-fluid properties to assist in mobilizing trapped oil, which suggests a new mechanism and a new application prospect of nanoparticles for enhanced oil recovery. Wasan and Nikolove (Wasan and Nikolov, 2003) have experimentally investigated the wetting behaviour of nanofluids and proved that the wetting behaviour changes if the liquid contains nanoparticles. This investigation has been further reported by Kondiparty (Kondiparty et al., 2011) that the disjoining pressure gradient drives further spreading of the nanoparticles and it can be large enough to separate an oil droplet from the solid surface. Because the spreading of liquids on solid substrates is of interest to many practical applications and industrial processes, the dynamic motion of three-phase triple lines for nanoparticles was studied both in experimental investigations and theoretical work (Sefiane et al., 2008). Actually, the dynamics of contact line is decided by the driven force due to the out of balance surface tension force, the adhesion force between solid and liquid phase and the resistant force due to viscosity (Vafaei and Wen, 2010). Recently, Wang et al. (Wang, F. and Wu, H., 2013) found that the local volume concentration plays a significant role on the shape of the nanofluids/oil interface. Large nanoparticle concentration may enhance the effect of the disjoining pressure on the spreading of the nanofluid film. Wang et al. (Wang, F.-C. and Wu, H.-A., 2013; Wang and Zhao, 2013) further observed a significant enhancement in the oil removal efficiency using nanofluids with nanoparticles. Moreover, when the charge on each particle exceeds a threshold value, the oil droplet could detach from the solid surface spontaneously and completely. However, the above mechanism has been always debated by some researchers, because they claimed that their experimental results show that nanofluid have few effects on enhanced oil recovery. Contradictory results have been reported regarding to the effect of nanoparticles on EOR, for instance, Hendraningrat et al. (Hendraningrat et al., 2013) showed that the maximum oil recovery was increased by 14.29% of OOIP by using nanofluid; Hu et al. (Hu et al., 2016) reported that the best total cumulative recovery occurred with a total oil recovery of 41.8% of OOIP; whereas Bayat et al. (Esfandyari Bayat et al., 2014) observed only a 2% increase over OOIP for tertiary oil recovery using the same nanofluid.

Three methods have been used previously for studying the chemical flooding process for enhanced oil recovery, which is experimental, molecular dynamics

simulation and numerical computational fluid dynamics simulation. For the experimental method, previous experiments mainly focus on the core-scale (or lab-scale) flooding process. Different nanoparticles and surfactant materials have been used as the displacing fluid to investigate their transport breakthrough curve, pressure drop and oil recovery percentages (Gou et al., 2015; Hu et al., 2017; Peng et al., 2017; Yan et al., 2015). The disadvantage of core-scale experiments lies on the observation limitation of the insight information capture. Nano-scale multiphase modelling has also been conducted by molecular dynamic methods (Kunieda et al., 2012). It mainly brings some significant results for the mechanism insights. However, the high cost of molecular dynamics simulation method leads to the difficulty of simulating the multiphase flow characteristic due to both the length scale and time scale limitation. For the numerical simulation method, previous computational fluid dynamics simulations mostly focus on study of multiphase flow in the connecting micro-channels of core plugs or microfluidic systems (Afsharpoor et al., 2012; Clemens et al., 2013; Lv and Wang, 2015). The interaction of fluid flows from the crossing channel systems brings huge obstacles to focus on the insight description of the immiscible multiphase flow interaction mechanism.

4.1.3 Overview

Using EOR as an example, the work presented in Section 4.3 performs a fundamental flow study at the single pore scale to increase deeper understanding of oil displacement and water/oil flow characteristics in a water-wet pore channel with the application of VOF method, as introduced in Section 4.2.1. A pore-throat connecting channel is established under water-wet condition, as presented in Section 4.2.2, and a parametric study of the effect of viscosity and IFT at the same capillary number on oil displacement is performed, leading to the establishment of a flow map and the identification of the different roles of viscosity and IFT on the oil snap-off phenomenon during EOR processes.

Moreover, the pore-scale flooding process for both oil-saturated and oil-unsaturated pores was further investigated in Section 4.4 for enhanced oil recovery. The same VOF methodology as described in Section 4.2.1 was adopted in this study. A single pore body/throat connecting channel was established to investigate the wettability and interfacial tension effects on the water/oil flow interaction in pore scale, as shown in Section 4.2.2 with further details. The results can provide some insights into the basic understanding of the nanoparticles, surfactant, and nanoparticles-surfactant hybrid flooding process for enhanced oil recovery.

4.2 Model Descriptions

4.2.1 Mathematical Model

The two-phase flow of oil and water in this simulation is described by the incompressible Navier-Stokes equations:

$$\begin{cases} \frac{\partial}{\partial t}\rho \boldsymbol{u} + \rho\nabla\cdot(\boldsymbol{uu}) = -\nabla p + \mu\nabla\cdot(\nabla \boldsymbol{u} + \boldsymbol{\nabla u}^{\mathrm{T}}) + \boldsymbol{F} + \rho \boldsymbol{g} \\ \nabla\cdot\boldsymbol{u} = 0 \end{cases} \quad (4\text{-}1)$$

where $\boldsymbol{u}$ is the velocity vector; ρ is the density fluid; μ is the viscosity of fluid; p is the static pressure; $\boldsymbol{F}$ is the general body force which is the volume surface tension $\boldsymbol{F}_{\mathrm{vol}}$ in this simulation; and $\boldsymbol{g}$ is the gravitational acceleration, which is neglected in this simulation due to its minor influence at the pore scale. The superscript 'T' denotes the matrix transpose.

The finite-volume based the CFD code FLUENT is used to solve the Navier-Stokes equations numerically. The volume of fluid (VOF) method is adopted to describe oil/water two phase flow. The volume fraction equation is used for tracking the interface between multiple phases:

$$\frac{\partial(\alpha_i\rho_i)}{\partial t} + \nabla\cdot(\alpha_i\rho_i\boldsymbol{u}) = \rho_i S_{\alpha_i} + \sum_{j=1}^{n}(\dot{m}_{ji} - \dot{m}_{ij}) \quad (4\text{-}2)$$

where m_{ji} and m_{ij} are the mass transfer from each other between phase i and phase j, both m_{ji} and m_{ij} are zero in this simulation due to the no mass-transfer assumption between water and oil phase in this work; $S_{\alpha i}$) is the source term of i^{th} fluid; ρ_i is the density of i^{th} fluid; and $\boldsymbol{u}$ is the flow velocity vector. The volume fraction α_i is defined as follows:

$$\begin{cases} \alpha_i = 0 : \textit{the cell is empty with no traced fluid inside} \\ 0 < \alpha_i < 1 \quad : \textit{the cell contains the interface} \\ \alpha_i = 1 \quad : \textit{the cell is full of the } i^{th} \textit{ fluid} \\ \sum_{p=1}^{n}\alpha_p = 1 : \textit{the cell must be filled with eithersingle fluid phase or a combination} \end{cases} \quad (4\text{-}3)$$

The fluid properties at the interface are given by: $\begin{cases} \rho = \sum \alpha_i\rho_i \\ \mu = \sum \alpha_i\mu_i \end{cases}$, which are averaged volume fraction for an n-phase system.

The continuum surface force (CSF) model (Brackbill et al., 1992) is used to calculate the curvature of the interface and volume surface tension. In the CSF model, the volume surface force has the following form: $\boldsymbol{F}_{vol} = \sigma\kappa\nabla\alpha_i$ where σ is the interfacial tension, and κ is the curvature, which is defined as: $\kappa = \nabla\cdot\boldsymbol{n}$, where $\boldsymbol{n}$ is the unit normal vector of the interface, $\boldsymbol{n} = \frac{\boldsymbol{\nabla}\alpha_i}{|\boldsymbol{\nabla}\alpha_i|}$.

The pressure based unsteady solver is used for the simulation by using the following algorithm: the pressure-implicit with splitting of operators (PISO) for pressure-velocity coupling, the least squares cell-based scheme for gradient

spatial discretization, the pressure-staggered option (PRESTO) for pressure spatial discretization, the geometric reconstruction approach for volume fraction spatial discretization, and the first order explicit scheme for temporal discretization.

4.2.2 Physical Models

According to the previous studies (Bagrintseva, 2015; Nelson, 2009), pore-throat sizes (diameters) are generally greater than 2 μm in conventional reservoir rocks. Geometrical reasoning and experimental data suggest that conventional reservoir rocks have aspect ratios, i.e., the ratio of pore body size to pore throat size, in the range of 5:1 to 10:1 (Coalson et al., 1994). In this work, a two-dimensional pore body-throat connecting channel is proposed with an aspect ratio of 7:1 as the standard case, shown in Figure 4.1. The radius of the connecting pore throats $d/2$ is 2.5 μm, and the radius R_1 of the circular pore is 17.5 μm. The connections between pore bodies and throats are optimised with a curve of radius R_2 = 2.5 μm. The side length L of the pore-throat connecting channel is 175 μm. A unit length in the z direct perpendicular to the figure is applied to allow 2-D simulation. This represents a typical geometry in microchips used for pore-scale study and some reservoir pores. The shadow region refers to the solid reservoir rock. Due to the scale of the channel, the gravity effect is neglected in this work. For such simple geometries, it has been shown by many studies that 2D simulation is adequate to capture the complex multiphase flow dynamics (Beresnev and Deng, 2010; Deng et al., 2015; Deng and Cardenas, 2013; Schlüter et al., 2016; Tryggvason et al., 2001), and is adopted in this work.

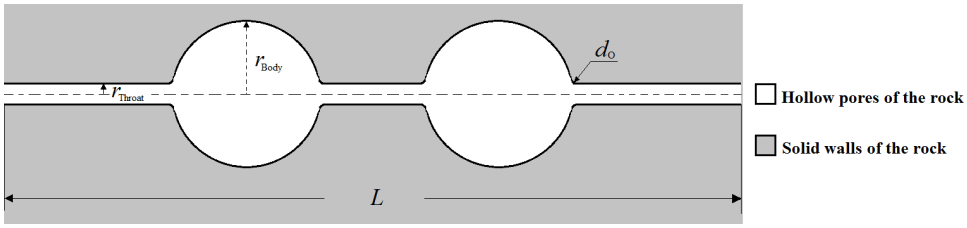

Figure 4.1 Schematic of the two-dimensional pore-throat configuration

4.3 Effects of Interfacial Tension and Wettability on the non-Wetting Oil Snap-Off Phenomenon

4.3.1 Simulation Details

4.3.1.1 Fluid properties

The properties of crude oil and water are affected by various factors, such as temperature and pressure. Considering that during a flooding process, the reservoir pressure and temperature are generally constant, constant fluid

properties are assumed, and no heat transfer occurs between the two-phase flows. A pure water-wet sandstone pore surface is assumed here. According to the typical oil-recovery applications, assuming the water viscosity of 0.001 Pa·s and a typical oil viscosity of 0.01 Pa·s (White and Corfield, 2006), the ratio of μ_w/μ_o for the standard case is set as 0.1. Both the density of the core fluid and displacing fluid are set as 1000 kg/m^3 (Deng, 2010). The standard oil/water interfacial tension with a value of 0.052 N/m is taken from the reference (Lv and Wang, 2015).

4.3.1.2 Initial and boundary conditions

The initial interface configuration used in this work is shown in Figure 4.2, which initial oil saturation is 73.97%. The red part represents the oil phase, while the blue part represents the water phase. A uniform water-film thickness of 1.5 μm was used as an initial pattern for a completely water-wet situation, where the contact angle is zero between the aqueous phase and the rock surface.

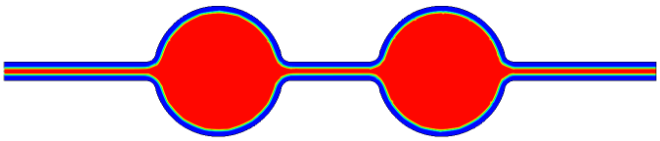

Figure 4.2 The initial configuration snapshot of the water wet pore

The boundary condition for the left inlet is the velocity inlet, where the inlet velocity with 0.005 m/s of the invading phase (water) is calculated from the average flow rate used in a typical EOR operation. It is obtained by assuming water as the reservoir's most abundant phase and Darcy's Law applied. It states that $Q_D = (\frac{\kappa^* \cdot A}{\mu_w})p_x$, where κ^* is the permeability, A is the cross-sectional area, μ_w is water viscosity and p_x is the background pressure gradient. To convert Q_D to an estimated velocity in a single channel, below equation is obtained, $u = (\frac{\kappa*}{\mu_w \cdot \varphi})p_x$, where φ is the porosity. The maximum background pressure gradients of a typical oil field, p_x, are on the order of 10^6 Pa/m, and the high end of reservoir permeability κ^* is on the order of 10^{-11} m^2 (Saffman and Taylor, 1958). For most reservoir rocks, porosity varies from less than 1% to 40%, thus the capillary number varies from an order of 10^{-2} to 10^{-6}. The outlet of the pore is specified as the pressure outlet. The boundary conditions for the pore wall are the adiabatic boundary and no-slip condition. The constant total flow rate is maintained in this work.

4.3.2 Grid independency and numerical validation

Grid-refinement studies are performed to ensure that the computed profiles and the time evolution of the fluid-fluid interface are grid independent. The structured

rectangular grid is used for simulations in this study with refined grids near the boundaries, generated by the meshing code ICEM CFD. Initially, a grid independence study is performed in a water-wet system originally saturated with oil. A time evolution of 10^{-9} s is used for calculations to satisfy the *Courant* number constrain.

The process of water flooding through an oil-saturated pore is applied as a classic and standard example of multiphase flow dynamics for the grid independency test here. Figure 4.3 shows the water/oil distributions after the flooding time of 10.0 ms and 100 ms in the displacement process at different mesh resolutions. The oil/water distributions are nearly the same, with some small variations at the water/oil interface. The higher the resolution, the sharper the interface is. Based on the grid sensitivity test results, the differences of the predicted pressure drop among the five grid systems are 9.74%, 6.04%, 3.68%, 0.46%, and 0.28% respectively. Therefore, considering both computational accuracy and efficiency, the fourth mesh system with 35276 computational grids is selected for all simulations. From the comparison, it could be seen that the capillary pressure from the simulation satisfies the Laplace theory quite well.

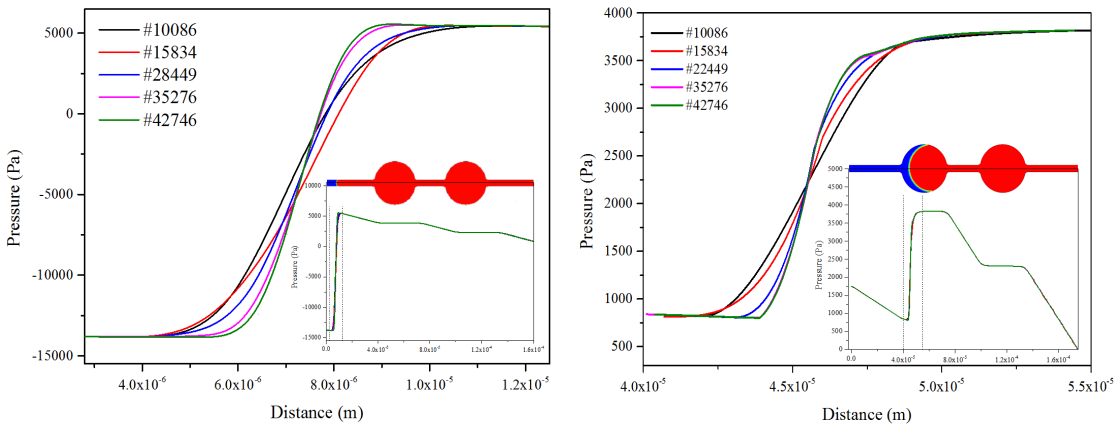

(a) *t*=10 ms (b) *t*=100 ms

Figure 4.3 Grid independency study for the initial oil-saturated channel

4.3.3 Snap-off phenomenon of oil phase in water-wet pores

In this section, water invasion at the pore scale is modelled as the standard case. The water/oil phase distribution evolutions with time are shown in Figure 4.4. It could be seen that the “snap-off” phenomenon can occur during the imbibition process, but only in the pore throat region. The phenomenon in which a wetting phase in the corners pinches off the non-wetting phase in the middle of the pore throat is referred to snap-off, which is a dominant mechanism for residual trapped oil in porous media. At the pore scale, capillary force plays an important role and can prevent the non-wetting phase from flowing. The snap-off process is mainly

dependent on the physical geometry of pore channels, wettability and interfacial tension (Kiss et al., 1982). At the first stage of the displacement, water tends to flow through the films, thus a swelling of the water film appears. As water invasion continues, the filling grows so that eventually the wetting fluid is able to fill the pore throat, making the snap-off happen. As the non-wetting phase cannot fill the next pore body rapidly and cannot keep the capillary pressure on the pore throat high enough, it is consequently pinched off by the wetting phase, which remains in the pore throat. This process continues intermittently until the second pore body is filled up, and the non-wetting phase in both pore bodies can stay connected without being snapped off. Ultimately, the oil phase is snapped off with seven discontinuous parts and stuck in the pore geometries, as shown in the final state in Figure 4.4. This stuck phenomenon of the oil phase is consistent with previous experimental results (Sheng, 2015), which demonstrated that a critical capillary number to mobilize discontinuous oil is higher than that to mobilize continuous oil.

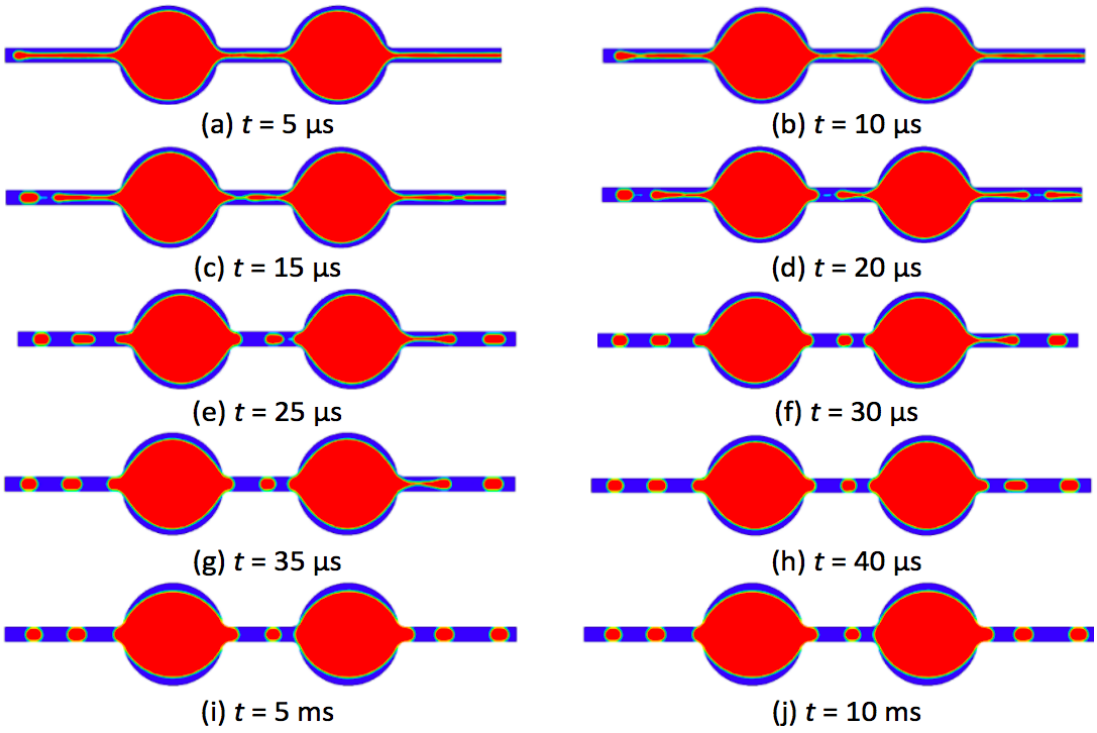

Figure 4.4 Standard traditional water flooding process, Ca=3.56×10^{-5}

An example pressure distribution along the central axis along horizontal direction after 1.0 ms is shown in Figure 4.5. Under the same condition, the smaller capillary diameter leads to a larger capillary pressure. Capillary force by a snap-off mechanism makes the oil phase unconnected, forming high pressure islands that prevent the recovery of oil.

After the non-wetting phase forms pockets that are disconnected from the continuous phase, it is considered to be trapped and plug water channels. At the

displacing time of 1.0 ms, the remaining oil fraction in the pore channel is 73.97%, which suggest that for this particular case simulated, traditional water flooding would not increase oil recovery rate significantly: nearly all the residual oil is trapped in the pore channel due to the capillary effect. In order to increase the capillary number and suppress the snap-off phenomenon at the pore scale, the viscosity and interfacial tension effects on the displacement for the water-wet pores are studied in the next section.

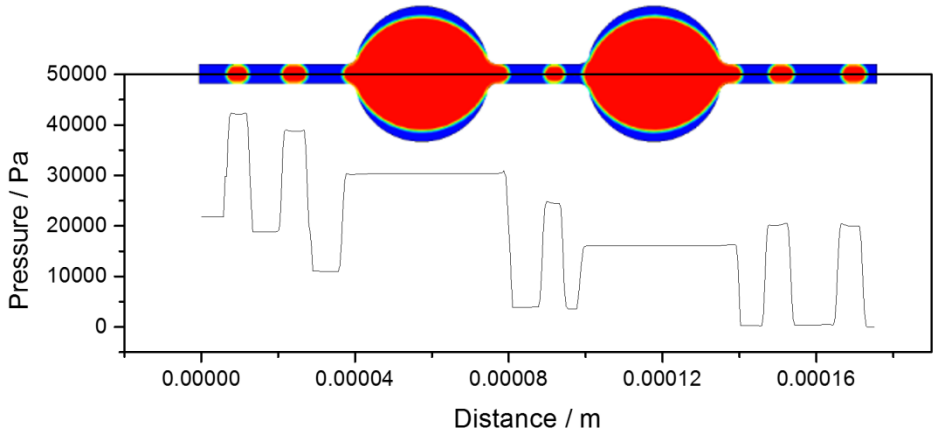

Figure 4.5 Pressure distribution along the central axis along horizontal direction

4.3.4 The effects of interfacial tension and viscosity on the displacement for water-wet pores

The effects of IFT and viscosity on the displacement were simulated by 17 case studies, as shown in Table 4.1. The simulation results of Case 1, as the standard case of traditional water flooding process, have been presented in the Section 4.3.4. For the IFT effect study, the IFT between the invading fluid and oil phase was varied from 0.05 N/m to 0.0005 N/m at a given viscosity of 0.001 Pa.s (Case 1~9). To simulate the effect of the invading fluid viscosity, the viscosity of the invading fluid was varied from 0.001 to 0.05 Pa.s at a given IFT value of 0.05 N/m (Case 1, 10~16). The corresponding capillary number distribution is within the range of 3.56×10^{-5} to 3.56×10^{-3}. An optimal case (Case 17) was also investigated with the minimum test IFT of 0.0005 N/m and the maximum test viscosity of 0.05 Pa·s, with a corresponding capillary number of 1.780×10^{-1}.

Compared with the standard case, the simulation results of IFT and viscosity effects from Case 2 to Case 16 show that the pattern of the interface-shape evolution does not change dramatically, the snap-off phenomenon still occurs for all the cases at larger capillary numbers. However, the snap-off time was postponed significantly as compared with the traditional water flooding scenario and the number of the snapped-off positions was decreased (i.e., less than seven parts). For comparisons, the snap-off time in this work refers to the time of the

third break-up position for the oil phase. A dimensionless snap-off time τ is defined as $\tau = \tau_s/\tau_0$, where τ_0 is the standard snap-off time for traditional water flooding (Case 1). By using the dimensionless time and the capillary number, the snap-off time vs the channel capillary number is shown in Figure 4.6. It can be seen that a lower IFT has stronger effects on postponing the snap-off time, which is beneficial for keeping the oil phase continuously.

Table 4.1 Parameters used in the study of viscosity and interfacial tension effects

Case No.	μ_0, Pa·s	σ, N/m	*Ca*	Viscosity Ratio μ_o/μ_i	Case No.	σ_0, N/m	μ_i, Pa·s	*Ca*	Viscosity Ratio μ_o/μ_i
1		**0.05**	3.560×10^{-5}		10		0.0025	8.900×10^{-5}	4:1
2		0.04	4.450×10^{-5}		11		0.005	1.780×10^{-4}	2:1
3		0.03	5.933×10^{-5}		12		0.01	3.560×10^{-4}	1:1
4		0.02	8.900×10^{-5}		13	0.05	0.02	7.120×10^{-4}	1:2
5	**0.001**	0.01	1.780×10^{-4}	10:1	14		0.03	1.068×10^{-3}	1:3
6		0.005	3.560×10^{-4}		15		0.04	1.424×10^{-3}	1:4
7		0.0025	7.120×10^{-4}		16		0.05	1.780×10^{-3}	1:5
8		0.001	1.780×10^{-3}			σ, N/m	μ, Pa·s	*Ca*	
9		0.0005	3.560×10^{-3}		17	0.0005	0.05	1.780×10^{-1}	1:5

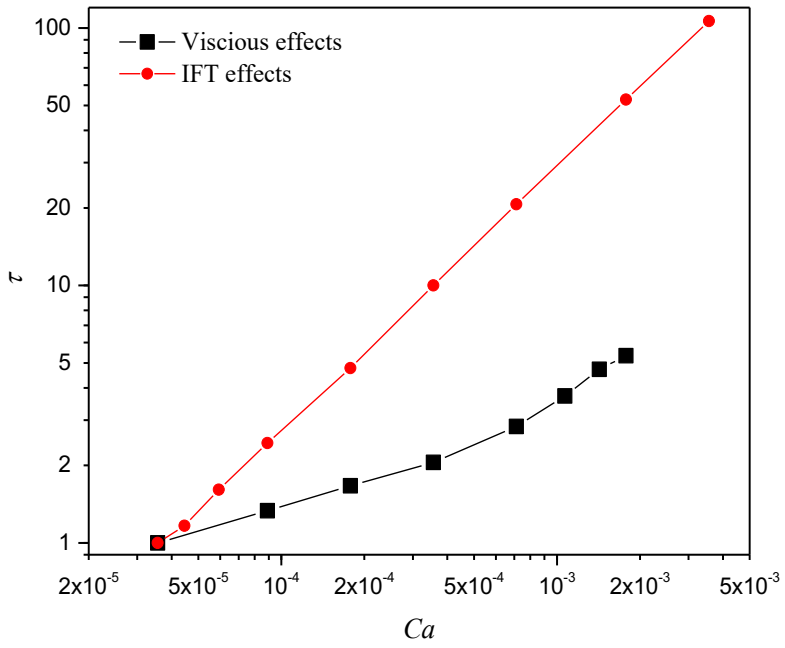

Figure 4.6 The effect of the capillary number *Ca* on the snap-off dimensionless time

The effects of viscosity and interfacial tension on the oil recovery factor at the snap-off time are shown in Figure 4.7. It can be observed that: i) Due to the snap-off phenomenon still existing, the oil recovery rates for all the cases are still remaining at a low level; ii) Though a low IFT flooding can postpone the snap-off time, larger viscosity of the invading fluid shows better recovery performance at the snap-off time. The viscosity effect on oil recovery is due to a decreased mobility difference between the displacing and displaced fluid by decreasing the capillary forces in comparison with viscous force, which is beneficial for oil recovery; iii) Different oil recovery rates can be obtained under the same capillary number conditions, which differs from the macro-scale experimental conclusions, where it reported that the EOR effect is mainly dependent on the capillary number. A comparative example of water/oil mobilization profile by the IFT and viscosity effect respectively at a fixed $Ca = 3.56\times10^{-4}$ is shown in Figure 4.8.

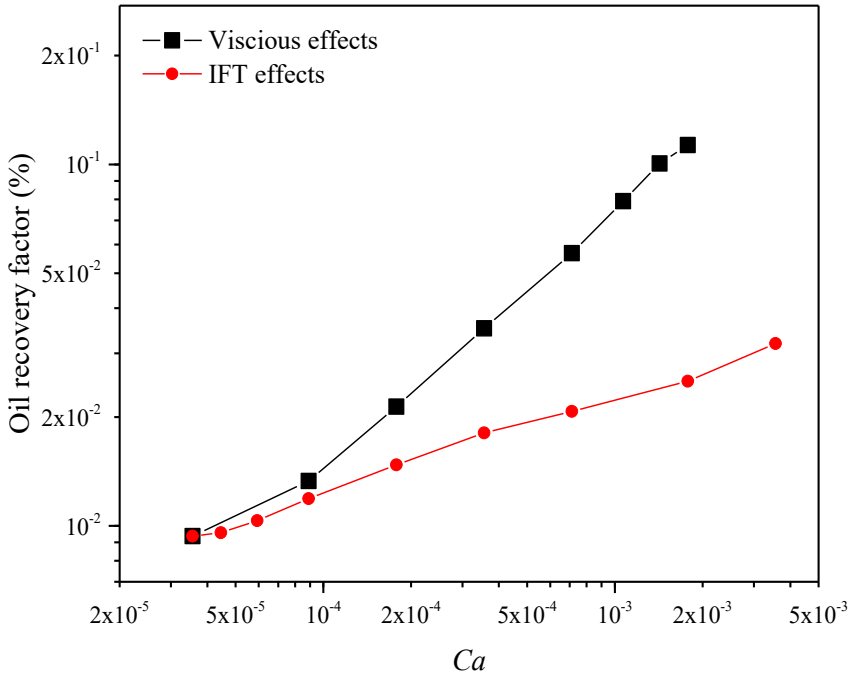

Figure 4.7 The capillary number effects on the oil recovery factor

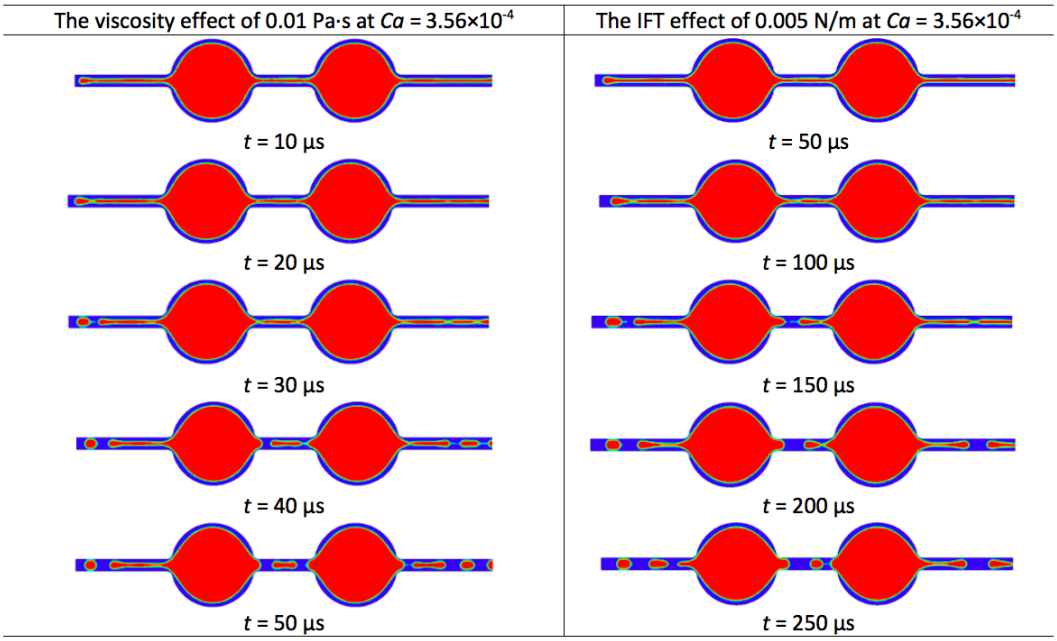

Figure 4.8 Comparisons of water/oil mobilization profile under the same capillary number $Ca = 3.56\times10^{-4}$ with the viscosity and IFT effect respectively

For the optimal case (Case 17) with the minimum test IFT of 0.0005 N/m and the maximum test viscosity of 0.05 Pa·s, which corresponding to a capillary number of 1.780×10^{-1}, the water/oil phase distribution during the displacement process is shown in Figure 4.9. It can be seen that although the collar in pore throats is growing in time, no snap-off is observed. A stable displacement process is achieved during the flooding, instead of snap-off or viscous fingering flow happening previously. This stable displacement contributes to nearly one hundred percentage of oil recovery, which represents the ideal situation for macroscale oil recovery. It could be concluded that by increasing the displacing viscosity and decreasing the interfacial tension between oil and water at the same time, a stable displacement could be achieved, instead of the snap-off phenomenon, which is beneficial to oil recovery in the field scale.

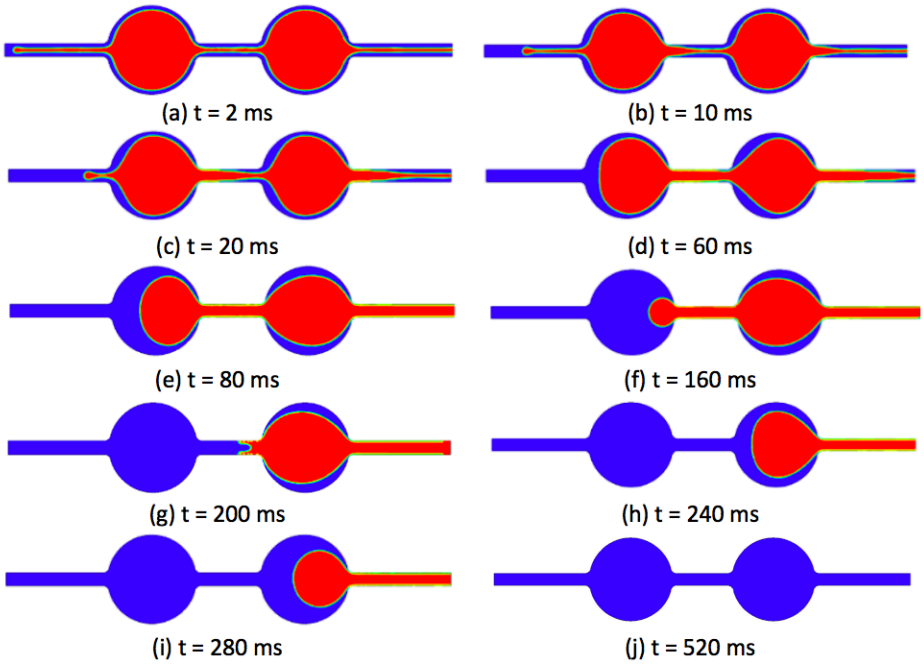

Figure 4.9 Water/oil phase distribution during the displacement process for Model 17 (Ca =1.780×10^{-1})

Figure 4.10 shows the pressure distribution profile along the centre of x axis with the capillary number of 1.780×10^{-1} at the time of 2.0 μs. It can be observed that the pressure reduces gradually with the injection of invading fluid in the first stage, and it stays constant when water enters the middle pore. After water flows into the right throat, the pressure reduces continuously until the water breaks through. The pressure difference between the inlet and outlet is around 10^4 Pa, which is much smaller comparing to the traditional water flooding case, as shown in Figure 4.5. In addition, the high-pressure islands associated with the snapped off phenomenon are disappeared.

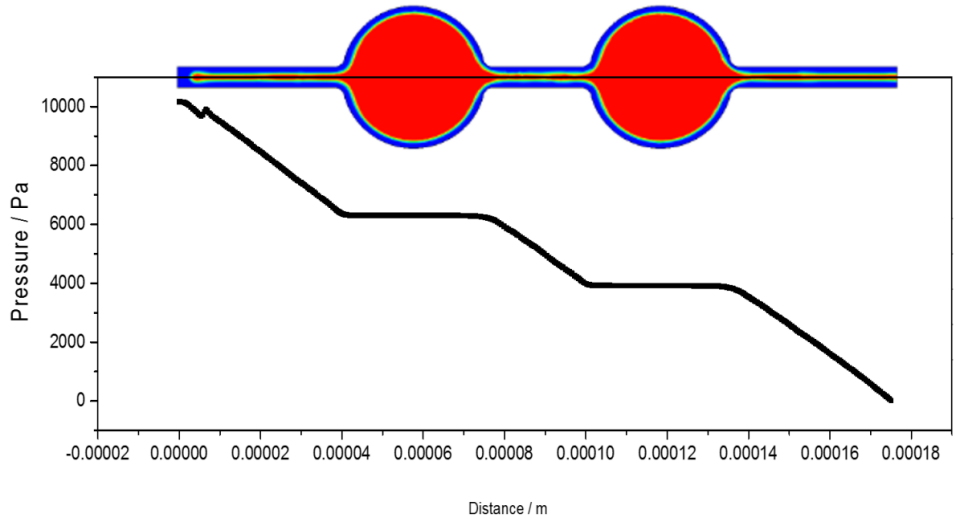

Figure 4.10 The pressure distribution profile along the centre of *x* axis for Ca =1.780×10^{-1}

4.3.5 The effects of interfacial tension on the displacement process at the same capillary number

Traditional flooding theory claimed that capillary effects will have obviously negative influences on oil recovery in macroscale when $Ca < 10^{-5}$, due to the trapped effects. Above simulation suggests that the same capillary number could render different oil recovery factors at the single pore scale. Therefore, this section focuses on the flow characteristic of flooding process for a given capillary number. With the same injecting velocity, four *Ca* number conditions with totally 28 scenarios were simulated here (i.e. in combination with different interfacial tension and invading viscosities), which was 8.90×10^{-5}, 3.56×10^{-4}, 1.78×10^{-3} and 1.78×10^{-2} respectively.

Three kinds of flow regimes are observed from the simulation results due to the effects of IFT and viscosity, which are snapped-off flow regime, transient flow regime and the stable flow regime, respectively. Hereinto, the snapped-off flow regime is defined as the final oil phase distribution with six or seven discontinuous parts; the stable flow regime refers to the displacement process with no snap-off position appearance, though with a tendency towards snapped-off due to the capillary effect; the flow with one to five discontinuous oil phase is termed as the transient flow regimes, which lies between the snapped-off and the stable displacement state. An example of each flow regime is shown in Figure 4.11.

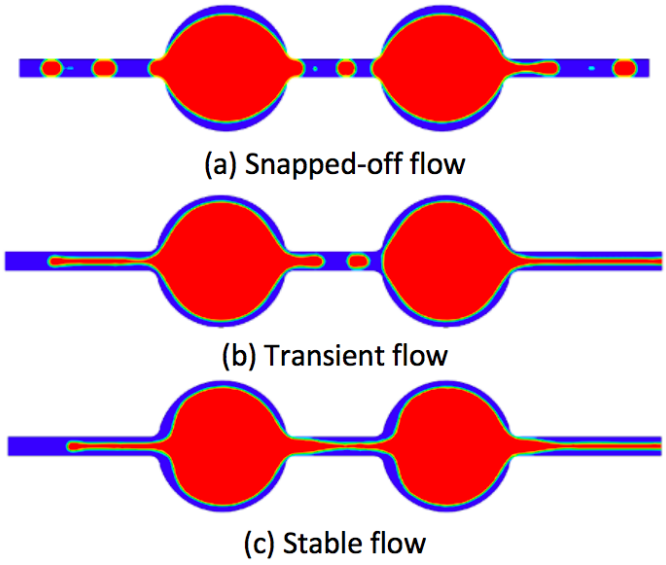

Figure 4.11 An example of the three flow regimes: (a) Snapped-off flow with *Ca* = 1.78×10^{-3} (b) Transient flow with *Ca* = 1.78×10^{-3} (c) stable flow regime with *Ca* = 1.78×10^{-2}

The flow regime distributions of all the 28 cases and the corresponding final oil recovery rates are concluded in Figure 4.12. The scatters of the interfacial tension, viscosity and the final EOR recovery factor are plotted on a logarithmic

scale. Three colours of each scatter are corresponding with the three flow regime types, which are blue, dark yellow and magenta respectively. The red colour is used to represent the pore-scale EOR recovery factor for these 28 scenarios, which is shown in the right *y* axis. The displacement scenarios with same capillary numbers are indicated by four shapes of points. The slopes of the four orange dash lines are all the same, which can reflect that the displacements are conducted with the same injecting and average velocity conditions. Additional 17 cases mentioned in Section 4.3.4.3 are also plotted with cross mark as the supplementary comparison. For the pore structure studied in this work with the completely water-wet state, the simulation results show that: i) By altering the invading viscosity and IFT between two phases, oil different recovery factors and flow characteristics during the displacement process can be obtained; ii)The same capillary number can result in different oil recovery factors due to the existence of different flow regimes; iii) The critical capillary number for mobilizing all the oil phase in this strongly water-wet pores is at a level of between 10^{-3} and 10^{-2}, which is consistent with previous experimental results (Setu et al., 2013); iv) Different flow regimes are related to different pore-scale EOR recovery factors (RF): the snapped-off regime mainly leads to a RF around zero percentage; the transient flow can result in 2 ~ 5 % of oil recovery; and nearly one hundred percentage for the stable displacement process; v) The three flow regime distributions can be divided into three separate zones, separated by the two black dash lines in this figure, which is more related to the variations of IFT than the invading viscosity.

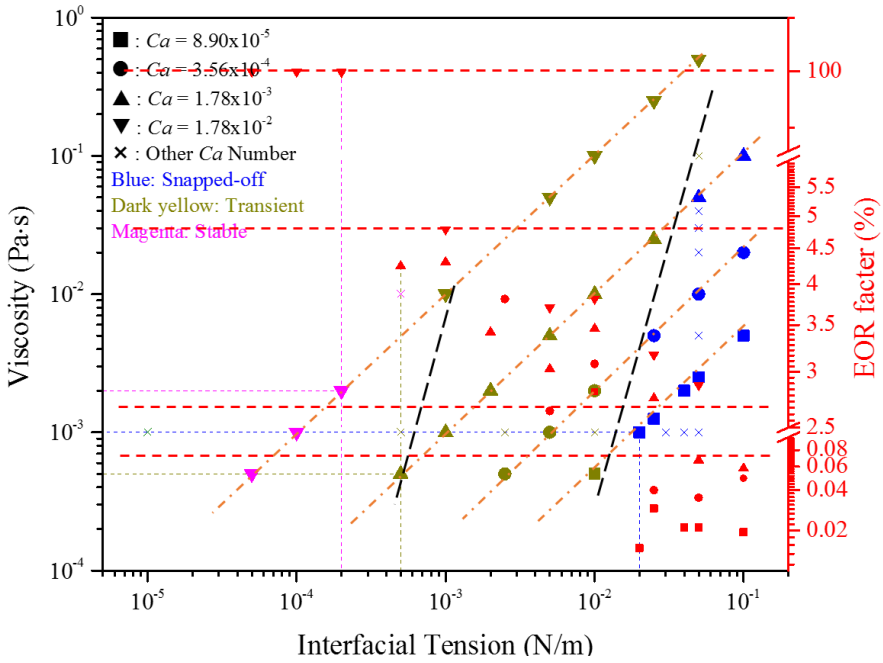

Figure 4.12 Flow regime distributions of each case and the corresponding final EOR recovery factors

4.3.6 The effect of the ultralow interfacial tension on the displacement process

Above studies have showed that reducing IFT of oil-water is one of the most important mechanisms for enhancing oil recovery. However, a common belief that ultralow IFT (i.e., less than the order of magnitude of 10^{-3} mN/m) values are needed for good performance in EOR has been recently questioned (Saffman and Taylor, 1958). To investigate if ultralow IFT is feasible for enhanced oil recovery, a case of IFT =50 nN/m was simulated with a corresponding capillary number of 35.6.

In a completely water-wet pore channel, the water/oil flow characterization results can be observed in Figure 4.13. At the beginning of displacement, a stable interface advances as a concave meniscus. Then the interface turns to a convex meniscus and finally, it displays as a viscous fingering profile. Though there is no snap-off phenomenon happening in the capillary, there are still large quantities of oil remaining in the pore channel due to the fingering flow. The fingering has all the characteristics of the Saffman-Taylor (Saffman and Taylor, 1958) instability, which appears when a less viscous fluid pushes a more viscous fluid in a thin channel. The interface between the fluids develops an instability, leading to the formation of finger-like patterns. Similar fingering flow regime has also been observed experimentally by Setu et al. (Setu et al., 2013) at an IFT= 50 nN/m.

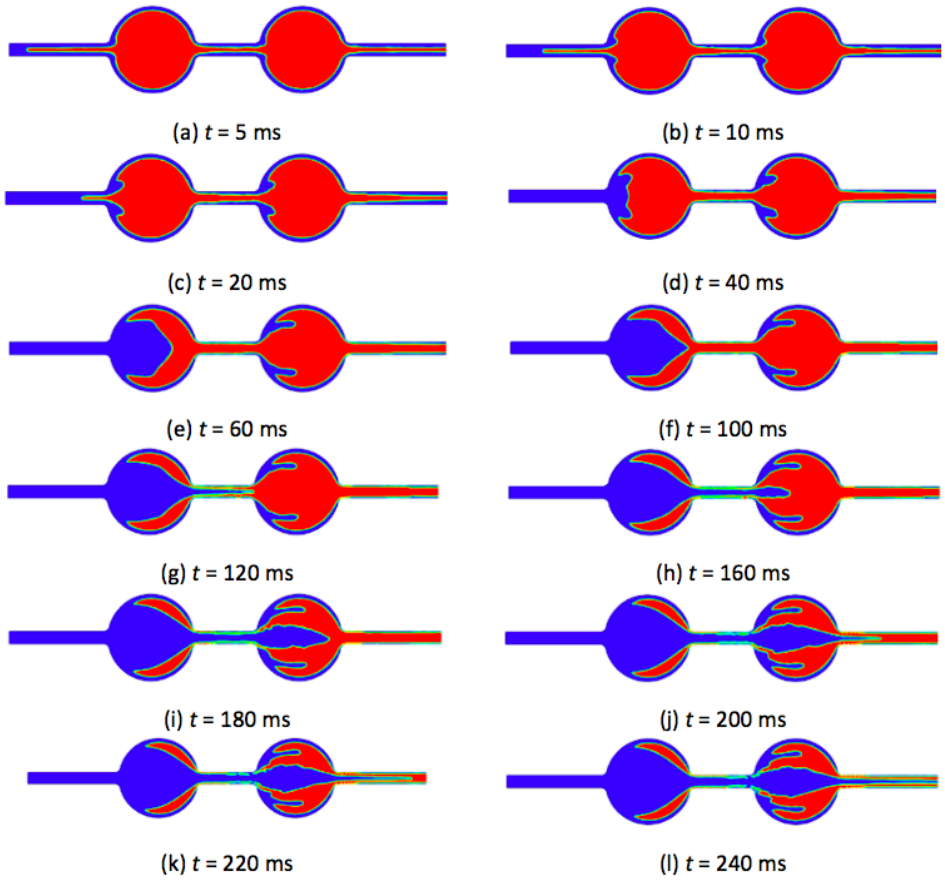

Figure 4.13 Viscous Fingering at ultralow interfacial tension (σ=50 nN/m)

According to the numerical results, the remaining oil fraction is around 0.32 at the breakthrough time of the displacing fluid, which leads to a pore-scale recovery factor of 56.80%. Compared to traditional water flooding with the snap-off flow regime, the oil recovery factor is largely enhanced. However, nearly half of the oil is still remained in the pore channel. Such results support the recent questioning on the effect of IFT, i.e., an ultralow IFT may not achieve the expected EOR effect at a similar capillary number (Zhang, Haiyan et al., 2010). Some recent flooding experiments (Yu et al., 2010) also showed that in some cases, there is no straightforward correlation between lowered IFT and enhanced recovery rate.

Figure 4.14 shows the pressure distribution along the centre of *x* axis at *t* = 10 ms. It can be seen that the pressure dropped slowly along the pore-scale channel during the flooding process. The pressure difference between the inlet and outlet is around 354.2 Pa, which is much smaller than traditional water flooding and polymer/surfactant flooding. Therefore, chemical flooding with ultralow IFT could have encouraging effects of reducing injection pressure.

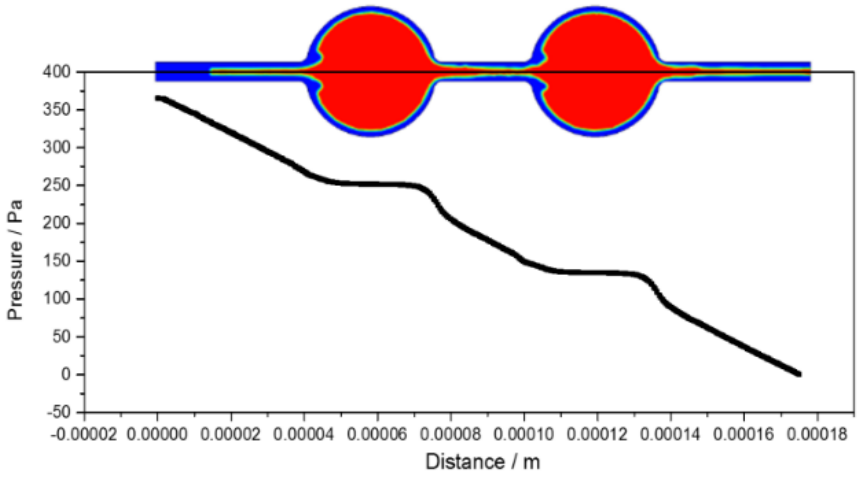

Figure 4.14 The pressure distribution profile along the centre of *x* axis at ultralow interfacial tension (50 nN/m)

4.4 Effects of Interfacial Tension and Wettability on the Capillary Trapping

4.4.1 Abstract

For enhanced oil recovery (EOR), the oil/water flow characteristic during the flooding process was numerically investigated with volume-of-fluid method in pore scale. A two-dimensional pore throat-body connecting structure was established in this work. Four scenarios were simulated in this work: For oil-saturated pores, the wettability effect on the flooding process was studied; for oil-unsaturated pores, three effects were modelled to investigate the oil/water phase flow behaviors for enhanced oil recovery, which were respectively the wettability effect, the interfacial tension (IFT) effect, and the combined wettability/IFT effect. The results show that, oil saturated pores with the water-wet state of can lead to 25% ~ 40% more oil recovery than with the oil-wet state; the remaining oil mainly stays in the near wall region of the pore bodies for oil-wet saturated pores. For the oil-unsaturated pores, the wettability effects on the flooding process can help oil detaching from the pore walls. By decreasing the oil/water interfacial tension and altering the wettability from oil-wet to water-wet state, the remaining oil can be enhanced successfully. The wettability-IFT combined effect shows better EOR potential compared with decreasing the interfacial tension alone under the oil-wet condition. The simulation results in this work are consistent with previous experimental and MD simulation conclusions. The combination effect of the IFT reducing and wettability alteration can become a part of recovery mechanism in this study for the nanoparticles, surfactant, and nanoparticle-surfactant hybrid flooding process for enhanced oil recovery.

4.4.2 Simulation Details

4.4.2.1 Fluid properties

Similar to the work conducted in Section 4.3, constant fluid properties are assumed in this pore-scale simulation work, and no heat transfer occurs between the two-phase flows and pore walls. By assuming the invading fluid (e.g., water) viscosity of 0.001 Pa·s and a typical oil viscosity of 0.01 Pa·s (White and Corfield, 2006), the ratio of μ_w/μ_o for the standard case is set to ten. Both the density of the core fluid and displacing fluid are set as 1000 kg/m^3 (Deng, 2010). The standard oil/water interfacial tension with a value of 52 mN/m is taken from the reference (Lv and Wang, 2015). To investigate the interfacial effect on the flooding process for oil unsaturated pore, an ultralow oil/water IFT value of 52 μm/m was used, which can be obtained by the surfactant assistant practically.

4.4.2.2 Initial and boundary conditions

Four scenarios were simulated in this work: For oil-saturated pores, the wettability effect on the flooding process was studied; For oil-unsaturated pores, three effects were modelled to investigate the oil/water phase flow behaviours for enhanced oil recovery, which were respectively the wettability effect, the IFT effect, and the combined wettability/IFT effect. The initial oil/water phase distribution for both the oil saturated and unsaturated pores is shown in Figure 4.15. The red part represents the oil phase, while the blue part represents the water phase.

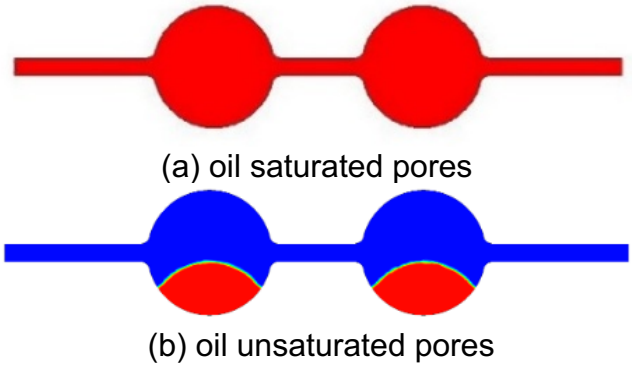

(a) oil saturated pores

(b) oil unsaturated pores

Figure 4.15 The initial oil/water phase distribution for the oil saturated and unsaturated pores

For oil saturated pores, one-hundred percentage of the initial oil volume fraction was established; the water contact angle varied from 0° to 180° was simulated to present different wettability states of the pore rocks. For oil unsaturated pores, a random initial wettability state was set with an initial oil volume fraction of 19.298%; different ultimate constant water contact angle varied from 0° to 150° was set to simulate the flooding process when the wettability alters. It is notable

that, this initial oil volume fraction of 19.298% can be reasonably considered as a proper value for this single-pore channel investigation, not only because it cannot be directly compared with the average remaining oil volume fraction in the overall oil field before EOR, but also can lead to an easier visualization of the contact angle when studying the wettability effect as an oil droplet size. Besides, to focus on the wettability and interfacial effects on the flooding process for enhanced oil recovery, the same injecting velocity of the invading fluid was used by all the cases in this work as a standard value of 0.005 m/s.

4.4.3 The wettability effect on the flooding process in oil saturated pores

Different reservoir rocks have widely different wetting characteristics. The degree of wettability can vary even within a single reservoir (Skauge et al., 2007). In this section, the water flooding process for an initial oil-saturated pore was simulated under the different wettability conditions. Seven cases were studied to simulate the flow characteristic and oil recovery factor, which water contact angle was 0º, 30º, 60º, 90º, 120º, 150º, 180º, respectively.

Figure 4.16 shows the oil/water phase distribution evolution with time under the completely oil-wet state (water contact angle θ = 180º) with water flooding. It can be observed that water firstly flows from the inlet to the pore throat, pushing the initial saturated oil out from the outlet. Most oil in the pore throat part is flushed out before water flows into the pore body, though small amounts of oil sticking onto the rock walls due to the strongly oil-wet condition. After the water flow flooding from the first pore body to the second pore throat, partial oil phase is remaining near the walls with the concave meniscus shape corresponding to the water flow streamline. The multiphase flow transport characteristics repeat in the next following pore throat and body structures until water breakthrough occurs.

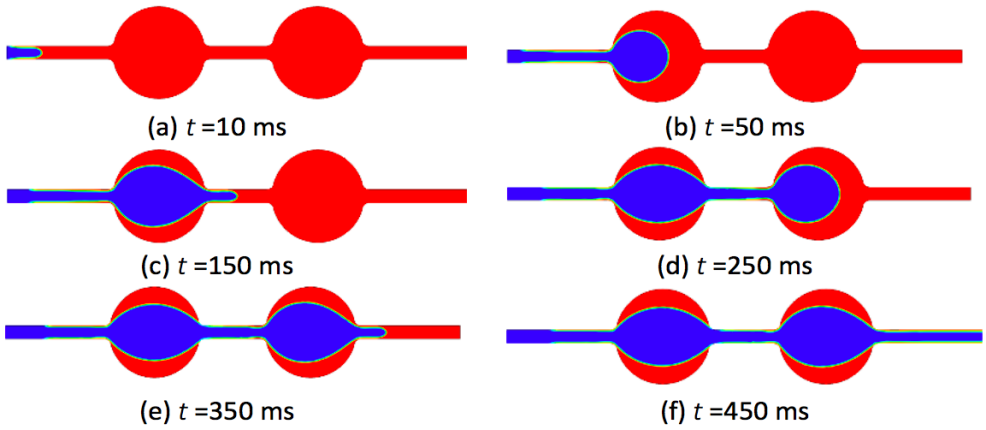

Figure 4.16 Flooding process under the completely oil-wet state

The intermediate state (water contact angle θ = 90º) between water-wet and oil-wet was illustrated for the water flooding process in Figure 4.17. Differing from the flow characteristics under the completely water-wet state above, two convex meniscus of oil form in the pore throat when water flows through the pore throat due to the contact angle, which has also been observed previously with experiments by Zhang et al. (Zhang, Hua et al., 2014). While the water continues flowing from the first pore throat into the first pore body, the two convex oil meniscuses are growing big, flowing forward, and finally settling at the pore-body wall close to the connecting site. Besides these two oil meniscuses remaining in the first pore body, the initial oil inside the first pore body is completely recovered as the invading fluid flooding by. The same flow characteristics repeat in the following pore throat/body structures. As the fifth and sixth oil meniscus is flooded away from the pore outlet, only four symmetrical oil meniscus remains inside the pore after a long-term flooding.

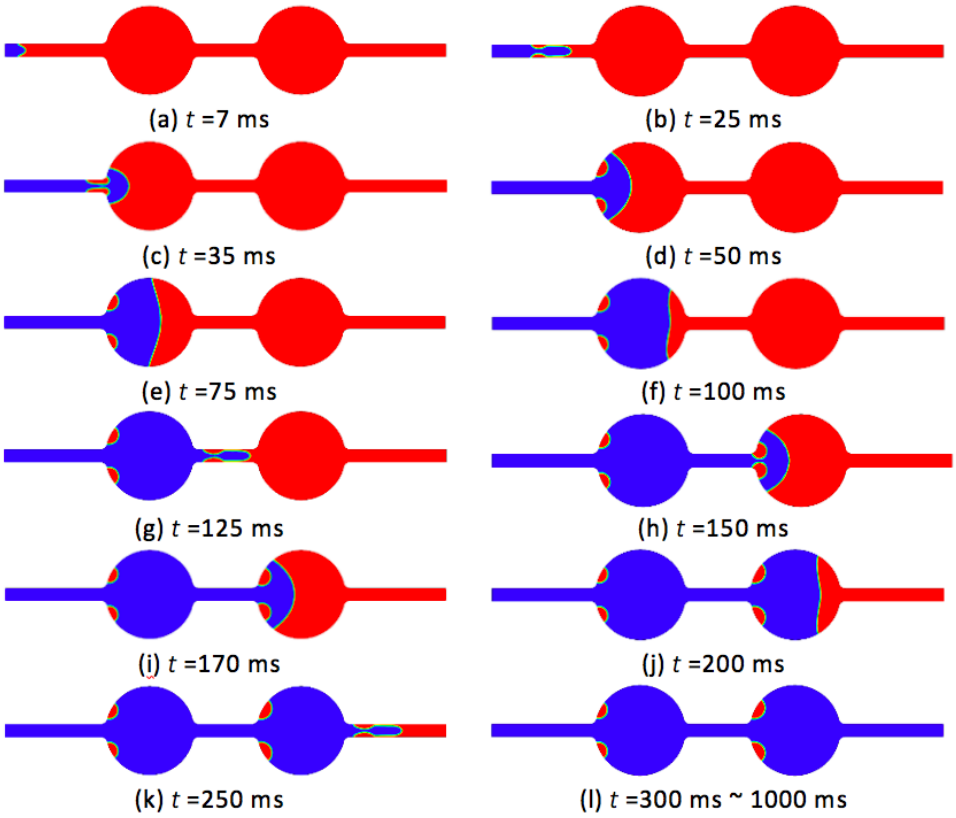

Figure 4.17 Flooding process under the intermediate wet state

For an initial oil-saturated pore with completely water-wet state, the water flooding process can be observed from Figure 4.18. An ideal and stable flow situation occurs during the flooding process, with a one-hundred percent of oil recovery factor after the invading fluid flowing out from the outlet.

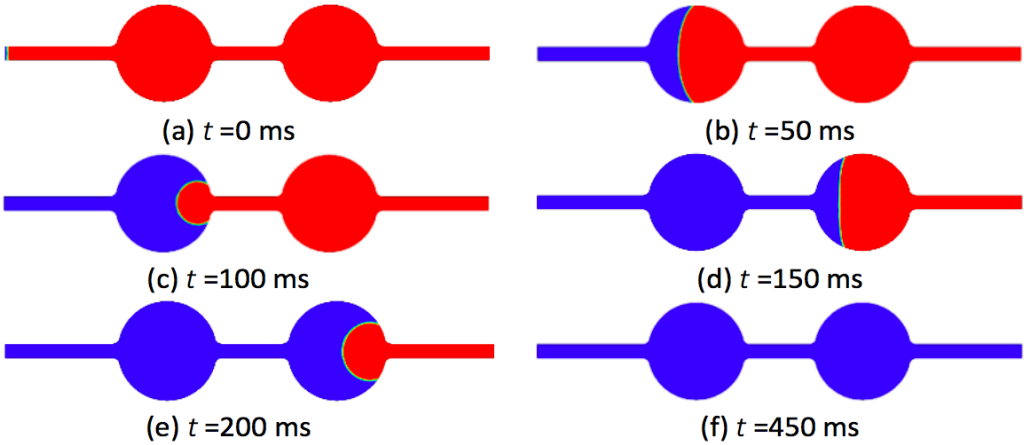

Figure 4.18 The flooding process under the completely water-wet state

The detail oil recovery factor results after the water flooding of the seven wettability scenarios (water contact angle is 0º, 30º, 60º, 90º, 120º, 150º, 180º) are concluded in Figure 4.19. It can be seen that the oil recovery factor turns out to be between 60% and 75% under the oil-wet state (water contact angle larger than 90º). As the pore wettability convert from the oil-wet state to the intermediate state, the oil recovery factor increases as high as 96%. As long as under the water-wet condition (water contact angle smaller than 90º), a one-hundred percent of oil recovery factor can be obtained, with no oil phase remaining in the pore structure after the flooding process.

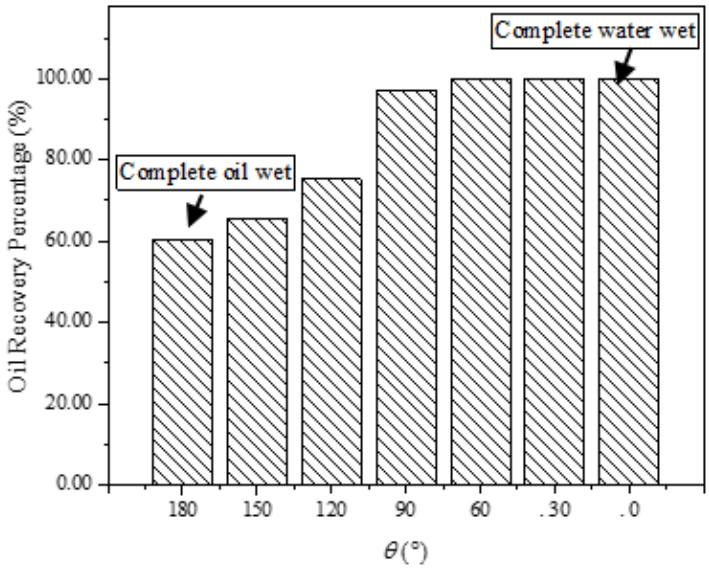

Figure 4.19 The effect of wettability situation on the final oil recovery factor

Three main ideas can be concluded from the above numerical results: i) After the primary oil recovery, the remaining oil mostly stays in the near-wall region of the pore body; ii) The water-wet state is beneficial for obtaining an ideal oil recovery results; iii) For enhanced oil recovery, if the wettability can be altered from the original oil-wet state to the water-wet state, a higher EOR factor may be obtained.

As mentioned in the introduction of Section 4.1.2, nanoparticle colloids have been proved to possess the capability of altering the wettability between the oil/water phases and pore walls (Wasan and Nikolov, 2003). Based on this idea, six cases with different initial and final wettability were simulated in the next section to symbolize the wettability effects on the flooding process for enhanced oil recovery.

4.4.4 The wettability effect on the flooding process in oil unsaturated pores

The wettability effects on the flooding process have been modelled in the initial oil-unsaturated model for enhanced oil recovery. With different initial and final wettability of the pore system, the flow characteristic of the flooding process with wettability alterations can be simulated. Practically, the wettability alteration can be realized by the assistant of nanoparticles, which has been proved by previous molecular simulation for its capacity of altering the wettability between the two-phase flow and the rock walls (Wang, F. and Wu, H., 2013). Different nanoparticle materials, concentration, and other factors can lead to different ultimate wettability (Wang, F.-C. and Wu, H.-A., 2013; Wang and Zhao, 2013).

A random wettability was used as an initial state, as shown in Figure 4.15(b). Six ultimate wettability was set to symbolize the nanoparticle effects on the wettability changing, which ultimate water contact angle is 0º, 30º, 60º, 90º, 120º, 150º, respectively. Hereinto, it is notable that the wettability is the only variable, which means the viscosity of the invading fluid and the interfacial tension between water and oil keep at the same value.

Taking two cases as examples, with an ultimate wettability of 90º and 0º, the flooding process of the oil/water phase distribution evolution via time is shown in Figure 4.20. It can be observed that the settling shape of the oil phase changes along with time for both cases. However, the oil settling position is keeping still during the displacement. After a long-term flooding, no oil phase comes out from the pore outlet. Even for the completely water-wet ultimate state, though the completely water-wet state leads to the oil detachment from the pore walls, the oil recovery factor still remains at a zero percent after a long-term flooding process.

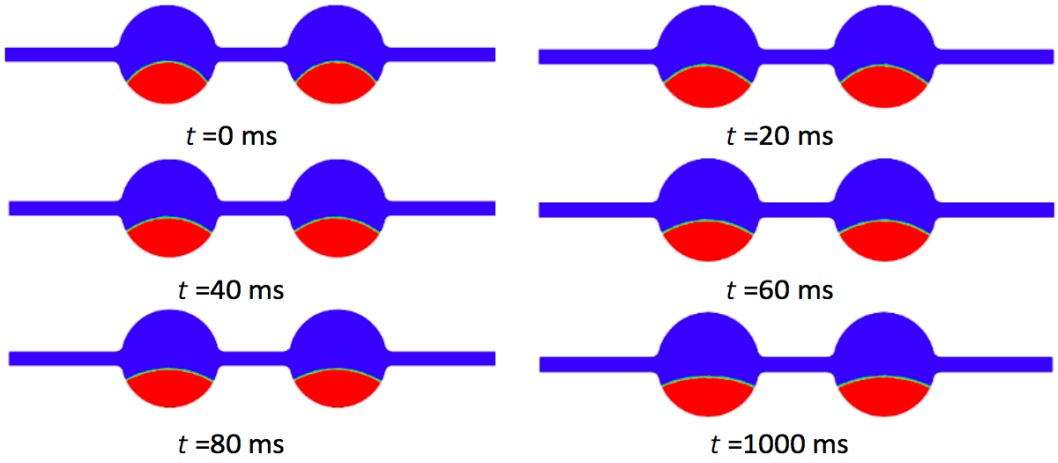

(a) From random initial state to final intermediate wet state (water contact angle is 90º)

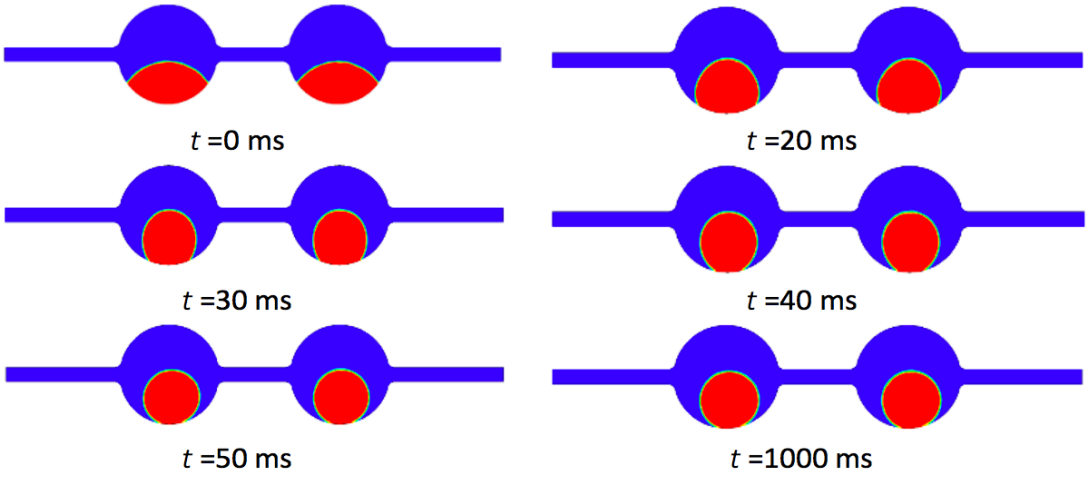

(b) From random initial state to final completely water-wet state (water contact angle is 0º)

Figure 4.20 The effect of wettability situation on the final oil recovery factor Phase distribution state via time evolution for the nanofluid flooding case

The final oil/water phase distribution of the six cases is compared in Figure 4.21, where ultimate water contact angle is 0º, 30º, 60º, 90º, 120º, 150º, respectively. The similar wettability effect on the oil detaching from pore walls have been also found by Wang et al. (Wang, F.-C. and Wu, H.-A., 2013; Wang and Zhao, 2013) with molecular dynamics simulation method, as shown in Figure 4.22. However, according to the numerical simulation results, the oil recovery factor still remains at a zero percent after a long-term flooding process for all cases. The final EOR factor turns out to be zero percent though the wettability alteration.

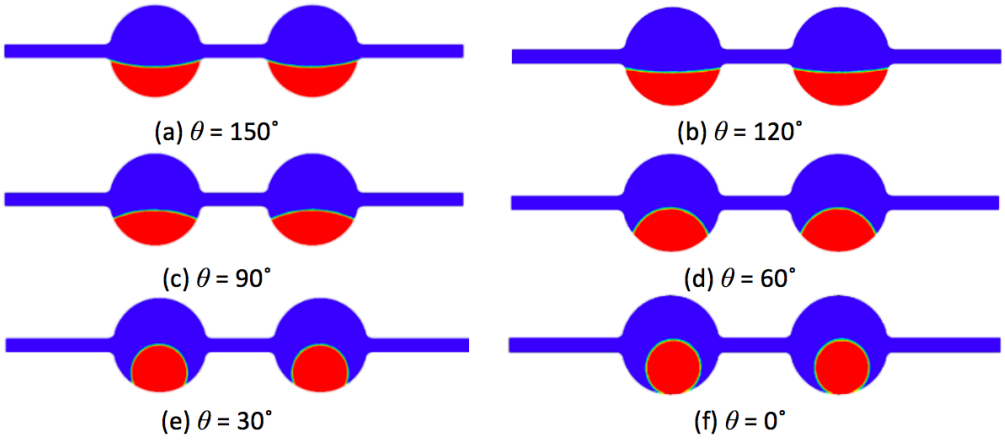

Figure 4.21 Final phase distributions at different wettability alteration state (contact angle from 150° to 0°)

For having an insight of the detailed flow characteristics, the streamline of the invading fluid for the wettability alteration from initial random state to the completely water-wet state with 0° ultimate contact angle is shown in Figure 4.22. It can be seen that after a long-term displacement, the invading fluid mainly forms two flow regimes: one is the stable laminar-like flow flowing bypass the oil droplet from the inlet to the outlet; the other is the vortex-like flow occurring at both the left and right side of the oil droplet.

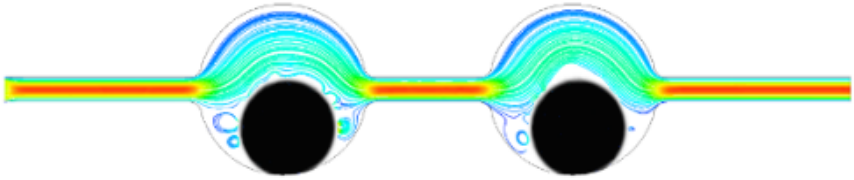

Figure 4.22 The streamline of the invading fluid for the wettability alteration to the completely water-wet state

Above analysis on the numerical results can contribute to a conclusion that, altering the wettability from oil-wet to water-wet state can contribute to the oil detachment from pore walls, but cannot lead to an ideal EOR condition due to the capillary effect. This finding is not only consistent with the molecular dynamics simulation results of Wang et al (Wang, F. and Wu, H., 2013), who claimed that the wettability effect on the oil detachment; but also consistent with the experimental results of Bayat el al. (Esfandyari Bayat et al., 2014), who demonstrated that no obvious EOR factor increasing had been observed with nanofluid flooding, with only a 2% increase. The trapped oil droplet can be explained by the capillary effect theory. The concept of capillary number *Ca* has been used as a dimensionless value to characterize the ratio of viscous forces to surface or interfacial tension forces between two immiscible liquids with an equation of $Ca=\boldsymbol{u}_{in}\cdot\mu/\sigma$, where $\boldsymbol{u}_{in}$ is the fluid velocity, μ is fluid viscosity and σ is

the interfacial tension between oil and water. The average capillary number *Ca* of these six cases is calculated to be 1.78×10^{-5}, which has been claimed that the capillary effects play a dominant role on the trapped oil with *Ca* at a level of 10^{-5} (Sheng, 2015).

4.4.5 The wettability/IFT combined effect on the flooding process in unsaturated pores

To investigate the capillary effects on this flooding process, the wettability/IFT combined effect was studied in this section.

Besides the wettability alteration from completely oil-wet to water-wet state, the interfacial tension between water and oil phase was also decreased from 52 mN/m to 52 μN/m in this scenario. Practically, this IFT decreasing can be realized by adding surfactants into the invading fluid to obtain an ultralow IFT state. Therefore, this scenario can reflect the wettability/IFT combined effect on the flooding process for EOR.

For the initial completely oil-wet case, with the same injecting velocity of the invading fluid, the oil/water phase distribution along the time evolution is shown in Figure 4.23. At the early stage of flooding, the remaining oil settling state gradually changes from the completely oil-wet of sticking-wall state to the water-wet of droplet-like state. Differing from the case in the last section, both of the oil droplets move forward from the pore body to the next pore throat with the invading fluid together, instead of staying still inside of the pore body. Due to the converted water-wet state, oil would not stick onto the pore walls during the flooding process. After a long-term flooding, all oil phase is displaced outside of the pore geometry. The enhanced oil recovery factor reaches to one hundred percent.

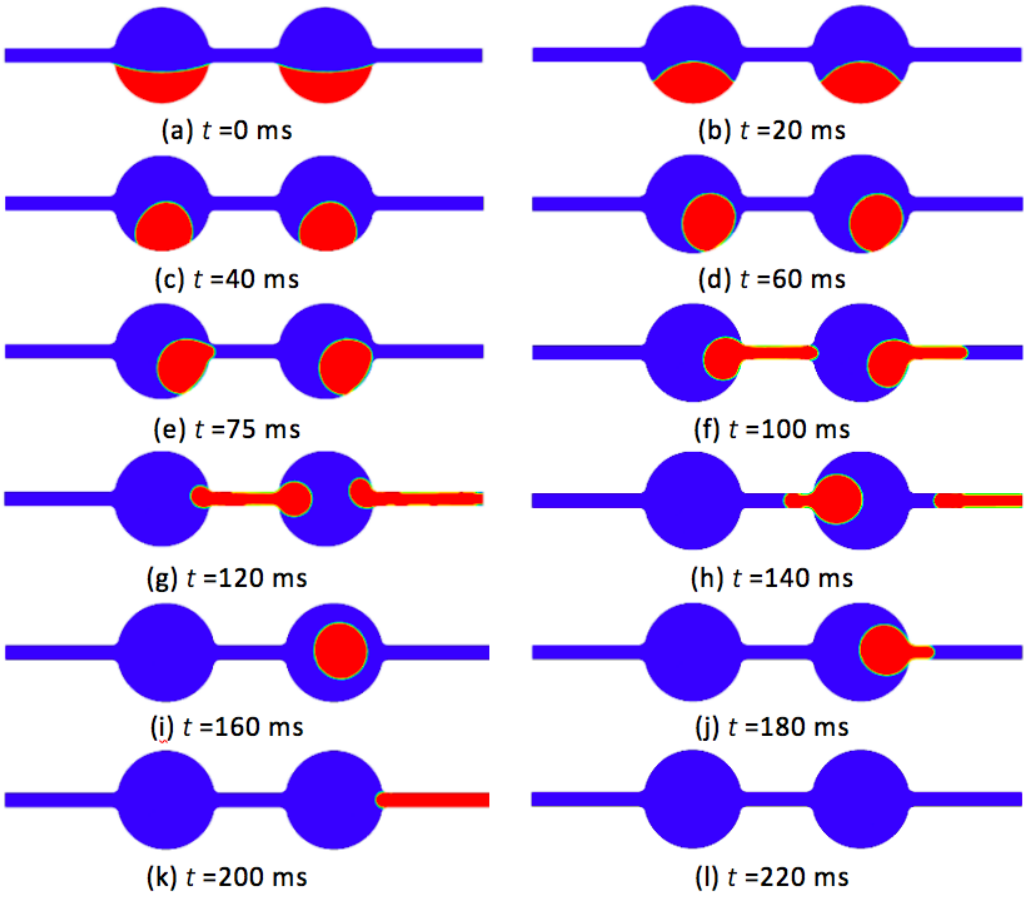

Figure 4.23 Phase distributions along the time evolution for the nanofluid-surfactant flooding case

The only difference between this scenario and the one in the last section is the interfacial tension decreasing between water and oil. The average capillary number *Ca* of this case is calculated to be 1.78×10^{-2}, which is much higher than the capillary-effect dominant range. The remaining oil turns out to be not trapped inside the pore bodies any more but be stably displaced outside of pores. The streamline of the invading fluid during the displacing period is shown in Figure 4.24. It can be observed that two vortexes appear at the left upper and lower area of each pore body. The left lower vortexes can also be observed in the "wettability-effect only" flooding case. But the appearances of the other two vortexes are focused on the left upper stream side, which lead to the imbalance drive to push the oil droplet moving forward.

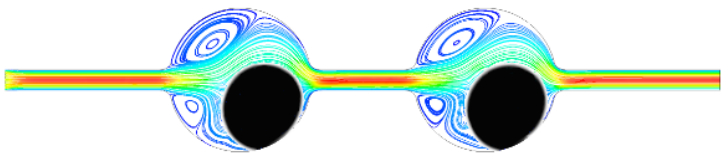

Figure 4.24 The streamline of the invading fluid for the wettability/IFT combined effect case

4.4.6 The Interfacial tension effect on the flooding process in unsaturated pores

Since the wettability-alone effect and the wettability/IFT combined effect had been investigated, the IFT-alone effect on the flooding process was simulated in this section.

For comparison, the IFT-alone effect on the flooding process was simulated in this section, which IFT was decreased from 52 mN/m to 52 μN/m. The whole displacement was conducted under the completely oil-wet state, which water contact angle is 180°.

The phase distributions along the time evolution are shown in Figure 4.25. It can be observed that, the settling position of the convex oil meniscus remains still during the displacement due to the oil-wet condition. However, due to the low oil/water IFT, a thin surface region of oil phase is gradually moving forward with the invading fluid and adjoining to the pore walls all the time, until flowing out from the pore outlet. After a long-term displacement, the interface between oil and water is too low to go through into the next pore throat. Finally, partial oil phase is trapped inside of the pore structure.

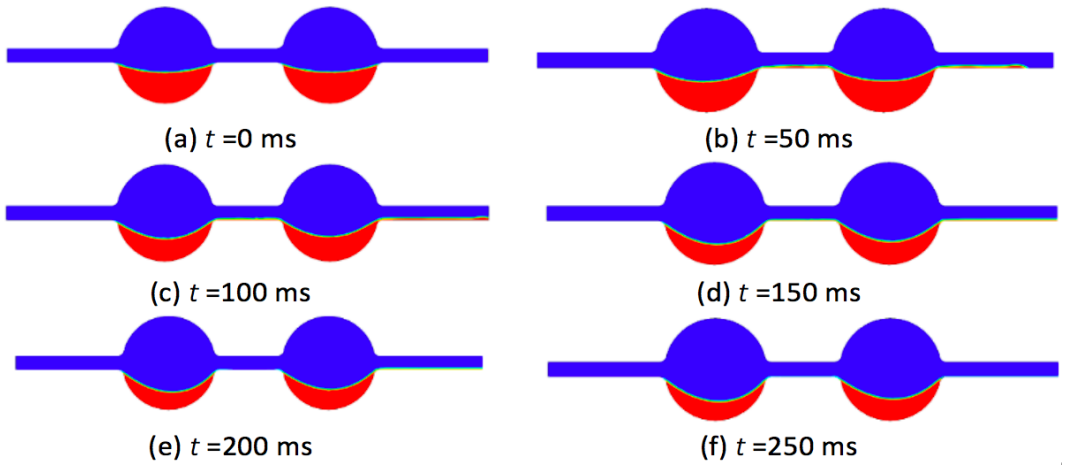

Figure 4.25 Phase distributions along the time evolution for the surfactant flooding case

To have an insight flow characteristic during the flooding process, Figure 4.26 shows the streamline of the invading fluid at the time of 100 ms. It can be seen that the vortex flow appears at the upper region inside of each pore body. Due to the completely oil-wet condition, the displacing fluid cannot invade between the oil phases and pore walls, which was previously explained as the disjoining pressure effect. Though the IFT is low enough to resist the capillary effects, an

ideal oil recovery factor still cannot be obtained due to the oil attachment, which is caused by the wettability effects.

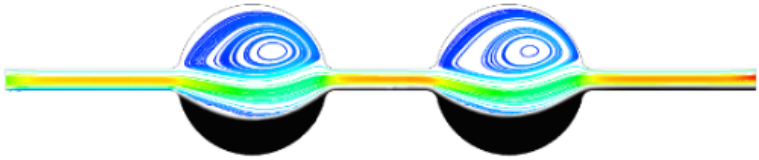

Figure 4.26 The streamline of the invading fluid for the IFT effect case

4.4.7 Comprehensive comparison of the EOR factor for the wettability and IFT effects on flooding process in unsaturated pores

Figure 4.27 is shown in this section to compare the wettability and interfacial tension effects on the EOR factor for the flooding process in initial oil-wet unsaturated pores. For all the three cases, the initial oil volume fraction is all 19.367%. It can be seen that: (i) for wettability-alone effects (case 1), the oil recovery factor turns out to be zero percent; (ii) for IFT-alone effects (case 2), the enhanced oil accounts for 30.793% of the initial oil saturation; (iii) for the wettability/capillary combination effects (case 3), all the oil is displaced out of the pore structure with no remaining, which contribute to a factor of one hundred percentage. This result can give an idea to the following conclusions: (i) altering the wettability from oil-wet to water-wet state can contribute to the oil detachment from pore walls; (ii) the oil detachment from pore walls may not lead to the oil recovery enhancement due to the capillary effect; the lower capillary number can result in the oil phase trapping inside of pores; (iii) decreasing the interfacial tension between oil and water alone, can enhance partial oil phase out of pore structures, but still lead to the oil remaining due to the oil-wet state; (iv) both the wettability and capillary effect are significant for enhanced oil recovery. Only with both water-wettability alteration and low capillary effects, an ideal EOR result can be obtained.

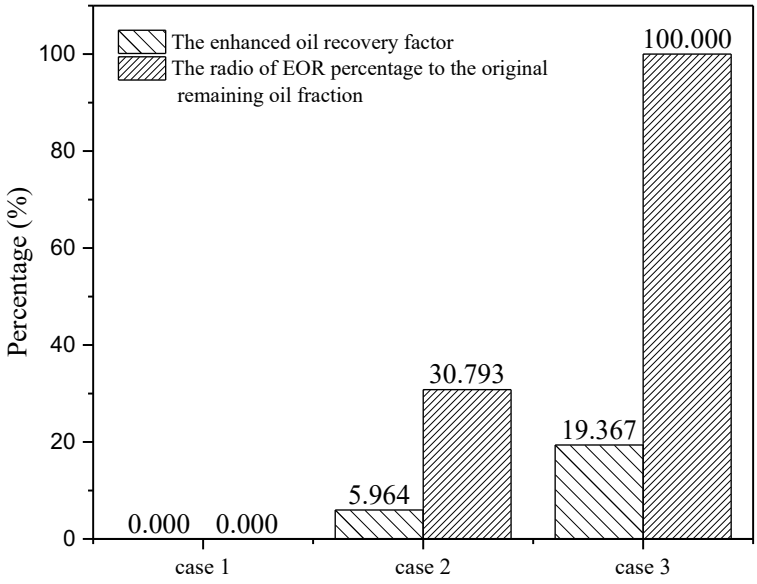

Figure 4.27 Oil recovery factors using different flooding method for initial oil-wet unsaturated pores

4.5 Conclusion

The effects of viscosity, interfacial tension and capillary number on the water/oil flow characteristics during the displacement process were simulated at the single pore scale by the VOF method. A pore-throat connecting channel was established to investigate the flooding process under water-wet condition. A flow regime was established revealing the different influences of viscosity and IFT. Moreover, the effects of wettability and capillary effects were simulated numerically at pore scale in this section. The simulation results can be concluded as follows:

- The initial continuous oil phase would be snapped off into several discontinuous oil ganglia by water and trapped into the pore channel due to the dominance of capillary effect, which would cause a low oil recovery rate at the macro-scale.
- For water-wet pores, the snap-off phenomenon can be weakened by increasing the invading viscosity or decreasing the IFT respectively. Decreasing IFT mainly keeps oil phase staying continuously, while the increasing viscosity of invading fluid could enhance the confined fluid mobilization. Both are beneficial to enhanced oil recovery at the pore scale.
- Through increasing the invading viscosity and decreasing the IFT at the same time, the oil recovery factor would be efficiently enhanced by altering the flow regime from the snapped-off regime to the stable displacement condition.

- For water-wet pores, the same capillary number can lead to different flow regimes and oil recovery factors, due to the different effects from viscosity and IFT. For the pore geometry studied in this work, the snapped-off regime mainly can lead to a very small recovery factor; the transient flow can result in 2~5% of oil recovery, and a one hundred percentage of recovery factor can be obtained with the stable flow at the single pore scale.
- When the IFT is decreased to an ultralow level, viscous fingering regime would happen in the pore channel though the injecting pressure can be reduced. A large capillary number would not always lead to a large recovery factor.
- A stable displacement process can be achieved by properly increasing the displacing viscosity and decreasing the IFT between oil and water. Ultralow oil/water interfacial tension is not necessarily due to the fingering possibility.
- In contrast, water-wet state has significantly positive effects on oil recovery at pore scale in oil saturated pores.
- For enhanced oil recovery, though the water-wet wettability can contribute to detach the oil phase from pore walls, the oil detachment from pore walls may not lead to the oil recovery enhancement due to the capillary effect.
- Decreasing the interfacial tension between oil and water alone, can enhance partial oil phase out of pore structures, but makes few effects on the oil detachment from pore walls;
- Both the wettability and capillary effect are significant for enhanced oil recovery. Only with both water-wettability alteration and a low capillary effect, can an ideal EOR result be obtained. The simulation results in this work are consistent with previous experimental and MD simulation conclusions, and can present an explanation of the nanofluid, surfactant, and nanofluid-surfactant hybrid flooding flow mechanism regarding to wettability and interfacial tension effects for enhanced oil recovery. Generally, only with both water-wet state and low capillary effects, can an ideal EOR result be obtained.

Chapter 5
Atomistic-Scale Simulation of Multiphase Flow Interactions with Molecular Dynamics Method

5.1 Introduction

Previous chapter identifies the importance of wettability in oil recovery processes. Wettability is a complex phenomenon, defined at the oil/water/surface contact regime, and shows the fluid affinity towards the substrate surface in the presence of two different phases. It affects the fluid mobility significantly, hence the EOR effect. The wettablity variation is at the heart of EOR and can be influence by many factors, from the liquid phase, oil phase to the substrate surface properties. Modifying the flooding fluid properties by varying its salt type and concentration has been recently proposed as a potential economical way for EOR, termed as low salinity flooding, however the fundamental mechanism of the low salnity and its effect on wettablity change is still unclear, which is addressed in this chapter at the nanoscale.

5.1.1 The salinity effect on the liquid/liquid interface for EOR applications

Low salinity flooding, i.e. injecting lower-salinity water (usually specified as having a 1:1 electrolyte concentration of less than about 5,000 ppm) into formation water, has been of interest as an EOR technique since the publication of the first experimental evidence by Jadhunandan and Morrow (Jadhunandan, 1990; Morrow and Buckley, 2011). Due to the complexities of oil components and reservoir rock formations, the recovery mechanisms underpinning the low-salinity EOR process are still unclear. Two physical properties which, when manipulated, are influential on low-salinity EOR phenomena are substrate wettability and the interfacial tension (IFT) between the oil and brine, when reduced (Nasralla and Nasr-El-Din, 2014). The interfaces between immiscible liquids are therefore fundamental in understanding EOR mechanisms. The interfacial tension (IFT) between oil and water is one of the key properties determining the mobility of trapped oil in reservoir rocks (Nicolini et al., 2017; Underwood, T. et al., 2015; Zhang, H. et al., 2010). However, experimental measurements for liquid-liquid interfaces at nanoscale are still very difficult to achieve because such interfaces are diffuse in comparison with solid/liquid interfaces. Consequently, experimental measurements at liquid/liquid interfaces are often associated with large uncertainties, and the detection of the influence of structural properties of oil at the interface is challenging.

An appropriate atomistic approach to explore effects associated with confinement and small length-scales is classical Molecular Dynamics (MD), which has been recently adopted to provide fundamental information on the molecular interactions and fluid flow at nanoscale. The current MD studies, however, have been exclusively focused on two-phase equilibrium between water and a single oil component, the presence of substrate and the vapor phase, which could have significant influence on the interfacial properties, has not been considered explicitly.

5.1.2 Low-salinity effects on the wettability for EOR applications

A number of laboratory and field studies have shown that use of low-salinity water injection could modify the substrate wettability and increase oil recovery rate in sandstone reservoirs (Pereira et al., 2014). Understanding the wettability of mineral surfaces is crucial not only for EOR from conventional and non-conventional oil fields, but also for the geological sealing of oil and gas by cap rocks (Ershadi et al., 2015). Though there is general agreement that the EOR effect by low-salinity water flooding is related to modification of substrate wettability creating more hydrophilic surfaces, the underpinning mechanism leading to wettability change is still a matter of debate (Al Shalabi et al., 2014; Myint and Firoozabadi, 2015; Puntervold et al., 2015; Tian and Wang, 2018).

It has been noted that the observed low-salinity EOR effects have been mainly for sandstone reservoirs containing clay minerals, where organic materials initially adsorbed on the clay may be desorbed due to an increase in pH caused by the desorption of active ions in the presence of low salinity (Barnaji et al., 2016; Hilner et al., 2015; McMillan et al., 2016). In addition, a number of mechanisms such as sweep-efficiency improvement, interfacial tension (IFT) reduction, multi-component ionic exchange, and electrical double layer (EDL) expansion (Lashkarbolooki et al., 2016; Nasralla and Nasr-El-Din, 2014) have been proposed to explain the wettability alteration. However, the low-salinity effect in carbonate rocks, the largest share in reservoirs, has been less explored and the results are very contradictory (Ghanbari and Dehghanpour, 2015; Nasralla et al., 2013). It has been shown experimentally that the effects of salinity on carbonates are quite different to those on sandstone cores (Al-Anssari et al., 2016; Sheng, 2014; Yousef et al., 2011). The rock minerology, especially the presence of anhydrite in carbonate rocks, could affect the low salinity effect significantly (Austad et al., 2011; Jackson et al., 2016; RezaeiDoust et al., 2011; Shariatpanahi, S. et al., 2016; Shariatpanahi, S.F. et al., 2010). The effect of multiple-component ionic exchange between adsorbed oil components, cations

in the salt water and mineral surfaces has been proposed (Chen et al., 2018; Zhang, P. et al., 2007), and the effect of IFT reduction was found to be too small to explain the experimental results (Kumar and Mandal, 2016; Mahani et al., 2015; Sakthivel et al., 2017).

It is believed that controversies relating to experimental observations of the low-salinity effect are caused, mainly, by the complexities of oil components, the water environment and the minerology of reservoir rocks. From the perspective of design of experiments, many of the key process parameters are closely interrelated making it very challenging to change one while keeping others unchanged, which in turn makes identification of the mechanism difficult. With rapid advances in high-performance computers and continuous development of force field potentials in the last few decades, molecular dynamics (MD) simulation has been widely used to investigate the complicated interactions between minerals, water, and organic materials at the atomic level. These studies have advanced our understanding of the low salinity effect from an atomistic perspective for clay sandstones, whereas an understanding for carbonate rocks remains very limited.

5.1.3 Overview of this chapter

To study the salinity effects on the water/oil/vapor equilibrium interactions, the detailed model construction is presented in Section 5.2. Four interface systems were investigated by MD simulations in this section, namely n-decane/vapor interface, water/vapor interface, salt-water/n-decane interface, and salt-water/decane/vapor interface systems, respectively. The purpose of this contribution is twofold, firstly to demonstrate the suitability of the choice of interatomic force field and calculation set-up by applying MD to model the bulk interface between vapor and liquid phases (water, containing varying concentrations of sodium chloride, and n-decane); and secondly to apply the approach to the more complex cases of the salt water/n-decane interface and salt water/n-decane/vapor interface systems. The influences of aqueous NaCl solutions with six different concentrations from 0.00 M (deionized water) to 1.00 M were conducted to investigate the salinity effects on the interface. The species' radial distribution function (RDF), density distributions, interface thickness, contact angle and the IFT were calculated and analysed in each system to reveal the fundamental influence of salts for low-salinity EOR application.

Moreover, the effects of surface charge in altering the wettability of calcite mineral surfaces, in the presence of different salt concentrations, were investigated using classical, equilibrium MD simulation (EMD) methods in Section 5.3. In addition, the impact of changes in wettability on the hydrodynamics of the fluids confined

in calcite nanopores during the flooding process were investigated using non-equilibrium MD simulation (NEMD) methods.

5.2 Molecular dynamics simulation of the salinity effect on the n-decane/water/vapor interfacial equilibrium

5.2.1 Introduction

The salinity effect on the interface between water and oil was investigated here using the Molecular Dynamics (MD) simulation method. n-Decane was selected as a representative oil component, SPC/E water and OPLS-AA force fields were used to describe the water/oil/ionic interactions for salt water and n-decane molecules. Equilibrium MD simulations were firstly conducted to study the n-decane/vapor and salt-water/vapor interface systems at six different NaCl concentrations (0 M, 0.05 M, 0.10 M, 0.20 M, 0.50 M and 1.00 M). The water/oil interface was then investigated by calculating bulk density distribution, radial distribution function, interface thickness and water/oil interfacial tension (IFT). Sufficiently long MD simulations of water/n-decane/vapor were performed, followed by an analysis of the effect of salinity on the water/oil/vapor interface. The IFT values for the water/vacuum interface, n-decane/vacuum interface and water/n-decane interface were obtained from the pressure tensor distribution after system equilibration, with values of 71.43, 20.54 and 65.33 mN/m, respectively, which agreed well with experimental and numerical results reported in the literature. An optimal salinity around 0.20 M was identified corresponding to a maximum interfacial thickness between water and oil phase, which resulted in a minimum water/oil IFT value and a maximum value for the oil/water contact angle, a condition beneficial for enhanced oil recovery.

5.2.2 Models and simulation details

To study the salinity effects on the water/oil/vapor equilibrium interactions, the detailed model construction is presented in this section. In the following, the MD simulation technique is described along with the details on how the molecular pressure tensors, density profiles, interfacial tension and interfacial thickness are extracted from the simulations.

5.2.2.1 Model Construction

To investigate the salinity effect on the water/oil/vapor interfacial equilibrium, n-decane ($C_{10}H_{22}$) molecules were considered as representative of oil components in this work. Aqueous NaCl solutions were selected as a representative 1:1 electrolyte with six different salt concentrations, which were 0.00 M (deionized (DI) water), 0.05 M, 0.10 M, 0.20 M, 0.50 M, and 1.00 M, respectively.

Figure 5.1 shows the simulation procedure and the initial configurations of systems: (a) The validation of this simulation methodology is firstly demonstrated by a careful benchmark of the approach on smaller systems representing n-decane/vapor and salt-water/vapor interfaces. In Section 5.2.3.1: both n-decane/vapor interface system and salt-water/vapor system were constructed by building one n-decane or water slab in the middle of a cubic box with two vapor space aside; (b) To investigate the salt-water/n-decane interface in Section 5.2.3.2, two rectangular aqueous electrolyte blocks were built separated by a distance of 4.0 Å, and the intervening volume element was filled with n-decane molecules randomly orientated; (c) For the salt-water/n-decane/vapor interface system investigation in Section 5.2.3.3, a three-phase system was established to visualise the contact angle directly by initially inserting an n-decane droplet onto a water slab, with a separation distance of 4.0 Å. The Packmol (Martínez et al., 2009) package was used to construct all the initial configurations for the simulations with both water and n-decane molecules randomly distributed and orientated in the simulation box initially.

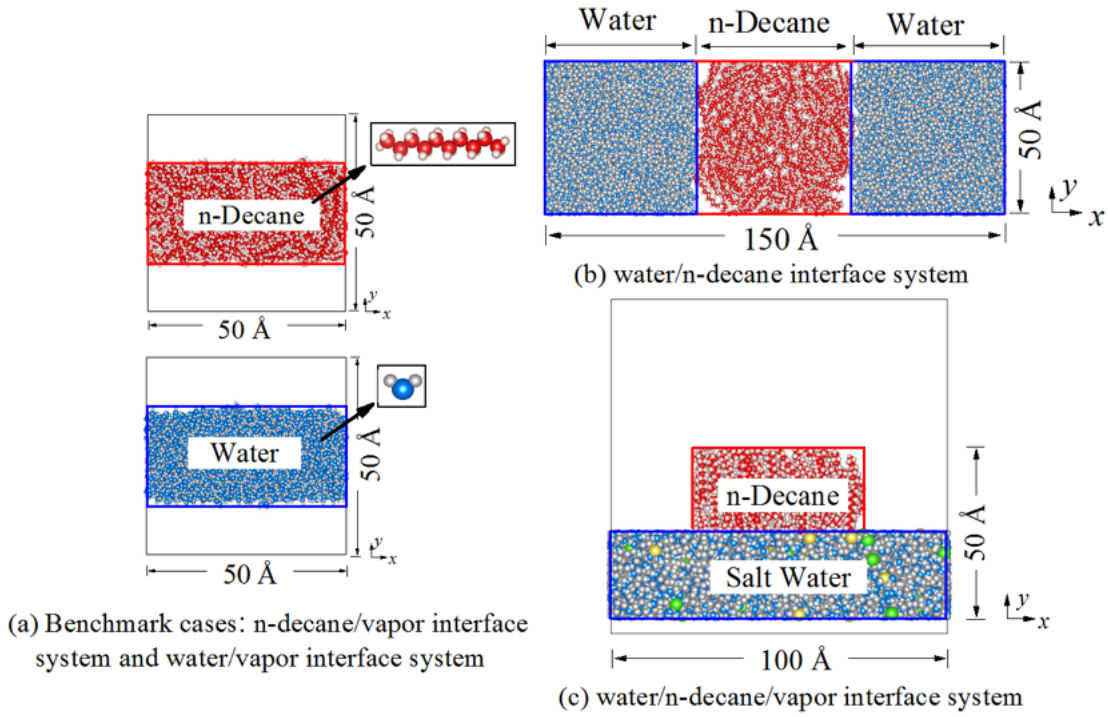

Figure 5.1 Initial configurations of the simulated systems

To remove any high strain for the initial configurations, energy minimization was performed using the steepest descent method before the equilibrium MD simulations were carried out. Periodical boundary conditions were used in all systems with different spatial dimensions as shown in Figure 5.1 with a total density of 1.00 g/cm^3 for the water phase and 0.73 g/cm^3 for the oil phase.

5.2.2.2 Force Fields

In these simulations, n-decane interactions were described using the all-atom model of the OPLS-AA force field (Berendsen et al., 1987), and the SPC/E force field was used for water (Jorgensen and Tirado-Rives, 1988). The sodium and chloride ions were modelled as charged Lennard-Jones particles (Martínez et al., 2009). These force fields were tested extensively and successfully used in previous simulations (Dang and Smith, 1993; Mohammed and Mansoori, 2018; Underwood, T. et al., 2015; Underwood, T.R. and Greenwell, 2018). The total energy is given by Equation (5-1), including both the intra- and intermolecular interactions:

$$E_{total} = E_{bond} + E_{angle} + E_{dihedral} + E_{torsion} + E_{vdw} + E_{coulombic} \quad (5\text{-}1)$$

where E_{total}, E_{bond}, E_{angle}, $E_{dihedral}$, $E_{torsion}$, E_{vdw} and $E_{coulombic}$ are the total energy, bond-stretching, angle-bending, dihedral-energy, torsion energy, van der Waals and electrostatic components, respectively. The Lennard-Jones potential parameters (ε_{ij} and σ_{ij}) between different atom types were obtained using Lorentz-Berthelot combining rules.

In all these simulations, all the atoms were free to adjust their positions to attain equilibrium structures.

5.2.2.3 Equilibrium molecular dynamics simulation details

All equilibrium MD calculations were performed using the DL_POLY molecular simulation package (Smith et al., 2002). The Leapfrog integration algorithm was used with a time step of 1.0 fs in all these simulations. The potential energy was evaluated with a 10 Å cut-off for the short-range van der Waals interaction, and the Ewald summation for the Columbic interactions was calculated with a precision of 1×10^{-6}. A Berendsen thermostat with a relaxation time of 0.1 ps was used to control the system temperature. To remove initial strain, energy minimization (steepest descent) was performed on the initial configuration for 1×10^{4} steps. The MD simulation was subsequently started in the NPT ensemble with an equilibration period of 50 ps at 0.10 MPa and with initial velocities taken for a Maxwellian distribution at 300 K and meanwhile coupling the system to an external heat bath at 300 K with a constant time step of 0.001 ps. After equilibration, the volume of the system was then kept fixed, and another 5 ns of NVT ensemble simulation was conducted with all covalent bond lengths, as well as the water bond angle, constrained by the procedure SHAKE (tolerance 1×10^{-5} nm).

5.2.2.4 Calculation methods

Here, the pressure tensor for the interface system was obtained by using the virial equation, Equation (5-2),

$$P_{\alpha\beta} = \frac{1}{V}\left(\sum_{i=1}^{N} m_i v_{i\alpha} v_{i\beta} + \sum_{i=1}^{N-1}\sum_{j=i+1}^{N} F_{ij\alpha} r_{ij\beta}\right) \quad (5\text{-}2)$$

where, $P_{\alpha\beta}$ is an element in the pressure tensor, α and β are the direction components; V is the volume, m_i is the mass of particle i, $v_{i\alpha}$ is its velocity in the α direction, $F_{ij\alpha}$ is the α component of the total force on particle i due to particle j, and $r_{ij\beta}$ is the β component of the vector (r_i - r_j). The kinetic contribution to the pressure is given by the first term in this equation, and the virial contribution is given by the second. The three diagonal elements in the pressure tensor represent the relevant pressure components.

The interfacial tension γ of the salt-water/n-decane interface normal to the x-axis can be calculated from the pressure tensor distribution after equilibration using the mechanical definition (Hill, 1960; Ono and Kondo, 1960) as Equation (5-3)

$$\gamma = -\int (p'(x) - p)dx \quad (5\text{-}3)$$

where $p'(x)$ is the lateral pressure, p is the bulk pressure, and the integral is defined over the boundary layer. With two interfaces perpendicular to the x axis, this gives the following relationship, Equation (5-4), for the interfacial tension

$$\gamma = -\frac{1}{2}\left(\frac{p_y + p_z}{2} - p_x\right) L_x \quad (5\text{-}4)$$

in which $p_\alpha = P_{\alpha\alpha}$ ($\alpha = x, y, z$) and L_x is the box length in the x direction used for the calculation.

The planar density profiles for the simulations can be used to describe the probability of finding an atom within a planar element d_{fc} along a Cartesian axis, using Equation (5-5)

$$\rho(f_c) = n_f / N df_c \quad (5\text{-}5)$$

where the value N is the number of total atoms and n_f is the number of atoms within a planar element d_{fc}.

To characterize the thickness of the water/oil interface in the simulations, the “10-90” interfacial thickness criterion was adopted by defining the interfacial thickness to be the distance between two positions where the density varies from 10% to 90% of the density of the bulk phase.

5.2.3 Benchmark cases for validation: (a) n-decane/vapor interfacial equilibrium and (b) effects of salinity on the salt-water/vapor interfacial equilibrium simulations

The validation of the simulation strategy is demonstrated by a careful benchmarking of the approach on simpler systems namely n-decane/vapor and salt-water/vapor interfaces as reported in this section. After 5 ns of simulation time for both systems, the energy, pressures and temperatures of all components were considered to be equilibrated. This was checked in one case by extending the simulation time by a further 3 ns with no significant changes observed in the relevant parameter values. It should be noted that the calculated densities of the n-decane phase in the n-decane/vapor system (0.728 ± 0.063) g/cm^3 and water phase in each salt-water/vapor systems (0.998 ± 0.027) g/cm^3 agree well with those of the pure bulk phases 0.73 g/cm^3 for n-decane and 1.00 g/cm^3 for water). This shows that the simulation is sufficiently long for studying a realistic interface between two bulk phases.

The radial distribution function (RDF) of molecules in both n-decane/vapor and DI-water/vapor interface systems were sampled as shown in Figure 5.2: (1) The interaction between two n-decane molecules can be seen from the RDF profiles in Figure 5.2(a), where intra- and inter-molecular correlations are mixed. As far as the intermolecular correlations are concerned, it is clear that the oscillations around g(r) = 1 are close to the cutoff radius. *Trans* (*T*) and *Gauche* (*G*) conformation positions of carbon atom neighbours in a molecule can also be observed, followed with successive *GT* and *TT* conformations as marked in Figure 5.2(a). To characterize the conformations of n-decane molecules in the n-decane/vapor interface system, the probability density functions (PDF) distribution for the n-decane molecules as a function of the internal dihedral angle $\Phi_{C\text{-}C\text{-}C\text{-}C}$ was calculated as shown in Figure 5.2(a), where the peaks observed at $\Phi_{C\text{-}C\text{-}C\text{-}C} = 0°$ and $\Phi_{C\text{-}C\text{-}C\text{-}C} = \pm 120°$ correspond respectively to trans (*T*) and gauche (G^+ and G^-) conformations. The magnitudes of the G^+ and G^- peaks are very close, corresponding with the symmetry of the dihedral potential energy. (2) The RDFs between water molecules are presented in Figure 5.2(b). It can be observed that g(r) equals 0 at short distance, which indicates strong repulsive forces between two water molecules in the short range. The first peak occurs at 2.8 Å with g(r) arriving around a value of 3, which can be interpreted as indicating that it is three times more likely to find two oxygen atoms in different water molecules at this separation. At longer distances, $g(r)$ between two water molecules approaches a value of one indicating there is no long-range order. The RDF profiles of both n-decane and water components are in good agreement with

previous MD simulations and experimental results with no shifts for the two main peaks (Alejandre et al., 1995; Ryckaert and Bellemans, 1978; Senapati and Berkowitz, 2001).

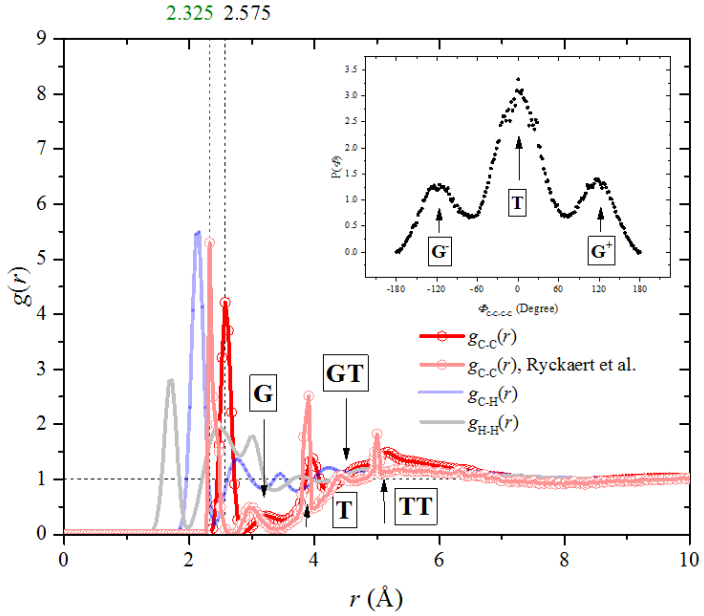

(a) RDFs for the n-decane/vapor interface system

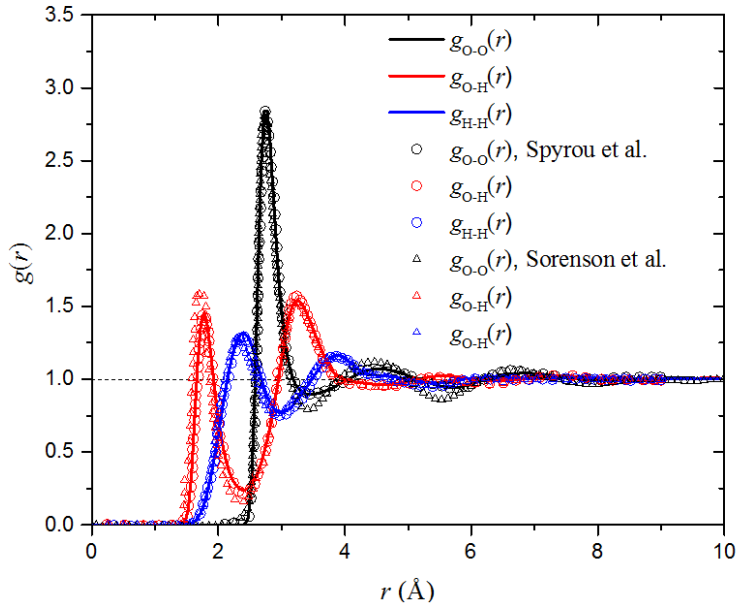

(b) RDFs for the DI-water/vapor interface system

Figure 5.2 Radial distribution function (RDF) profiles for the n-decane/vapor interface and DI-water/vapor interface systems (Alejandre et al., 1995; Ryckaert and Bellemans, 1978; Senapati and Berkowitz, 2001)

A series of 5 ns MD simulations of aqueous NaCl solutions at different concentrations (0.00 M, 0.05 M, 0.10 M, 0.20 M, 0.50 M and 1.00 M) were also

performed for investigating the salinity effect on the water/vapor interface. The structure of the salt-water/vapor interface was investigated by calculating the mass density profiles along z direction perpendicular to the interfacial plane *xy*, as shown in Figure 5.3, along with the corresponding snapshots from the top and side views. The results show that the ion concentration has little effect on the bulk water density, with a stable overall value around 1.0 g/cm^3. Besides, although ions move thermodynamically within the water phase as shown in Figure 5.3, both sodium and chloride ions are repelled from the water/vapor interface, leaving an almost ion-free interface layer, as shown in the ion density distribution profiles in Figure 5.3. This phenomenon behaves in accord with the standard theory of the air/water interface for electrolytes (Spyrou, 2009) and is reflected experimentally by an increase in the measured surface tension. When the water salinity is lower than 0.20 M, the chloride ions penetrate towards the interface next to the ion-free layer, and exhibit a concentration peak, followed by a subsurface depletion. The repulsion of counter-ions and the subsurface neutrality requirement demonstrates the fact that the sodium cations are dragged by the anions and consequently exhibit a subsurface peak. However, this effect becomes weakened when the water salinity is larger than 0.20 M.

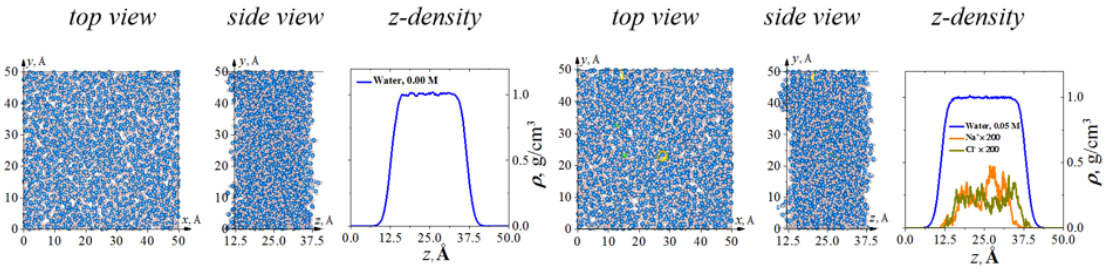

(a) DI water (b) water with salinity of 0.05 M

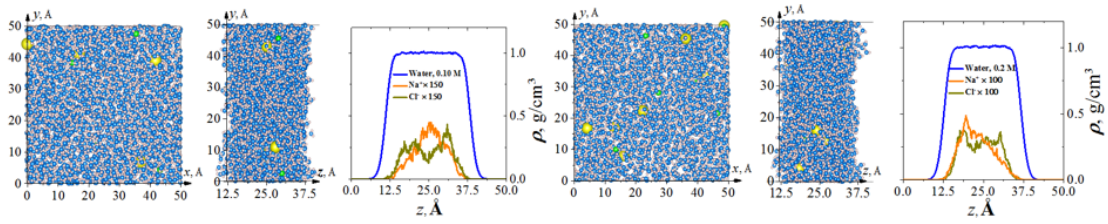

(b) water with salinity of 0.10 M (c) water with salinity of 0.20 M

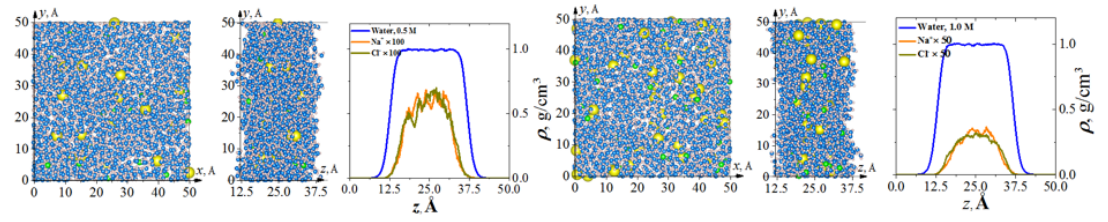

(d) water with salinity of 0.50 M (e) water with salinity of 1.00 M

Figure 5.3 Top and side views of the final snapshots for the six aqueous NaCl solution systems, and their corresponding z-density profiles for the various components

To further confirm that an equilibrated system had been obtained in the simulations, the IFT between salt water and the vapor phase was calculated from the molecular pressure tensor with 1 ns of time averaging, as displayed in Figure 5.4. Though the IFT between water and vapor increases with an increase of salinity, the influence of salinity on water/vapor IFT becomes less above a concentration of 0.10 M, where the water/vapor IFT approaches a constant value around 74 mN/m. The typical equilibrated n-decane/vapor and DI-water/vapor IFT values of 20.54±1.87 mN/m and 71.43±0.57 mN/m are obtained by averaging the last 2 ns simulation period with an averaged step of 10 ps, which values and their associated uncertainties are in good agreements with other experimental and MD simulation results (Jang et al., 2004; Zeppieri et al., 2001), as summarized in Table 5.1, indicating the validity and stability of the calculation setup. Using the same MD simulation method and calculation setup, the interface systems between salt water and the n-decane phase were simulated and the results are reported in the next section.

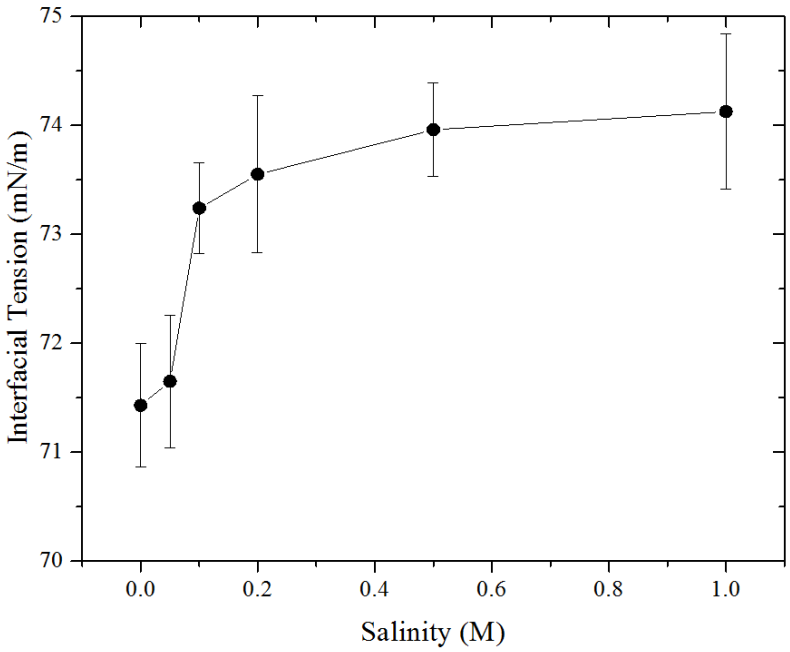

Figure 5.4 The salinity effect on the interfacial tension of the water/vacuum interface

Table 5.1 n-Decane/vacuum and DI-water/vacuum IFT Comparisons at 300 K

	n-Decane/vacuum IFT, mN/m	DI-water/vacuum IFT, mN/m
The calculated value	20.54±1.87	71.43±0.57
Experimental Result (Zeppieri et al., 2001)	23.20	71.72
MD simulation value (Jang et al., 2004)	21.77±2.31	70.94±2.25

5.2.4 Effects of salinity on salt-water/n-Decane Interfacial Equilibrium

The salinity effect on the water/n-decane interface system is reported in this section at six electrolyte concentrations of 0.00 M, 0.05 M, 0.10 M, 0.20 M, 0.50 M and 1.00 M, respectively.

Figure 5.5 presents the final equilibrium-configuration snapshots of the salt-water/n-decane interface system after 5 ns simulations representing different NaCl concentrations, along with the number density profiles of each system along the *x*-axis direction, perpendicular to the water/n-decane interface. It is clear that in every case the salt-water/n-decane system consists of two phases with two, well-defined interfaces, as can be deduced from the representation of the water and organic phase molecular density along the direction perpendicular to the interface, representing the immiscibility of salt water and organics phases. In addition, an almost ion-free layer can also be observed at the salt water/n-decane interface.

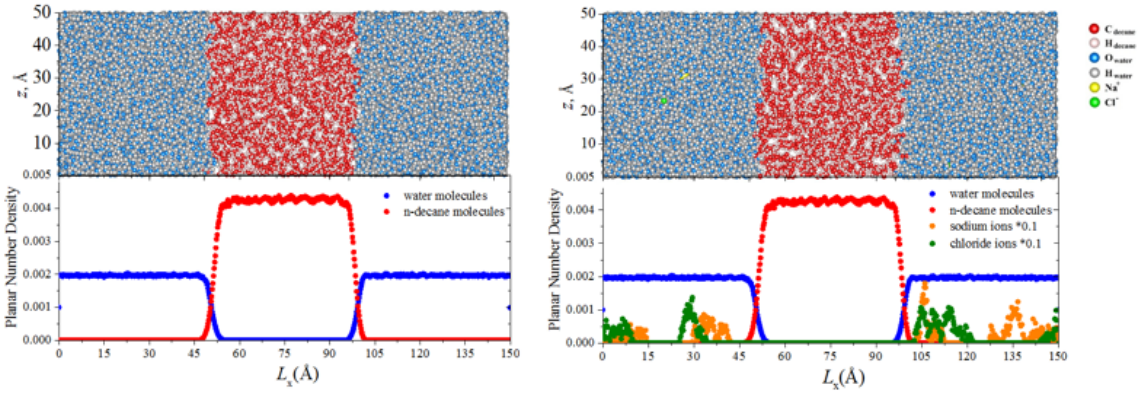

(a) 0 M (b) 0.05 M

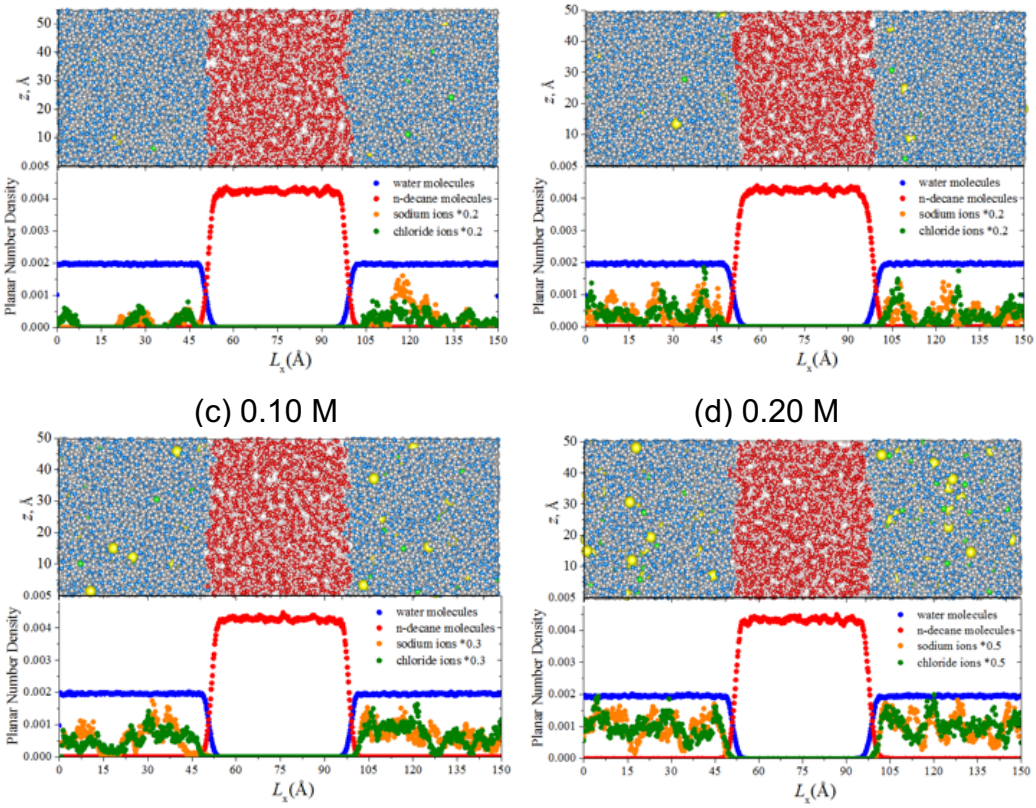

(c) 0.10 M (d) 0.20 M

(e) 0.50 M (f) 1.00 M

Figure 5.5 n-decane/salt-water equilibrated interfaces at different salinities

To characterize the salt water/n-decane interface thickness, the "10-90" interfacial thickness criterion, derived from the density profiles, of both salt water and n-decane phases along the x-axis direction in the salt water/n-decane interface system are illustrated in Figure 5.6 for salt concentration of 0.00 M and 0.20 M. Bulk density values for the water and n-decane phases are observed with values around 1.00 and 0.73 g/cm^3, respectively, with the interface density transition profiles in between.

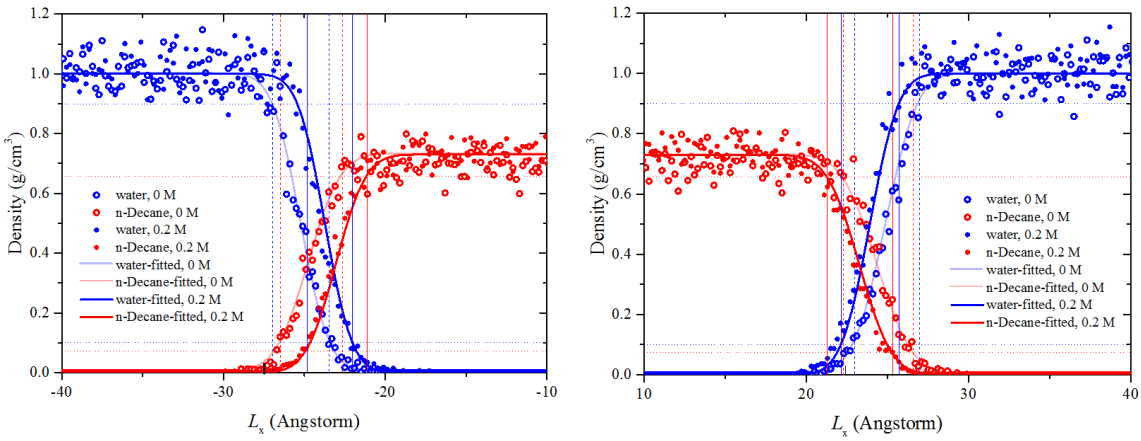

Figure 5.6 Planar (yz) density profiles ρ(fc) as a function of the box length Lx system and the definition of "10-90" interfacial thickness for the salt water/n-decane system

Figure 5.7 shows the salinity effect on both the interfacial thickness and IFT for the salt-water/n-decane interface systems. With an increase in salt concentration from 0.00 M to 1.00 M, the salt-water/n-decane interfacial thickness has a maximum value when the salt concentration is 0.20 M, as shown in Figure 5.7(a). Through averaging the IFT fluctuation profile in the period of the last 1 ns with an averaging time step of 10 ps, the corresponding IFT between salt water and n-decane is shown in Figure 5.7(b). The result indicates an opposite trend in the variation of interfacial thickness with an increase of water salinity. A minimum water/decane IFT value of 61.8 mN/m is predicted at an electrolyte concentration of 0.20 M. The typical calculated DI-water/n-decane interfacial thickness value of 4.5 ± 0.7 Å and IFT of 65.33±0.12 mN/m are obtained, which is comparable with published experimental and simulation results (Berendsen et al., 1987; Jang et al., 2004; Mitrinović et al., 2000) as presented in Table 5.2.

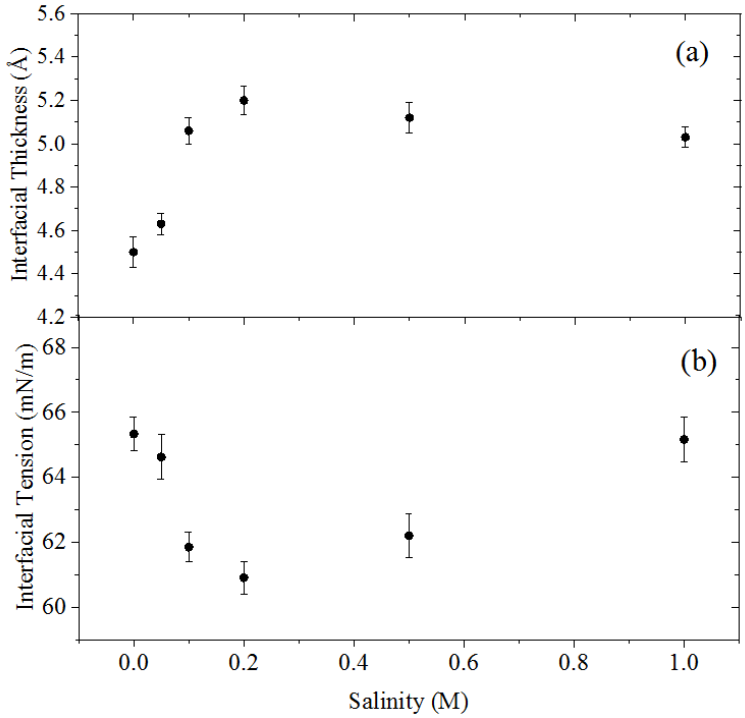

Figure 5.7 (a) "10-90" interfacial thickness, and (b) interfacial tension as function of salinity for n-decane/salt water interface

Table 5.2 Interfacial thickness and IFT between n-Decane and DI-water at 300 K for the water/n-decane

	Interfacial thickness t, Å	Interfacial tension γ, mN/m
The calculated value	4.5±0.7	65.33±0.12
Experimental Result (Mitrinović et al., 2000)	4.6±0.2	51.72
MD simulation value (Berendsen et al., 1987)	6.5	58.32
MD simulation value (Jang et al., 2004)	3.90	66±4

To identify the mechanism by which monovalent ions affect the salt water/oil interface, the radial distribution functions for each component in the salt-water/n-decane binary systems are analysed in Figure 5.8. It can be observed from the Figure 5.8(a) that the presence of ions has little effect on the interactions between n-decane molecules in the oil phase. This is due to the insolubility of ions in the decane phase, which is indicated in Figure 5.8(b) where no dominant peak appeared in the RDF profile, and the ions remain in the water phase. The solubility of the electrolyte ions in the water phase explains the first peak in the RDF profile between ions and water molecules, as shown in Figure 5.8(c), which represents the hydration structure of the ions. The effect of salinity on the molecular structure of the water phase is displayed in Figure 5.8(d). It can be seen that the second peak in the water molecule pair correlation function gradually disappears with increasing electrolyte concentration, indicating that the presence of ions forces water molecules to occupy interstitial positions and thus, no well-defined second hydration shell is found around a central water molecule. For the interaction between aqueous Na^+ and Cl^- ions, shown in Figure 5.8(e), the first peaks at around 3 Å show the presence of contact ion pairs in the solution. The second peak, at around 5.2 Å, corresponds to the presence of solvent separated ion pairs in NaCl solutions. With the increase of electrolyte concentration, the probability of contact ion pair formation increases and that of solvent separated ion pair formation decreases for the solution. The effect of salinity on the interaction between water and the decane phase can be observed from the RDF profile between water and decane molecules, as shown in Figure 5.8(f). No significant peaks can be observed here, but only a continuously increasing trend, which is consistent with the immiscibility of water and n-decane phases. However, an

apparent curvature change is manifested along the increasing RDF profile between 3 and 6 Å, indicating adsorption interactions between water and the n-decane phase at the salt-water/n-decane interface. It can be seen that the weakest adsorption between water and n-decane occurs when the electrolye concentration is 0.20 M, demonstrating the loosest of the interface structures. This phenomenon also corresponds to the calculated equilibrium "10-90" interfacial thickness variations with water salinity, which is caused by the combination of attractive interactions between the water/ions and repulsive interactions between the n-decane/ions, which control the IFT between salt water and n-decane phase.

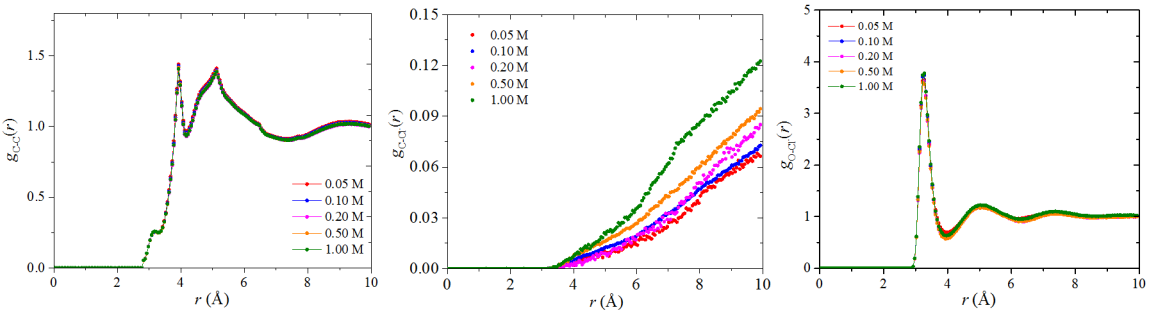

(a) decane carbon – decane carbon (b) decane carbon – chloride ions (c) water oxygen-chloride ions

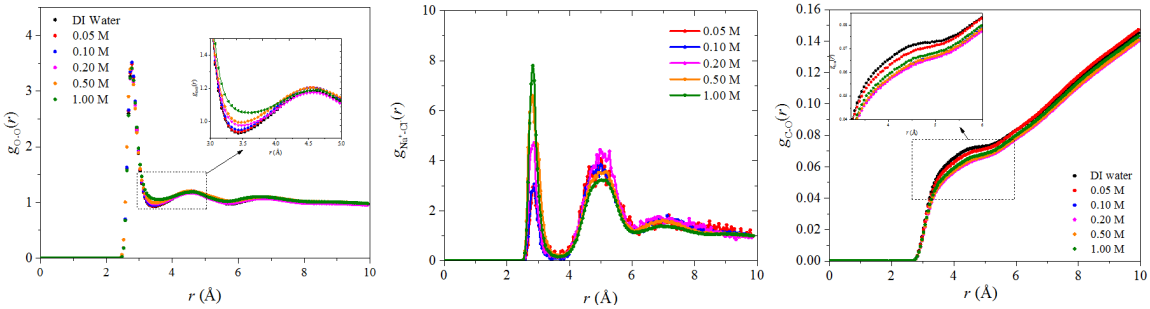

(d) water oxygen - water oxygen (e) sodium ions - chloride ions (f) water oxygen – decane carbon

Figure 5.8 The radial distribution functions for salt-water/n-decane interface system

5.2.5 The effect of the salinity on the n-Decane/water/vapor three phase system

MD simulation results concerning the effect of salinity on the n-decane/water/vapor three-phase system are presented in this section. As the initial simulation configurations outlined in Section 5.2.2.1, the rectangular n-decane phase and water slab systems were created with a minimum distance of 4 Å. The final snapshots of an n-decane/water/vapor interface unit cell with different salinities, after 5.0 ns of simulation time, are shown in Figure 5.9. It can

be observed that the n-decane molecules have relaxed to form a droplet shape, approaching a lens on the water slab surface caused by attractive interactions due to the van der Waals and Columbic forces between the constituent molecules. After spreading of the n-decane droplet on the water surface it finally forms an elliptically shaped droplet on the water slab surface. After equilibration, the n-decane droplet keeps its shape apart from the effect of thermal fluctuations, as shown in Figure 5.9.

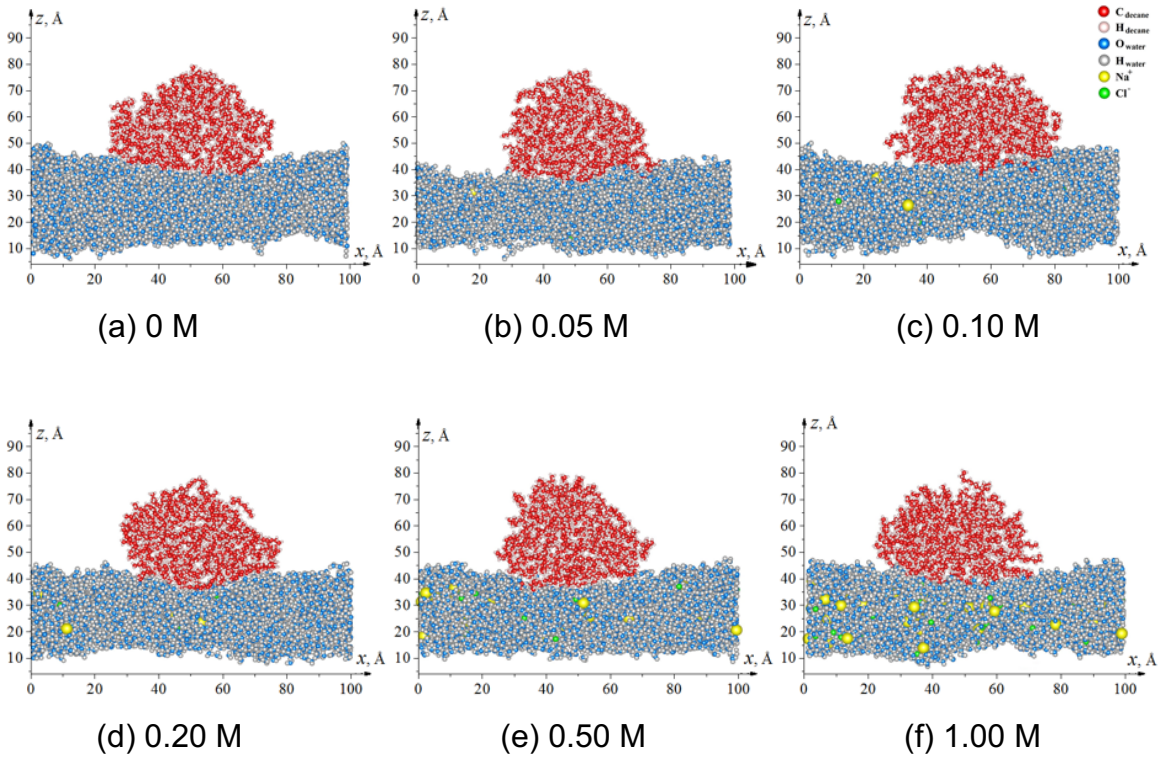

(a) 0 M (b) 0.05 M (c) 0.10 M

(d) 0.20 M (e) 0.50 M (f) 1.00 M

Figure 5.9 Series of snapshots of decane-salinity water-vacuum three phase system

During the MD simulation, the three-phase system remains continuous in z-axis direction, as shown in Figure 5.10. To investigate the detail of the shape of the n-decane/salt-water/vapor three-phase system, the Gibbs dividing surface was calculated from the density profiles of n-decane and water phases along the z-axis direction, as presented in Figure 5.11. The contact angles were thus obtained from the directions of the upper and lower sides of the n-decane droplet (Kunieda et al., 2012), which were fitted as a sphere with a least squares method. The contact angle variation with water salinity for the three-phase system is presented in Figure 5.12(a), which indicates a maximum contact angle value of 64.88º at a salinity of 0.20 M. The corresponding interfacial tension variations between salt water and n-decane phases shown in Figure 5.12(b) have an opposite trend to the contact angle variations. An optimal minimum water/n-decane IFT occurs at

a salt concentration of 0.20 M, and such a minimum is considered optimal for enhanced oil recovery. Qualitatively such a trend is consistent with some experimental studies at the macroscale (Al-Khafaji et al., 2017).

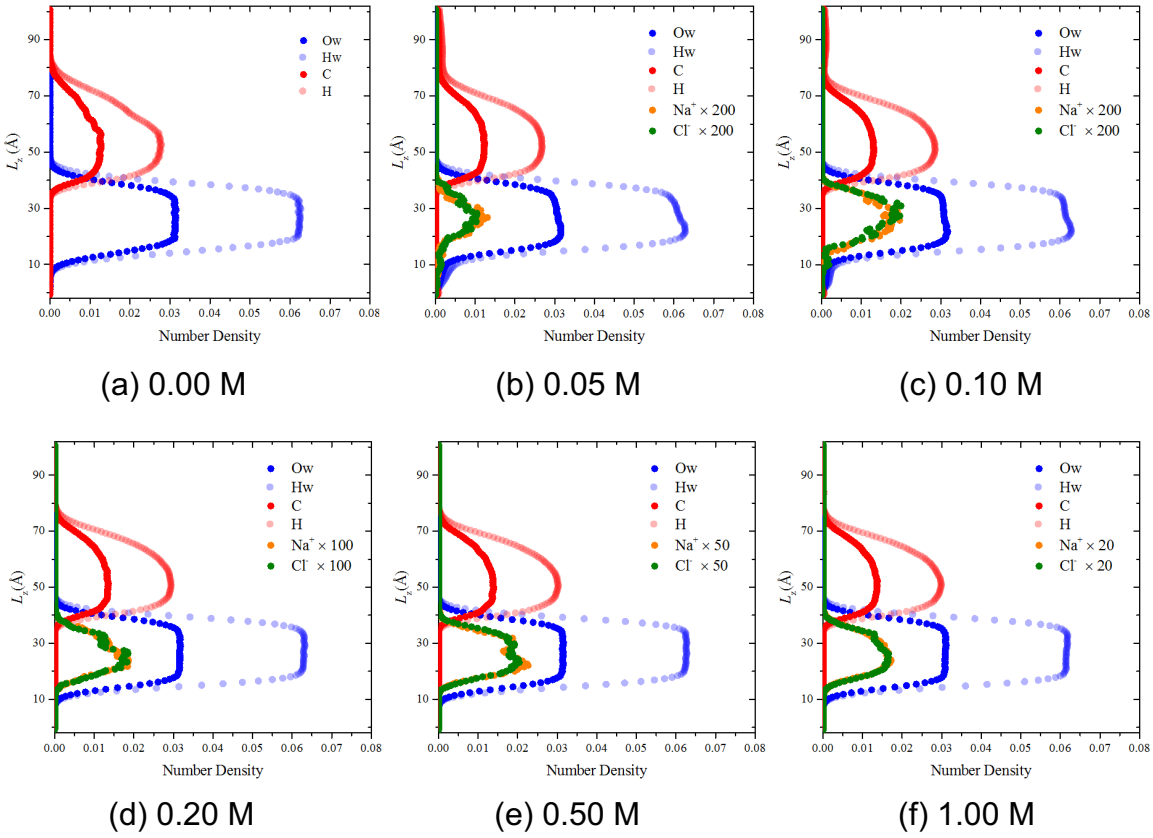

Figure 5.10 Number density along z-axis direction of decane-salinity water-vacuum three phase system

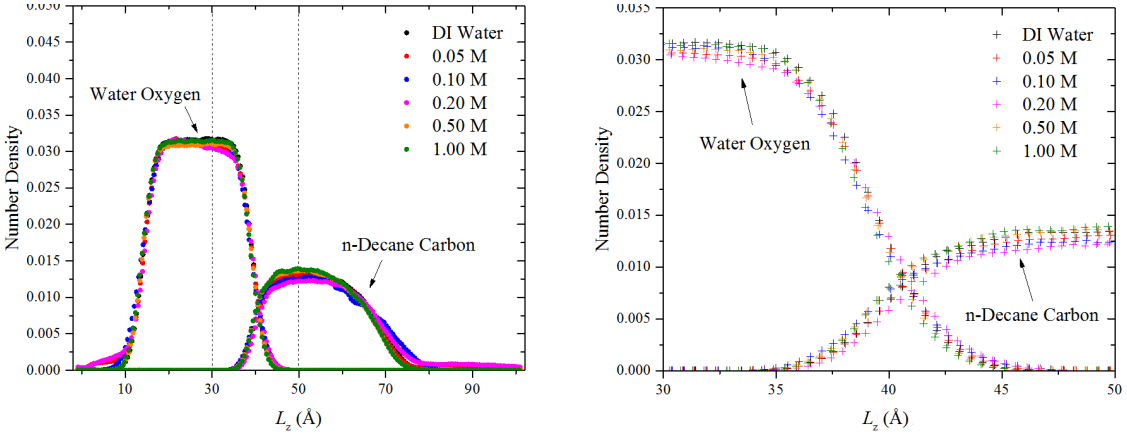

Figure 5.11 z-density distribution of water oxygen and n-decane carbon at different electrolyte concentrations

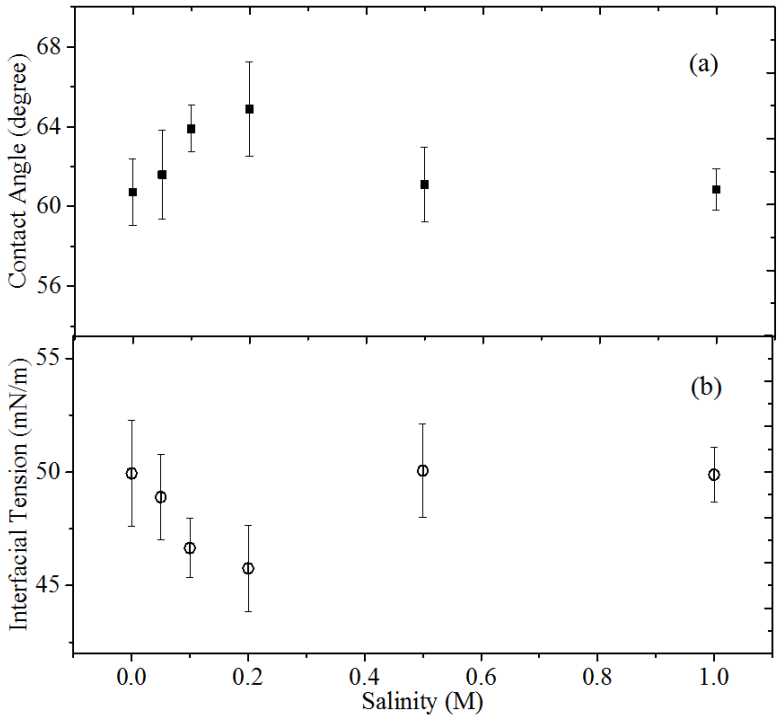

Figure 5.12 (a) "10-90" interfacial thickness, and (b) surface tension as a function of salinity for n-decane/water/vapor three-phase interface system

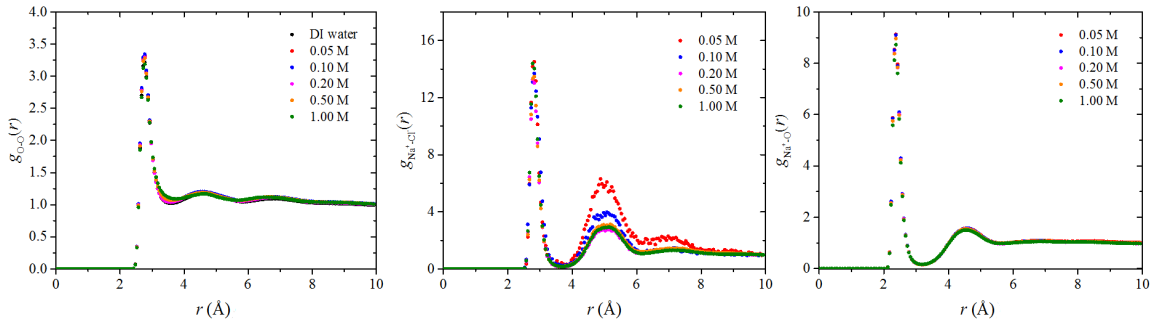

(a) Water oxygen – Water oxygen (b) Sodium ions – Chloride ions (c) Sodium ions – Water oxygen

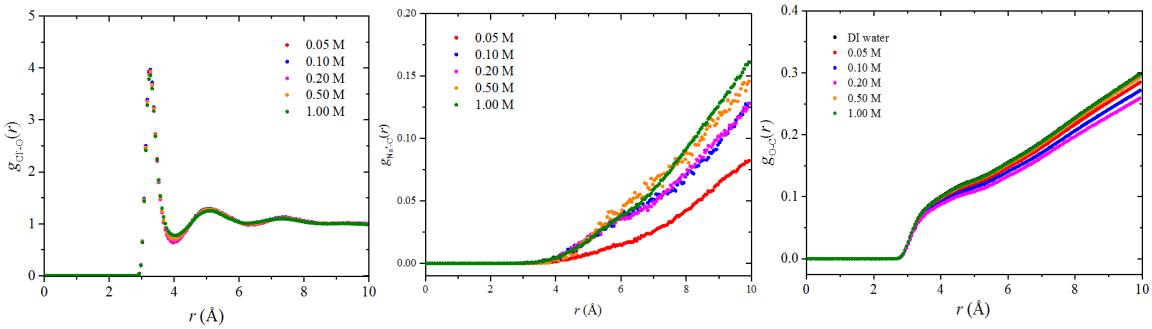

(d) Chloride ions - Water oxygen (e) Sodium ions – Decane carbon (f) Water oxygen – Decane carbon

Figure 5.13 Radial distribution function for water/n-decane/vapor system with different salinity

The radial distribution function profiles for salt-water/n-decane/vapor system are shown in Figure 5.13. The salinity effects on the water-water, water-ions interaction profiles of salt-water/n-decane/vapor three phase interface system is similar to that for the salt-water/n-decane interface system, as shown in Figure 5.13(a, b). Both the sodium and chloride ion hydration effect can also be observed as presented in Figure 5.13(c, d). Figure 5.13(e) characterises the sodium ion and n-decane molecule interactions as a function of electrolyte concentration. No dominant peaks are observed in the RDF profile between ions and molecules of n-decane in the organic phase, which indicates that all ions remain in the water slab phase instead of transferring to the n-decane phase. Combining the hydration effect of the ions and the repulsion effect between ions and the oil phase, the overall water-oil interaction is shown in Figure 5.13(f), which suggests that the loosest interface structure between water and n-decane phases is manifested when the electrolyte concentration is around 0.20 M. Qualitatively such trends are consistent with experimental studies at the macroscale (Al-Khafaji et al., 2017).

The work presented in the next section, Section 5.3, focuses on investigating the salt-water/oil/vapor interactions in a mineral nano slit pore. Both the salinity effect and mineral surface substrate on the oil wettability and recovery factor during EOR are discussed in the next section.

5.3 Molecular dynamics simulation of the surface charge and salinity effects on the n-decane wettability in a nanoslit pore

5.3.1 Introduction

Low salinity flooding has been proposed as a promising method for enhanced oil recovery technique, but the underlying mechanism is unclear especially for carbonate reservoirs. This work investigates the water salinity effects on the wettability alteration of nano-slit pores with three types of calcite surfaces (i.e., a neutral surface, and {0001} surface with positive and negative charged surfaces) by classical equilibrium molecular dynamic (EMD) simulations. Non-equilibrium MD simulations (NEMD) are conducted subsequently to reveal the influence of wettability on the oil transport properties in a nanopore under different salt

concentrations of sodium chloride (NaCl) (0.20 M, 0.50 M, and 1.00 M). Results show that the increasing water salinity has little effect on the wettability alteration in a nanopore with the neutral calcite surfaces. For calcite nanoslit pore with charged surfaces, however, the electrostatic interaction influences the distributions of anions and cations, which alter the surface wettability to be more hydrophilic due to the hydration effect of ions at elevated salt concentrations. While partially decane-wet calcite neutral surface inhibits greatly the movement of oil droplet in the pore, higher oil mobility is achieved for nanopores with charged inner surfaces, especially under a higher salt concentration.

5.3.2 Models and simulation details

5.3.2.1 Model Construction

The initial configurations for the simulation models, as illustrated in Figure 5.14, were generated using the Material Studio (MS) package (Module, 2011). Each simulation system was composed of two parts namely, an immobile (solid) part consisting of nano-slit pore walls and a mobile (fluid) part consisting of a salt/water/oil mixture.

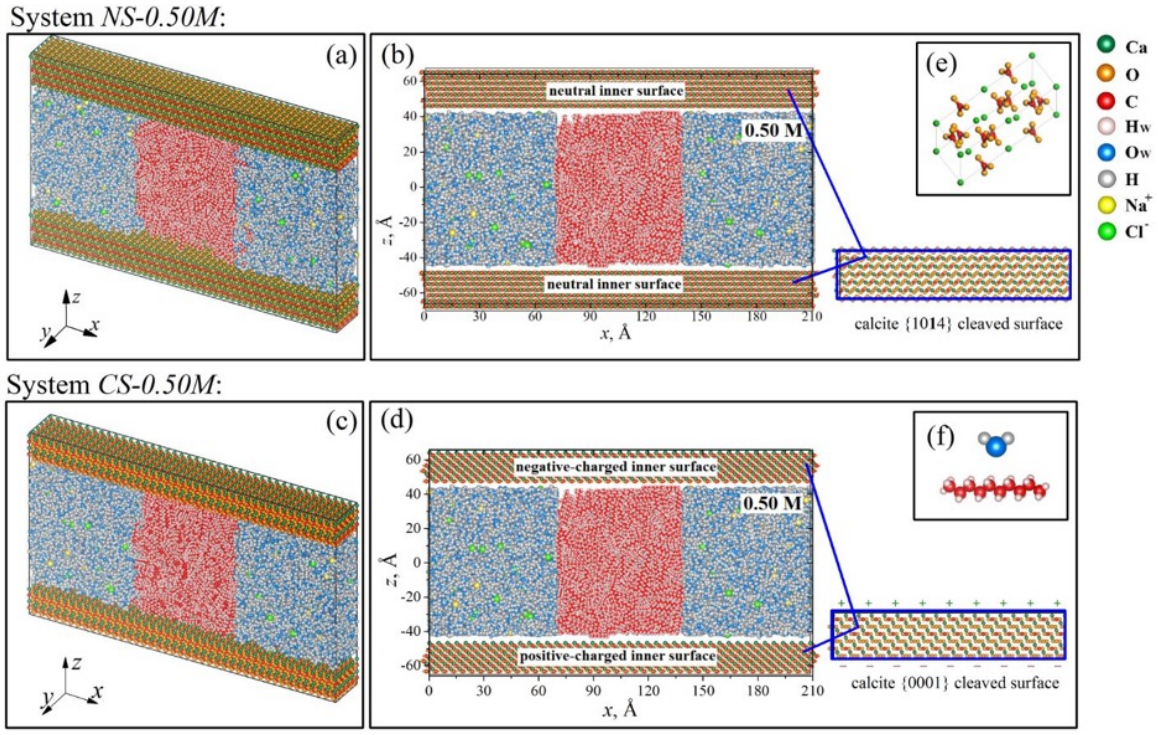

Figure 5.14 Schematic illustration of initial configurations: (a) Perspective view of System “NS-0.50M”, (b) Side view of System “NS-0.50M”, with zoom-in image of calcite $\{10\bar{1}4\}$ surface, (c) Perspective view of System “CS-0.50M”, (d) Side view of System “CS-0.50M” with zoom-in image of calcite {0001} surface, (e) The unit cell of calcite, $CaCO_3$, (f) Atomistic structure of water (H_2O) and n-decane ($C_{10}H_{22}$)

The walls of the slit nanopore were composed of two parallel calcite surfaces, where the length along the *x*-axis direction and the separation distance between the mineral surfaces along the *z*-axis direction were fixed at 21 nm and 9 nm, respectively. The rhombohedral structure of calcite, which has space group $R\bar{3}c$, and hexagonal unit cell parameters $a = b = 4.988$ Å, $c = 17.061$ Å; $\alpha = \beta = 90°$, $\gamma = 120°$ (Zussman et al., 1992) was used to create an atomistic model of the calcite surfaces. Calcite $\{10\bar{1}4\}$ and $\{0001\}$ cleavage surfaces (Roberto et al., 2010; Shen et al., 2013; Song et al., 2009) were considered as representative of neutral and charged slabs to form nanoslit walls. In the case of calcite $\{10\bar{1}4\}$ surfaces, being the most stable surface of calcite and dominating its observed morphology, Ca^{2+} and CO_3^{2-} are located in the same layers, and this close packed and alternating arrangement of the oppositely charged ions makes the calcite $\{10\bar{1}4\}$ surface overall non-polar and neutral. Concerning the $\{0001\}$ form of calcite, it contains alternating planes of Ca^{2+} and CO_3^{2-} groups situated in separate layers, as a result that the calcite $\{0001\}$ plane is terminated by either Ca^{2+}-rich (carrying positive charge) or CO_3^{2-} rich (carrying negative charge), leading to a positively or negatively charged surface, respectively. Here, each calcite slab contains six and seven atomic layers (perpendicular to the *x* direction) for the calcite $\{10\bar{1}4\}$ and $\{0001\}$ surface, which is sufficient to reproduce bulk-like properties at the centre of the slab and to obtain a careful description of the surface (de Leeuw and Parker, 1997; Raiteri and Gale, 2010; Raiteri et al., 2010).

For the fluid in the pore region between the two mineral slabs, two rectangular aqueous electrolyte blocks were built with a 7-nm separation distance along the x-axis direction, and the intervening volume element was filled with oil molecules initially randomly orientated. As a simulant for the hydrocarbon-bearing geofluids, neutral non-polar n-decane ($C_{10}H_{22}$) was used as the representative non-polar oil phase. Aqueous sodium chloride (NaCl) solution was employed as the salt water phase to simulate geological fluids (brines). The number of water and decane molecules was calculated using a water density of 0.998 g/cm^3 and oil density of 0.730 g/cm^3, respectively. All the ions were initially randomly inserted into the aqueous region to avoid biased adsorption. Water salinities of 0.20 M, 0.50 M,

and 1.00 M were applied to investigate the effect of salt concentration on the wettability of each mineral surface.

In total, six separate initial configurations were set up for both EMD and NEMD simulations with the variations of surface charge and water salinity, namely, NS-0.20M, NS-0.50M, NS-1.00M, CS-0.20M, CS-0.50M and CS-1.00M, respectively (where “NS” and “CS” stand for Neutral Surface and Charged Surface respectively; followed by a number as a specification of the water salinity in Molarity unit “M”). All configuration snapshots were rendered using the VESTA software (Momma and Izumi, 2008). It is notable that, for each simulation, the parallel calcite slabs were fixed, and two gaps of 5.0 Å were introduced to the top and bottom of the fluid simulation cell to avoid any unphysical interactions amongst fluid species at the mineral surfaces.

5.3.2.2 Force Fields Employed in the Simulations

The Simple Point Charge / Extended (SPC/E) rigid water model (Berendsen et al., 1987) was used to describe water molecular-interactions. The OPLS-AA (Optimized Potentials for Liquid Simulations – All Atoms) force field (Jorgensen and Tirado-Rives, 1988) was utilized to describe the interactions among atoms in the n-decane phase. This force field is parameterized for organic systems and has been demonstrated to reproduce physically accurate representations of hydrocarbons and similar organic molecules, and is compatible with SPC/E water (Ballal et al., 2014). The ions were modelled as charged Lennard-Jones particles, with potential parameters proposed by Koneshan et al. (Koneshan et al., 1998). The model developed by Raiteri et al. (Raiteri et al., 2010) was employed to model calcite surfaces. This model has been shown to be consistent with the other force fields applied (Fenter, Paul et al., 2013). The Lennard-Jones potential parameters (ε_{ij} and σ_{ij}) between different atom types, were obtained using Lorentz-Berthelot combining rules (Hansen and McDonald, 1990).

5.3.2.3 Equilibrium Molecular Dynamics Simulation (EMD)

All EMD calculations were performed using the DL_POLY simulation package (Smith et al., 2002). The equations of motion were solved by the leap-frog algorithm with a SHAKE subroutine with a time step of 0.5 fs. The potential energy was evaluated with a 12.0 Å cutoff for the short-range van der Waals interaction, and the Ewald summation method for the Coulombic interactions was calculated with a precision of 1×10^{-6}. Every simulation was initialized with an energy minimization run to reduce excessive forces for the system. The minimization procedure was accomplished using the steepest descents algorithm. Subsequently, all the simulations were run for a 50 ps equilibration period in a

constant number of particles, pressure and temperature (NPT) ensemble with a velocity-rescale Berendsen thermostat. This equilibration period was followed by a 5 ns production run in the NVT ensemble where the number of particles (N), the simulation box volume (V), and the temperature (T) were kept constant. The periodic boundary conditions were applied to all three spatial dimensions. All simulations were run to present ambient conditions, a pressure of 1 bar, and a temperature of 300 K using a velocity scaling method. It was necessary to run the simulations at ambient rather than reservoir temperatures, as the available calcite force field has been parameterized to model systems under ambient conditions. Considerable validation would be required against, for example, neutron scattering data to ensure the force field holds for higher temperatures and pressures, work presently ongoing for future studies.

5.3.2.4 Non-Equilibrium Molecular Dynamics Simulation (NEMD)

All NEMD simulations were performed using the DL_POLY package (Smith et al., 2002) as well. The hydrodynamic behaviour of various water/n-decane/salts fluids confined in a slit pore constructed by calcite $\{10\bar{1}4\}$ and $\{0001\}$ slabs was investigated. The specific strategy was started from the final equilibrium configurations calculated through EMD simulation, and then a constant external force F_x of 0.001 kcal/(mol·Å) was applied to each atom of the pore fluid. This large pressure gradient is necessary because the fluid flow through pores is slow, and it will take an extremely long simulation to achieve a stable flooding state. A further 4 ns NVT ensemble NEMD simulation was carried out for each system. The *x*-directional velocity of each water molecule confined in the slot pore region during the final 1 ns was sampled every 0.5 ps in bins of width 0.20 Å in the *z*-direction and then averaged. The velocity of the n-decane molecular cluster was averaged for the final 1 ns to represent the velocity of the n-decane cluster.

5.3.3 EMD simulation of the surface charge effects

To investigate the surface charge effect on the water/oil/mineral equilibrium interactions, the final-configuration snapshots of the salt-water/n-decane/calcite systems with neutral and charged pore wall surfaces (systems NS-0.50M and CS-0.50M) after 5 ns EMD simulation period are presented in Figure 5.15, along with the corresponding number density profiles of each species in the z-axis direction. The results show that n-decane phases for both systems are aggregated and formed as droplet-like clusters, surrounded by the salt water phase. Na^+ and Cl^- ions in both systems are found to always remain in the water phase, without any diffusion into the oil phase. The water and n-decane phases are immiscible, forming a curved interface due to the interfacial tension effect. However, different n-decane wettability on the mineral pore walls can be found

from the different adsorbing state of n-decane clusters caused by the pore surface charge. For the system NS-0.50M with the neutral pore surfaces, the solid slabs exhibit partial decane-wettability, with parts of the n-decane molecules directly adsorbing onto the surface, as shown in Figure 5.15(a); In contract, for system CS-0.50M with the charged pore surface, both positive-charged and negative-charged slabs ($\{0001\}$ Ca^{2+} and $\{0001\}$ CO_3^{2-} surfaces) manifest greater hydrophilic characteristics.

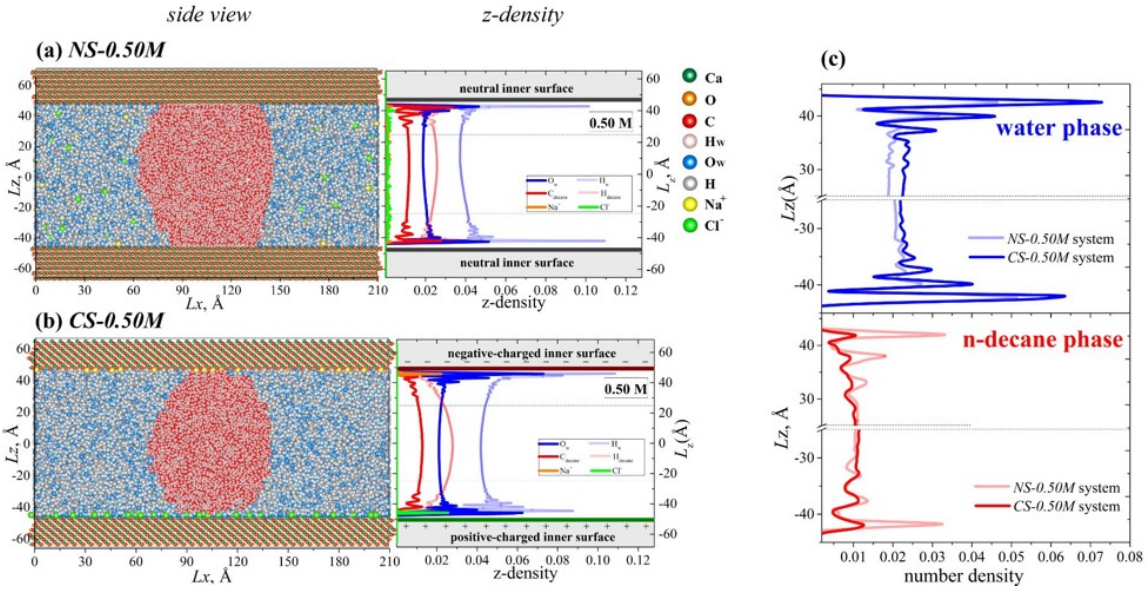

Figure 5.15 Side view snapshots of final equilibrium configuration and corresponding number density profiles along z-axis direction for (a) NS-0.50M and (b) CS-0.50M systems, with (c) zoom-in comparison profiles of water and n-decane phase distributions near the calcite pore surfaces

The atomic number density distributions along the z-axis direction for both systems in Figure 5.15 are obtained by averaging the trajectories of each atomic species along the last 1 ns of the equilibrium simulations. The water and n-decane phase z-density profiles close to the pore wall region, as enlarged in Figure 5.15(c), show that the confining of the surface causes both water and n-decane molecules to adopt particular configurations near the calcite surfaces, forming structured adsorption layers. Such an observation is consistent with the experimental results of Geissbuhler et al (Fenter, P et al., 2000) via the surface X-ray scattering method, and the MD simulation results of Kerisit et al (Kerisit and Parker, 2004). For system NS-0.50M, the appearance of the first n-decane peak in Figure 5.15(c) shows that the neutral calcite surface is partially oil-wet, which is consistent with the direct visualization from the configuration snapshots after equilibration. For system CS-0.50M with charged surfaces, the reduced peak of the n-decane phase near the surface in the z-density profile indicates that both

the upper and lower mineral surfaces ($\{0001\}$ Ca and $\{0001\}$ CO_3 surfaces) become more hydrophilic. In addition, the z-density profile for system NS-0.50M also indicates that, Na^+ and Cl^- ions appear at a fine distance to the calcite surface, suggesting outer-sphere adsorption. But for system CS-0.50M, all the ions are found within the inner-sphere complexes distances.

The distinctive difference in the distribution of ions between the cases of charged and non-charged surfaces can be visualized in Figure 5.16(a). Instead of randomly distributing in the water phase as for the neutral system NS-0.50M, Na^+ and Cl^- ions in system CS-0.50M are adsorbed by the $\{0001\}$ CO_3^{2-} and $\{0001\}$ Ca^{2+} surfaces respectively, which is driven by the strong electrostatic interactions between ions and the charged surfaces: (1) At each layer of the $\{10\bar{1}4\}$ surface, Ca^{2+} and CO_3^{2-} ions are arranged alternately, which consequently makes the direct coordination of the sodium or chloride ions to the neutral calcite surface unfavourable. (2) The $\{0001\}$ surfaces contain alternating planes of Ca^{2+} and CO_3^{2-} ions, which produces a dipole moment perpendicular to the surface. Polar surfaces are unstable by themselves and need either reconstruction to neutralize the dipole moment or to adsorb ions to remove the dipole moment. The distribution of cations and anions is therefore influenced by both $\{0001\}$ CO_3^{2-} termination and $\{0001\}$ Ca^{2+} termination, respectively. After reaching equilibrium, Cl- ions make direct contact with the Ca^{2+} atoms on the $\{0001\}$ Ca^{2+} termination, which is consistent with MD results by Lgor et al. (Vasconcelos et al., 2007). Such distinct differences of the adsorption behaviour are originated from different electrostatic interactions between the ions and surfaces.

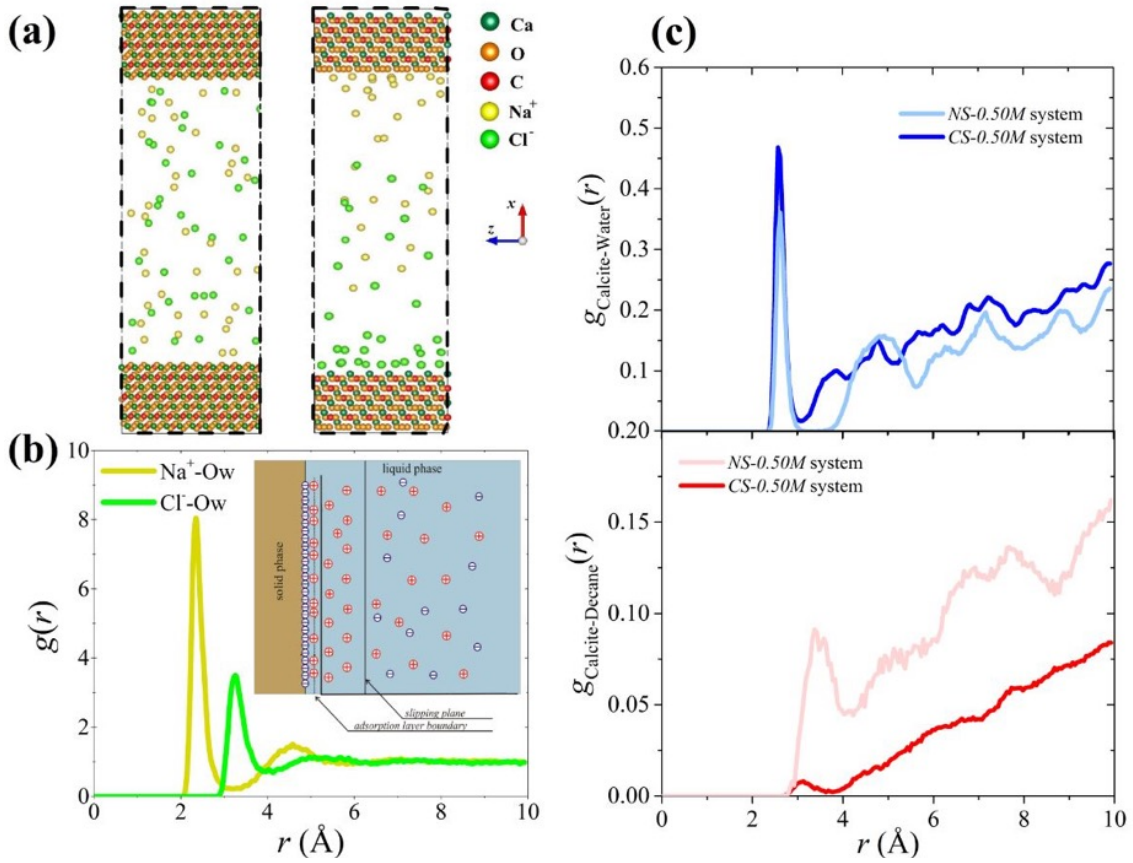

Figure 5.16 Illustrations of (a) the ion distribution visualization in NS-0.50M and CS-0.50M systems, and the RDF profiles of system CS-0.50M for (b) ions/water, (c) water/calcite, and n-decane/calcite interactions

As reviewed earlier, several mechanisms have been proposed to explain the low-salinity effect for enhanced oil recovery, including electric double layer (EDL) expansion, multi-component ionic exchange and pH level reaction. The ion distributions following equilibration observed in this work suggests that EDL theory could explain the salinity effect for charged surfaces, where Na^+ and Cl^- ions exhibit an EDL distribution effect due to the opposite surface charge. The ions are predominantly fully coordinated by water molecules, which can be observed from the radial distribution functions (RDF or g(r)) profiles shown in Figure 5.16(b). Both Na^+ and Cl^- have great hydration capacity and can induce water molecules close to the calcite surfaces, as reflected by the dominant peak appearing in Figure 5.16(b). For instance, the sharp peaks indicate the highly ordered water structure around Na^+ ions, and the first valleys of the Na^+-O_w RDF are deep and wide indicating that the first and second solvation shells are clearly separated. The first maximum of the RDF is at 2.43 Å for Na^+, consistent with previous work (Chowdhuri and Chandra, 2001). Such a strong peak suggests that

dense water clusters are formed around Na^+, which can diffuse with Na^+ in the solution. The RDF profile of salt water/decane/calcite interactions for both systems, as shown in Figure 5.16(c), clearly shows that the surface charge has significant effects on both water/calcite interactions and decane/calcite interactions. The sharp peak in calcite/water RDF profile at 2.6 Å suggests that water is adsorbed on both neutral and charged surfaces, consistent with the MD results of Cooke et al. (Cooke et al., 2010). Both the reduced maximum-value in the dominant peak of the calcite/water RDF profile and increased maximum-value in the dominant peak of the calcite/n-decane RDF profile for CS-0.50M system in Figure 5.16(c) suggest weaker n-decane molecule adsorptions on the charged surface. It can be concluded that charged pore surfaces combining with the effect of salinity can lead to improved water-wet performance due to electrostatic interactions between the ions and surfaces, and the ion hydration effects.

5.3.4 EMD simulation of the surface charge and salinity effects

To reveal the effect of salinity and surface charge on the surface wettability, three salt water concentrations of 0.20 M, 0.50 M and 1.00 M were simulated along with two types of pore walls (i.e., neutral inner surface, and charged inner surface), which simulations are named as NS-0.20M, NS-0.50M, NS-1.00M, CS-0.20M, CS-0.50M, and CS-1.00M, respectively.

The final equilibrium configuration snapshots after 5 ns simulations are presented in Figure 5.17, along with the z-density profiles for each species. Dominant peaks of the water phase, from z-density profiles, close to the solid-pore surfaces appear in all cases, which indicates the presence of structured layers of water due to water adsorption onto the pore walls. Away from the near pore-wall region, uniform bulk properties are observed for both water and n-decane phases. The salinity appears to have less effect on the water/n-decane wettability for the neutral pore, as shown in Figure 5.17(a-c). In contrast, Figure 5.17(d-f) shows that the wettability alteration of the charged calcite $\{0001\}$ surface is highly dependent on the salinity of the fluid. At a salinity of 0.20 M with charged pore surfaces (system CS-0.20M), the $\{0001\}$ surface exhibits partial decane-wettability, with decane molecules directly interacting with the surface. However, as the water salinity increase, the contact area between n-decane and the calcite surface decreases. At a salinity of 0.50 M (system CS-0.50M), both calcite $\{0001\}$ Ca^{2+} and $\{0001\}$ CO_3^{2-} surfaces manifest greater hydrophilic characteristics. With a further increase of water salinity in the CS-1.00M system, the calcite surface becomes completely water-wet.

Comparisons of salinity effect on the n-decane phase distribution along the z-axis direction are presented in Figure 5.17(g, h). Figure 5.17(g) shows that the water

salinity has little effect on the n-decane molecular distribution for neutral surfaces. However, for nanopores with charged inner surfaces, the maximum value of the dominant peak of the n-decane phase close to the fluid/wall interfaces decreases when the salinity is increased from 0.20 M to 0.50 M. At a water salinity of 1.00 M, no adsorption of n-decane molecules on the charged pore wall is observed with the total disappearance of the peaks close to the near-wall regions, as shown in Figure 5.17(h).

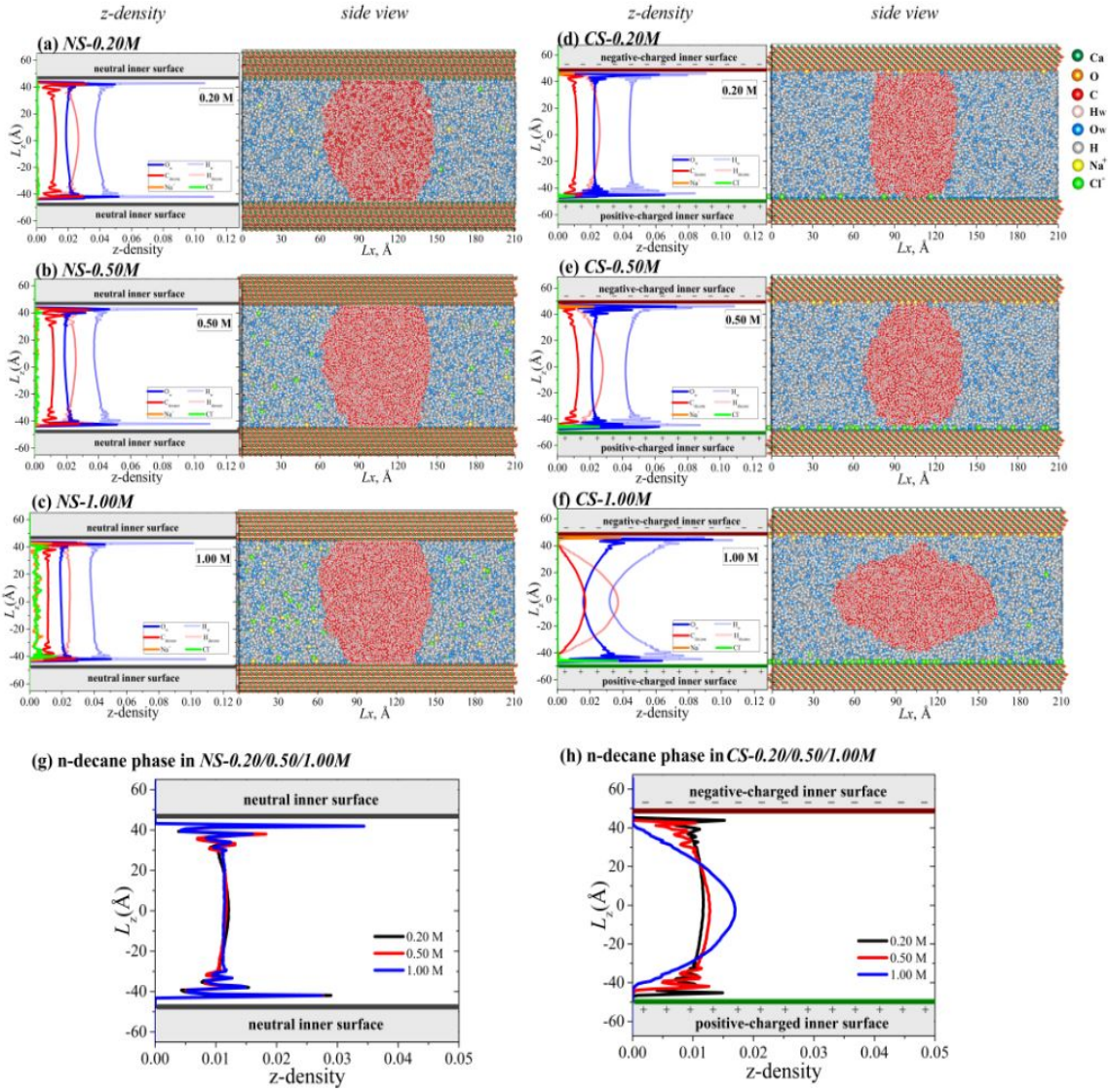

Figure 5.17 Combination effects of the pore surface charge and water salinity on the oil adsorption in a nano pore: (a-f) number density profile along z-axis direction, and corresponding xz-plane side view snapshot of final equilibrium configuration for each system, (g) n-decane phase number density along z-axis direction with variations of water salinity in a neutral pore, (h) n-decane phase number density along z-axis direction with variations of water salinity in a charged pore

RDF profiles from Figure 5.18(a, b), demonstrate the water/calcite and n-decane/calcite interactions for systems with neutral pore surfaces. With an increase in water salinity from 0.00 M to 1.00 M, little effect can be observed on either the water/calcite or decane/calcite interactions. In contrast, RDFs for charged pore surfaces, as shown in Figure 5.18(c, d), show that the hydrophilicity of charged calcite surfaces can be enhanced by increasing the salt concentration. For n-decane/calcite interactions, as shown in Figure 5.18(d), the maximum values of the first peaks, at around 3.2 Å, gradually decrease with the decrease in salinity. At 1.00 M, the peak vanishes indicating a completely water-wet condition.

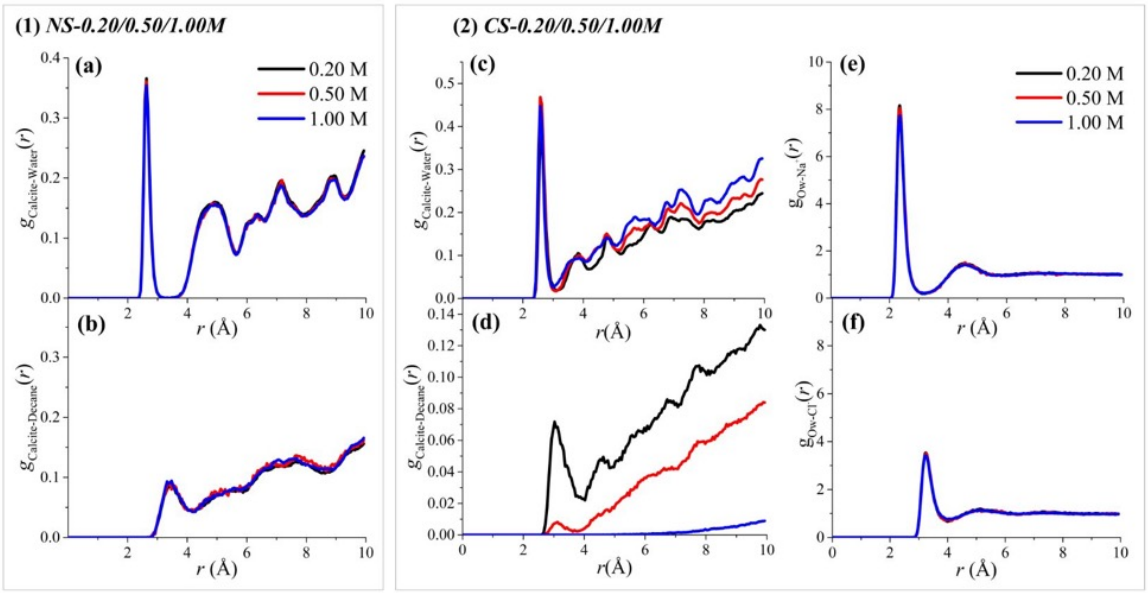

Figure 5.18 Radial distribution function profiles for (1) NS-0.20M/0.50M/1.00M systems and (2) CS-0.20M/0.50M/1.00M systems

RDF profiles for sodium and chloride ions interacting with water molecules for CS-0.20M/0.50M/1.00M systems are illustrated in Figure 5.18(e, f). It is observed that an increase in water salinity has less impact on the hydration effect of ions in the aqueous solution. However, for the systems with charged pores, the increase in water salinity leads to an increase in counter-ions, which results in an enhancement of surface hydrophilicity. Previous MD simulations of charged clay-layers also indicated the influence of counter-ions on the wettability of charged surfaces (Ma and Holditch, 2015; Underwood, T. et al., 2015; Zhang, L. et al., 2016), consistent with the presented simulation results, revealing that the hydrophobicity of charged calcite surface decreases with an increase in water salinity. Taking Rajam's experimental work (Ma and Holditch, 2015) as an example, incorporation of Li^+ into the carbonate layer could result in preferential

stabilization of the $\{0001\}$ calcite surfaces by the neutralization of the surface dipole without the requirement for surface reconstruction. Thus, the growth is relatively fast with the consequence that the $\{0001\}$ face is not observed under normal, synthetic conditions through experimental approaches. The relatively high Li^+ concentrations required in the above experiments suggests a specific electrostatic shielding of the $\{0001\}$ face due to Li^+ ions located in surface sites.

It can be concluded that with the increase of water salinity, strong electrostatic interactions between ions and charged surface can be found, which can cause strong ion adsorption at a distance away from the inner sphere complexes to cause the EDL expansion effect. The strong hydration effects of the adsorbed ions on the charged surface can promote surface wettability towards increased hydrophilicity which is beneficial for oil detachment.

5.3.5 NEMD simulation of the wettability effect on the oil transport

Using NEMD simulation methods, the effect of surface wettability on the hydrodynamics of pore fluids during the flooding process is reported in this section for EOR applications. All NEMD calculations were conducted by resuming simulations from the final configuration computed from the previous 5 ns EMD simulations whilst applying a constant external force F_x of 0.001 kcal/(mol·Å) to the pore fluid.

As illustrated in Figure 5.19(a), the NEMD simulation for system NS-0.50M starts from the equilibrium wettability state after 5 ns, where the neutral calcite surface is, initially, partially hydrophobic through oil adsorption. By introducing an external force F_x, the fluids confined in the nano slit pore are displaced as the flooding proceeds. The multiphase fluid-distribution configuration snapshots after another 4 ns show that all n-decane molecules move as a cluster under the external force. Due to the partial oil-wettability, the velocity of the oil interface near to the calcite slab boundary is much slower than that of the middle bulk-phase, as shown in Figure 5.19(c), which leads to the formation of a meniscus interface during the flooding process. The oil adsorption effects can also be observed from the dominant peak of the decane z-density profile, shown in Figure 5.19(c). This phenomenon indicates that oil adsorption can restrict the mobility of the oil interface close to the calcite slabs with lower velocities in the pore boundary region, which is disadvantageous for EOR applications.

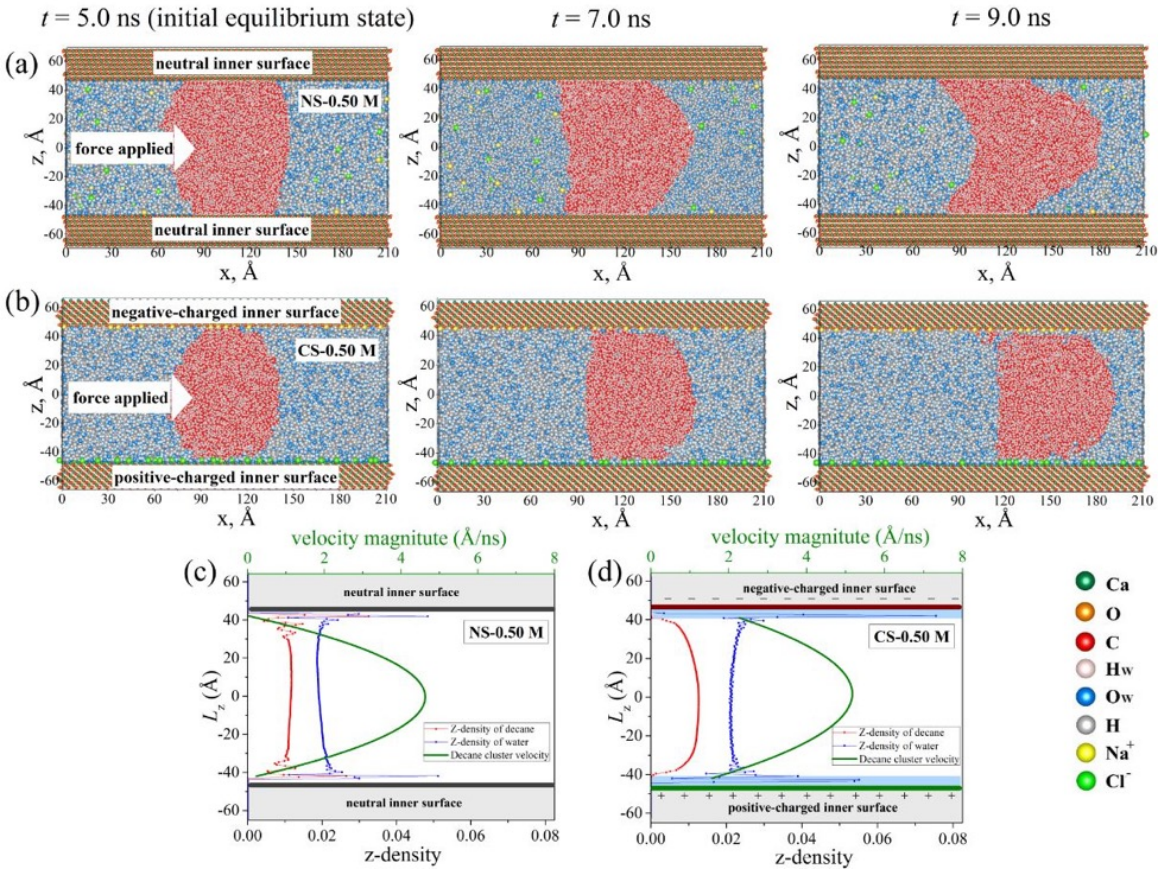

Figure 5.19 The configuration snapshots during the NEMD simulations for (a) NS-0.50M system and (b) CS-0.50M system, associating with the average z-density profiles of each phases, and the average n-decane velocity profile along z-aixs directions for (c) NS-0.50M system and (d) CS-0.50M system

Compared with the neutral system, the initial equilibrium configuration for the CS-0.50M system exhibits more water-wet characteristic, as shown in Figure 5.19(b), due to the effects of ions and surface charge on the wettability. When fluid is displaced under this water-wet condition, the movement of decane molecules is quite distinct from that in system NS-0.50M. The velocity of the n-decane cluster close to the pore surface is much greater, as presented in Figure 5.19(d). This phenomenon can be attributed to the effects of wettability alteration, which convert the slab inner-boundary into a hydrophilic surface as shown by the dominant peak of water z-density profile near the slabs in Figure 5.19(d). The n-decane cluster is hence expelled from the slit pore walls by a shielding layer of water molecules. Overall, n-decane molecules tend to migrate faster than with the non-charged surface, showing the significant influence of the hydrophilicity of the wall.

As shown in Figure 5.20(b), with a further increase in the salt concentration to 1.00 M, compared with system CS-0.50M, the hydrophilicity of pore walls in

system CS-1.00M is enhanced due to stronger ion hydration effects. n-Decane molecules tend to aggregate together and are completely detached from the charged surface, transporting collectively as a cluster under the external force. Both the water/decane z-density profiles and velocity profile of the decane cluster are apparently unsymmetrical in Figure 5.20(d), corresponding to the different hydration intensities of sodium and chloride ions, Figure 5.16(b).

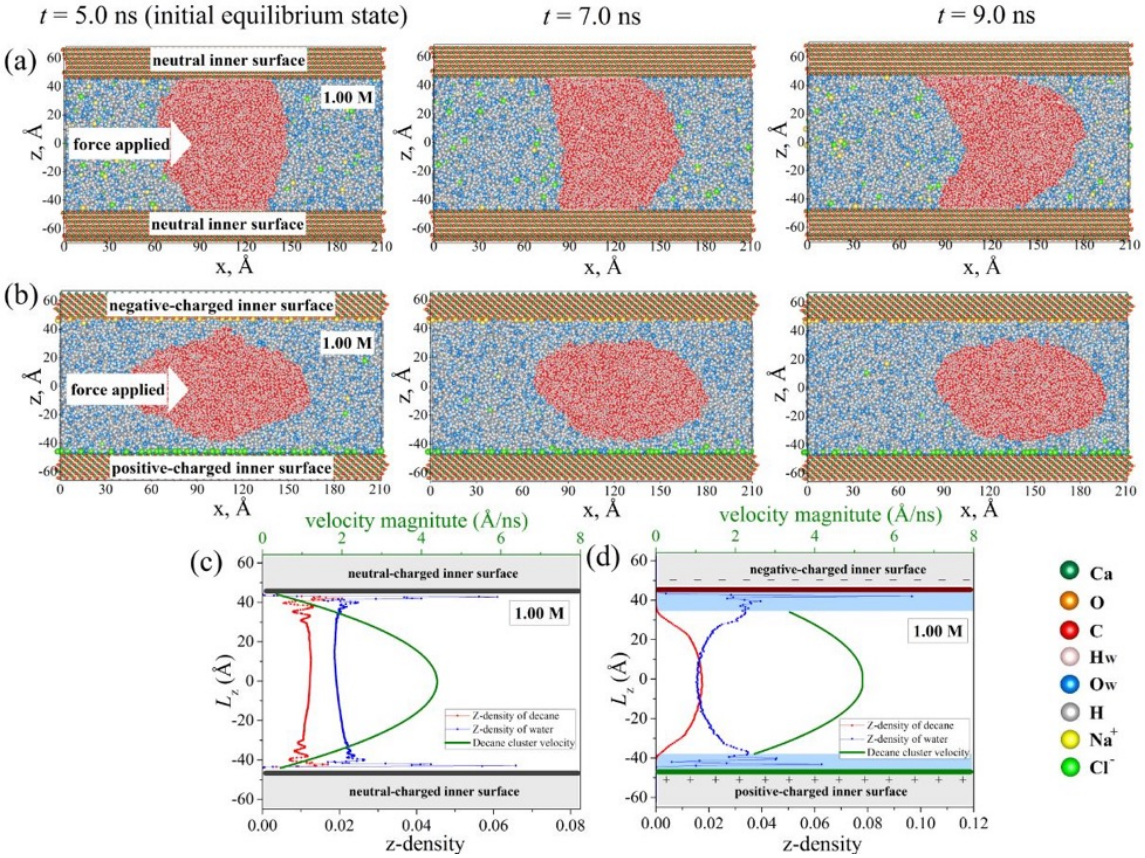

Figure 5.20 The configuration snapshots during the NEMD simulations for (a) NS-1.00M system and (b) CS-1.00M system, associating with the average z-density profiles of each phases, and the average n-decane velocity profile along z-aixs directions for (c) NS-1.00M system and (d) CS-1.00M system

The centre-of-mass (COM) trajectories of the n-decane molecule-cluster in the xz plane, under different surface charge and water salinity conditions, are plotted in Figure 5.21(a) to investigate the oil motion during the flooding process. The corresponding average velocity of n-decane along the x-axis direction is presented in Figure 5.21(b). The analysis shows that better displacement performance can be obtained under conditions of greater water salinity in charged calcite nanopores, which is beneficial for enhanced oil recovery. Clearly the presence of hydrophilic surfaces in pore walls can greatly influence the hydrodynamics of the pore fluid.

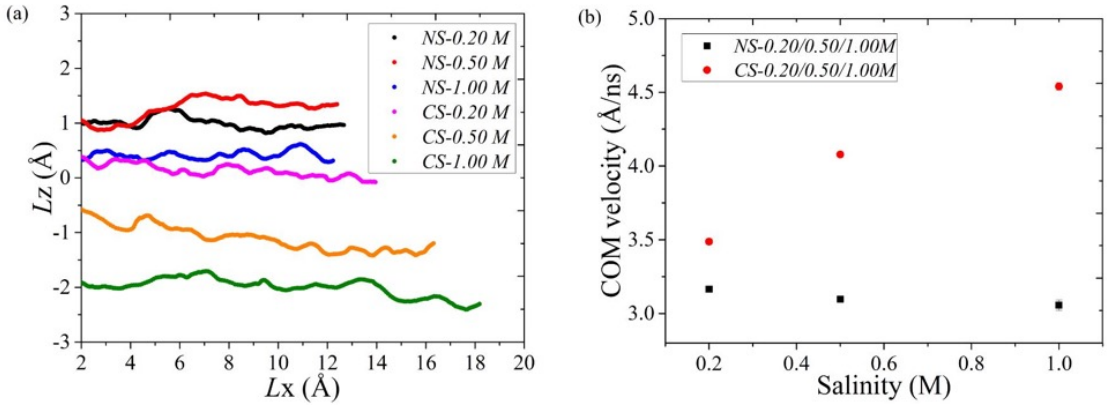

Figure 5.21 n-Decane phase transport properties in a calcite nanopore: (a) Planar COM trajectories of the n-decane cluster, and (b) average velocity along the x-axis direction for all system

5.4 Conclusion

As part of increasing deeper understanding of the cause of substrate wettability variation and the mechanism that underpins experimental observations of a benefit in injecting low-salinity water for enhanced oil recovery, molecular dynamics simulations at the nanoscale have been performed in this Chapter to identify: i) effect of water salinity on the nano-scale water/oil interfacial equilibrium, ii) effect of surface charge and water salinity on the wettability variation of a mineral surface, and iii) the wettability effect on oil displacement in a nano-pore via non-equilibrium molecular dynamics (NEMD) simulation. The results have been analysed in the context of addressing the mechanism underpinning the alteration of surface wettability in carbonate rock reservoirs. The simulation results can be summarized as followed:

- The interfacial tension (IFT) of the water/vapor interface, n-decane/vapor and water/n-decane interfaces were calculated from the pressure tensor distribution after the simulations reached an equilibrated state, with values of 71.43, 20.54 and 65.33 mN/m, respectively. The calculated IFT values showed a good agreement with previous experimental and simulation results.
- An optimal water salinity value was observed around 0.20 M for the equilibrated water/oil interface system which had the maximum interfacial thickness between water and oil phase, corresponding to the minimum water/oil IFT value.
- An optimal water salinity condition at around 0.20 M was also predicted by investigating the equilibrium water/oil/vapor interface system with the maximum contact angle between the water and oil phase, contributing to

the minimum salt water/oil IFT value, which is a condition beneficial for enhanced oil recovery.

- At a water salinity of 0.50 M, the neutral calcite nanopore exhibited partially oil wet characteristics after equilibration with oil attaching and adsorbing onto the neutral surface. The charged calcite slit-pore caused a distribution of anion and cation through adsorption, in response to the electrostatic field, which altered the surface wettability to produce hydrophilic surfaces due to the hydration effect around the ions.
- An increase in water salinity did not affect significantly the oil wettability of the neutral calcite surface, and a random distribution of ions was maintained in the water phase. However, for the charged nanoslit pore, greater water salinity enhanced the mineral surface hydrophilicity by altering the surface from partially water wet to completely water wet. At a water salinity of 1.00 M, all n-decane molecules were completely detached from the charged mineral surface by the salt water shield layers.
- The non-equilibrium MD simulation results for the flooding process showed that n-decane molecules tended to aggregate and transport as a cluster under the external flooding force. However, partial decane-wettability of calcite surfaces inhibited significantly the oil movement in the pore region. The combination of the effects of ion hydration and the electrostatic effect of ion adsorption on the charged surface led to a clear enhancement in oil transport, and hence indicated the potential for increased oil recovery in a calcite pore.

Chapter 6
Multi-Scale Simulation of Flow Dynamics with Hybrid CFD-MD Coupling Method: Implementation, validation and application

6.1 Introduction

Though MD simulation method is capable of fully resolving flow fields in nanoscale confined flows, macroscopic problems are still far beyond the reach of MD simulations due to the prohibitively large computational expense of modelling discrete particles. CFD simulation methods, while capable of solving macro-scale problems efficiency, is incapable of resolving features and flow dynamics on the scale of nanometres due to the breakdown of the continuum assumption. To meet the twin goals of accuracy and efficiency, the multi-scale hybrid CFD-MD coupling simulation method offers a reasonable solution by limiting MD calculation to only a small region where atomistic-level resolution is necessary and using continuum methods away from this region. A hybrid CFD-MD coupling scheme for simulating multi-scale (micro- and nano-) fluidic systems is further developed in this chapter.

This chapter presents fundamental multi-scale investigations on flow dynamics modelling for EOR applications using hybrid CFD-MD coupling simulation method following three steps, i.e., implementation, validation and application. The detailed mathematical model and the structure of code developments are demonstrated in Section 6.2 and 6.3, respectively. To verify this hybrid CFD-MD coupling simulation method, the Couette flow in a nanochannel with LJ argon liquid is chosen to simulate in Section 6.4, which results are verified against an analytic solution. The Couette flow simulation with real water liquid in a calcite channel is conducted using the multiscale hybrid CFD-MD coupling scheme in Section 6.5.1. Section 6.5.2 presents the shear flow investigation of oil phase with hybrid CFD-MD coupling simulation method to analyse the calcite surface wettability. The water salinity effect on multiscale shear flow dynamics is investigated in Section 6.5.3 to reveal the salt effect on the water wettability in a calcite slit pore. The multiscale shear flow dynamics study is extended from single phase to multiphase scenarios in Section 6.5.4, where the water salinity effect on the multiphase flow shear dynamics is presented in Section 6.5.5. Conclusions from these studies are drawn in Section 6.6.

6.2 Mathematical Model

6.2.1 Domain Decomposition Method

To develop the multiscale hybrid CFD-MD coupling simulation method, the LJ argon liquid Couette flow in a nanochannel is investigated using domain decomposition method as an example. Figure 6.1 illustrates a general schematic of the methodology: The domain is subdivided into an atomistic (A) domain (MD domain) and a continuum domain (CFD domain); The atomistic domain consists of a solid wall at the bottom of the domain and a liquid region above; The continuum domain is comprised a liquid region with a no-slip wall boundary condition at the top; The two domains coincide in an overlap region, where the two solutions are transferred and consistent. Both the continuum domain and the atomistic domain are three-dimensional.

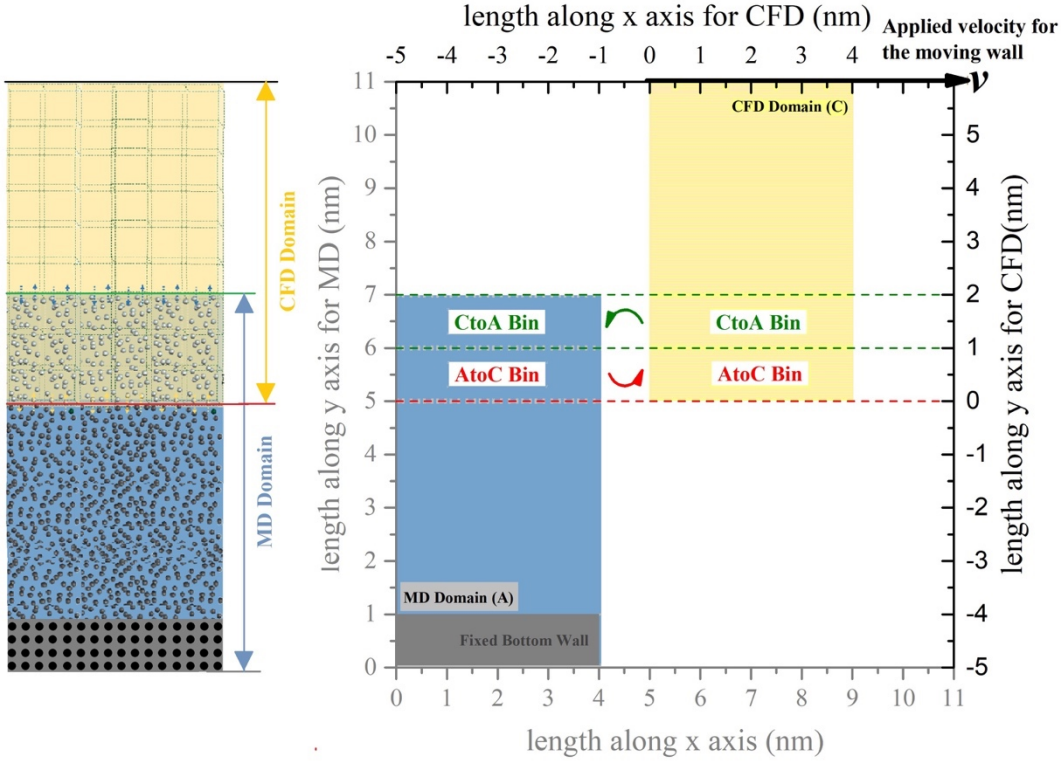

Figure 6.1 A general schematic illustration of the hybrid CFD-MD coupling simulation method.

An initial shear velocity along the x direction is applied on the top wall of the CFD region. The atomistic domain is calculated with MD simulation method, while the continuum domain is simulated with CFD simulation method by solving the Navier – Stokes Equation. The consistency of velocity distributions between CFD and MD simulations is realized by the constraint dynamics control within the overlapping region, which is comprised by “atomistic to continuum (A to C)” and “continuum to atomistic (C to A)” sub-regions.

6.2.2 Continuum (C) Domain – CFD domain

In the continuum domain, the incompressible Navier – Stokes equations are solved, which are given by

$$\frac{\partial \mathbf{u}}{\partial t} + \nabla \cdot (\mathbf{u}\mathbf{u}) = -\frac{1}{\rho}\nabla p + \frac{\mu}{\rho}\nabla^2 \mathbf{u} \tag{6-1}$$

$$\nabla \cdot \mathbf{u} = 0 \tag{6-2}$$

where **u** is the velocity, ρ is the density, *P* is the pressure, and μ is the viscosity.

The entire continuum domain is initialized to have zero velocity field. The velocity at the top of the continuum domain is set to a constant value u_{max} as the top wall is the moving wall in the Couette flow. The velocity gradient is set to zero at the left and right boundaries while the non-constant bottom velocity boundary condition of this CFD domain is calculated from the atomistic domain. The three-dimensional Navier – Stokes equations are solved using the PISO algorithm implemented in the icoFoam solver in OpenFOAM.

The density of the fluid in CFD simulations is chosen to match the average density of the fluid in the atomistic domain. The use of the correct viscosity in this CFD calculation is also essential for proper coupling to ensure that momentum diffuses identically in both CFD and MD domains. The viscosity is calculated from separate pure MD simulations in the next section, Section 6.2.3.

6.2.3 Shear viscosity calculation in atomistic domain

The shear viscosity used in the Navier – Stokes equations of the continuum domain is calculated from separate pure MD simulations. The viscosity μ can be calculated through the autocorrelation function of the ensemble average (as denoted by the angle brackets) of the shear stress:

$$\mu = \frac{V}{k_B T}\int_0^\infty \langle \sigma_{\alpha\beta}(0) \cdot \sigma_{\alpha\beta}(t) \rangle \, dt \tag{6-3}$$

The shear stress $\sigma_{\alpha\beta}$ is given by the off-diagonal terms of the stress tensor

$$\sigma_{\alpha\beta} = -\frac{1}{V}\left[\sum_i m_i v_{i\alpha} v_{i\beta} + \frac{1}{2}\sum_i \sum_{j,j\neq i} r_{ij\alpha} F_{ij\beta}\right] \tag{6-4}$$

where V is the volume, α and β are the x, y or z components, $v_{i\alpha}$ is the velocity of atom i in the α direction, $r_{ij\alpha}$ is the distance between atoms i and j in the α direction, and $F_{ij\beta}$ is the β component of the force due to atom j acting onto atom i.

A total of 10.0 ns MD simulations were run to drive the system becoming equilibrium. A Nose-Hoover thermostat was used to maintain the constant temperature requirement of 300 K for both LJ liquid argon system and liquid water system. The average viscosity for the simulations of the argon liquid and water liquid was 1.079×10^{-4} and 8.37×10^{-4} kg/ms, respectively.

6.2.4 Atomistic (A) Domain

For the Couette flow dynamics simulation of liquid argon presented in Section 6.4, the Lennard-Jones potential is used to model the interactions between argon fluid particles within the atomistic domain, which is defined as follows,

$$\Phi_{LJ}(r_{ij}) = \begin{cases} 4\varepsilon\left[\left(\frac{\sigma}{r_{ij}}\right)^{12} - \left(\frac{\sigma}{r_{ij}}\right)^{6}\right] - 4\varepsilon\left[\left(\frac{\sigma}{r_c}\right)^{12} - \left(\frac{\sigma}{r_c}\right)^{6}\right] & \text{for } r_{ij} \le r_c \\ 0 & \text{for } r_{ij} > r_c \end{cases} \quad (6\text{-}5)$$

where r_{ij} is the distance between argon particles *i* and *j*, r_c is the cutoff radius, ε is the potential well depth, and σ is the zero potential-distance. For LJ argon fluid, the adopted LJ parameters are as follows: σ = 3.4 Å, ε = 1.67 × 10^{-21} J, and *m* = 6.63 × 10^{-26} kg, where *m* is the argon particle mass. A cutoff radius of $r_c = 3.5\sigma$ is used to reduce the computational time. The solid particles forming the bottom wall are arranged in (1 1 1) planes of an FCC crystal structure with the same density as the liquid region. The interactions between the solid particles of the bottom wall are described by a Lennard-Jones potential with the same σ but a well depth 9 times larger than the liquid-liquid interactions ($\varepsilon_{ss} = 9.0\varepsilon$), to ensure that the solid crystal structure remains intact. The solid-liquid particle interactions are set to 75% of the liquid-liquid interactions ($\varepsilon_{sl} = 0.75\varepsilon$) to ensure a no-slip boundary condition between the wall and the fluid. This is important to facilitate comparison to the analytic solution which assumes no slip. The solid atoms are assigned a fixed zero velocity. To prevent particles from leaving the atomistic domain, a reflecting boundary condition is imposed at the top of the atomistic domain. The liquid region is set up in an FCC structure with a lattice parameter consistent with the desired average density and allowed to equilibrate during the initialization period. After the initialization period of the atomistic domain is completed, the temporal concurrent coupling to the continuum solution begins. For water and oil liquid, the SPC/E and OPLS-AA force field model are applied as same as the pure MD simulation descriptions in Chapter 5.

6.2.5 Overlap region

The overlap region is subdivided into three regions: A to C region, buffer region, and C to A region.

6.2.5.1 Boundary condition from atomistic to continuum (A to C region)

The velocity boundary condition on the continuum domain is achieved through the time averaging the atomic velocities. The continuum velocity $\mathbf{u}_i$ in the i^{th} A to C bin is given as the average of the particle velocities **v** within bin *i*,

$$\mathbf{u}_i = \langle \frac{1}{N_i} \sum_{k=0}^{k=N_i} \mathbf{v}_k \rangle \quad (6\text{-}6)$$

where the angle brackets indicate a time average. The velocity is averaged over a given number of time steps, typically the total number of time steps since the previous A to C communication. For this study, an average of 500 atomistic time steps was used.

6.2.5.2 Boundary condition from continuum to atomistic (C to A region)

The particles in the atomistic domain are coupled to the continuum solution via constraint dynamics. The C to A region is comprised of multiple bins, and within each C to A bin, it contains multiple continuum cells. Therefore, the average continuum velocity ***u*** within each C to A bin is the average of the velocities stored at cell centres within that bin. The average atomistic velocity in C to A bin *i* is constraited be equal to the mean continuum velocity $\mathbf{u}_i$,

$$\frac{1}{N_J}\sum_i \mathbf{v}_i = \boldsymbol{u}_J(t) \tag{6-7}$$

where N_J is the number of particles within cell *J*.

Taking a Lagrangian derivative of the Equation 6-7,

$$\frac{1}{N_J}\sum_i \ddot{x}_i = \frac{d\boldsymbol{u}_J(t)}{dt} \tag{6-8}$$

A general solution of the constraint equation can be written as,

$$\ddot{x}_i = \frac{d\boldsymbol{u}_J(t)}{dt} + \zeta_i \tag{6-9}$$

where ζ_i is a variable whose sum over the cell is constrained as,

$$\sum_i \zeta_i = 0 \tag{6-10}$$

From the MD equations of motion,

$$\ddot{x}_i = \frac{F_i}{m} \tag{6-11}$$

where,

$$F_i = -\frac{\partial}{\partial x_i}\sum_{j\neq i} \Phi(r_{ij}) \tag{6-12}$$

$$\ddot{x}_\iota = -\frac{1}{m}\frac{\partial}{\partial x_i}\sum_{j\neq i} \Phi(r_{ij}) \tag{6-13}$$

The combination of the equation (6-9) and (6-11) gives,

$$\zeta_i = \ddot{x}_i - \frac{d\boldsymbol{u}_J(t)}{dt} \tag{6-14}$$

$$\zeta_i = \frac{F_i}{m} - \frac{d\boldsymbol{u}_J(t)}{dt} \tag{6-15}$$

The combination of the equation (6-8) and (6-15) gives,

$$\zeta_i = \frac{F_i}{m} - \frac{1}{N_J}\sum_i \ddot{x}_i \tag{6-16}$$

The combination of the equation (6-11) and (6-16) gives,

$$\zeta_i = \frac{F_i}{m} - \frac{1}{mN_J}\sum_{i=1}^{N_J} F_i \tag{6-17}$$

The combination of the equation (6-9) and (6-17) gives,

$$\ddot{x}_i = \frac{F_i}{m} - \frac{1}{mN_J}\sum_{i=1}^{N_J} F_i + \frac{d\boldsymbol{u}_J(t)}{dt} \quad (6\text{-}18)$$

Then the equation (6-18) can be discretized as

$$\frac{x(t+\Delta t_{MD})-2x(t)+x(t-\Delta t_{MD})}{\Delta t_{MD}^2} = \frac{F_i}{m} - \frac{1}{N_J}\sum_{i=1}^{N_J}\frac{F_i}{m} + \frac{d\boldsymbol{u}_J(t)}{dt} \quad (6\text{-}19)$$

$$\frac{x(t+\Delta t_{MD})-2x(t)+x(t-\Delta t_{MD})}{\Delta t_{MD}^2} = \frac{F_i}{m} - \frac{1}{N_J}\sum_{i=1}^{N_J}\frac{F_i}{m} + \frac{\boldsymbol{u}_J(t+\Delta t_{MD})-\boldsymbol{u}_J(t)}{\Delta t_{MD}} \quad (6\text{-}20)$$

$$\frac{x(t+\Delta t_{MD})-2x(t)+x(t-\Delta t_{MD})}{\Delta t_{MD}^2} = \frac{F_i}{m} - \frac{1}{N_J}\sum_{i=1}^{N_J}\frac{F_i}{m} - \left(\frac{\boldsymbol{u}_J(t)}{\Delta t_{MD}} - \frac{\boldsymbol{u}_J(t+\Delta t_{MD})}{\Delta t_{MD}}\right) \quad (6\text{-}21)$$

$$\frac{x(t+\Delta t_{MD})-2x(t)+x(t-\Delta t_{MD})}{\Delta t_{MD}^2} = \frac{F_i}{m} - \frac{1}{N_J}\sum_{i=1}^{N_J}\frac{F_i}{m} - \frac{1}{\Delta t_{MD}}\left(\boldsymbol{u}_J(t) - \boldsymbol{u}_J(t+\Delta t_{MD})\right) \quad (6\text{-}22)$$

Finally, applying this constraint to the new velocity of atom *j* located within C to A bin *i* is given as (Nie et al., 2004)

$$\frac{x(t+\Delta t_{MD})-2x(t)+x(t-\Delta t_{MD})}{\Delta t_{MD}^2} = \frac{F_i}{m} - \frac{1}{N_J}\sum_{i=1}^{N_J}\frac{F_i}{m} - \frac{1}{\Delta t_{MD}}\left(\frac{1}{N_J}\sum_{i=1}^{N_J}\dot{x(t)}_\iota - \boldsymbol{u}_J(t+\Delta t_{MD})\right) \quad (6\text{-}23)$$

6.2.5.3 Buffer region

The buffer region, located between the A to C region and the C to A region, serves to minimize the feedback between the two regions of communication. Within the buffer region there are no constraints or communication of any kind in either domain. The buffer region should be as small as possible to reduce the computational expense associated with overlap, while at the same time being large enough to relax as buffering. For the flow configurations investigation here, approximately 30% of the overlap region is treated as the buffer to effectively minimize any negative interactions between the A to C region and C to A region.

6.2.6 Concurrent coupling

It is worth to notice that it is necessary to choose a proper time step for the hybrid CFD-MD coupling simulation and averaging time for the atomistic domain. Since OpenFOAM is the main driver code, the time step in the continuum domain must satisfy the Courant condition,

$$\frac{u_\alpha \Delta t_c}{\Delta x_\alpha} < 1 \quad (6\text{-}24)$$

where Δx is the mesh length in the continuum phase, and u_α is the velocity in the α component. Due to the thermal fluctuating nature of the atomistic boundary condition on the continuum solution, as excessively small timestep, on the order of the atomistic mean free time, can lead to insufficiently averaged atomistic velocities and can result in very large velocities on the continuum boundary. This in turn can cause numerical instabilities to arise in the continuum domain. For the given geometry, the time step in OpenFOAM is set to 2×10^{-14} s. Each continuum time step corresponds to 100 atomistic time steps, $\Delta t_C = 100\Delta t_A$. This allows for sufficient time averaging of the atomistic velocities. Due to the inherent fluctuating nature of the MD velocity averaging, a sufficiently small timestep should be chosen to operate well below a Courant number of 1.

6.3 Computational Development

The overall structure of the hybrid scheme code is shown in Figure 6.2. The hybrid CFD-MD coupling simulation begins after the atomistic domain equilibrium calculations. Then at t = 0, the continuum solver begins for 1 continuum time step and then the first C to A communication of overlap region set points occurs. Sequentially, the atomistic domain is advanced 100 atomistic time steps. The result averages from those 100 atomistic time steps are used as the A to C boundary conditions. The continuum solution is then further advanced one continuum time step. The next C to A communication occurs afterwards, followed by the next 100 atomistic time step calculation. The process is repeated for the remaining simulation until the final time step of continuum phase calculation is completed.

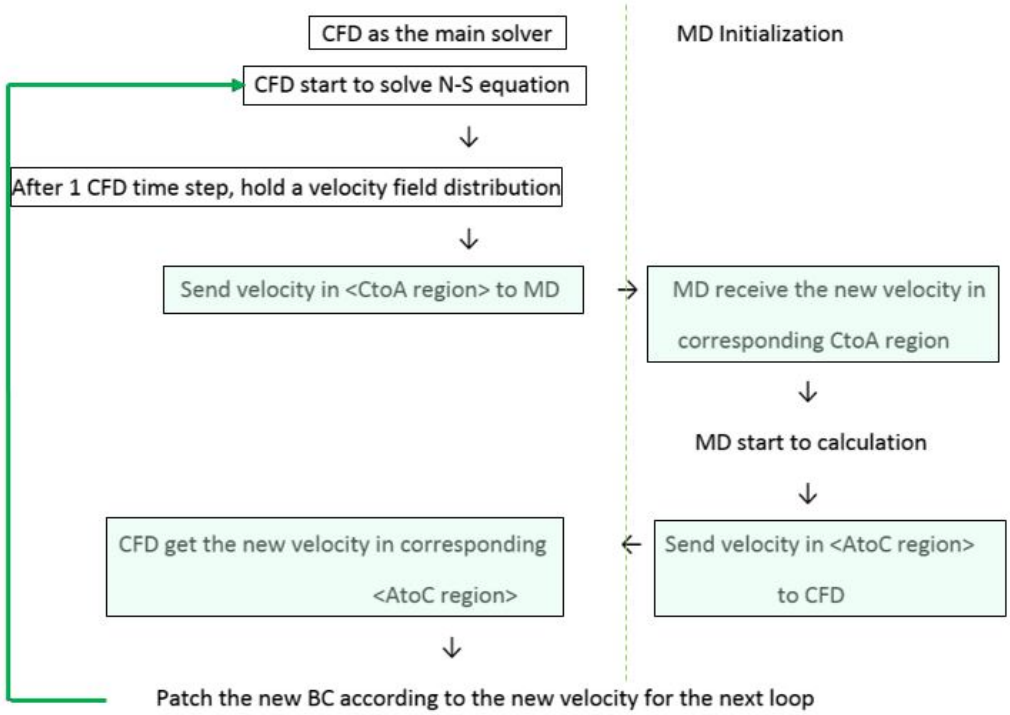

Figure 6.2 The structure of the multiscale hybrid CFD-MD coupling scheme code

In this hybrid CFD-MD coupling simulation scheme, the continuum solver OpenFOAM serves as the main driver code, and the atomistic solver LAMMPS is compiled as a shared library to be called from within the continuum solver. A C++ code development is based on the incompressible, Newtonian, single phase solver icoFoam, and then compiled as a new OpenFOAM application.

6.4 Validation of the coupler: Couette Flow

To validate the hybrid CFD-MD coupling scheme code, the Couette flow dynamics with liquid LJ argon was studied in this section. The entire continuum

domain was initialized with the zero bulk-velocity. At the time of t = 0, the top wall in the continuum domain was set to move with a velocity of $u_x = u_{max} = 1$ (LJ unit, dimensionless), and the fixed wall in the atomistic domain.

The entire domain was constructed by the atomistic domain and continuum domain, respectively. The atomistic MD domain spanned the region from (0, -5, 0) to (30, 30, 100) LJ dimensionless unit, while the continuum region spanned from (0, 23, 0) to (30, 53, 100) LJ dimensionless unit. Thus, the height of the overlap region was 7 LJ dimensionless unit in the *y* direction, which corresponded to approximately 13% overlap in the *y* direction. The overlap region was divided into a single bin in the *x* and *z* direction, and 5 equal bins in the *y* direction. Among these, the top 3 bins were treated as C to A bins, the last bin was the A to C bins, where in the middle were buffer. The total height of this liquid channel was 53. In the meanwhile, the continuum domain was divided into 30 × 30× 100 cells.

The resulting velocity profiles from the hybrid CFD-MD coupling model were compared to its analytic solution of the Couette flow given as,

$$u(y,t) = \frac{u_{wall}y}{L_y} + \frac{2u_{wall}}{\pi}\sum_{n=1}^{\infty}\frac{\cos(n\pi)}{n} \times \sin(\frac{n\pi y}{L_y}) \exp\left(-\frac{\nu n^2\pi^2 t}{L_y^2}\right) \qquad (6\text{-}25)$$

where L_y is the distance between the two walls, and ν is the kinematic viscosity. CFD and MD domains were divided into 25 bins and 11 bins, respectively, in the *y* direction. The local atomic and continuum velocities were averaged spatially within each bin over the time length shown in the legends of Figure 6.3 to smooth the natural atomistic thermal fluctuations. The transient velocity profiles over total time scale of 2.0 ns with the hybrid CFD-MD coupling scheme in Figure 6.3 shows a good agreement with the analytical solution, and the steady-state profile is linear as expected.

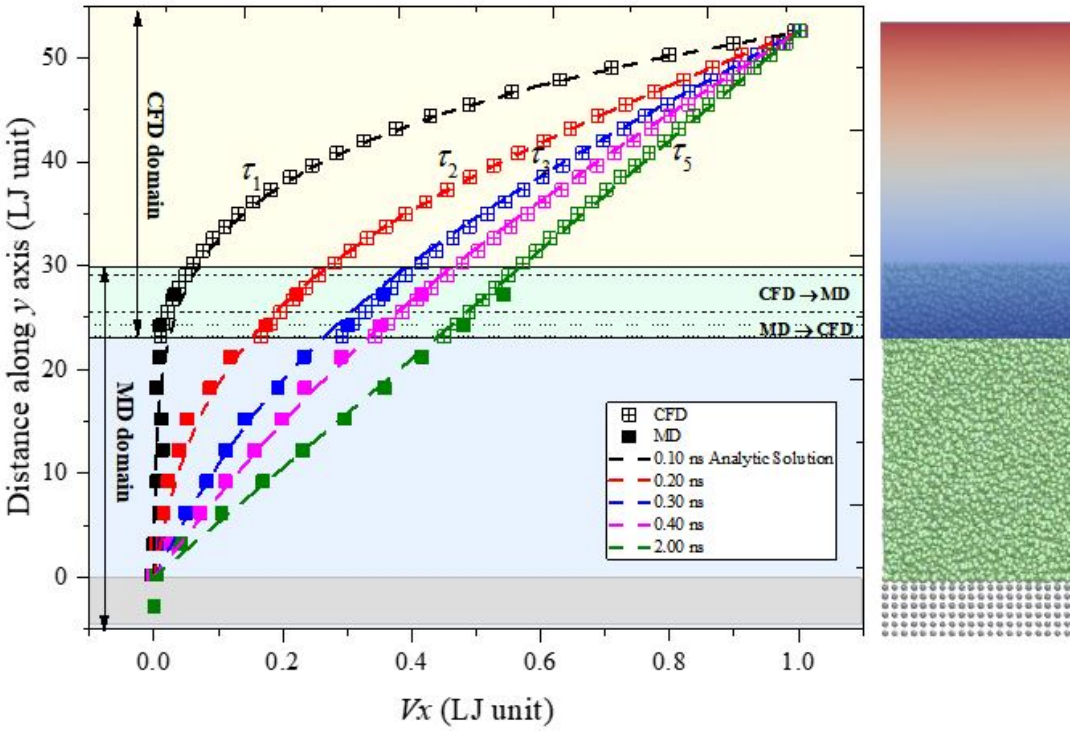

Figure 6.3 Couette LJ liquid argon flow velocity distribution variations with time evolutions associated with the analytic solution and the configuration snapshots.

Overall, the hybrid CFD-MD coupling model developed here, through the combination of OpenFOAM and LAMMPS platforms, agrees well with the analytic solution for Couette flow with LJ liquid argon. Through the coupling algorithm, this model offers large potential computational savings over full atomistic simulations, and more molecular-level insights over full continuum simulation. This advantage is expected to become ever more dramatic for larger systems due to the savings by partially replacing atomistic calculations with significantly less computationally expensive continuum calculation.

6.5 The application of hybrid CFD-MD coupling method on shear flow dynamics during EOR

6.5.1 Hybrid CFD-MD coupling simulation of water shear flow dynamics in a calcite nano pore

To apply the hybrid CFD-MD coupling scheme on the multiscale flow dynamics phenomenon for micro-/nano-EOR, the simulation of Couette flow with real water liquid in a calcite channel was conducted. The hybrid CFD-MD coupling simulation of water Couette flow was comprised by two domains, CFD domain and MD domain, coinciding with the overlap region: The upper region was described by the continuum N-S equations using CFD simulation method; the

bottom region with discrete atoms was simulated by MD method. Periodic boundary conditions were applied in the *x* and *z* direction.

In the CFD subdomain, the three-dimensional incompressible N-S equations based on the continuum assumption were solved using the PISO algorithm implemented by the solver icoFoam in OpenFOAM. At the time of $t = 0$, the top wall in the CFD domain was set to move with a velocity of 157.90 m/s. It is notable that the same velocity boundary condition for the top wall with a value of 157.90 m/s in the CFD region is adopted in all the remaining investigations presented in this chapter.

During the coupling procedure, the velocity in the CFD domain was firstly sent to MD domain through the C to A region after one CFD time step. Then the non-equilibrium MD simulation was run driving by the imported velocity from CFD for 500 MD time steps. The average velocity within the A to C region of MD simulation was further sent to CFD simulation as the new boundary condition, and another loop began. It is notable that the coupling scheme requires a good match of the water density and viscosity properties in both CFD and MD simulations. Therefore, a pre-processing of pure MD simulation was required to obtain the density and viscosity of the bulk water phase, and then set them as the variable properties for the continuum simulations. The water shear viscosity and density used in the Navier – Stokes equations of the continuum domain is calculated from separate pure pre-MD simulation, as described in Section 6.2.3. In this pre-processing MD simulation, the SPC/E water fluid was confined between two parallel walls at y = 0 and 10 nm. A total of 10.0 ns MD simulations were run after the system becomes equilibrium. A Nose-Hoover thermostat was used to maintain the constant temperature requirement. The “block-averaging” approach was adopted in this work to determine the value for the water viscosity. By averaging the last 2.0 ns of the MD trajectory with an averaging step of 10 ps, the mean bulk density and viscosity for the simulation of the water liquid was 0.998 kg/m^3 and 8.37×10^{-4} kg/ms. These values were set as the water bulk properties required by the CFD domain calculation with the hybrid CFD-MD coupling method.

The initial configuration of the MD domain model was generated using the Packmol Package, which was composed of the water liquid as the flow fluid, and a fixed mineral surface as the pore wall. SPC/E water molecules were considered as representative of the water phase; a {10**1**4} calcite slab with the neutral nonpolar surface, being the most stable surface of calcite and dominating its observed morphology, was used as the solid phase. The rhombohedral structure of calcite, which space group R3C, and hexagonal unit cell parameters $a = b =$

4.988 Å, c = 17.061 Å, α = 90°, β = 120° was used to create an atomistic model of the calcite surfaces. The model developed by Raiteri et al. (Raiteri et al., 2010) was employed to model calcite surfaces. The Lennard-Jones potential parameters between different atom types, were obtained using geometric combining rules. The potential energy was evaluated with a 12.0 Å cutoff for the short-range van der Waals interaction, and the Ewald summation method for the Coulombic interactions was calculated with a precision of 1×10^{-6}. The periodic boundary conditions were applied to the *x* and *z* directions. To prevent particles from leaving the atomistic domain, a reflecting boundary condition was imposed at the top of the atomistic domain. An equilibrium MD was conducted in the NVT ensemble, where the number of particles (N), the simulation box volume (V), and the temperature (T) were kept constant. The equilibrium state of the water/calcite system after 10.0 ns calculation was used as the initial configuration for the MD subdomain in the hybrid CFD-MD coupling simulation.

Figure 6.4 reveals the transient velocity profiles of DI-water sheared in a calcite mineral pore, associating with the equilibrium configuration snapshot for the entire coupling domain. The result shows that, i) before the coupling simulation starts, the CFD internal flow velocity magnitude is zero; the same zero bulk velocity of water molecules can be obtained in MD domain, with all water molecules randomly moving as the equilibrium state; ii) after the start of the hybrid CFD-MD coupling simulation, the velocity of CFD domain is gradually increasing due to the shear velocity applied on the top wall as the CFD simulation boundary conditions; iii) then in the CFD-MD coupling region, the velocity transfer between CFD and MD domains shows a good agreement in each side; iv) the top-layer velocity in MD domain imposed from the CFD domain drives the remaining water molecules to move; v) after loops, a linear velocity profile of water phase along the *y* direction can be observed throughout the whole CFD-MD coupling domain. The good coordinating agreements of velocity magnitude in each time period between CFD and MD domains indicate that a good implementation capability of this hybrid coupling scheme for the application of water shear flow dynamics simulation.

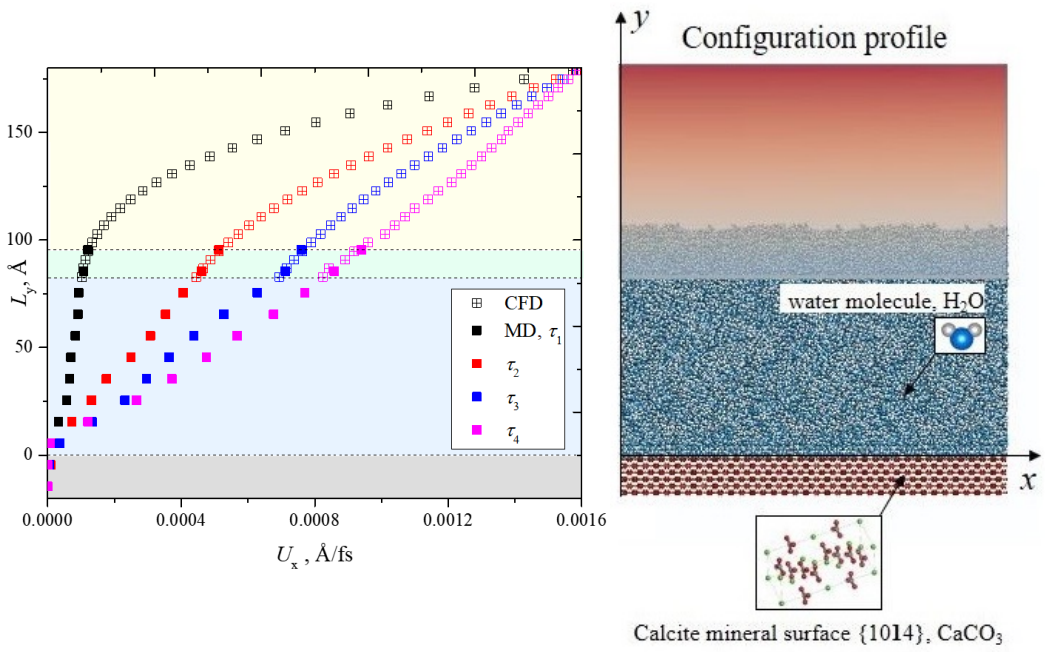

Figure 6.4 Couette water flow transient velocity profiles with hybrid CFD-MD coupling simulation method associated with the configuration snapshot after equilibrium.

The purpose of this hybrid CFD-MD coupling scheme is to reduce the computational cost of a pure atomistic simulation without sacrificing molecular-lever accuracy. To verify its computational performance over fully atomistic simulations, the result was also compared to pure MD and pure CFD simulations, respectively, as shown in Figure 6.5. The pure MD channel is similar with the hybrid CFD-MD channel, except that it requires an additional solid wall at the top of the domain. The distance between the two walls was held as 18.0 nm as well.

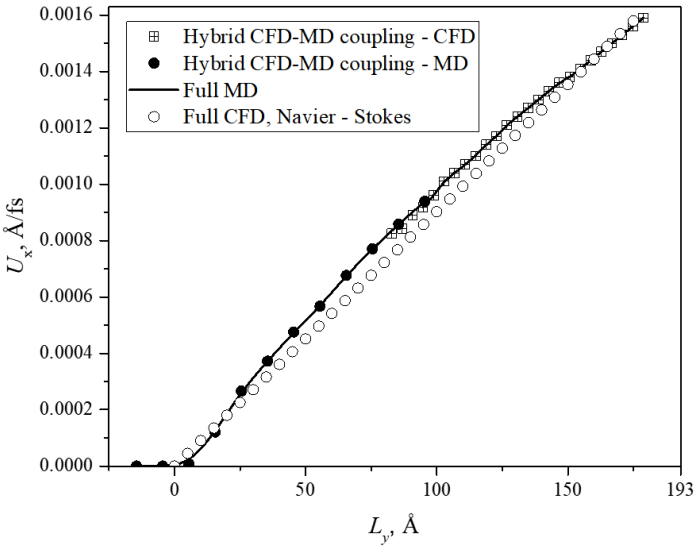

Figure 6.5 Comparisons of the steady-state velocity profiles from full CFD and full MD simulations for the water/calcite system

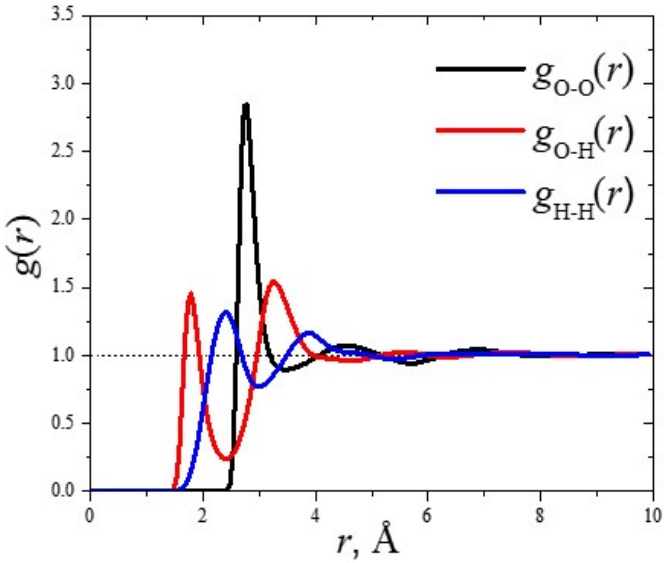

Figure 6.6 The RDF profiles of the water liquid molecular interactions in the MD subdomain with hybrid CFD-MD coupling scheme

The advantage of the hybrid CFD-MD coupling simulation is the implementation of both less computational consumption and greater accuracy: i) Compared with a sole MD simulation for the entire domain, around half of the computational time is saved with the usage of this hybrid CFD-MD simulation scheme. After reaching to the steady stare, the linear bulk velocity profile is obtained. ii) Besides, the molecular-level information can be captured by the MD simulation in the atomistic domain. the water molecular interaction and atomistic-scale density distribution are presented in Figure 6.6 and 6.7. Both the short-range order and no long-range order can be found for water molecule interactions from Figure 6.6.

This hydrophilic characteristic of calcite surface can also be found by analysing the density profile of water phase along the *y* direction, as presented in Figure 6.7: i) A slightly higher water density distribution near the water/calcite interface suggests the adsorption phenomenon of water onto the calcite surface. This interface effect appears within the range of 16 Å on the top of the solid surface. The result indicates that if the dimension scale for liquid/solid interface simulation is less than ~2 nm, the continuum assumption fails due to the atomistic interactions. The adsorption of water on the calcite slab suggests the partial hydrophilicity characteristic of the calcite surface. ii) When the dimension is far away from the liquid/solid interface (greater than 2 nm), the molecular water density distribution is consistent with the bulk phase density, with the average water density of 0.998 kg/m^3. It indicates that this hybrid scheme requires sufficiently large enough size for the MD domain, especially close to the critical

interface, to ensure that the proper bulk parameters, consistent with the continuum assumption, are coupled with the CFD simulation, instead of interface properties.

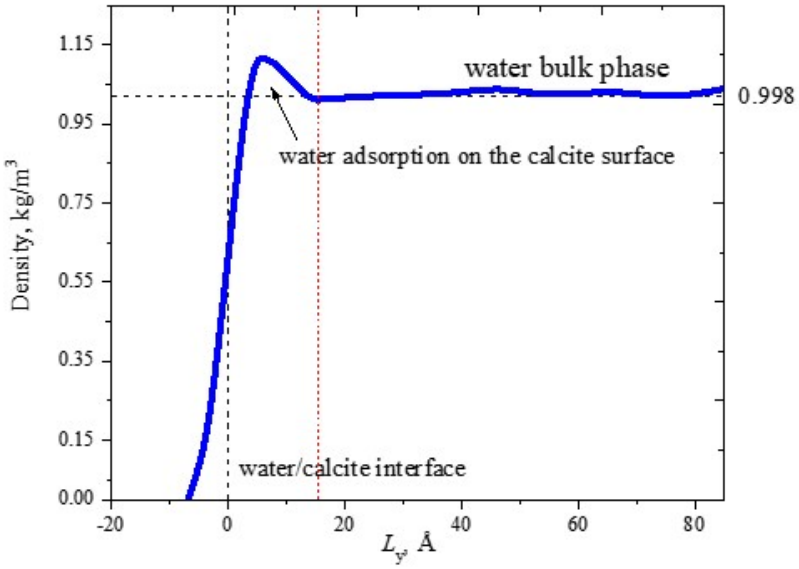

Figure 6.7 The density distributions of water phase for the MD domain along the *y* direction with hybrid CFD-MD coupling scheme for water/calcite system

Above results show the great potential of this hybrid CFD-MD coupling simulation methodology with the advantages of better computational performance and greater simulation accuracy. Both macro-scale water flow dynamics characteristic and molecular-scale interactions close to the interface can be obtained. The hydrophilicity of calcite surface can also be analysed with this hybrid scheme.

6.5.2 Hybrid CFD-MD coupling simulation of oil shear flow dynamics to investigate the calcite surface wettability

The oil phase flow dynamics in the mineral channel is also required to investigate for EOR applications. Therefore, the hybrid CFD-MD coupling simulation is applied to study the multi-scale flow and molecular dynamics phenomenon in a calcite pore. Neutral non-polar n-decane $C_{10}H_{22}$ was used as the representative non-polar oil phase. The OPLS-AA force field was utilized to describe the interactions among atoms in the n-decane phase. This force field is parameterized for organic systems. The model developed by Raiteri at al. was employed to model calcite surfaces. These two force fields have been shown to be compatible with each other. The total energy is including both the intra- and inter-molecular interactions, given as follows:

$$E_{total} = E_{bond} + E_{angle} + E_{dihedral} + E_{torsion} + E_{vdw} + E_{coulombic} \qquad (6\text{-}24)$$

where E_{total}, E_{bond}, E_{angle}, $E_{dihedral}$, $E_{torsion}$, E_{vdw} and $E_{coulombic}$ are the total energy, bond-streching, angle-bending, dihedral-energy, torsion energy, van der Waals

and electrostatic components, respectively. The Lennard-Jones potential parameters between difference atom types were obtained using geometric combining rules. The potential energy was evaluated with a 12.0 Å cut-off for the short-range van der Waals interaction, and the Eward summation method for the Coulombic interactions was calculated with a precision of 1×10^{-6}. Initially, the fluid and both top and bottom walls are stationary. To start the shear, the top wall in the CFD region is brought to a constant velocity. The momentum equation is given as follows,

$$\frac{\partial u}{\partial t} = \nu \frac{\partial^2 u}{\partial y^2}$$

where ν is the kinematic viscosity. Figure 6.8 shows the developing results of the transient velocity profiles for n-decane fluid flow with hybrid CFD-MD coupling simulation method, associating with the configuration snapshot after equilibrium. It can be found that, similar to the water/calcite system, the velocity transfer between CFD and MD subdomain shows a good performance with a close matching in the overlapping region. The fully-developed velocity along the *y* direction is linear after oil liquid flow reaching the steady state. The hybrid CFD-MD simulation results are comparable with full CFD and full MD simulation as shown in Figure 6.9.

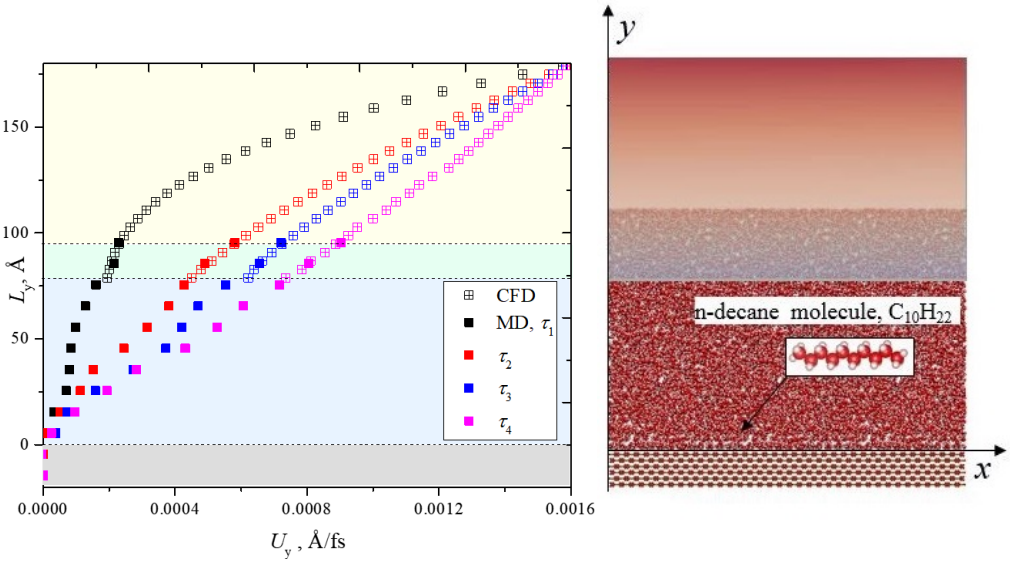

Figure 6.8 Velocity profiles of n-decane fluid flow with time evolutions using hybrid CFD-MD coupling simulation method associated with the configuration snapshot after equilibrium.

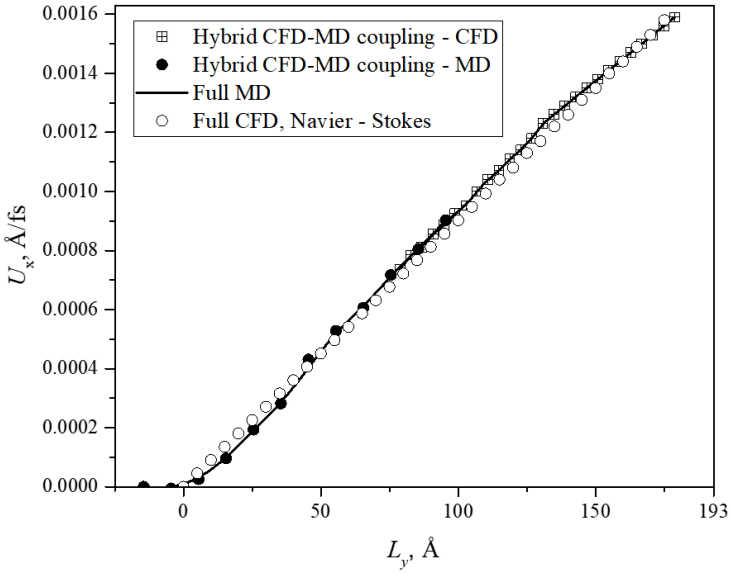

Figure 6.9 Comparisons of the steady-state velocity profiles from full CFD and full MD simulations for the n-decane/calcite system

The interaction between two n-decane molecules can be seen from the RDF profiles in Figure 6.10, which is consistent with the pure MD simulation result of n-decane phase. As far as the intermolecular correlations are concerned, it is clear that the oscillations around $g(r) = 1$ are close to the cut-off radius. Trans (T) and Gauche (G) confirmation positions of carbon atom neighbours in a molecule can also be observed, followed with successive GT and TT conformations as well.

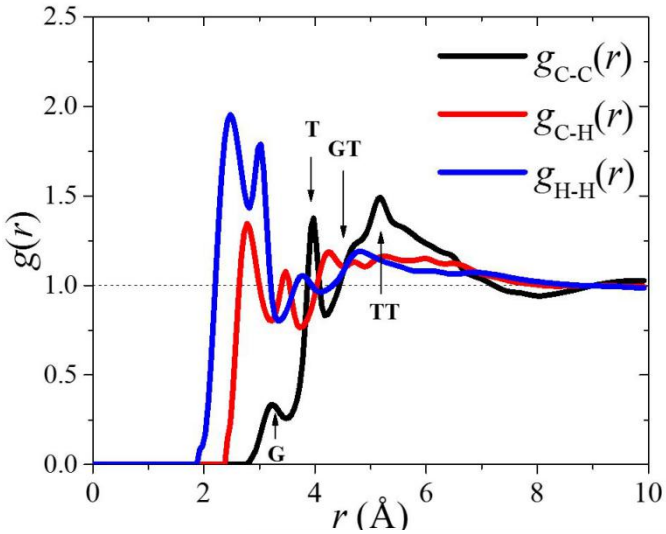

Figure 6.10 RDF profiles of n-decane molecular interactions for n-decane /calcite system with hybrid CFD-MD coupling simulation method

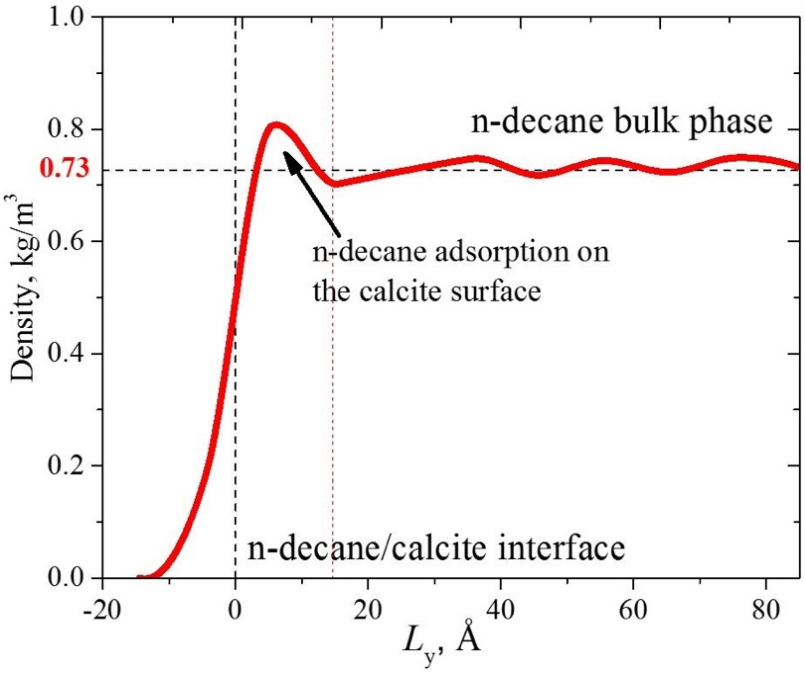

Figure 6.11 The density distributions of oil phase for the MD domain along the *y* direction with hybrid CFD-MD coupling scheme

Figure 6.11 shows the density distributions of oil phase for the MD domain along the y direction with hybrid CFD-MD coupling scheme. An obvious peak can be found around the n-decane/calcite interface within the range of 2 nm on the top of the mineral surface along the *y* direction. It indicates that oil molecules are adsorbed on the solid surface, where the adsorption interactions lead to a denser concentration at the atomistic level. This phenomenon shows a good agreement with the pure MD simulation results, suggesting a partially hydrophobic characteristic of the calcite surface. Both Figure 6.7 and Figure 6.11 demonstrate the intermediate wettability of the calcite slabs. More oil/water wettability preference of the calcite solid is analysed in Figure 6.12 with further details.

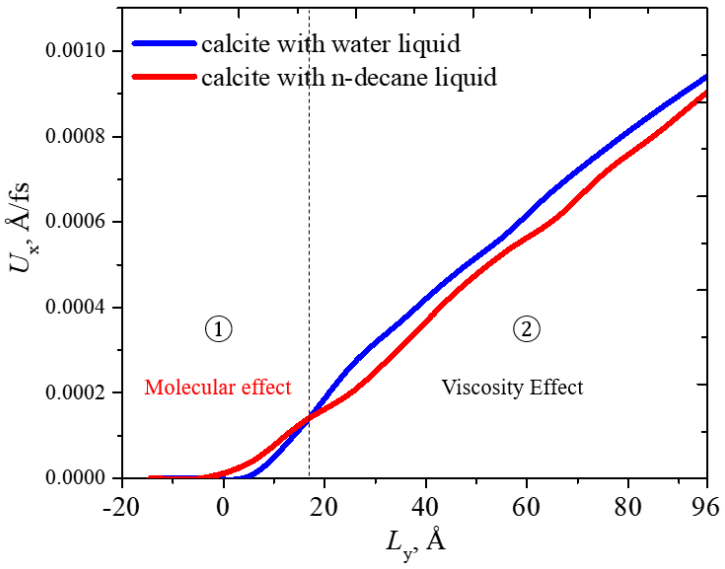

Figure 6.12 The comparison of fluid velocity U_x along the *y* direction at the atomistic region between DI-water/calcite system and n-decane/calcite system

Figure 6.12 presents the comparison of fluid velocity U_x along the y direction at the atomistic region between DI-water/calcite system and n-decane/calcite system after the same simulation time of 5 ns. The intersection point at around 1.8 nm along the *y* direction divides the entire flow domain into two sub-regions, marked with Region 1 and Region 2: i) The velocity distribution of oil phase in Region 2 is shown smaller than that of water phase. This phenomenon can be explained with the viscosity effect, since oil phase with a greater kinematic viscosity responds shower for the momentum transfer than water phase, which mechanism is consistent with the continuum assumption at the macro scale. ii) The velocity magnitude of oil phase in Region 1 shows slightly larger than that of water phase, which indicates that the mobility of water phase near to the calcite mineral surface is weaker than oil phase. It suggests that the stronger adsorption of water liquid on the calcite mineral surface is obtained, compared to the n-decane/calcite interactions near to the interface. Combining with the appearance of density peaks in both Figure 6.7 and Figure 6.11, it can be concluded that the calcite surface is neither complete water-wet, nor complete oil-wet. Instead, it processes the intermediate wettability characteristic, but to be specific, more water-wet. The partially hydrophilicity of the calcite surface can also be verified through pure MD simulation in Chapter 5, with an observation of the oil contact angle less than 90 degrees. Overall, this hybrid CFD-MD multi-scale coupling simulation method performs its good capability to both capture the molecular

dynamics around the interface and save the entire computational cost for simulating the oil/calcite system.

6.5.3 The salt effect on the water wettability in a calcite nano pore

To apply the hybrid CFD-MD coupling scheme on the multiscale flow dynamics phenomenon for micro-/nano-EOR, the simulation of Couette flow with DI water liquid in a calcite channel has been conducted in Section 6.5.1. The salt-water/calcite system is studied in this section using this hybrid CFD-MD coupling scheme in this section to investigate the salt effect on the wettability of the calcite mineral surface. Aqueous sodium chloride (NaCl) solution was employed as the salt water phase to simulate geological fluids (brines). The ions were modelled as charged Lennard-Jones particles, with potential parameters propose by Kneshan et al. (Koneshan et al., 1998).

Water salinity of 1.00 M were applied to study the effect of salt concentration on the wettability of the calcite mineral surface using this hybrid CFD-MD coupling scheme, as shown in Figure 6.13: For the MD domain, a number of sodium and chloride ions was inserted into the water phase to achieve an overall salinity of 1.00 M; The same density and velocity properties of salt water with DI water was setup for the CFD calculation by ignoring the salt effect on the bulk physical properties based on the continuum assumption; An overlap region was also applied between the CFD and MD domain as the hand-shaking platform.

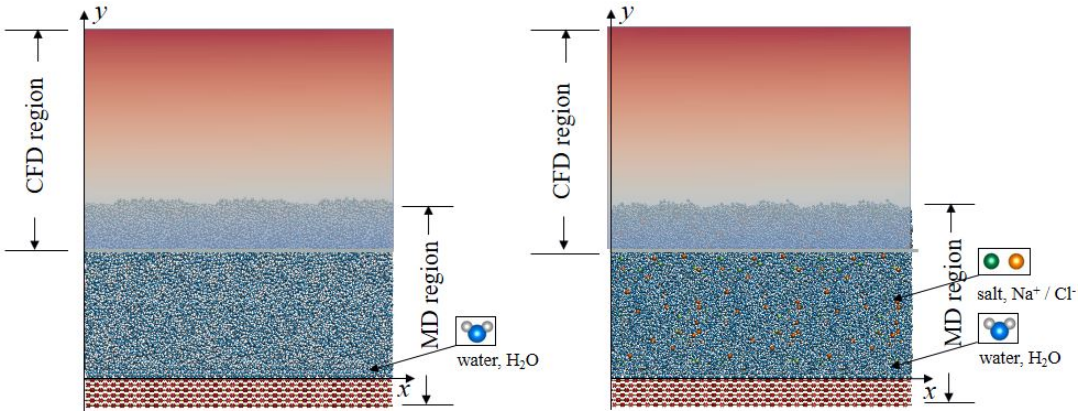

Figure 6.13 The configuration snapshot illustrations of the entire domain for the hybrid CFD-MD coupling simulations of the pure-water/calcite system (left) and the salt-water/calcite system (right).

A pre-EMD simulation for 10.0 ns period is conducted for the sole MD subdomain to achieve the final equilibrium MD configuration; then as the start of the hybrid CFD-MD coupling simulation, the velocity of the salt water in the CFD subdomain is gradually increasing due to the shear velocity applied on the top wall as the CFD simulation boundary conditions; through the overlap hand-shaking platform, the average velocity of C to A region in MD subdomain, imposed from the CFD

domain, drives the remaining water molecules to move; the average velocity of A to C subdomain in MD region is further used to reset the bottom boundary conditions of CFD domain; after loops, a linear velocity profile of water phase along the *y* direction can be observed throughout the whole CFD-MD coupling domain. The results of the transient velocity profiles for the salt water shear flow dynamics, associating with the configuration snapshot of the final steady state are presented in Figure 6.14. In the CFD-MD coupling region, the velocity transfer between CFD and MD domains shows a good agreement in each side, which result is also consistent with the full MD and full Navier-Stokes solutions, as shown in Figure 6.15.

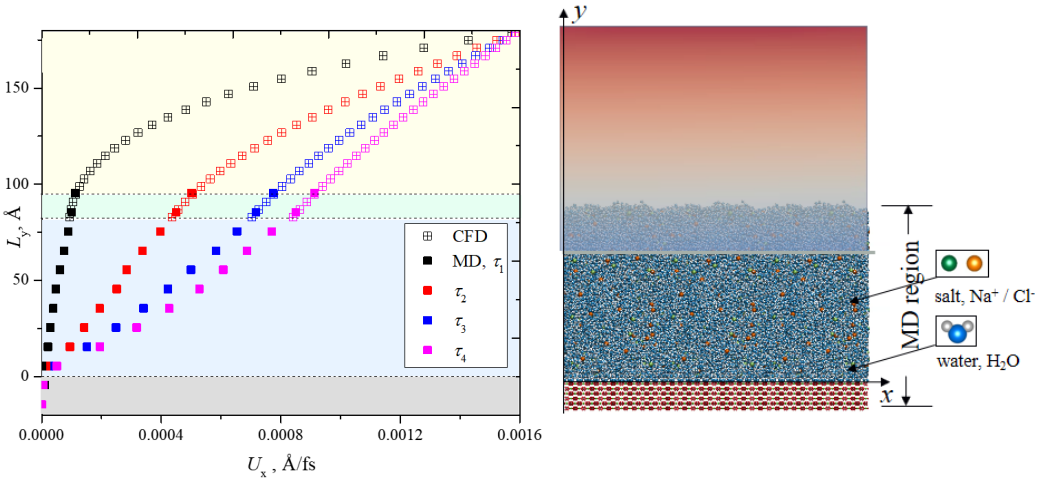

Figure 6.14 Couette water transient velocity profiles with hybrid CFD-MD coupling simulation method associated with the configuration snapshot after equilibrium for salt-water (NaCl, 1.0 M)/calcite system.

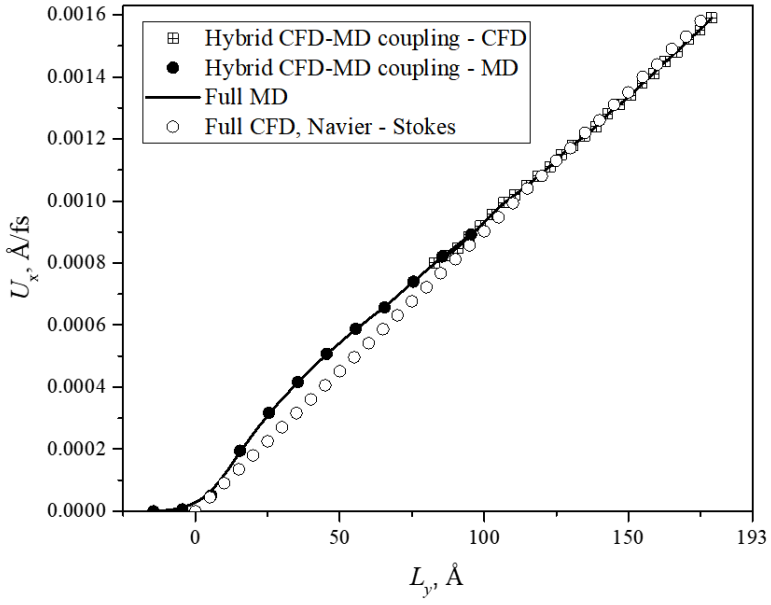

Figure 6.15 Comparisons of the steady-state velocity profiles from full CFD simulations and full MD simulations for the salt-water/calcite system

Figure 6.16 shows the density distribution comparison along the *y* direction for both DI-water/calcite system and salt-water/calcite system. The results suggest that the density along the *y* direction for salt-water/calcite system is slightly greater than that of DI-water/calcite system in both interface region and bulk region, due to the addition of ions. While a higher peak is found for the salt-water/calcite system, it cannot suggest an enhancement of the adsorption interactions between liquid and surface due to the presence of sodium and chloride ions. To identify the salt effects on the surface wettability, the comparison of velocity along the y direction is required to further analyse as follows.

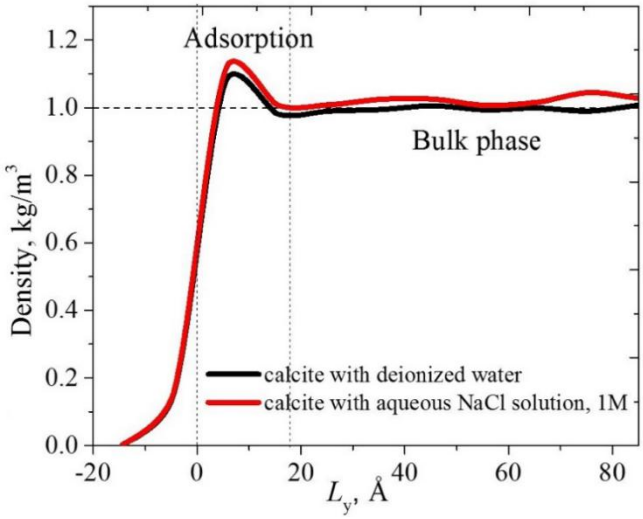

Figure 6.16 The density distributions of water-phase for the MD domain with hybrid CFD-MD coupling scheme for both (a) DI-water/calcite system, and (b) salt-water (NaCl, 1.0 M)/calcite system.

The comparison of the steady velocity profile along the *y* direction in MD domain between DI-water/calcite and salt-water/calcite system is zoomed-in in Figure 6.17. It can be observed that there is a “intersection point” at around 5 nm along the *y* direction for the two velocity distribution profiles: before this intersection point, the velocity for the salt-water/calcite system shows greater than that in DI-water/calcite system, which indicates that the presence of salt can enhance the mobility of water molecules located close to the liquid/solid interface; the opposite trend can be found at the range behind the intersection point, which suggests that the addition of salt into the water phase would slightly increase the kinetic viscosity of the liquid phase, leading to a smaller slope for the velocity profile.

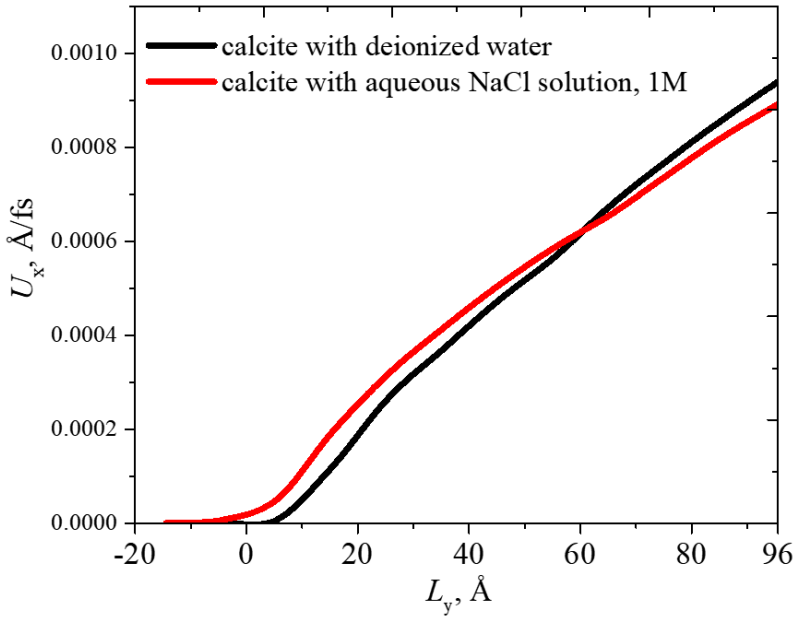

Figure 6.17 The comparison of steady velocity profiles in MD region with hybrid CFD-MD coupling simulation method for both DI-water/calcite system and salt-water (NaCl, 1.00 M) / calcite system

In Figure 6.17, the greater velocity distribution near to the liquid/solid interface with the addition of salts indicates an enhancement effect of salts on the water wettability of the calcite surface. It is notable that this atomistic-scale effect on the interface flow dynamics appears within a range of 6.5 nm thickness above the slab surface. This is inconsistent with the adsorption layer location through analysing the density distribution at the atomistic scale shown in Figure 6.12, which critical thickness is around 2 nm along the *y* direction.

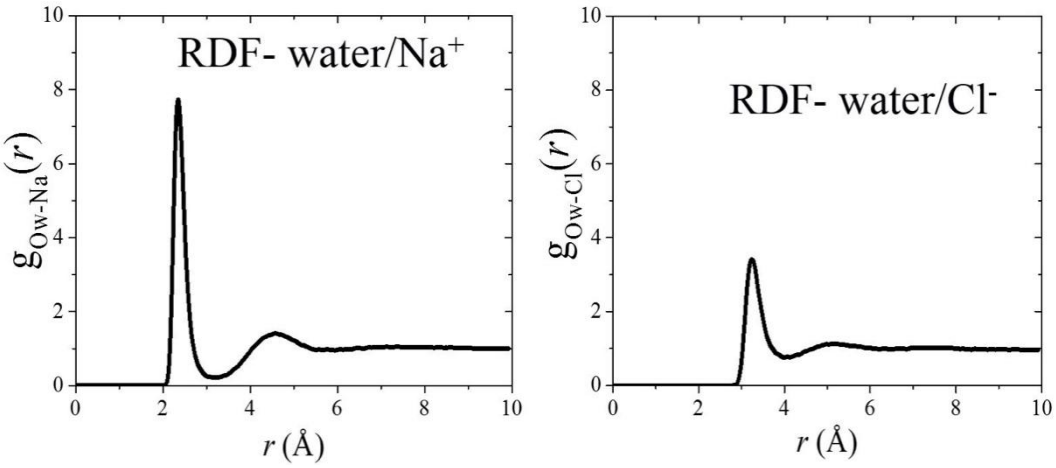

(a) O_w-Na^+ (b) O_w-Cl^-

Figure 6.18 The RDF profiles of the water liquid and ions molecular interactions in the MD subdomain with hybrid CFD-MD coupling scheme

This expansion of the critical range caused by the presence of salts can be explained by the hydration effect of ions, as shown in Figure 6.18. The ions are predominantly fully coordinated by water molecules, which can be observed from the RDF profiles shown in Figure 6.18(a, b). The first sharp peaks for both Na^+ and Cl^- ions indicate the highly ordered water structure around the ions, suggesting their great hydration capacity. Since the ions are having randomly thermal dynamics motion in the water liquid phase confined in the non-polar channel, it may cause the expansion of the critical range due to the hydration effects of ions.

6.5.4 The water/oil binary liquid (multiphase) shear flow dynamics in an oil-wet calcite pore

The application of hybrid CFD-MD coupling simulation on the single-phase scenarios (DI water, salt water, or n-decane) has been presented previously. The objective of the research in this section is to apply the coupling scheme to a multiphase Couette flow dynamics phenomenon with water/n-decane binary liquid fluid. The shear flow simulation of water/oil binary liquid in an oil-wet calcite pore is considered in this section as a representative situation pertinent to the EOR applications. This hybrid CFD-MD multi-scale coupling simulation requires a reasonable organisation and pre-definition of CFD, MD and the overlapping domain. To capture the atomistic-level phenomenon around the oil/mineral interface and the immiscible water/oil interface, the MD domain is established for the entire calcite slab, oil phase, and partial water phase near to the water/oil interface, as shown in Figure 6.19. The remaining water phase, which locates far away enough from the water/oil interface, is defined as the CFD simulation domain by assuming the bulk water as the continuum phase. In this way, the CFD-MD overlapping zone still contains single phase fluid of water, so the developed code for this hybrid CFD-MD coupling scheme can still be applied to this scenario. It is notable that, according to the summary from single-phase flow dynamics simulation results, the size of the MD simulation region among the entire coupling domain should be large enough to ensure that the correct bulk physical properties, rather than interface properties, are coupled between CFD and MD simulations. Therefore, the size of the initial multi-phase configuration is doubled, compared to the single-phase model proposed in the previous sections in this chapter.

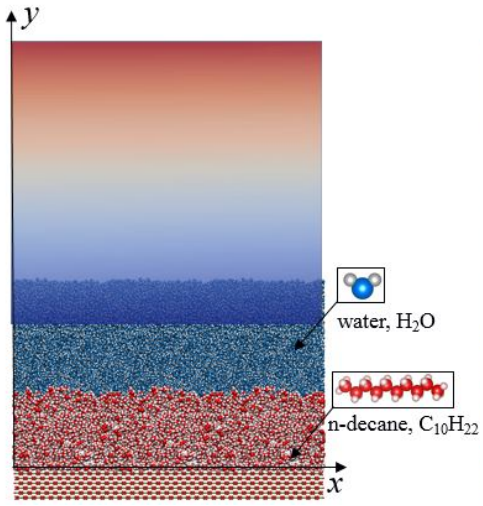

Figure 6.19 The configuration illustration of the water/oil binary liquid flow configuration

Figure 6.20 shows the developing results of the transient velocity profiles for the water/n-decane binary liquid shear flow with hybrid CFD-MD coupling simulation method. It can be found that, similar to the single-phase system, the velocity consistency between CFD and MD subdomain shows a good performance with a close matching in the overlap region. The fully-developed velocity along the *y* direction is linear after binary liquid flow becoming steady. The hybrid CFD-MD simulation results are comparable with full MD simulation and full CFD calculations with VOF model as shown in Figure 6.21. Based on the results with both coupling method and full MD method, it can be found that the oil steady-state shear velocity distribution near to the solid wall is prohibited because of the adsorption interactions between n-decane molecules and calcite crystal surface. Due to the no-slip boundary condition assumptions between oil and the bottom calcite surface in full CFD calculations, it can lead to an overestimation of the prediction for the steady velocity distribution near the oil/calcite interface.

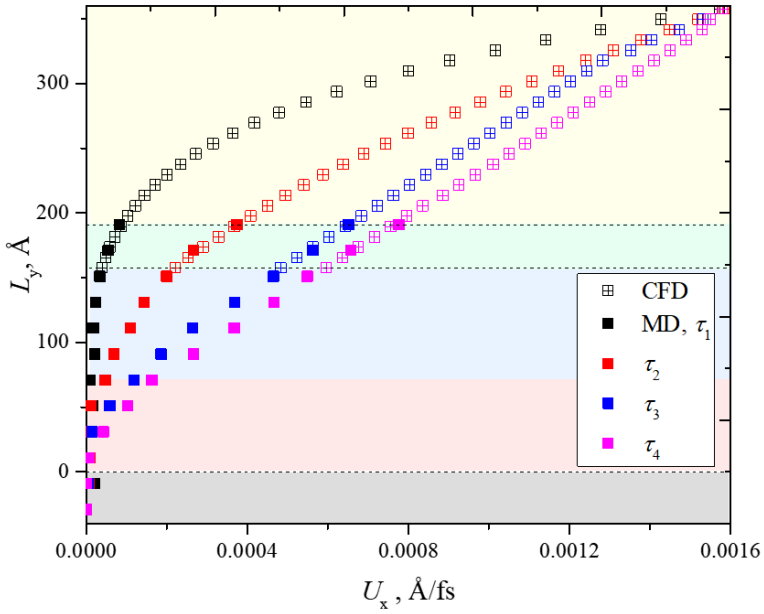

Figure 6.20 Couette flow velocity profiles with time evolutions using hybrid CFD-MD coupling simulation method for binary-liquid (water/n-decane) / calcite system.

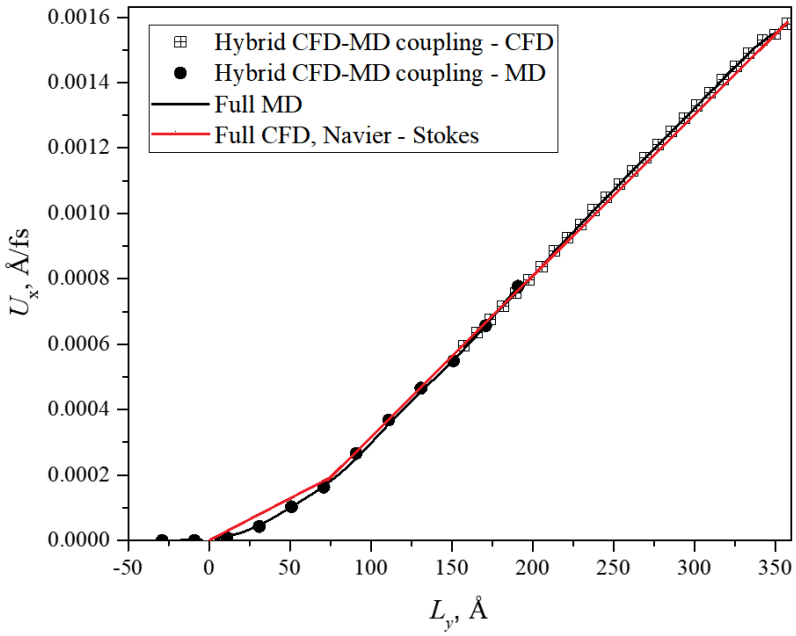

Figure 6.21 Comparisons of the steady-state velocity profiles from full CFD simulations and full MD simulations for the DI-water/oil binary liquid/calcite system

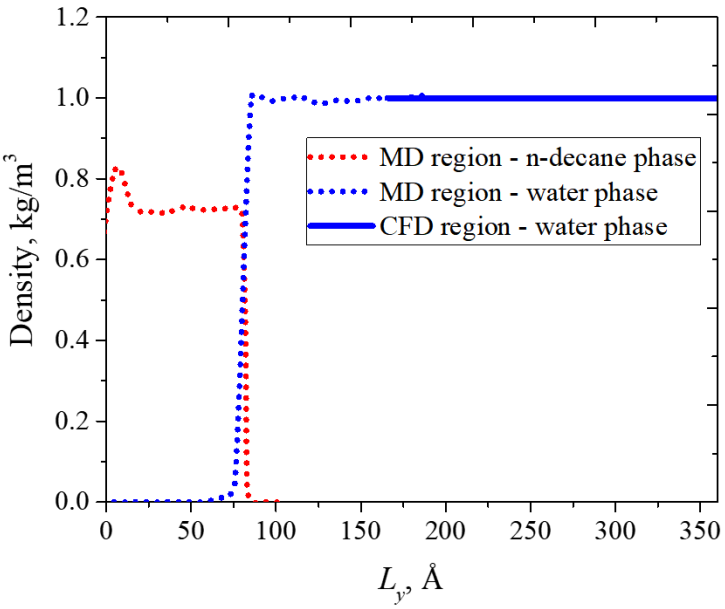

Figure 6.22 Density distribution along the y direction of the entire domain for the DI-water/oil binary liquid/calcite system

Further physical analysis of the density distribution along the y direction of the entire domain for the water/oil binary liquid/calcite system can be found in Figure 6.22. The results show that there is an oil density peak occurring at the interface between oil and calcite due to the molecular adsorption interactions; the average bulk density of the n-decane and water phase in the MD domain are around 0.731 and 0.998 kg/m^3, respectively, which are coherent with the water density distribution in both the overlap domain and the CFD domain; the interface between water and n-decane phase can also been observed from the density distribution in the MD domain, where the interfacial thickness is calculated as 4.52 Å with the "10-90" criteria. This calculation result from hybrid CFD-MD coupling method agrees with the full MD simulation result presented in Chapter 5 as well. It can be indicated that with the application of the hybrid CFD-MD coupling scheme, the computational efficiency and the nano-scale information can both be achieved and enhanced at the same time.

6.5.5 The salt effect on the water/oil multi-phase shear flow dynamics in an oil-wet calcite pore

Similar to the model described in the Section 6.5.4, the hybrid CFD-MD coupling method is employed to the Couette flow dynamics simulation for binary-liquid/calcite system with water, n-decane and salt ions as the working fluid in this section, which configuration snapshot is presented in Figure 6.23. The aqueous sodium chloride solution with the concentration of 1.0 M is applied as the salt water phase in the MD domain, attaching to an n-decane layer on the surface of calcite inorganic slab.

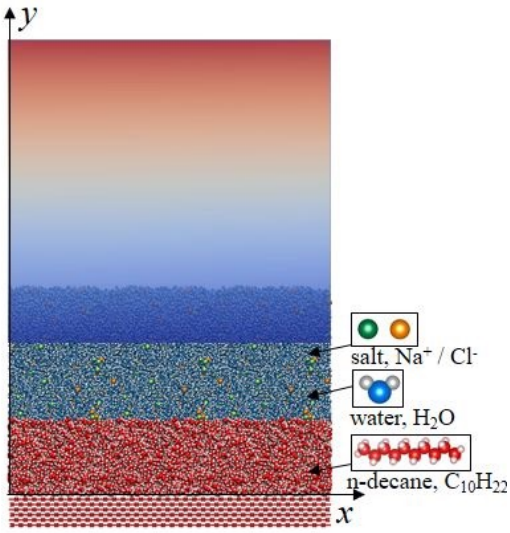

Figure 6.23 The configuration illustration of the salt-water/oil binary liquid flow configuration

Figure 6.24 shows the time-evolution results of the shear velocity profiles for the salt-water/n-decane binary liquid shear flow with hybrid CFD-MD coupling simulation method. Associating with an illustration snapshot as shown in Figure 6.23, it can be also seen that the velocity consistency between CFD and MD subdomain performs very well with a highly matching in the overlap region. The fully-developed velocity along the *y* direction is almost linear for the steady state of the binary liquid shear flow. The hybrid CFD-MD simulation results also show a consistent trend with full MD simulation and full CFD calculations with the VOF model as shown in Figure 6.25. In addition, Figure 6.25 shows the overestimation of the full CFD simulations with the VOF model, due to the ignoration of the molecular-scale adsorption interactions between oil and calcite surface. Comparing with the full MD simulation method, using the hybrid CFD-MD coupling model could not only achieve a result which is highly consistent with the full MD simulation results, but also dramatically save the computational cost by replacing half of the full MD calculation domain with CFD domain.

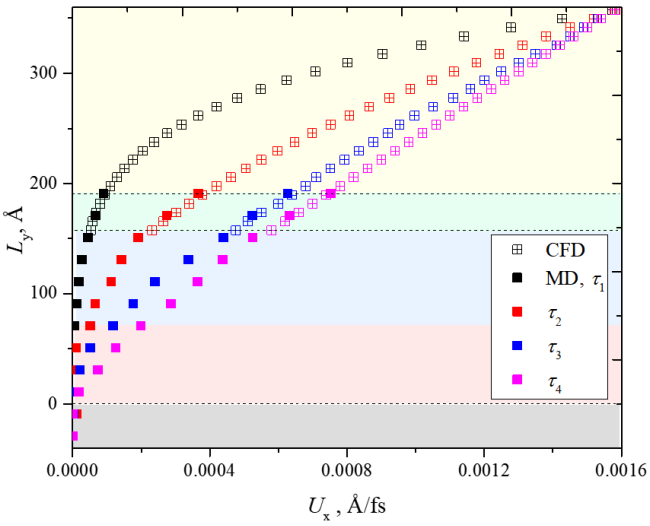

Figure 6.24 Couette flow velocity profiles with time evolutions using hybrid CFD-MD coupling simulation method for binary-liquid (salt-water/n-decane) / calcite system.

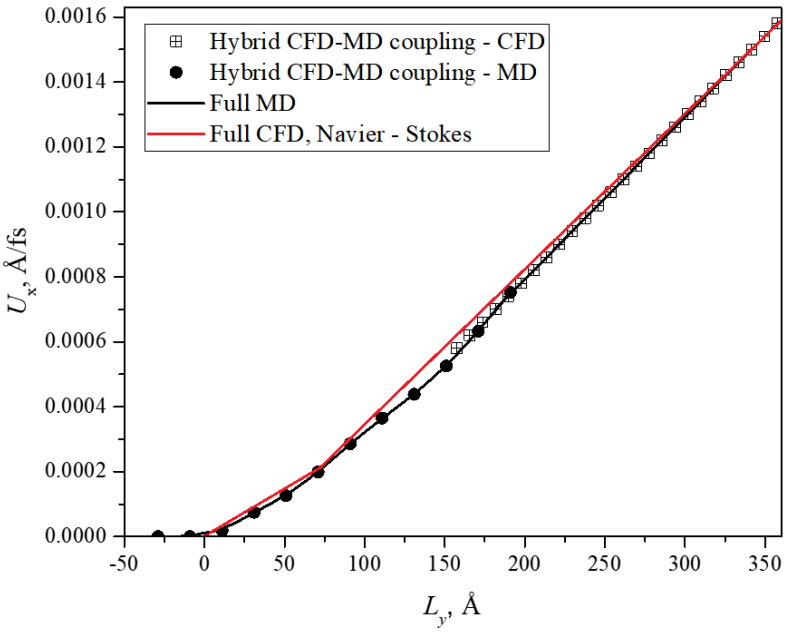

Figure 6.25 Comparisons of the steady-state velocity profiles from full CFD simulations and full MD simulations for the salt-water/oil (binary liquid) /calcite system

The salt effect on the shear flow dynamic characteristics of the binary-liquid/calcite system with hybrid CFD-MD coupling simulation method is presented in Figure 6.26. Through comparing the velocity profiles in MD domain with hybrid CFD-MD coupling simulation method for both DI-water/n-decane/calcite system and salt-water (NaCl, 1.00 M) / n-decane/ calcite system,

it can be observed that the presence of ions in the water phase can enhance the shear mobility of n-decane layer close to the mineral surface. This is due to the ion effects on the shear stress on the water/oil interface.

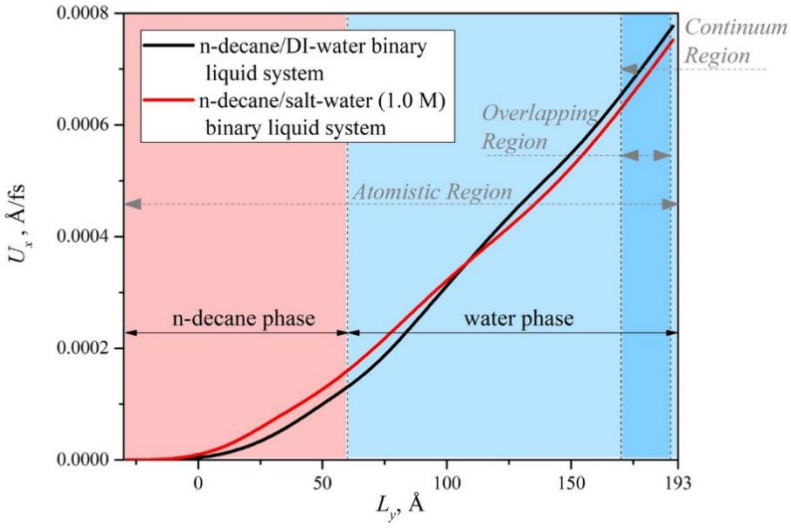

Figure 6.26 The comparison of velocity profiles in MD domain with hybrid CFD-MD coupling simulation method for both DI-water/n-decane/calcite system and salt-water (NaCl, 1.00 M) / n-decane / calcite system.

6.6 Conclusion

Motivated by the achievement of both computational efficiency and molecular-level accuracy, multiscale hybrid CFD-MD coupling simulation method was employed for the EOR applications in this chapter. The workflow contained three-fold: methodology implementation, validation, and application:

- Methodology implementation: The domain decomposition method was adopted by dividing the investigated system into three regions to realize the hybrid CFD-MD coupling simulation scheme, which were continuum region, atomistic region, and continuum-atomistic overlapping region. The coupling code was developed with C++ language based on the OpenFOAM platform by compiling the LAMMPS package to a callable library, where the continuum region was solved by Navier-Stokes equations with OpenFOAM package, while the atomistic region was solved by MD simulation based on the LAMMPS library. The constraint dynamics equations proposed by Nie et al. were applied in the overlapping region to ensure the consistency of each CFD and MD solutions.
- Methodology validation: Couette flow of LJ liquid argon was adopted as a benchmark case to investigate the velocity profiles with time evolutions to

verify this multiscale hybrid CFD-MD coupling scheme. The simulation result showed that multi-scale hybrid CFD-MD coupling simulation method is identical to the sudden started Couette flow with LJ liquid argon by comparing with its analytical solution.

- EOR applications: The multi-scale hybrid CFD-MD coupling simulation method was finally extended to five shear flow systems related to the EOR applications, which were water/calcite system, salt-water/calcite system, n-decane/calcite system, DI-water/n-decane/calcite system, and salt-water/n-decane/calcite system, respectively. It showed that the presence of salt could affect the relative mobility of oil/water flow, exhibiting a distinctive velocity profile near the substrate. By comparing with each corresponding full MD and CFD simulations, the hybrid CFD-MD simulation showed its advantages of both higher computational efficiency and better molecular-level accuracy on the solutions for EOR applications.

Chapter 7
Conclusion and Future Plan

This work conducted a multi-scale numerical study to explore fundamentally micro/nano-scale multiphase flow interactions, especially the wettability effect, to underpin future EOR applications. Three different approaches are used: i) CFD simulation of flooding process at the pore scale (micrometer range) with the identification of the governing parameters; ii) MD simulation of the interfacial properties and water/oil displacement at the nanoscale, with a particular focus on the salt influence on wettability variation, and iii) Multiscale CFD-MD coupling and simulation for different shear flows to achieve both higher computational efficiency and better molecular-level accuracy, as summarized below.

7.1 Pore-scale simulations of multiphase flow dynamics for chemical EOR applications

This part examined the effects of viscosity, interfacial tension and capillary number on the water/oil flow characteristics during the displacement process at the single pore scale by the VOF method in a pore-throat connecting channel.

- A flow regime was established revealing the different influences of viscosity and IFT, revealing that Capillary number alone is not the deciding factor for oil recovery
- The initial continuous oil phase would be snapped off into several discontinuous oil ganglia by water and trapped into the pore channel due to the dominance of capillary effect, which would cause a low oil recovery rate at the macro-scale.
- For water-wet pores, the snap-off phenomenon can be weakened by increasing the invading viscosity or decreasing the IFT respectively. Decreasing IFT mainly keeps oil phase staying continuously, while the increasing viscosity of invading fluid could enhance the confined fluid mobilization. Both are beneficial to enhanced oil recovery at the pore scale.
- Through increasing the invading viscosity and decreasing the IFT at the same time, the oil recovery factor would be efficiently enhanced by altering the flow regime from the snapped-off regime to the stable displacement condition.
- For water-wet pores, the same capillary number can lead to different flow regimes and oil recovery factors, due to the different effects from viscosity and IFT. For the pore geometry studied in this work, the snapped-off regime mainly can lead to a very small recovery factor; the transient flow can result in 2~5%

of oil recovery, and a one hundred percentage of recovery factor can be obtained with the stable flow at the single pore scale. When the IFT is decreased to an ultralow level, viscous fingering regime would happen in the pore channel though the injecting pressure can be reduced. A large capillary number would not always lead to a large recovery factor. A stable displacement process can be achieved by properly increasing the displacing viscosity and decreasing the IFT between oil and water. Ultralow oil/water interfacial tension is not necessarily due to the fingering possibility.

- Water-wet state has significantly positive effects on oil recovery at pore scale in oil saturated pores. Though the water-wet wettability can contribute to detach the oil phase from pore walls, the oil detachment from pore walls may not lead to the oil recovery enhancement due to the capillary effect. Decreasing IFT between oil and water alone, can enhance partial oil phase out of pore structures, but makes few effects on the oil detachment from pore walls;
- Both the wettability and capillary effect are significant for enhanced oil recovery. Only with both water-wettability alteration a low capillary effects, can an ideal EOR result be obtained. The simulation results in this work are consistent with previous experimental and MD simulation conclusions, and can present an explanation of the nanofluid, surfactant, and nanofluid-surfactant hybrid flooding flow mechanism regarding to wettability and IFT effects for enhanced oil recovery. Generally, only with both water-wet state and low capillary effects, can an ideal EOR result be obtained.

7.2.2 Atomistic-scale simulations of multicomponent interactions for low-salinity EOR applications

This part provides molecular level insight into salt-water/oil/vapor interactions and interfacial equilibrium properties, which offers hitherto un-accessed resolution for EOR applications by using atomistic MD simulation method.

- The interfacial tension of the water/vapor interface, n-decane/vapor and water/n-decane interfaces were calculated from the pressure tensor distribution after the simulations reached an equilibrated state, with values of 71.43, 20.54 and 65.33 mN/m, respectively. The calculated IFT values show a good agreement with previous experimental and simulation results.
- An optimal water salinity value was observed around 0.20 M for the equilibrated water/oil interface system which has the maximum interfacial thickness between water and oil phase, corresponding to the minimum

water/oil IFT value. An optimal water salinity condition at around 0.20 M was also predicted by investigating the equilibrium water/oil/vapor interface system with the maximum contact angle between the water and oil phase, contributing to the minimum salt water/oil IFT value, which is a condition beneficial for enhanced oil recovery.

- The effects of pore surface charge and water salinity on water/oil/minerals interactions (EMD simulation), and oil displacement in a calcite nanopore (NEMD simulation) have been analysed in the context of addressing the mechanism underpinning the alteration of surface wettability in carbonate rock reservoirs.
- At a water salinity of 0.50 M, the neutral calcite nanopore exhibits partially oil wet characteristics after equilibration with oil attaching and adsorbing onto the neutral surface. The charged calcite slit-pore caused a distribution of anion and cation through adsorption, in response to the electrostatic field, which altered the surface wettability to produce hydrophilic surfaces due to the hydration effect around the ions. In addition, an increase in water salinity did not affect significantly the oil wettability of the neutral calcite surface, and a random distribution of ions was maintained in the water phase.
- For the charged nano-slit pore, greater water salinity enhanced the mineral surface hydrophilicity by altering the surface from partially water wet to completely water wet. At a water salinity of 1.00 M, all n-decane molecules were completely detached from the charged mineral surface by the salt water shield layers.
- The non-equilibrium MD simulation results for the flooding process show that n-decane molecules tended to aggregate and transport as a cluster under the external flooding force. However, partial decane-wettability of calcite surfaces inhibited significantly the oil movement in the pore region.
- The combination of the effects of ion hydration and the electrostatic effect of ion adsorption on the charged surface led to a clear enhancement in oil transport, and hence indicated the potential for increased oil recovery in a calcite pore.

7.2.3 Multiscale hybrid continuum-atomistic coupling simulation: Implementation, validation, and EOR applications

This part developed and validated the CFD-MD coupling scheme to achieve both computational efficiency and molecular-level accuracy.

- Multiscale hybrid CFD-MD coupling simulation method is implemented by dividing the investigated system into three regions with domain decomposition method. The entire investigated system is divided into three regions, which are continuum region, atomistic region, and continuum-atomistic overlapping region, respectively. The coupling code has been developed with C++ language based on the OpenFOAM platform by compiling the LAMMPS package to a callable library. The continuum region is solved by Navier-Stokes equations with OpenFOAM package, while the atomistic region is solved by MD simulation based on the LAMMPS library. The constraint dynamics equations proposed by Nie et al. are applied in the overlapping region to ensure the consistency of each CFD and MD solutions.
- To verify this multiscale hybrid CFD-MD coupling scheme, the Couette flow of LJ liquid argon is adopted as a standard case to investigate the velocity profiles with time evolutions. The analytical solution of Couette flow is applied to compare with the solutions from hybrid CFD-MD coupling simulation.
- After the multi-scale hybrid CFD-MD coupling simulation method is identical to the verification case of impulse started Couette flow with LJ liquid argon, this methodology is extended to five shear flow systems related to the EOR applications, which are water/calcite system, salt-water/calcite system, n-decane/calcite system, DI-water/n-decane/calcite system, and salt-water/n-decane/calcite system, respectively. It revealed that the presence of salt could affect the relative mobility of oil/water flow, exhibiting a distinctive velocity profile near the substrate.
- Through comparing with each corresponding full MD and CFD simulations, the hybrid CFD-MD simulation shows its advantages of both higher computational efficiency and better molecular-level accuracy on the solutions for EOR applications.

7.3 Suggestions for Future Work

Since the successful application of multiscale hybrid CFD-MD coupling method on the fundamental EOR phenomenon analysis, future work is suggested to focus on further upscaling investigations of more complicated EOR systems by the medication of the current multiscale coupling scheme.

- The investigated EOR system can be enlarged to macro scale by further extending the CFD region, where multiscale coupling results can be directly compared with experimental observations.

- High pressure and high temperature conditions can be extended from the current analysis of the EOR systems;
- Multicomponent oil can be employed in the molecular-level description of the oil phase to replace the existing n-decane phase;
- Different types of salts can be further investigated to analyse the ionic strength effect of salts on the low-salinity effect, e.g. $MgCl_2$, $CaCl_2$.
- Multiphase flow dynamics model, e.g., VOF model, can be potentially applied to the calculation in the overlapping region of multiscale coupling simulation. The transient interface, rather more than the steady interface, can be further captured by this mean. Flux coupling will be required to realise this advanced coupling scheme. The USHER algorithm may be employed to insert the new solvent particles at locations where the transient interface has a time-dependent evolution. The heat transfer characteristics can also be considered by solving the additional energy equations.
- The multiscale coupling methodology has more potential applications in spite of EOR. It also shows its advances in multiscale insight investigations of other industries, e.g. shale gas recovery industry, aerodynamics industry, etc.

References

Afkhami, S., Zaleski, S. and Bussmann, M. 2009. A mesh-dependent model for applying dynamic contact angles to VOF simulations. *Journal of computational physics.* **228**(15), pp.5370-5389.

Afsharpoor, A., Balhoff, M.T., Bonnecaze, R. and Huh, C. 2012. CFD modeling of the effect of polymer elasticity on residual oil saturation at the pore-scale. *Journal of Petroleum Science and Engineering.* **94**, pp.79-88.

Aker, E., Måløy, K.J. and Hansen, A. 2000a. Viscous stabilization of 2D drainage displacements with trapping. *Physical review letters.* **84**(20), p4589.

Aker, E., Måløy, K.J., Hansen, A. and Basak, S. 2000b. Burst dynamics during drainage displacements in porous media: Simulations and experiments. *EPL (Europhysics Letters).* **51**(1), p55.

Al-Anssari, S., Barifcani, A., Wang, S., Maxim, L. and Iglauer, S. 2016. Wettability alteration of oil-wet carbonate by silica nanofluid. *Journal of colloid and interface science.* **461**, pp.435-442.

Al-Gharbi, M.S. and Blunt, M.J. 2003. A 2D Dynamic pore network model for modeling primary drainage. In: *Proceedings of the ESF Workshop on Multiphase Flow in Porous Media, Delft*.

Al-Gharbi, M.S.H. 2004. *Dynamic pore-scale modelling of two-phase flow*. thesis, University of London.

Al Shalabi, E.W., Sepehrnoori, K. and Delshad, M. 2014. Mechanisms behind low salinity water injection in carbonate reservoirs. *Fuel.* **121**, pp.11-19.

Allen, M. and Tildesley, D. 1987. Molecular Simulation of Liquids. *Clarendon, Oxford.*

Alotaibi, M.B. and Nasr-El-Din, H.A. 2009. Salinity of injection water and its impact on oil recovery. In: *EUROPEC/EAGE conference and exhibition*: Society of Petroleum Engineers.

Andrew, M., Bijeljic, B. and Blunt, M.J. 2014. Pore-by-pore capillary pressure measurements using X-ray microtomography at reservoir conditions: Curvature, snap-off, and remobilization of residual CO2. *Water Resources Research.* **50**(11), pp.8760-8774.

Ansys, C. 2006. Solver theory guide. *Ansys CFX Release.* **11**, pp.1996-2006.

Arns, C.H., Knackstedt, M.A., Pinczewski, W.V. and Garboczi, E.J. 2002. Computation of linear elastic properties from microtomographic images: Methodology and agreement between theory and experiment. *Geophysics.* **67**(5), pp.1396-1405.

Arriola, A., Willhite, G.P. and Green, D.W. 1983. Trapping of oil drops in a noncircular pore throat and mobilization upon contact with a surfactant. *Society of Petroleum Engineers Journal.* **23**(01), pp.99-114.

Austad, T., Shariatpanahi, S., Strand, S., Black, C. and Webb, K. 2011. Conditions for a low-salinity enhanced oil recovery (EOR) effect in carbonate oil reservoirs. *Energy & fuels.* **26**(1), pp.569-575.

Aveyard, R. and Saleem, S.M. 1976. Interfacial tensions at alkane-aqueous electrolyte interfaces. *Journal of the Chemical Society, Faraday Transactions 1: Physical Chemistry in Condensed Phases.* **72**, pp.1609-1617.

Ayatollahi, S. and Zerafat, M.M. 2012. Nanotechnology-assisted EOR techniques: New solutions to old challenges. In: *SPE international oilfield nanotechnology conference and exhibition*: Society of Petroleum Engineers.

Badakshan, A. and Bakes, P. 1990. The influence of temperature and surfactant concentration on interfacial tension of saline water and hydrocarbon systems in relation to enhanced oil recovery by chemical flooding.
Bandara, U., Tartakovsky, A.M., Oostrom, M., Palmer, B.J., Grate, J. and Zhang, C. 2013. Smoothed particle hydrodynamics pore-scale simulations of unstable immiscible flow in porous media. *Advances in water resources.* **62**, pp.356-369.
Bandara, U.C., Tartakovsky, A.M. and Palmer, B.J. 2011. Pore-scale study of capillary trapping mechanism during CO2 injection in geological formations. *International Journal of Greenhouse Gas Control.* **5**(6), pp.1566-1577.
Bankura, A., Carnevale, V. and Klein, M.L. 2013. Hydration structure of salt solutions from ab initio molecular dynamics. *The Journal of chemical physics.* **138**(1), p014501.
Barnaji, M.J., Pourafshary, P. and Rasaie, M.R. 2016. Visual investigation of the effects of clay minerals on enhancement of oil recovery by low salinity water flooding. *Fuel.* **184**, pp.826-835.
Berendsen, H., Grigera, J. and Straatsma, T. 1987. The missing term in effective pair potentials. *Journal of Physical Chemistry.* **91**(24), pp.6269-6271.
Beresnev, I.A. and Deng, W. 2010. Theory of breakup of core fluids surrounded by a wetting annulus in sinusoidally constricted capillary channels. *Physics of Fluids.* **22**(1), p012105.
Berg, S., Ott, H., Klapp, S.A., Schwing, A., Neiteler, R., Brussee, N., Makurat, A., Leu, L., Enzmann, F. and Schwarz, J.-O. 2013. Real-time 3D imaging of Haines jumps in porous media flow. *Proceedings of the National Academy of Sciences.* **110**(10), pp.3755-3759.
Blunt, M.J., Bijeljic, B., Dong, H., Gharbi, O., Iglauer, S., Mostaghimi, P., Paluszny, A. and Pentland, C. 2013. Pore-scale imaging and modelling. *Advances in Water Resources.* **51**, pp.197-216.
Blunt, M.J., Jackson, M.D., Piri, M. and Valvatne, P.H. 2002. Detailed physics, predictive capabilities and macroscopic consequences for pore-network models of multiphase flow. *Advances in Water Resources.* **25**(8-12), pp.1069-1089.
Borg, M.K., Macpherson, G.B. and Reese, J.M. 2010. Controllers for imposing continuum-to-molecular boundary conditions in arbitrary fluid flow geometries. *Molecular Simulation.* **36**(10), pp.745-757.
Brackbill, J., Kothe, D.B. and Zemach, C. 1992. A continuum method for modeling surface tension. *Journal of computational physics.* **100**(2), pp.335-354.
Bresme, F., Chacón, E., Tarazona, P. and Tay, K. 2008. Intrinsic structure of hydrophobic surfaces: The oil-water interface. *Physical review letters.* **101**(5), p056102.
Brown, M.A., D'Auria, R., Kuo, I.-F.W., Krisch, M.J., Starr, D.E., Bluhm, H., Tobias, D.J. and Hemminger, J.C. 2008. Ion spatial distributions at the liquid–vapor interface of aqueous potassium fluoride solutions. *Physical Chemistry Chemical Physics.* **10**(32), pp.4778-4784.
Bruneval, F., Donadio, D. and Parrinello, M. 2007. Molecular dynamics study of the solvation of calcium carbonate in water. *The Journal of Physical Chemistry B.* **111**(42), pp.12219-12227.
Buckley, S.E. and Leverett, M. 1942. Mechanism of fluid displacement in sands. *Transactions of the AIME.* **146**(01), pp.107-116.
Cai, B.-Y., Yang, J.-T. and Guo, T.-M. 1996. Interfacial tension of hydrocarbon+ water/brine systems under high pressure. *Journal of chemical & engineering data.* **41**(3), pp.493-496.

Chang, H.-Y., Li, X., Li, H. and Karniadakis, G.E. 2016. MD/DPD multiscale framework for predicting morphology and stresses of red blood cells in health and disease. *PLoS computational biology.* **12**(10), pe1005173.
Chen, Y., Xie, Q., Sari, A., Brady, P.V. and Saeedi, A. 2018. Oil/water/rock wettability: Influencing factors and implications for low salinity water flooding in carbonate reservoirs. *Fuel.* **215**, pp.171-177.
Clemens, T., Tsikouris, K., Buchgraber, M., Castanier, L.M. and Kovscek, A. 2013. Pore-Scale Evaluation of Polymers Displacing Viscous Oil--Computational-Fluid-Dynamics Simulation of Micromodel Experiments. *Spe Reservoir Evaluation & Engineering.* **16**(02), pp.144-154.
Coles, M., Hazlett, R., Spanne, P., Soll, W., Muegge, E. and Jones, K. 1998. Pore level imaging of fluid transport using synchrotron X-ray microtomography. *Journal of Petroleum Science and Engineering.* **19**(1-2), pp.55-63.
Cooke, D.J., Gray, R.J., Sand, K.K., Stipp, S.L.S. and Elliott, J. 2010. Interaction of ethanol and water with the {1014} surface of calcite. *Langmuir.* **26**(18), pp.14520-14529.
Cosden, I.A. and Lukes, J.R. 2013. A hybrid atomistic–continuum model for fluid flow using LAMMPS and OpenFOAM. *Computer Physics Communications.* **184**(8), pp.1958-1965.
D'Auria, R. and Tobias, D.J. 2009. Relation between Surface Tension and Ion Adsorption at the Air− Water Interface: A Molecular Dynamics Simulation Study. *The Journal of Physical Chemistry A.* **113**(26), pp.7286-7293.
de Leeuw, N. and Parker, S. 1997. Atomistic simulation of the effect of molecular adsorption of water on the surface structure and energies of calcite surfaces. *Journal of the Chemical Society, Faraday Transactions.* **93**(3), pp.467-475.
De Leeuw, N. and Parker, S. 2000. Modeling absorption and segregation of magnesium and cadmium ions to calcite surfaces: Introducing MgCO 3 and CdCO 3 potential models. *The Journal of Chemical Physics.* **112**(9), pp.4326-4333.
De Leeuw, N., Parker, S. and Harding, J. 1999. Molecular dynamics simulation of crystal dissolution from calcite steps. *Physical Review B.* **60**(19), p13792.
De Leeuw, N., Parker, S. and Rao, K.H. 1998. Modeling the competitive adsorption of water and methanoic acid on calcite and fluorite surfaces. *Langmuir.* **14**(20), pp.5900-5906.
de Leeuw, N.H. and Parker, S.C. 1998. Surface structure and morphology of calcium carbonate polymorphs calcite, aragonite, and vaterite: an atomistic approach. *The Journal of Physical Chemistry B.* **102**(16), pp.2914-2922.
De Serio, M., Mohapatra, H., Zenobi, R. and Deckert, V. 2006. Investigation of the liquid–liquid interface with high spatial resolution using near-field Raman spectroscopy. *Chemical physics letters.* **417**(4-6), pp.452-456.
Deng, W. 2010. Quantitative aspects of vibratory mobilization and break-up of non-wetting fluids in porous media.
Deng, W., Balhoff, M. and Cardenas, M.B. 2015. Influence of dynamic factors on nonwetting fluid snap-off in pores. *Water Resources Research.* **51**(11), pp.9182-9189.
Deng, W., Cardenas, M.B. and Bennett, P.C. 2014. Extended Roof snap-off for a continuous nonwetting fluid and an example case for supercritical CO2. *Advances in water resources.* **64**, pp.34-46.
Doscher, T. and Wise, F. 1976. Enhanced crude oil recovery potential-an estimate. *Journal of Petroleum Technology.* **28**(05), pp.575-585.

Dove, M., Hagen, M., Harris, M., Powell, B., Steigenberger, U. and Winkler, B. 1992. Anomalous inelastic neutron scattering from calcite. *Journal of Physics: Condensed Matter.* **4**(11), p2761.
Dove, M.T., Winkler, B., Leslie, M., Harris, M.J. and Salje, E.K. 1992. A new interatomic potential model for calcite; applications to lattice dynamics studies, phase transition, and isotope fractionation. *American Mineralogist.* **77**(3-4), pp.244-250.
Du, Q., Freysz, E. and Shen, Y.R. 1994. Surface vibrational spectroscopic studies of hydrogen bonding and hydrophobicity. *Science.* **264**(5160), pp.826-828.
Dunsmuir, J.H., Ferguson, S., D'Amico, K. and Stokes, J. 1991. X-ray microtomography: a new tool for the characterization of porous media. In: *SPE annual technical conference and exhibition*: Society of Petroleum Engineers.
Ershadi, M., Alaei, M., Rashidi, A., Ramazani, A. and Khosravani, S. 2015. Carbonate and sandstone reservoirs wettability improvement without using surfactants for Chemical Enhanced Oil Recovery (C-EOR). *Fuel.* **153**, pp.408-415.
Esfandyari Bayat, A., Junin, R., Samsuri, A., Piroozian, A. and Hokmabadi, M. 2014. Impact of metal oxide nanoparticles on enhanced oil recovery from limestone media at several temperatures. *Energy & Fuels.* **28**(10), pp.6255-6266.
Fatt, I. 1956. The network model of porous media. 3. Dynamic properties of networks with tube radius distribution. *Transactions of the American institute of mining and metallurgical engineers.* **207**(7), pp.164-181.
Fattah Hesary, K. 2017. Hybrid Atomistic–Continuum Simulation Methodology for Handling Nanoparticle-Wall Interaction.
Fenter, P., Geissbühler, P., DiMasi, E., Srajer, G., Sorensen, L. and Sturchio, N. 2000. Surface speciation of calcite observed in situ by high-resolution X-ray reflectivity. *Geochimica et Cosmochimica Acta.* **64**(7), pp.1221-1228.
Fenter, P., Kerisit, S., Raiteri, P. and Gale, J.D. 2013. Is the calcite–water interface understood? Direct comparisons of molecular dynamics simulations with specular X-ray reflectivity data. *The Journal of Physical Chemistry C.* **117**(10), pp.5028-5042.
Ferrari, A. and Lunati, I. 2013. Direct numerical simulations of interface dynamics to link capillary pressure and total surface energy. *Advances in water resources.* **57**, pp.19-31.
Fisler, D.K., Gale, J.D. and Cygan, R.T. 2000. A shell model for the simulation of rhombohedral carbonate minerals and their point defects. *American Mineralogist.* **85**(1), pp.217-224.
Flekkøy, E., Wagner, G. and Feder, J. 2000. Hybrid model for combined particle and continuum dynamics. *EPL (Europhysics Letters).* **52**(3), p271.
Fluent, A. 2009. 12.0 Theory Guide. *Ansys Inc.* **5**(5).
Freeman, C.L., Asteriadis, I., Yang, M. and Harding, J.H. 2009. Interactions of organic molecules with calcite and magnesite surfaces. *The Journal of Physical Chemistry C.* **113**(9), pp.3666-3673.
Freeman, C.L., Harding, J.H., Cooke, D.J., Elliott, J.A., Lardge, J.S. and Duffy, D.M. 2007. New forcefields for modeling biomineralization processes. *The Journal of Physical Chemistry C.* **111**(32), pp.11943-11951.
Fukai, J., Shiiba, Y., Yamamoto, T., Miyatake, O., Poulikakos, D., Megaridis, C. and Zhao, Z. 1995. Wetting effects on the spreading of a liquid droplet colliding with a flat surface: experiment and modeling. *Physics of Fluids.* **7**(2), pp.236-247.

Geissbühler, P., Fenter, P., DiMasi, E., Srajer, G., Sorensen, L. and Sturchio, N. 2004. Three-dimensional structure of the calcite–water interface by surface X-ray scattering. *Surface Science.* **573**(2), pp.191-203.
Ghanbari, E. and Dehghanpour, H. 2015. Impact of rock fabric on water imbibition and salt diffusion in gas shales. *International Journal of Coal Geology.* **138**, pp.55-67.
Goldstein, H. 2011. *Classical mechanics.* Pearson Education India.
Goniva, C., Kloss, C. and Pirker, S. 2009. Towards fast parallel CFD-DEM: An open-source perspective. In: *Open Source CFD International Conference*.
Gou, S., Luo, S., Liu, T., Xia, H., Jing, D., Zhang, Q., Li, S., Li, Z. and Guo, Q. 2015. Thermally stable imidazoline-based sulfonate copolymers for enhanced oil recovery. *RSC advances.* **5**(104), pp.85165-85173.
Hadjiconstantinou, N.G. 1999. Hybrid atomistic–continuum formulations and the moving contact-line problem. *Journal of Computational Physics.* **154**(2), pp.245-265.
Hadjiconstantinou, N.G. and Patera, A.T. 1997. Heterogeneous atomistic-continuum representations for dense fluid systems. *International Journal of Modern Physics C.* **8**(04), pp.967-976.
He, X. and Luo, L.-S. 1997. Lattice Boltzmann model for the incompressible Navier–Stokes equation. *Journal of statistical Physics.* **88**(3-4), pp.927-944.
Hendraningrat, L., Li, S. and Torsæter, O. 2013. A coreflood investigation of nanofluid enhanced oil recovery. *Journal of Petroleum Science and Engineering.* **111**, pp.128-138.
Hess, B., Kutzner, C., Van Der Spoel, D. and Lindahl, E. 2008. GROMACS 4: algorithms for highly efficient, load-balanced, and scalable molecular simulation. *Journal of chemical theory and computation.* **4**(3), pp.435-447.
Hilner, E., Andersson, M.P., Hassenkam, T., Matthiesen, J., Salino, P. and Stipp, S.L.S. 2015. The effect of ionic strength on oil adhesion in sandstone–the search for the low salinity mechanism. *Scientific reports.* **5**, p9933.
Hirt, C.W. and Nichols, B.D. 1981. Volume of fluid (VOF) method for the dynamics of free boundaries. *Journal of computational physics.* **39**(1), pp.201-225.
Horgue, P., Augier, F., Duru, P., Prat, M. and Quintard, M. 2013. Experimental and numerical study of two-phase flows in arrays of cylinders. *Chemical Engineering Science.* **102**, pp.335-345.
Hu, Z., Zhao, J., Gao, H., Nourafkan, E. and Wen, D. 2017. Transport and deposition of carbon nanoparticles in saturated porous media. *Energies.* **10**(8), p1151.
Humphrey, W., Dalke, A. and Schulten, K. 1996. VMD: visual molecular dynamics. *Journal of molecular graphics.* **14**(1), pp.33-38.
Hunt, P.K., Engler, P. and Bajsarowicz, C. 1988. Computed tomography as a core analysis tool: Applications, instrument evaluation, and image improvement techniques. *Journal of Petroleum Technology.* **40**(09), pp.1,203-201,210.
Ikeda, N., Aratono, M. and Motomura, K. 1992. Thermodynamic study on the adsorption of sodium chloride at the water/hexane interface. *Journal of colloid and interface science.* **149**(1), pp.208-215.
Irving, J. and Kirkwood, J.G. 1950. The statistical mechanical theory of transport processes. IV. The equations of hydrodynamics. *The Journal of chemical physics.* **18**(6), pp.817-829.
Jackson, M.D., Al-Mahrouqi, D. and Vinogradov, J. 2016. Zeta potential in oil-water-carbonate systems and its impact on oil recovery during controlled salinity water-flooding. *Scientific reports.* **6**, p37363.

Jackson, R. and Price, G. 1992. A transferable interatomic potential for calcium carbonate. *Molecular simulation.* **9**(2), pp.175-177.
Jacobsen, N.G., Fuhrman, D.R. and Fredsøe, J. 2012. A wave generation toolbox for the open-source CFD library: OpenFoam®. *International Journal for Numerical Methods in Fluids.* **70**(9), pp.1073-1088.
Jadhunandan, P.P. 1990. *Effects of brine composition, crude oil, and aging conditions on wettability and oil recovery*. thesis, Department of Petroleum Engineering, New Mexico Institute of Mining & Technology.
Jang, S.S., Lin, S.-T., Maiti, P.K., Blanco, M., Goddard, W.A., Shuler, P. and Tang, Y. 2004. Molecular dynamics study of a surfactant-mediated decane−water interface: effect of molecular architecture of alkyl benzene sulfonate. *The Journal of Physical Chemistry B.* **108**(32), pp.12130-12140.
Joekar Niasar, V., Hassanizadeh, S., Pyrak-Nolte, L. and Berentsen, C. 2009. Simulating drainage and imbibition experiments in a high-porosity micromodel using an unstructured pore network model. *Water resources research.* **45**(2).
Jorgensen, W.L. and Tirado-Rives, J. 1988. The OPLS [optimized potentials for liquid simulations] potential functions for proteins, energy minimizations for crystals of cyclic peptides and crambin. *Journal of the American Chemical Society.* **110**(6), pp.1657-1666.
Jungwirth, P. and Tobias, D.J. 2006. Specific ion effects at the air/water interface. *Chemical reviews.* **106**(4), pp.1259-1281.
Kerisit, S., Cooke, D.J., Spagnoli, D. and Parker, S.C. 2005. Molecular dynamics simulations of the interactions between water and inorganic solids. *Journal of Materials Chemistry.* **15**(14), pp.1454-1462.
Kerisit, S. and Parker, S.C. 2004. Free energy of adsorption of water and metal ions on the {1014} calcite surface. *Journal of the American Chemical Society.* **126**(32), pp.10152-10161.
Kerisit, S., Parker, S.C. and Harding, J.H. 2003. Atomistic simulation of the dissociative adsorption of water on calcite surfaces. *The Journal of Physical Chemistry B.* **107**(31), pp.7676-7682.
Khusainova, A., Nielsen, S.M., Pedersen, H.H., Woodley, J.M. and Shapiro, A. 2015. Study of wettability of calcite surfaces using oil–brine–enzyme systems for enhanced oil recovery applications. *Journal of Petroleum Science and Engineering.* **127**, pp.53-64.
Kiss, É., Pintér, J. and Wolfram, E. 1982. Dynamics of oil/water displacement in capillary tubes with periodically varying diameter. *Colloid and Polymer Science.* **260**(8), pp.808-810.
Kondiparty, K., Nikolov, A., Wu, S. and Wasan, D. 2011. Wetting and spreading of nanofluids on solid surfaces driven by the structural disjoining pressure: statics analysis and experiments. *Langmuir.* **27**(7), pp.3324-3335.
Kumar, M., Knackstedt, M.A., Senden, T.J., Sheppard, A.P. and Middleton, J.P. 2010. Visualizing and quantifying the residual phase distribution in core material. *Petrophysics.* **51**(05).
Kunieda, M. 2012. Molecular Dynamics Study of Oil-Water Interfacial Equilibrium in Petroleum Engineering.
Kunieda, M., Liang, Y., Fukunaka, Y., Matsuoka, T., Takamura, K., Loahardjo, N., Winoto, W. and Morrow, N.R. 2012. Spreading of multi-component oils on water. *Energy & Fuels.* **26**(5), pp.2736-2741.
Lashkarbolooki, M., Riazi, M., Ayatollahi, S. and Hezave, A.Z. 2016. Synergy effects of ions, resin, and asphaltene on interfacial tension of acidic crude oil and low–high salinity brines. *Fuel.* **165**, pp.75-85.

Lerdahl, T.R., Oren, P.-E. and Bakke, S. 2000. A predictive network model for three-phase flow in porous media. In: *SPE/DOE Improved Oil Recovery Symposium*: Society of Petroleum Engineers.
Li, J., Liao, D. and Yip, S. 1998. Coupling continuum to molecular-dynamics simulation: Reflecting particle method and the field estimator. *Physical Review E.* **57**(6), p7259.
Liu, J., Chen, S., Nie, X. and Robbins, M.O. 2007. A continuum–atomistic simulation of heat transfer in micro-and nano-flows. *Journal of Computational Physics.* **227**(1), pp.279-291.
Lv, M. and Wang, S. 2015. Pore-scale modeling of a water/oil two-phase flow in hot water flooding for enhanced oil recovery. *RSC Advances.* **5**(104), pp.85373-85382.
Madonna, C., Quintal, B., Frehner, M., Almqvist, B.S., Tisato, N., Pistone, M., Marone, F. and Saenger, E.H. 2013. Synchrotron-based X-ray tomographic microscopy for rock physics investigationsSynchrotron-based rock images. *Geophysics.* **78**(1), pp.D53-D64.
Mahani, H., Keya, A.L., Berg, S., Bartels, W.-B., Nasralla, R. and Rossen, W.R. 2015. Insights into the mechanism of wettability alteration by low-salinity flooding (LSF) in carbonates. *Energy & Fuels.* **29**(3), pp.1352-1367.
Martínez, L., Andrade, R., Birgin, E.G. and Martínez, J.M. 2009. PACKMOL: a package for building initial configurations for molecular dynamics simulations. *Journal of computational chemistry.* **30**(13), pp.2157-2164.
McMillan, M.D., Rahnema, H., Romiluy, J. and Kitty, F.J. 2016. Effect of exposure time and crude oil composition on low-salinity water flooding. *Fuel.* **185**, pp.263-272.
Meakin, P. and Tartakovsky, A.M. 2009. Modeling and simulation of pore-scale multiphase fluid flow and reactive transport in fractured and porous media. *Reviews of Geophysics.* **47**(3).
Michaud-Agrawal, N., Denning, E.J., Woolf, T.B. and Beckstein, O. 2011. MDAnalysis: a toolkit for the analysis of molecular dynamics simulations. *Journal of computational chemistry.* **32**(10), pp.2319-2327.
Mitrinović, D.M., Tikhonov, A.M., Li, M., Huang, Z. and Schlossman, M.L. 2000. Noncapillary-wave structure at the water-alkane interface. *Physical review letters.* **85**(3), p582.
Module, F. 2011. Material Studio 6.0. *Accelrys Inc., San Diego, CA.*
Momma, K. and Izumi, F. 2008. VESTA: a three-dimensional visualization system for electronic and structural analysis. *Journal of Applied Crystallography.* **41**(3), pp.653-658.
Monaghan, J.J. 1994. Simulating free surface flows with SPH. *Journal of computational physics.* **110**(2), pp.399-406.
Morrow, N. and Buckley, J. 2011. Improved oil recovery by low-salinity waterflooding. *Journal of Petroleum Technology.* **63**(05), pp.106-112.
Muskat, M. 1953. Oil recovery—100 per cent? *Industrial & Engineering Chemistry.* **45**(7), pp.1401-1405.
Myint, P.C. and Firoozabadi, A. 2015. Thin liquid films in improved oil recovery from low-salinity brine. *Current Opinion in Colloid & Interface Science.* **20**(2), pp.105-114.
Nasralla, R.A., Bataweel, M.A. and Nasr-El-Din, H.A. 2013. Investigation of wettability alteration and oil-recovery improvement by low-salinity water in sandstone rock. *Journal of Canadian Petroleum Technology.* **52**(02), pp.144-154.

Nasralla, R.A. and Nasr-El-Din, H.A. 2014. Double-layer expansion: is it a primary mechanism of improved oil recovery by low-salinity waterflooding? *SPE Reservoir Evaluation & Engineering.* **17**(01), pp.49-59.
Neumann, P., Flohr, H., Arora, R., Jarmatz, P., Tchipev, N. and Bungartz, H.-J. 2016. MaMiCo: Software design for parallel molecular-continuum flow simulations. *Computer Physics Communications.* **200**, pp.324-335.
Nicolini, J.V., Ferraz, H.C. and Borges, C.P. 2017. Effect of seawater ionic composition modified by nanofiltration on enhanced oil recovery in Berea sandstone. *Fuel.* **203**, pp.222-232.
Nie, X., Chen, S. and Robbins, M.O. 2004. A continuum and molecular dynamics hybrid method for micro-and nano-fluid flow. *Journal of Fluid Mechanics.* **500**, pp.55-64.
Noh, W.F. and Woodward, P. 1976. SLIC (simple line interface calculation). In: *Proceedings of the fifth international conference on numerical methods in fluid dynamics June 28–July 2, 1976 Twente University, Enschede*: Springer, pp.330-340.
O'connell, S.T. and Thompson, P.A. 1995. Molecular dynamics–continuum hybrid computations: a tool for studying complex fluid flows. *Physical Review E.* **52**(6), pR5792.
Olajire, A.A. 2014. Review of ASP EOR (alkaline surfactant polymer enhanced oil recovery) technology in the petroleum industry: Prospects and challenges. *Energy.* **77**, pp.963-982.
Otomo, H., Fan, H., Hazlett, R., Li, Y., Staroselsky, I., Zhang, R. and Chen, H. 2015. Simulation of residual oil displacement in a sinusoidal channel with the lattice Boltzmann method. *Comptes Rendus Mécanique.* **343**(10-11), pp.559-570.
Pak, T., Butler, I., Geiger, S., van Dijke, M.I., Jiang, Z., Elphick, S. and Sorbie, K.S. 2013. Pore-Scale Visualisation of Two-Phase Fluid Displacement Processes in a Carbonate Rock using X-ray micro-TomographyTechnique. In: *SPE Reservoir Characterization and Simulation Conference and Exhibition*: Society of Petroleum Engineers.
Pavese, A., Catti, M., Parker, S. and Wall, A. 1996. Modelling of the thermal dependence of structural and elastic properties of calcite, CaCO 3. *Physics and chemistry of minerals.* **23**(2), pp.89-93.
Pavese, A., Catti, M., Price, G. and Jackson, R. 1992. Interatomic potentials for CaCO 3 polymorphs (calcite and aragonite), fitted to elastic and vibrational data. *Physics and chemistry of minerals.* **19**(2), pp.80-87.
Peng, B., Zhang, L., Luo, J., Wang, P., Ding, B., Zeng, M. and Cheng, Z. 2017. A review of nanomaterials for nanofluid enhanced oil recovery. *RSC Advances.* **7**(51), pp.32246-32254.
Pereira, J.F., Costa, R., Foios, N. and Coutinho, J.A. 2014. Ionic liquid enhanced oil recovery in sand-pack columns. *Fuel.* **134**, pp.196-200.
Plimpton, S., Crozier, P. and Thompson, A. 2007. LAMMPS-large-scale atomic/molecular massively parallel simulator. *Sandia National Laboratories.* **18**, p43.
Porter, M.L., Schaap, M.G. and Wildenschild, D. 2009. Lattice-Boltzmann simulations of the capillary pressure–saturation–interfacial area relationship for porous media. *Advances in Water Resources.* **32**(11), pp.1632-1640.
Puntervold, T., Strand, S., Ellouz, R. and Austad, T. 2015. Modified seawater as a smart EOR fluid in chalk. *Journal of Petroleum Science and Engineering.* **133**, pp.440-443.

Raeini, A.Q., Bijeljic, B. and Blunt, M.J. 2015. Modelling capillary trapping using finite-volume simulation of two-phase flow directly on micro-CT images. *Advances in water resources.* **83**, pp.102-110.
Rahman, A. 1964. Correlations in the motion of atoms in liquid argon. *Physical Review.* **136**(2A), pA405.
Raiteri, P., Gale, J.D., Quigley, D. and Rodger, P.M. 2010. Derivation of an accurate force-field for simulating the growth of calcium carbonate from aqueous solution: a new model for the calcite− water interface. *The Journal of Physical Chemistry C.* **114**(13), pp.5997-6010.
Ransohoff, T., Gauglitz, P. and Radke, C. 1987. Snap-off of gas bubbles in smoothly constricted noncircular capillaries. *AIChE Journal.* **33**(5), pp.753-765.
Ransohoff, T. and Radke, C. 1988. Laminar flow of a wetting liquid along the corners of a predominantly gas-occupied noncircular pore. *Journal of colloid and interface science.* **121**(2), pp.392-401.
Ranut, P., Nobile, E. and Mancini, L. 2014. High resolution microtomography-based CFD simulation of flow and heat transfer in aluminum metal foams. *Applied thermal engineering.* **69**(1-2), pp.230-240.
Ren, X.-G., Wang, Q., Xu, L.-Y., Yang, W.-J. and Xu, X.-H. 2017. HACPar: An efficient parallel multiscale framework for hybrid atomistic–continuum simulation at the micro-and nanoscale. *Advances in Mechanical Engineering.* **9**(8), p1687814017714730.
RezaeiDoust, A., Puntervold, T. and Austad, T. 2011. Chemical verification of the EOR mechanism by using low saline/smart water in sandstone. *Energy & Fuels.* **25**(5), pp.2151-2162.
Rohl, A.L., Wright, K. and Gale, J.D. 2003. Evidence from surface phonons for the (2× 1) reconstruction of the (1014) surface of calcite from computer simulation. *American Mineralogist.* **88**(5-6), pp.921-925.
Roof, J. 1970. Snap-off of oil droplets in water-wet pores. *Society of Petroleum Engineers Journal.* **10**(01), pp.85-90.
Sakthivel, S., Velusamy, S., Nair, V.C., Sharma, T. and Sangwai, J.S. 2017. Interfacial tension of crude oil-water system with imidazolium and lactam-based ionic liquids and their evaluation for enhanced oil recovery under high saline environment. *Fuel.* **191**, pp.239-250.
Scatena, L., Brown, M. and Richmond, G. 2001. Water at hydrophobic surfaces: weak hydrogen bonding and strong orientation effects. *Science.* **292**(5518), pp.908-912.
Schaap, M.G., Porter, M.L., Christensen, B.S. and Wildenschild, D. 2007. Comparison of pressure-saturation characteristics derived from computed tomography and lattice Boltzmann simulations. *Water Resources Research.* **43**(12).
Sefiane, K., Skilling, J. and MacGillivray, J. 2008. Contact line motion and dynamic wetting of nanofluid solutions. *Advances in colloid and interface science.* **138**(2), pp.101-120.
Serrano-Saldaña, E., Domínguez-Ortiz, A., Pérez-Aguilar, H., Kornhauser-Strauss, I. and Rojas-González, F. 2004. Wettability of solid/brine/n-dodecane systems: experimental study of the effects of ionic strength and surfactant concentration. *Colloids and Surfaces A: Physicochemical and Engineering Aspects.* **241**(1-3), pp.343-349.
Setiawan, A., Suekane, T., Deguchi, Y. and Kusano, K. 2014. Three-dimensional imaging of pore-scale water flooding phenomena in water-wet and oil-wet porous media. *Journal of Flow Control, Measurement & Visualization.* **2**(02), p25.

Shan, X. and Chen, H. 1993. Lattice Boltzmann model for simulating flows with multiple phases and components. *Physical Review E.* **47**(3), p1815.
Shariatpanahi, S., Hopkins, P., Aksulu, H., Strand, S., Puntervold, T. and Austad, T. 2016. Water based EOR by wettability alteration in dolomite. *Energy & Fuels.* **30**(1), pp.180-187.
Shariatpanahi, S.F., Strand, S. and Austad, T. 2010. Evaluation of water-based enhanced oil recovery (EOR) by wettability alteration in a low-permeable fractured limestone oil reservoir. *Energy & Fuels.* **24**(11), pp.5997-6008.
Sheng, J. 2014. Critical review of low-salinity waterflooding. *Journal of Petroleum Science and Engineering.* **120**, pp.216-224.
Smith, E. 2014. On the coupling of molecular dynamics to continuum computational fluid dynamics.
Smith, W., Yong, C. and Rodger, P. 2002. DL_POLY: Application to molecular simulation. *Molecular Simulation.* **28**(5), pp.385-471.
Spagnoli, D., Cooke, D.J., Kerisit, S. and Parker, S.C. 2006a. Molecular dynamics simulations of the interaction between the surfaces of polar solids and aqueous solutions. *Journal of Materials Chemistry.* **16**(20), pp.1997-2006.
Spagnoli, D., Kerisit, S. and Parker, S.C. 2006b. Atomistic simulation of the free energies of dissolution of ions from flat and stepped calcite surfaces. *Journal of crystal growth.* **294**(1), pp.103-110.
Sun, J., He, Y.L. and Tao, W.Q. 2010. Scale effect on flow and thermal boundaries in micro-/nano-channel flow using molecular dynamics–continuum hybrid simulation method. *International journal for numerical methods in engineering.* **81**(2), pp.207-228.
Sun, L., Li, X., Hede, T., Tu, Y., Leck, C. and Ågren, H. 2012. Molecular dynamics simulations of the surface tension and structure of salt solutions and clusters. *The Journal of Physical Chemistry B.* **116**(10), pp.3198-3204.
Tartakovsky, A. and Meakin, P. 2005. Modeling of surface tension and contact angles with smoothed particle hydrodynamics. *Physical Review E.* **72**(2), p026301.
Thackeray, D.J. and Siders, P.D. 1998. Molecular-orbital and empirical-potential descriptions of CaCO 3. *Journal of the Chemical Society, Faraday Transactions.* **94**(18), pp.2653-2661.
Tiab, D. and Donaldson, E.C. 2015. *Petrophysics: theory and practice of measuring reservoir rock and fluid transport properties.* Gulf professional publishing.
Tian, H. and Wang, M. 2018. Electrokinetic mechanism of wettability alternation at oil-water-rock interface. *Surface Science Reports.*
Tildesley, D. and Allen, M. 1987. *Computer simulation of liquids. Clarendon*. Oxford.
Tomin, P. and Lunati, I. 2013. Hybrid Multiscale Finite Volume method for two-phase flow in porous media. *Journal of Computational Physics.* **250**, pp.293-307.
Tryggvason, G., Bunner, B., Esmaeeli, A., Juric, D., Al-Rawahi, N., Tauber, W., Han, J., Nas, S. and Jan, Y.-J. 2001. A front-tracking method for the computations of multiphase flow. *Journal of Computational Physics.* **169**(2), pp.708-759.
Turgman-Cohen, S., Araque, J.C., Hoek, E.M. and Escobedo, F.A. 2013. Molecular dynamics of equilibrium and pressure-driven transport properties of water through LTA-type zeolites. *Langmuir.* **29**(40), pp.12389-12399.
Underwood, T., Erastova, V., Cubillas, P. and Greenwell, H.C. 2015. Molecular dynamic simulations of montmorillonite–organic interactions under varying

salinity: an insight into enhanced oil recovery. *The Journal of Physical Chemistry C.* **119**(13), pp.7282-7294.
Underwood, T.R. and Greenwell, H.C. 2018. The Water-Alkane Interface at Various NaCl Salt Concentrations: A Molecular Dynamics Study of the Readily Available Force Fields. *Scientific reports.* **8**(1), p352.
Vafaei, S. and Wen, D. 2010. The effect of gold nanoparticles on the spreading of triple line. *Microfluidics and Nanofluidics.* **8**(6), pp.843-848.
Van Buuren, A.R., Marrink, S.-J. and Berendsen, H.J. 1993. A molecular dynamics study of the decane/water interface. *Journal of Physical Chemistry.* **97**, pp.9206-9206.
Vogel, H.-J., Tölke, J., Schulz, V., Krafczyk, M. and Roth, K. 2005. Comparison of a lattice-Boltzmann model, a full-morphology model, and a pore network model for determining capillary pressure–saturation relationships. *Vadose Zone Journal.* **4**(2), pp.380-388.
Wang, F.-C. and Wu, H.-A. 2013. Enhanced oil droplet detachment from solid surfaces in charged nanoparticle suspensions. *Soft Matter.* **9**(33), pp.7974-7980.
Wang, F.-C. and Zhao, Y.-P. 2013. Contact angle hysteresis at the nanoscale: a molecular dynamics simulation study. *Colloid and Polymer Science.* **291**(2), pp.307-315.
Wang, F. and Wu, H. 2013. Molecular dynamics studies on spreading of nanofluids promoted by nanoparticle adsorption on solid surface. *Theoretical and Applied Mechanics Letters.* **3**(5).
Wang, Q., Xu, X.-H., Xu, L.-Y. and Chen, J. 2016. Formulation and optimization of load imbalance in the hybrid atomistic-continuum simulation based on geometric coupling.
Wasan, D.T. and Nikolov, A.D. 2003. Spreading of nanofluids on solids. *Nature.* **423**(6936), p156.
Werder, T., Walther, J.H. and Koumoutsakos, P. 2005. Hybrid atomistic–continuum method for the simulation of dense fluid flows. *Journal of Computational Physics.* **205**(1), pp.373-390.
Wright, K., Cygan, R.T. and Slater, B. 2001. Structure of the (101 [combining macron] 4) surfaces of calcite, dolomite and magnesite under wet and dry conditions. *Physical Chemistry Chemical Physics.* **3**(5), pp.839-844.
Yan, L., Yin, T., Yu, W., Shen, L., Lv, M. and Ye, Z. 2015. A water-soluble oil-displacing agent with tracer properties for enhancing oil recovery. *RSC Advances.* **5**(53), pp.42843-42847.
Yang, X., Scheibe, T.D., Richmond, M.C., Perkins, W.A., Vogt, S.J., Codd, S.L., Seymour, J.D. and McKinley, M.I. 2013. Direct numerical simulation of pore-scale flow in a bead pack: Comparison with magnetic resonance imaging observations. *Advances in water resources.* **54**, pp.228-241.
Yen, T., Soong, C. and Tzeng, P. 2007. Hybrid molecular dynamics-continuum simulation for nano/mesoscale channel flows. *Microfluidics and Nanofluidics.* **3**(6), pp.665-675.
Yong, C. 2010. DL_FIELD-a force field and model development tool for DL_POLY. *CSE Frontiers.* **2010**, pp.38-40.
Yong, C.W. and Todorov, I.T. 2017. DL_ANALYSER Notation for Atomic Interactions (DANAI): A Natural Annotation System for Molecular Interactions, Using Ethanoic Acid Liquid as a Test Case. *Molecules.* **23**(1), p36.
Youngs, T. 2010. Aten—An application for the creation, editing, and visualization of coordinates for glasses, liquids, crystals, and molecules. *Journal of computational chemistry.* **31**(3), pp.639-648.

Yousef, A.A., Al-Saleh, S.H., Al-Kaabi, A. and Al-Jawfi, M.S. 2011. Laboratory investigation of the impact of injection-water salinity and ionic content on oil recovery from carbonate reservoirs. *SPE Reservoir Evaluation & Engineering.* **14**(05), pp.578-593.
Yu, L. and Wardlaw, N.C. 1986. The influence of wettability and critical pore-throat size ratio on snap—off. *Journal of Colloid and Interface Science.* **109**(2), pp.461-472.
Yuen, P.S., Lister, M. and Nyburg, S. 1978. The four-center charge distribution of the carbonate ion and the lattice energies of calcite and aragonite. *The Journal of Chemical Physics.* **68**(4), pp.1936-1941.
Zeppieri, S., Rodríguez, J. and López de Ramos, A. 2001. Interfacial tension of alkane+ water systems. *Journal of Chemical & Engineering Data.* **46**(5), pp.1086-1088.
Zhang, C. and Carloni, P. 2012. Salt effects on water/hydrophobic liquid interfaces: a molecular dynamics study. *Journal of Physics: Condensed Matter.* **24**(12), p124109.
Zhang, H., Dong, M. and Zhao, S. 2010. Which one is more important in chemical flooding for enhanced court heavy oil recovery, lowering interfacial tension or reducing water mobility? *Energy & fuels.* **24**(3), pp.1829-1836.
Zhang, H., Nikolov, A. and Wasan, D. 2014. Enhanced oil recovery (EOR) using nanoparticle dispersions: underlying mechanism and imbibition experiments. *Energy & Fuels.* **28**(5), pp.3002-3009.
Zhang, L., Lu, X., Liu, X., Yang, K. and Zhou, H. 2016. Surface wettability of basal surfaces of clay minerals: Insights from molecular dynamics simulation. *Energy & Fuels.* **30**(1), pp.149-160.
Zhang, P., Tweheyo, M.T. and Austad, T. 2007. Wettability alteration and improved oil recovery by spontaneous imbibition of seawater into chalk: Impact of the potential determining ions Ca2+, Mg2+, and SO42−. *Colloids and Surfaces A: Physicochemical and Engineering Aspects.* **301**(1-3), pp.199-208.

Al-Anssari, S., Barifcani, A., Wang, S., Maxim, L. and Iglauer, S. 2016. Wettability alteration of oil-wet carbonate by silica nanofluid. *Journal of colloid and interface science.* **461**, pp.435-442.
Al-Khafaji, A., Neville, A., Wilson, M. and Wen, D. 2017. Effect of low salinity on the oil desorption efficiency from calcite and silica surfaces. *Energy & Fuels.* **31**(11), pp.11892-11901.
Al Shalabi, E.W., Sepehrnoori, K. and Delshad, M. 2014. Mechanisms behind low salinity water injection in carbonate reservoirs. *Fuel.* **121**, pp.11-19.
Alejandre, J., Tildesley, D.J. and Chapela, G.A. 1995. Fluid phase equilibria using molecular dynamics: the surface tension of chlorine and hexane. *Molecular Physics.* **85**(3), pp.651-663.
Austad, T., Shariatpanahi, S., Strand, S., Black, C. and Webb, K. 2011. Conditions for a low-salinity enhanced oil recovery (EOR) effect in carbonate oil reservoirs. *Energy & fuels.* **26**(1), pp.569-575.
Ballal, D., Venkataraman, P., Fouad, W.A., Cox, K.R. and Chapman, W.G. 2014. Isolating the non-polar contributions to the intermolecular potential for water-alkane interactions. *The Journal of chemical physics.* **141**(6), p064905.
Barnaji, M.J., Pourafshary, P. and Rasaie, M.R. 2016. Visual investigation of the effects of clay minerals on enhancement of oil recovery by low salinity water flooding. *Fuel.* **184**, pp.826-835.

Berendsen, H., Grigera, J. and Straatsma, T. 1987. The missing term in effective pair potentials. *Journal of Physical Chemistry.* **91**(24), pp.6269-6271.
Chen, Y., Xie, Q., Sari, A., Brady, P.V. and Saeedi, A. 2018. Oil/water/rock wettability: Influencing factors and implications for low salinity water flooding in carbonate reservoirs. *Fuel.* **215**, pp.171-177.
Chowdhuri, S. and Chandra, A. 2001. Molecular dynamics simulations of aqueous NaCl and KCl solutions: Effects of ion concentration on the single-particle, pair, and collective dynamical properties of ions and water molecules. *The Journal of Chemical Physics.* **115**(8), pp.3732-3741.
Cooke, D.J., Gray, R.J., Sand, K.K., Stipp, S.L.S. and Elliott, J. 2010. Interaction of ethanol and water with the {1014} surface of calcite. *Langmuir.* **26**(18), pp.14520-14529.
Dang, L.X. and Smith, D.E. 1993. Molecular dynamics simulations of aqueous ionic clusters using polarizable water. *The Journal of chemical physics.* **99**(9), pp.6950-6956.
de Leeuw, N. and Parker, S. 1997. Atomistic simulation of the effect of molecular adsorption of water on the surface structure and energies of calcite surfaces. *Journal of the Chemical Society, Faraday Transactions.* **93**(3), pp.467-475.
Ershadi, M., Alaei, M., Rashidi, A., Ramazani, A. and Khosravani, S. 2015. Carbonate and sandstone reservoirs wettability improvement without using surfactants for Chemical Enhanced Oil Recovery (C-EOR). *Fuel.* **153**, pp.408-415.
Fenter, P., Geissbühler, P., DiMasi, E., Srajer, G., Sorensen, L. and Sturchio, N. 2000. Surface speciation of calcite observed in situ by high-resolution X-ray reflectivity. *Geochimica et Cosmochimica Acta.* **64**(7), pp.1221-1228.
Fenter, P., Kerisit, S., Raiteri, P. and Gale, J.D. 2013. Is the calcite–water interface understood? Direct comparisons of molecular dynamics simulations with specular X-ray reflectivity data. *The Journal of Physical Chemistry C.* **117**(10), pp.5028-5042.
Ghanbari, E. and Dehghanpour, H. 2015. Impact of rock fabric on water imbibition and salt diffusion in gas shales. *International Journal of Coal Geology.* **138**, pp.55-67.
Hansen, J.-P. and McDonald, I.R. 1990. *Theory of simple liquids.* Elsevier.
Hill, T.L. 1960. *Statiscal-Thermodynamics.* Addison-Wesley.
Hilner, E., Andersson, M.P., Hassenkam, T., Matthiesen, J., Salino, P. and Stipp, S.L.S. 2015. The effect of ionic strength on oil adhesion in sandstone–the search for the low salinity mechanism. *Scientific reports.* **5**, p9933.
Jackson, M.D., Al-Mahrouqi, D. and Vinogradov, J. 2016. Zeta potential in oil-water-carbonate systems and its impact on oil recovery during controlled salinity water-flooding. *Scientific reports.* **6**, p37363.
Jadhunandan, P.P. 1990. *Effects of brine composition, crude oil, and aging conditions on wettability and oil recovery*. thesis, Department of Petroleum Engineering, New Mexico Institute of Mining & Technology.
Jang, S.S., Lin, S.-T., Maiti, P.K., Blanco, M., Goddard, W.A., Shuler, P. and Tang, Y. 2004. Molecular dynamics study of a surfactant-mediated decane− water interface: effect of molecular architecture of alkyl benzene sulfonate. *The Journal of Physical Chemistry B.* **108**(32), pp.12130-12140.
Jorgensen, W.L. and Tirado-Rives, J. 1988. The OPLS [optimized potentials for liquid simulations] potential functions for proteins, energy minimizations for crystals of cyclic peptides and crambin. *Journal of the American Chemical Society.* **110**(6), pp.1657-1666.

Kerisit, S. and Parker, S.C. 2004. Free energy of adsorption of water and metal ions on the {1014} calcite surface. *Journal of the American Chemical Society.* **126**(32), pp.10152-10161.
Koneshan, S., Rasaiah, J.C., Lynden-Bell, R. and Lee, S. 1998. Solvent structure, dynamics, and ion mobility in aqueous solutions at 25 C. *The Journal of Physical Chemistry B.* **102**(21), pp.4193-4204.
Kumar, S. and Mandal, A. 2016. Studies on interfacial behavior and wettability change phenomena by ionic and nonionic surfactants in presence of alkalis and salt for enhanced oil recovery. *Applied Surface Science.* **372**, pp.42-51.
Kunieda, M., Liang, Y., Fukunaka, Y., Matsuoka, T., Takamura, K., Loahardjo, N., Winoto, W. and Morrow, N.R. 2012. Spreading of multi-component oils on water. *Energy & Fuels.* **26**(5), pp.2736-2741.
Lashkarbolooki, M., Riazi, M., Ayatollahi, S. and Hezave, A.Z. 2016. Synergy effects of ions, resin, and asphaltene on interfacial tension of acidic crude oil and low–high salinity brines. *Fuel.* **165**, pp.75-85.
Ma, Y.Z. and Holditch, S. 2015. *Unconventional oil and gas resources handbook: Evaluation and development.* Gulf professional publishing.
Mahani, H., Keya, A.L., Berg, S., Bartels, W.-B., Nasralla, R. and Rossen, W.R. 2015. Insights into the mechanism of wettability alteration by low-salinity flooding (LSF) in carbonates. *Energy & Fuels.* **29**(3), pp.1352-1367.
Martínez, L., Andrade, R., Birgin, E.G. and Martínez, J.M. 2009. PACKMOL: a package for building initial configurations for molecular dynamics simulations. *Journal of computational chemistry.* **30**(13), pp.2157-2164.
McMillan, M.D., Rahnema, H., Romiluy, J. and Kitty, F.J. 2016. Effect of exposure time and crude oil composition on low-salinity water flooding. *Fuel.* **185**, pp.263-272.
Mitrinović, D.M., Tikhonov, A.M., Li, M., Huang, Z. and Schlossman, M.L. 2000. Noncapillary-wave structure at the water-alkane interface. *Physical review letters.* **85**(3), p582.
Module, F. 2011. Material Studio 6.0. *Accelrys Inc., San Diego, CA.*
Mohammed, S. and Mansoori, G.A. 2018. Effect of CO2 on the Interfacial and Transport Properties of Water/Binary and Asphaltenic Oils: Insights from Molecular Dynamics. *Energy & Fuels.* **32**(4), pp.5409-5417.
Momma, K. and Izumi, F. 2008. VESTA: a three-dimensional visualization system for electronic and structural analysis. *Journal of Applied Crystallography.* **41**(3), pp.653-658.
Morrow, N. and Buckley, J. 2011. Improved oil recovery by low-salinity waterflooding. *Journal of Petroleum Technology.* **63**(05), pp.106-112.
Myint, P.C. and Firoozabadi, A. 2015. Thin liquid films in improved oil recovery from low-salinity brine. *Current Opinion in Colloid & Interface Science.* **20**(2), pp.105-114.
Nasralla, R.A., Bataweel, M.A. and Nasr-El-Din, H.A. 2013. Investigation of wettability alteration and oil-recovery improvement by low-salinity water in sandstone rock. *Journal of Canadian Petroleum Technology.* **52**(02), pp.144-154.
Nasralla, R.A. and Nasr-El-Din, H.A. 2014. Double-layer expansion: is it a primary mechanism of improved oil recovery by low-salinity waterflooding? *SPE Reservoir Evaluation & Engineering.* **17**(01), pp.49-59.
Nicolini, J.V., Ferraz, H.C. and Borges, C.P. 2017. Effect of seawater ionic composition modified by nanofiltration on enhanced oil recovery in Berea sandstone. *Fuel.* **203**, pp.222-232.

Ono, S. and Kondo, S. 1960. Molecular theory of surface tension in liquids. *Structure of Liquids/Struktur der Flüssigkeiten.* Springer, pp.134-280.
Pereira, J.F., Costa, R., Foios, N. and Coutinho, J.A. 2014. Ionic liquid enhanced oil recovery in sand-pack columns. *Fuel.* **134**, pp.196-200.
Puntervold, T., Strand, S., Ellouz, R. and Austad, T. 2015. Modified seawater as a smart EOR fluid in chalk. *Journal of Petroleum Science and Engineering.* **133**, pp.440-443.
Raiteri, P. and Gale, J.D. 2010. Water is the key to nonclassical nucleation of amorphous calcium carbonate. *Journal of the American Chemical Society.* **132**(49), pp.17623-17634.
Raiteri, P., Gale, J.D., Quigley, D. and Rodger, P.M. 2010. Derivation of an accurate force-field for simulating the growth of calcium carbonate from aqueous solution: a new model for the calcite− water interface. *The Journal of Physical Chemistry C.* **114**(13), pp.5997-6010.
RezaeiDoust, A., Puntervold, T. and Austad, T. 2011. Chemical verification of the EOR mechanism by using low saline/smart water in sandstone. *Energy & Fuels.* **25**(5), pp.2151-2162.
Roberto, M.F., Marco, B. and Dino, A. 2010. Effect of the surface relaxation on the theoretical equilibrium shape of calcite. 1. The [001] zone. *Crystal Growth & Design.* **10**(9), pp.4096-4100.
Ryckaert, J.-P. and Bellemans, A. 1978. Molecular dynamics of liquid alkanes. *Faraday Discussions of the Chemical Society.* **66**, pp.95-106.
Sakthivel, S., Velusamy, S., Nair, V.C., Sharma, T. and Sangwai, J.S. 2017. Interfacial tension of crude oil-water system with imidazolium and lactam-based ionic liquids and their evaluation for enhanced oil recovery under high saline environment. *Fuel.* **191**, pp.239-250.
Senapati, S. and Berkowitz, M.L. 2001. Computer simulation study of the interface width of the liquid/liquid interface. *Physical review letters.* **87**(17), p176101.
Shariatpanahi, S., Hopkins, P., Aksulu, H., Strand, S., Puntervold, T. and Austad, T. 2016. Water based EOR by wettability alteration in dolomite. *Energy & Fuels.* **30**(1), pp.180-187.
Shariatpanahi, S.F., Strand, S. and Austad, T. 2010. Evaluation of water-based enhanced oil recovery (EOR) by wettability alteration in a low-permeable fractured limestone oil reservoir. *Energy & Fuels.* **24**(11), pp.5997-6008.
Shen, J.-W., Li, C., van der Vegt, N.F. and Peter, C. 2013. Understanding the control of mineralization by polyelectrolyte additives: simulation of preferential binding to calcite surfaces. *The Journal of Physical Chemistry C.* **117**(13), pp.6904-6913.
Sheng, J. 2014. Critical review of low-salinity waterflooding. *Journal of Petroleum Science and Engineering.* **120**, pp.216-224.
Smith, W., Yong, C. and Rodger, P. 2002. DL_POLY: Application to molecular simulation. *Molecular Simulation.* **28**(5), pp.385-471.
Song, R.-Q., Cölfen, H., Xu, A.-W., Hartmann, J.r. and Antonietti, M. 2009. Polyelectrolyte-directed nanoparticle aggregation: systematic morphogenesis of calcium carbonate by nonclassical crystallization. *Acs Nano.* **3**(7), pp.1966-1978.
Spyrou, M. 2009. *The Diffusion Coefficient of Water: A Neutron Scattering Study using Molecular Dynamics Simulations*. thesis, Tesis de Maestría, Surrey-Inglaterra.
Tian, H. and Wang, M. 2018. Electrokinetic mechanism of wettability alternation at oil-water-rock interface. *Surface Science Reports.*

Underwood, T., Erastova, V., Cubillas, P. and Greenwell, H.C. 2015. Molecular dynamic simulations of montmorillonite–organic interactions under varying salinity: an insight into enhanced oil recovery. *The Journal of Physical Chemistry C.* **119**(13), pp.7282-7294.
Underwood, T.R. and Greenwell, H.C. 2018. The Water-Alkane Interface at Various NaCl Salt Concentrations: A Molecular Dynamics Study of the Readily Available Force Fields. *Scientific reports.* **8**(1), p352.
Vasconcelos, I.F., Bunker, B.A. and Cygan, R.T. 2007. Molecular dynamics modeling of ion adsorption to the basal surfaces of kaolinite. *The Journal of Physical Chemistry C.* **111**(18), pp.6753-6762.
Yousef, A.A., Al-Saleh, S.H., Al-Kaabi, A. and Al-Jawfi, M.S. 2011. Laboratory investigation of the impact of injection-water salinity and ionic content on oil recovery from carbonate reservoirs. *SPE Reservoir Evaluation & Engineering.* **14**(05), pp.578-593.
Zeppieri, S., Rodríguez, J. and López de Ramos, A. 2001. Interfacial tension of alkane+ water systems. *Journal of Chemical & Engineering Data.* **46**(5), pp.1086-1088.
Zhang, H., Dong, M. and Zhao, S. 2010. Which one is more important in chemical flooding for enhanced court heavy oil recovery, lowering interfacial tension or reducing water mobility? *Energy & fuels.* **24**(3), pp.1829-1836.
Zhang, L., Lu, X., Liu, X., Yang, K. and Zhou, H. 2016. Surface wettability of basal surfaces of clay minerals: Insights from molecular dynamics simulation. *Energy & Fuels.* **30**(1), pp.149-160.
Zhang, P., Tweheyo, M.T. and Austad, T. 2007. Wettability alteration and improved oil recovery by spontaneous imbibition of seawater into chalk: Impact of the potential determining ions Ca2+, Mg2+, and SO42−. *Colloids and Surfaces A: Physicochemical and Engineering Aspects.* **301**(1-3), pp.199-208.
Zussman, J., Howie, R. and Deer, W. 1992. An introduction to the rock forming minerals. *Longman Group Ltd, New York, p 698Defant MJ, Drummond MS (1990) Derivation of some modern arc magmas by melting of young subducted lithosphere. Nature.* **347**, p662665Della.

Abidin, A., Puspasari, T. and Nugroho, W. 2012. Polymers for enhanced oil recovery technology. *Procedia Chemistry.* **4**, pp.11-16.
Afkhami, S., Zaleski, S. and Bussmann, M. 2009. A mesh-dependent model for applying dynamic contact angles to VOF simulations. *Journal of computational physics.* **228**(15), pp.5370-5389.
Afsharpoor, A., Balhoff, M.T., Bonnecaze, R. and Huh, C. 2012. CFD modeling of the effect of polymer elasticity on residual oil saturation at the pore-scale. *Journal of Petroleum Science and Engineering.* **94**, pp.79-88.
Andrew, M., Bijeljic, B. and Blunt, M.J. 2014. Pore-scale contact angle measurements at reservoir conditions using X-ray microtomography. *Advances in Water Resources.* **68**, pp.24-31.
Arns, C.H., Knackstedt, M.A., Pinczewski, W.V. and Garboczi, E.J. 2002. Computation of linear elastic properties from microtomographic images: Methodology and agreement between theory and experiment. *Geophysics.* **67**(5), pp.1396-1405.
Bagrintseva, K.I. 2015. *Carbonate reservoir rocks.* John Wiley & Sons.
Beresnev, I.A. and Deng, W. 2010. Theory of breakup of core fluids surrounded by a wetting annulus in sinusoidally constricted capillary channels. *Physics of Fluids.* **22**(1), p012105.

Brackbill, J., Kothe, D.B. and Zemach, C. 1992. A continuum method for modeling surface tension. *Journal of computational physics.* **100**(2), pp.335-354.
Clemens, T., Tsikouris, K., Buchgraber, M., Castanier, L.M. and Kovscek, A. 2013. Pore-Scale Evaluation of Polymers Displacing Viscous Oil--Computational-Fluid-Dynamics Simulation of Micromodel Experiments. *Spe Reservoir Evaluation & Engineering.* **16**(02), pp.144-154.
Coalson, E.B., Goolsby, S.M. and Franklin, M.H. 1994. Subtle seals and fluid-flow barriers in carbonate rocks.
Deng, W. 2010. Quantitative aspects of vibratory mobilization and break-up of non-wetting fluids in porous media.
Deng, W., Balhoff, M. and Cardenas, M.B. 2015. Influence of dynamic factors on nonwetting fluid snap-off in pores. *Water Resources Research.* **51**(11), pp.9182-9189.
Deng, W. and Cardenas, M.B. 2013. Dynamics and dislodgment from pore constrictions of a trapped nonwetting droplet stimulated by seismic waves. *Water Resources Research.* **49**(7), pp.4206-4218.
Esfandyari Bayat, A., Junin, R., Samsuri, A., Piroozian, A. and Hokmabadi, M. 2014. Impact of metal oxide nanoparticles on enhanced oil recovery from limestone media at several temperatures. *Energy & Fuels.* **28**(10), pp.6255-6266.
Ferrari, A. and Lunati, I. 2013. Direct numerical simulations of interface dynamics to link capillary pressure and total surface energy. *Advances in water resources.* **57**, pp.19-31.
Fukai, J., Shiiba, Y., Yamamoto, T., Miyatake, O., Poulikakos, D., Megaridis, C. and Zhao, Z. 1995. Wetting effects on the spreading of a liquid droplet colliding with a flat surface: experiment and modeling. *Physics of Fluids.* **7**(2), pp.236-247.
Gou, S., Luo, S., Liu, T., Xia, H., Jing, D., Zhang, Q., Li, S., Li, Z. and Guo, Q. 2015. Thermally stable imidazoline-based sulfonate copolymers for enhanced oil recovery. *RSC advances.* **5**(104), pp.85165-85173.
Hendraningrat, L., Li, S. and Torsæter, O. 2013. A coreflood investigation of nanofluid enhanced oil recovery. *Journal of Petroleum Science and Engineering.* **111**, pp.128-138.
Hirasaki, G., Miller, C.A. and Puerto, M. 2011. Recent advances in surfactant EOR. *SPE Journal.* **16**(04), pp.889-907.
Hirt, C.W. and Nichols, B.D. 1981. Volume of fluid (VOF) method for the dynamics of free boundaries. *Journal of computational physics.* **39**(1), pp.201-225.
Horgue, P., Augier, F., Duru, P., Prat, M. and Quintard, M. 2013. Experimental and numerical study of two-phase flows in arrays of cylinders. *Chemical Engineering Science.* **102**, pp.335-345.
Hu, Z., Azmi, S.M., Raza, G., Glover, P.W. and Wen, D. 2016. Nanoparticle-assisted water-flooding in Berea sandstones. *Energy & Fuels.* **30**(4), pp.2791-2804.
Hu, Z., Zhao, J., Gao, H., Nourafkan, E. and Wen, D. 2017. Transport and deposition of carbon nanoparticles in saturated porous media. *Energies.* **10**(8), p1151.
Kallel, W., van Dijke, M., Sorbie, K., Wood, R., Jiang, Z. and Harland, S. 2016. Modelling the effect of wettability distributions on oil recovery from microporous carbonate reservoirs. *Advances in water resources.* **95**, pp.317-328.
Kiss, É., Pintér, J. and Wolfram, E. 1982. Dynamics of oil/water displacement in capillary tubes with periodically varying diameter. *Colloid and Polymer Science.* **260**(8), pp.808-810.

Ko, K.M., Chon, B.H., Jang, S.B. and Jang, H.Y. 2014. Surfactant flooding characteristics of dodecyl alkyl sulfate for enhanced oil recovery. *Journal of Industrial and Engineering Chemistry.* **20**(1), pp.228-233.
Kondiparty, K., Nikolov, A., Wu, S. and Wasan, D. 2011. Wetting and spreading of nanofluids on solid surfaces driven by the structural disjoining pressure: statics analysis and experiments. *Langmuir.* **27**(7), pp.3324-3335.
Kunieda, M., Liang, Y., Fukunaka, Y., Matsuoka, T., Takamura, K., Loahardjo, N., Winoto, W. and Morrow, N.R. 2012. Spreading of multi-component oils on water. *Energy & Fuels.* **26**(5), pp.2736-2741.
Liu, R.C., Pallier, A., Brestaz, M., Pantoustier, N. and Tribet, C. 2007. Impact of polymer microstructure on the self-assembly of amphiphilic polymers in aqueous solutions. *Macromolecules.* **40**(12), pp.4276-4286.
Lv, M. and Wang, S. 2015. Pore-scale modeling of a water/oil two-phase flow in hot water flooding for enhanced oil recovery. *RSC Advances.* **5**(104), pp.85373-85382.
Matteo, C., Candido, P., Vera, R. and Francesca, V. 2012. Current and future nanotech applications in the oil industry. *American Journal of Applied Sciences.* **9**(6).
Meakin, P. and Tartakovsky, A.M. 2009. Modeling and simulation of pore-scale multiphase fluid flow and reactive transport in fractured and porous media. *Reviews of Geophysics.* **47**(3).
Meybodi, H.E., Kharrat, R. and Wang, X. 2011. Study of microscopic and macroscopic displacement behaviors of polymer solution in water-wet and oil-wet media. *Transport in porous media.* **89**(1), pp.97-120.
Nelson, P.H. 2009. Pore-throat sizes in sandstones, tight sandstones, and shales. *AAPG bulletin.* **93**(3), pp.329-340.
Olajire, A.A. 2014. Review of ASP EOR (alkaline surfactant polymer enhanced oil recovery) technology in the petroleum industry: Prospects and challenges. *Energy.* **77**, pp.963-982.
Peng, B., Zhang, L., Luo, J., Wang, P., Ding, B., Zeng, M. and Cheng, Z. 2017. A review of nanomaterials for nanofluid enhanced oil recovery. *RSC Advances.* **7**(51), pp.32246-32254.
Raeini, A.Q., Bijeljic, B. and Blunt, M.J. 2015. Modelling capillary trapping using finite-volume simulation of two-phase flow directly on micro-CT images. *Advances in water resources.* **83**, pp.102-110.
Raffa, P., Broekhuis, A.A. and Picchioni, F. 2016. Polymeric surfactants for enhanced oil recovery: a review. *Journal of Petroleum Science and Engineering.* **145**, pp.723-733.
Raffa, P., Wever, D.A.Z., Picchioni, F. and Broekhuis, A.A. 2015. Polymeric surfactants: synthesis, properties, and links to applications. *Chemical Reviews.* **115**(16), pp.8504-8563.
Saffman, P.G. and Taylor, G.I. 1958. The penetration of a fluid into a porous medium or Hele-Shaw cell containing a more viscous liquid. *Proc. R. Soc. Lond. A.* **245**(1242), pp.312-329.
Samanta, A., Ojha, K., Sarkar, A. and Mandal, A. 2011. Surfactant and surfactant-polymer flooding for enhanced oil recovery. *Advances in Petroleum Exploration and Development.* **2**(1), pp.13-18.
Schlüter, S., Berg, S., Rücker, M., Armstrong, R., Vogel, H.J., Hilfer, R. and Wildenschild, D. 2016. Pore-scale displacement mechanisms as a source of hysteresis for two-phase flow in porous media. *Water Resources Research.* **52**(3), pp.2194-2205.

Sefiane, K., Skilling, J. and MacGillivray, J. 2008. Contact line motion and dynamic wetting of nanofluid solutions. *Advances in colloid and interface science.* **138**(2), pp.101-120.
Setiawan, A., Suekane, T., Deguchi, Y. and Kusano, K. 2014. Three-dimensional imaging of pore-scale water flooding phenomena in water-wet and oil-wet porous media. *Journal of Flow Control, Measurement & Visualization.* **2**(02), p25.
Setu, S.A., Zacharoudiou, I., Davies, G.J., Bartolo, D., Moulinet, S., Louis, A.A., Yeomans, J.M. and Aarts, D.G. 2013. Viscous fingering at ultralow interfacial tension. *Soft Matter.* **9**(44), pp.10599-10605.
Sheng, J.J. 2015. Preferred calculation formula and buoyancy effect on capillary number. *Asia-Pacific Journal of Chemical Engineering.* **10**(3), pp.400-410.
Skauge, A., Spildo, K., Høiland, L. and Vik, B. 2007. Theoretical and experimental evidence of different wettability classes. *Journal of Petroleum Science and Engineering.* **57**(3-4), pp.321-333.
Tomin, P. and Lunati, I. 2013. Hybrid Multiscale Finite Volume method for two-phase flow in porous media. *Journal of Computational Physics.* **250**, pp.293-307.
Tryggvason, G., Bunner, B., Esmaeeli, A., Juric, D., Al-Rawahi, N., Tauber, W., Han, J., Nas, S. and Jan, Y.-J. 2001. A front-tracking method for the computations of multiphase flow. *Journal of Computational Physics.* **169**(2), pp.708-759.
Vafaei, S. and Wen, D. 2010. The effect of gold nanoparticles on the spreading of triple line. *Microfluidics and Nanofluidics.* **8**(6), pp.843-848.
Wang, F.-C. and Wu, H.-A. 2013. Enhanced oil droplet detachment from solid surfaces in charged nanoparticle suspensions. *Soft Matter.* **9**(33), pp.7974-7980.
Wang, F.-C. and Zhao, Y.-P. 2013. Contact angle hysteresis at the nanoscale: a molecular dynamics simulation study. *Colloid and Polymer Science.* **291**(2), pp.307-315.
Wang, F. and Wu, H. 2013. Molecular dynamics studies on spreading of nanofluids promoted by nanoparticle adsorption on solid surface. *Theoretical and Applied Mechanics Letters.* **3**(5).
Wasan, D.T. and Nikolov, A.D. 2003. Spreading of nanofluids on solids. *Nature.* **423**(6936), p156.
Wever, D., Picchioni, F. and Broekhuis, A. 2011. Polymers for enhanced oil recovery: a paradigm for structure–property relationship in aqueous solution. *Progress in Polymer Science.* **36**(11), pp.1558-1628.
White, F.M. and Corfield, I. 2006. *Viscous fluid flow, vol. 3*. McGraw-Hill New York.
Yan, L., Yin, T., Yu, W., Shen, L., Lv, M. and Ye, Z. 2015. A water-soluble oil-displacing agent with tracer properties for enhancing oil recovery. *RSC Advances.* **5**(53), pp.42843-42847.
Yang, X., Scheibe, T.D., Richmond, M.C., Perkins, W.A., Vogt, S.J., Codd, S.L., Seymour, J.D. and McKinley, M.I. 2013. Direct numerical simulation of pore-scale flow in a bead pack: Comparison with magnetic resonance imaging observations. *Advances in water resources.* **54**, pp.228-241.
Yu, Q., Jiang, H. and Zhao, C. 2010. Study of interfacial tension between oil and surfactant polymer flooding. *Petroleum Science and Technology.* **28**(18), pp.1846-1854.
Zhang, H., Dong, M. and Zhao, S. 2010. Which one is more important in chemical flooding for enhanced court heavy oil recovery, lowering interfacial tension or reducing water mobility? *Energy & fuels.* **24**(3), pp.1829-1836.
Zhang, H., Nikolov, A. and Wasan, D. 2014. Dewetting film dynamics inside a capillary using a micellar nanofluid. *Langmuir.* **30**(31), pp.9430-9435.

Andrew, M., Bijeljic, B. and Blunt, M.J. 2014. Pore-by-pore capillary pressure measurements using X-ray microtomography at reservoir conditions: Curvature, snap-off, and remobilization of residual CO2. *Water Resources Research.* **50**(11), pp.8760-8774.

Denney, D. 2009. Low-salinity waterflooding improves oil recovery-Historical field evidence. *Journal of Petroleum Technology.* **61**(01), pp.47-49.

Frenkel, D. and Smit, B. 2001. *Understanding molecular simulation: from algorithms to applications.* Elsevier.

Morrow, N. and Buckley, J. 2011. Improved oil recovery by low-salinity waterflooding. *Journal of Petroleum Technology.* **63**(05), pp.106-112.

Muggeridge, A., Cockin, A., Webb, K., Frampton, H., Collins, I., Moulds, T. and Salino, P. 2014. Recovery rates, enhanced oil recovery and technological limits. *Phil. Trans. R. Soc. A.* **372**(2006), p20120320.

Pak, T., Butler, I., Geiger, S., van Dijke, M.I., Jiang, Z., Elphick, S. and Sorbie, K.S. 2013. Pore-Scale Visualisation of Two-Phase Fluid Displacement Processes in a Carbonate Rock using X-ray micro-TomographyTechnique. In: *SPE Reservoir Characterization and Simulation Conference and Exhibition*: Society of Petroleum Engineers.

Sayegh, R., Faghri, M., Asako, Y. and Sundén, B. 2004. Direct simulation Monte Carlo of gaseous flow and heat transfer in a microchannel. *Heat and Fluid Flow in Microscale and Nanoscale Structures.*

Setiawan, A., Suekane, T., Deguchi, Y. and Kusano, K. 2014. Three-dimensional imaging of pore-scale water flooding phenomena in water-wet and oil-wet porous media. *Journal of Flow Control, Measurement & Visualization.* **2**(02), p25.

Smalley, P.C., Ross, A.W., Brown, C., Moulds, T.P. and Smith, M.J. 2009. Reservoir technical limits: a framework for maximizing recovery from oil fields. *SPE Reservoir Evaluation & Engineering.* **12**(04), pp.610-629.

Zerpa, L.E., Queipo, N.V., Pintos, S. and Salager, J.-L. 2005. An optimization methodology of alkaline–surfactant–polymer flooding processes using field scale numerical simulation and multiple surrogates. *Journal of Petroleum Science and Engineering.* **47**(3-4), pp.197-208.

Appendix A

Non-bonded parameters for water, n-decane, ions, and the calcite surface in Molecular Dynamics simulations

This appendix shows the definition of atom type, mass, charge, and Lennard-Jones parameters.

Table A1 Non-bonded parameters for water, n-decane, ions, and the calcite surface

Atom specification	Symbols	Mass, g/mol	Charge, *e*	ε_{ii}, kcal/mol	σ_{ii}, Å
For Water					
Oxygen atom in SPC/E water	OW	15.9994	-0.8476	0.1554	3.1660
Hydrogen atom in SPC/E water	HW	1.0080	0.4238	0.0000	0.0000
For n-Decane					
Carbon atom in –CH_3	C3	12.0115	-0.180	0.0660	3.5000
Carbon atom in –CH_2–	C2	12.0115	-0.120	0.0660	3.5000
Hydrogen atom in alkanes	HC	1.00797	0.060	0.0300	2.5000
For Aqueous Ions					
Aqueous sodium ion	Na	22.9900	1.0000	0.1301	2.350001
Aqueous chloride ion	Cl	35.4530	-1.0000	0.1001	4.39997
For Calcite					
Carbon atom in calcite	C	12.0107	1.123282	0.10492	2.8950
Calcium atom in calcite	Ca	40.0780	2.0000	0.10007	3.7500

Oxygen atom in calcite	O	15.9994	-1.041094	0.21009	2.9600

Appendix B

Bonded parameters for the water, n-decane, and the calcite surface in Molecular Dynamics simulations

This appendix shows the parameters in bonding interactions, which are given by:

$$U_{\mathrm{b}}(r_{ij}) = \frac{1}{2}k_{\mathrm{ij}}{}^{b}(r_{ij}\text{-}b_{ij})^2 \quad (1)$$

the parameters in angle interactions, which are given by:

$$U_{\theta}(\theta_{ijk}) = \frac{1}{2}k_{\mathrm{ijk}}{}^{\theta}(\theta_{ijk}\text{-}\theta_{ijk}{}^{0})^2 \quad (2)$$

the parameters in dihedral interactions, which is given by:

$$U_{d}(\phi_{ijkl}) = A_0+\frac{1}{2}\{A_1[1+\cos(\phi)]+A_2(1-\cos(2\phi))]+A_3[1+\cos(3\phi)]\} \quad (3)$$

Table A2 Bonded parameters for water, n-decane, and the calcite surface

	Bond type	k_r, kcal/(mol·Å^2)	r_0, Å
Bond stretch	OW-HW	554.1349	1.0000
	C2-C2	268.0000	1.5290
	C3-C2	268.0000	1.5290
	C3-HC	340.0000	1.0900
	C2-HC	340.0000	1.0900
	Angle type	k_θ, kcal/(mol·rad^2)	θ_0, deg
Angle bend	HW-OW-HW	45.7696	109.47
	C3-C2-C2	58.3500	112.70
	C2-C2-C2	58.3500	112.70
	HC-C3-C2	37.5000	110.70
	HC-C2-C2	37.5000	110.70

HC-C2-C3	37.5000	110.70
HC-C2-HC	33.0000	107.80
HC-C3-HC	33.0000	107.80

	Dihedral type	A_0, kcal/mol	A_1, kcal/mol	A_2, kcal/mol	A_3, kcal/mol
Dihedrals	C3-C2-C2-C2	0.000	1.300	-0.050	0.200
	C2-C2-C2-C2	0.000	1.300	-0.050	0.200
	HC-C3-C2-C2	0.000	0.000	0.000	0.300
	HC-C2-C2-C2	0.000	0.000	0.000	0.300
	HC-C2-C2-C3	0.000	0.000	0.000	0.300
	HC-C3-C2-HC	0.000	0.000	0.000	0.300
	HC-C2-C2-HC	0.000	0.000	0.000	0.300